A METHODOLOGY FOR THE VALIDATED DESIGN SPACE EXPLORATION OF FUEL CELL POWERED UNMANNED AERIAL VEHICLES

A Dissertation
Presented to
The Academic Faculty

by

Blake Almy Moffitt

In Partial Fulfillment
of the Requirements for the Degree
Doctor of Philosophy in the
School of Aerospace Engineering

Georgia Institute of Technology
May 2010

A METHODOLOGY FOR THE VALIDATED DESIGN SPACE EXPLORATION OF FUEL CELL POWERED UNMANNED AERIAL VEHICLES

Approved by:

Professor Dimitri N. Mavris,
Committee Chair
School of Aerospace Engineering
Georgia Institute of Technology

Dr. David E. Parekh
Vice President, Research, and Director
United Technologies Research Center
United Technologies Corporation

Professor Vitali Volovoi
School of Aerospace Engineering
Georgia Institute of Technology

Dr. Danielle S. Soban
School of Aerospace Engineering
Georgia Institute of Technology

Dr. Taewoo Nam
School of Aerospace Engineering
Georgia Institute of Technology

Date Approved: March 31, 2010

To my wife, Jan,

and my kids, Ethan, Almy and Nolan.

ACKNOWLEDGEMENTS

I would first like to thank my advisor, Professor Dimitri Mavris, for his support throughout my graduate studies at the Georgia Institute of Technology. Professor Mavris introduced me to the subject of this dissertation, redefined my understanding of the purpose of the PhD process, gave me freedom that provided an unparallel although sometimes challenging learning experience, and provided me with encouragement, correction, and support that all proved essential in completing this endeavor. Thank you Dr. Mavris for working tirelessly to provide me with this opportunity and help me realize my goals.

I must also give a considerable amount of credit to Dr. David Parekh. Dr. Parekh provided the initial inspiration to pursue this topic in detail and offered unending support throughout the seemingly insurmountable challenges that were overcome along the way. Dr. Parekh's unique ability to ask difficult questions helped me to continually define the research and gain a more valuable perspective on research in general.

Thanks is also well deserved by my committee members, Dr. Danielle Soban, Professor Vitali Volovoi, and Dr. Taewoo Nam. Each provided valuable support and technical expertise that helped me complete this project.

Thanks to my collaborator, Dr. Thomas Bradley. Thomas was there to support and compliment this work throughout the entire process. The successes of this work would not have been realized without his expertise, unmatched motivation, and constant support.

This work would not have been possible without significant financial support. I must thank the Aerospace Systems Design Laboratory, the Georgia Tech Research

Institute, the NASA University Research Engineering Technology Institute (URETI), and the United Technologies Employee Scholar Program for their role in making this research possible.

I must also thank the Georgia Institute of Technology. Various facilities, departments, professors, technicians, and students were called upon during this research. Collectively, they provided a resource that made everything possible.

This work would also not be possible without Dr. Frank J. Redd and Professor J. Clair Batty. As a young engineering student, Dr. Redd and Professor Batty treated me as a valuable colleague, praised my successes, corrected my mistakes, and most importantly, convinced me that I was capable of achieving this goal.

Finally, none of this would have been possible without my family. I have overtaxed my wife and children through this process yet they continue to love and support me. Thanks Ethan, Almy, and Nolan for you inspiration and love. Your enthusiasm, affection, and love have been invaluable. And most of all, thank you Jan for letting me pursue and complete this goal. Your lot has been the most difficult yet you have tirelessly faced the challenge of supporting your husband as he struggled through this endeavor. Thanks for keeping our family together and nurturing our beautiful children during this difficult process.

South Windsor, CT

November 5, 2009

TABLE OF CONTENTS

LIST OF TABLES

Page

LIST OF FIGURES

Page

LIST OF SYMBOLS AND ABBREVIATIONS

AR	wing aspect ratio
a	outside radius parameter of the fuselage
a_{ij}	coefficient in neural network equation
a_{RK}	Redlich-Kwong equation of state parameter a, $K^{1/2} \cdot m^6 \cdot Pa \cdot mol^{-2}$
b	fuselage tapering distance parameter
b	main wing span, m
b_{jk}	coefficient in neural network equation
b_{RK}	Redlich-Kwong equation of state parameter b, $m^3 \cdot mol^{-1}$
b_T	spanwise distance from wing root to location of tapered section, m
b_t	tail span, m
C_{Lwt}	lift coefficient of the wing and tail
C_D	drag coefficient
$\tilde{C}_D$	airfoil section drag coefficient
C_{Dcross}	cross flow drag coefficient
C_{Dfuse}	fuselage drag coefficient
C_{D0fuse}	fuselage drag coefficient at zero lift
C_{DLfuse}	fuselage drag coefficient due to lift
C_{Dbfuse}	drag due to the aft base of the fuselage
C_{Dwt}	drag coefficient of the wing and tail
C_{fuse}	fuselage skin friction coefficient
C_L	lift coefficient
$\tilde{C}_L$	airfoil section lift coefficient
C_n	yawing moment coefficient

C_{nb}	yawing stiffness, rad^{-1}
C_P	propeller power coefficient
C_Q	propeller torque coefficient
C_R	climb rate, m/min
C_T	propeller thrust coefficient
$C_{T,installed}$	propeller thrust coefficient modified for installation effects
c	wing root chord length, m
c_b	airfoil section chord length, m
c_j	coefficient in neural network equation
c_w	wing chord length, m
$\tilde{D}$	airfoil section drag, N
D_c	duty cycle of motor
d_{H2}	hydrogen tank diameter, m
d_{hv}	diameter of helicoidal vortex sheet far behind the propeller, m
d_k	coefficient in neural network equation
d_p	propeller diameter, m
E	expected value of a function
E_0	fuel cell zero current voltage at the cell level, A
E_m	motor voltage, V
F	Faraday's constant
F	pseudo objective function
FOS	factor of safety
f	Prandtl's tip loss factor
f	function
f_{2H}	upper limit of a function

f_{2L}	lower limit of a function
f_{2T}	target value of a function
f_{mount}	hydrogen tank mounting/bosses/tubing mass fraction
f_{λ}	fuel cell polarization curve parameter
G	Gibb's free energy, kJ/mol
G	biplane wing vertical distance, m
$G(r_{hv})$	Goldstein circulation function
G_R	gear ratio
g	constraint function
H	enthalpy, kJ/mol
H_j	unobserved hidden nodes in neural network
h	axial distance between adjacent turns of a vortex sheet
$\mathbf{I}$	identity matrix
I_0	motor current at zero load, A
I_{FC}	fuel cell current at full throttle, A
I_{fc}	fuel cell current, A
I_m	motor current,A
I_{max}	maximum fuel cell current, A
I_p	current dedicated to generating propulsion power, A
i	index counter
J	propeller advance ratio
j	fuel cell area specific current, $A \cdot cm^{-2}$
j	index counter
j_*	fuel cell polarization curve parameter
j_{D0}	fuel cell polarization curve parameter

K_c	propeller linear pitch over linear diameter ratio
K_v	motor voltage constant, rad/V, rpm/V
k	index counter
k_{blades}	number of propeller blades
k_{loss}	linear efficiency loss of the electric motor controller
$\tilde{L}$	airfoil section lift, N/m
L_{pay}	payload length, m
l	hydrogen storage tank length, m
l_f	fuselage length, m
l_{np}	distance from the center of gravity to the neutral point, m
l_t	length from the wing ¼ chord to the tail ¼ chord, m
M_{tip}	Mach number at the propeller tip
$m_{composite}$	mass of composite in hydrogen storage tank calculation, kg
m_{H2}	mass of hydrogen fuel, kg
m_{liner}	mass of the hydrogen storage tank liner, kg
m_{prop}	mass of the propeller, g
m_{reg}	mass of hydrogen regulator, kg
m_{tank}	mass of the hydrogen storage tank, kg
N	number of dimensions
$\dot{N}_{H2}$	hydrogen flow rate, mol/s
N_x	number of X variables in a neural network
n	index maximum
n_{cyl}	drag ratio of a finite versus infinite cylinder
n_e	moles of electrons transferred per mol of fuel consumed
OEC	overall evaluation criteria

P	probability
P_a	available propulsive power (thrust power), W
P_{atm}	atmospheric pressure, Pa
P_{H2}	hydrogen pressure, Pa
P_{req}	required propulsive power for steady level flight, W
Q	torque, N·m
Q_m	motor torque, N·m
R	radius of propeller, m
R_{cell}	fuel cell polarization curve resistance term, Ω
R_{cont}	resistance of the electric motor controller, Ω
Re#	Reynolds number
R_{gas}	universal gas constant, $J \cdot K^{-1} \cdot mol^{-2}$
R_{hv}	radius of the helicoidal vortex sheet far behind the propeller, m
R_m	resistance of motor, Ω
R_{wf}	wing-fuselage interference factor
r	spanwise distance along a propeller blade, m
r_{H2}	radius of compressed hydrogen tank, m
r_{hv}	radial distance along helicoidal vortex sheet far behind the propeller, m
S_{bfuse}	aft base area of the fuselage, m^2
SFC	power specific fuel consumption, $g \cdot kW^{-1} \cdot hr^{-1}$
S_H	S-shaped function in neural network
S_M	static margin
S_{plfuse}	cross-sectional area of the fuselage in the 2-D wing plane, m^2
S_t	tail planform area, m^2
S_w	wing planform area, m^2

$S_{wetfuse}$	wetted area of the fuselage, m^2
S_Y	identity function in neural network equation
T	thrust, N
$\tilde{T}$	propeller blade airfoil section thrust, N/m
$\mathbf{T}$	contributing analysis function
T_{req}	thrust required for steady level flight, N
$\mathbf{T}^{true}$	true or actual value of the output values of a contributing analysis
t_{H2}	thickness of composite overwrap in compressed cylinder, m
t_{liner}	hydrogen tank liner thickness, mm
U_{H2}	hydrogen utilization
V_0	motor voltage at zero load, V
V_∞	freestream air velocity, m/s
V_b	air velocity incident on a propeller blade section, m/s
V_c	rate of climb, m/s
V_{cell}	fuel cell voltage at the cell level, V/cell
V_{H2}	hydrogen gas volume, m^3
V_i	induced velocity for a propeller blade section, m/s
V_p	direct current voltage dedicated to generating propulsion, V power
V_m	motor voltage, V
V_{tail}	tail volume coefficient
V_{xi}	induced air velocity in the x direction, m/s
$V_{xi,hv}$	induced air velocity in the x direction far behind the propeller, m/s
V_η	fuel cell electrochemical potential term, V/cell
$V_{\theta i}$	induced air velocity in the θ direction, m/s

$V_{\theta i,hv}$	induced air velocity in the θ direction far behind the propeller, m/s
W	total aircraft weight, N
$W_{\%H2}$	weight percentage of hydrogen in a hydrogen storage system
W_{H2}	weight of hydrogen, N
$W_{storage}$	weight of a fuel storage system without any fuel, N
w	axial displacement velocity of the helical vortex sheets far behind the propeller
x	coordinate measured perpendicular to the propeller plane of rotation
x	coordinate axis x direction
$\mathbf{x}$	design variables vector
$\mathbf{x}^{true}$	vector of true value of the design variables
Y	compatibility equation
y	coordinate axis y direction
$\mathbf{y}$	output of a contributing analysis
y_{cubic}	3rd order response surface equation
y_{guess}	initial guess for a CA variable in a compatibility equation
y_k	output value of neural network equation
y_{output}	calculated values of a CA variable in a compatibility equation
$\mathbf{y}^{true}$	true or actual values
Z	fuselage over propeller diameter ratio
z	standard normal random variable
α	angle of attack, rad
α_b	propeller blade section angle of attack, rad
α_g	target probability
α_H	upper value of probability

α_L	lower value of probability
α_{L0}	airfoil zero lift angle of attack, rad
α_T	target value of probability
β	aerodynamic pitch angle of propeller blade section, rad
β_0	motor drag coefficient
β_0	constant term in response surface equation
β_c	geometric pitch angle of a propeller blade section, rad
β_i	linear term in response surface equation
β_{ii}	square term in response surface equation
β_{ij}	2^{nd} order cross term in response surface equation
β_{ijk}	3^{rd} order cross term in response surface equation
β_t	aerodynamic pitch angle at the propeller blade tip, rad
Γ	local section circulation, $m^2 \cdot s^{-1}$
Γ_t	anhedral angle of the inverted V-tail, rad
$\boldsymbol{\delta}$	bias error function for a contributing analysis
ΔC_D	drag offset
$\Delta\mathbf{T}$	bias error of a contributing analysis
$\Delta\mathbf{x}$	difference between design variables and their true values
$\Delta\mathbf{y}$	propagated uncertainty values
ε	error in response surface equation
ε_∞	advance angle of propeller blade section, rad
ε_b	angle between the incident velocity on propeller blade and the radial axis, rad
$\varepsilon_{b,hv}$	angular pitch of a helicoidal vortex sheet, rad
ε_i	induced angle of propeller blade section, rad

ζ	normalized radial distance along the propeller blade
ζ	penalty function
ζ_{hv}	normalized radial distance along helicoidal vortex sheet
η_{cont}	efficiency of the electric motor controller
η_{fc}	fuel cell efficiency
η_{p}	propeller efficiency
η_{SDP}	slow down efficiency multiplier for a pusher propeller
η_{SDT}	slow down efficiency multiplier for a tractor propeller
θ	angular coordinate in plane of propeller rotation, rad
κ	Goldstein proportionality constant
λ	fuel cell polarization curve parameter
λ	penalty function multiplier
λ_{hv}	induced velocity on the helicoidal vortex sheet far behind the propeller
$\boldsymbol{\xi}$	random vector to account for uncertainty in variables and calculations
ρ	air density, kg/m^3
ρ_{liner}	density of hydrogen tank liner, kg/m^3
ρ_{comp}	density of hydrogen tank composite overwrap material, kg/m^3
σ	standard deviation
σ_g	standard deviation of a calculated constraint equation value
$\bar{\sigma}_j$	contribution to overall propagated uncertainty
$\sigma\mathbf{T}$	standard deviation of uncertainty of a contributing analysis calculation
σx	standard deviation of the design variable x
$\sigma\mathbf{y}$	standard deviation of propagated uncertainty
τ_{max}	maximum stress in hydrogen compressed cylinder, GPa

Φ	standard normal cumulative distribution function
ω	angular rotation speed, rad/s
ω_m	angular motor speed, rad/s
AFC	Alkaline Fuel Cell
AFRL	Air Force Research Lab
AIASM	Architecture-Independent Aircraft Sizing Method
AMI	Adaptive Materials Inc.
ARPA	Advanced Research Project Agency
ASDL	Aerospace Systems Design Laboratory
BOP	Balance of Plant
CA	Contributing Analysis
CCP	Chance-Constrained Programming
CFD	Computational Fluid Dynamics
DARPA	Defense Advanced Research Projects Agency
DLR	Deutschen Zentrums für Luft und Raumfahrt
DMFC	Direct Methanol Fuel Cells
DOE	Design of Experiments
DOT	Department of Transporation
DSM	Design Structure Matrix
DSS	Deterministic Solution Sampling
EADS	European Aeronautic Defense and Space Company
ENFICA-FC	Environmentally Friendly Inter City Aircraft powered by Fuel Cells
ERAST	Environmental Research Aircraft and Sensor Technology
FPI	Fixed Point Iteration
GSE	Global Sensitivity Equation

GSV	Global Sensitivity Vector
GT	Georgia Institute of Technology
GT FCUAV	Georgia Tech Fuel Cell Unmanned Aerial Vehicle
GTRI	Georgia Tech Research Institute
FLOPS	Flight Optimization System
HALE	High Altitude Long Endurance
HFE	Heavy Fuel Engine
HiL	Hardware-in-the-Loop
IAI	Israel Aerospace Industries
ICE	Internal Combustion Engine
ISR	Intelligence, Surveillance, and Reconnaissance
KAIST	Korean Advanced Institute of Science and Technology
LHV	Lower Heating Value
LSM	Local Sensitivity Matrix
LSV	Local Sensitivity Vector
MCFC	Molten-Carbonate Fuel Cells
MCS	Monte Carlo Simulation
MDA	Multidisciplinary Design Analysis
MDO	Multi-disciplinary Design Optimization
MSU	Montana State University
NA	Nested Analysis
NACA	National Advisory Committee for Aeronautics
NASA	National Aeronautics and Space Administration
NLL	Numerical Lifting Line
NPSS	Numerical Propulsion System Simulator

NRL	Naval Research Lab
PEMFC	Polymer Electrolyte Membrane Fuel Cell
PAFC	Phosphoric Acid Fuel Cell
RBDO	Reliability Based Design Optimization
RDS	Robust Design Simulation
RSE	Response Surface Equation
RSM	Response Surface Methodology
SA	Simultaneous Analysis
SOFC	Solid Oxide Fuel Cell
SQP	Sequential Quadratic Programming
SSA	System Sensitivity Analysis
SUMT	Sequential Unconstrained Minimization Technique
UAV	Unmanned Aerial Vehicle
UE-UAV	Ulta Endurance Unmanned Aerial Vehicle
UIUC	University of Illinois at Urbana-Champaign
URETI	University Research Engineering Technology Institute

SUMMARY

Unmanned Aerial Vehicles (UAVs) are the most dynamic growth sector of the aerospace industry today. The need to provide persistent intelligence, surveillance, and reconnaissance for military operations is driving the planned acquisition of over 5,000 UAVs over the next five years. The most pressing need is for quiet, small UAVs with endurance beyond what is capable with advanced batteries or small internal combustion propulsion systems. Fuel cell systems demonstrate high efficiency, high specific energy, low noise, low temperature operation, modularity, and rapid refuelability making them a promising enabler of the small, quiet, and persistent UAVs that military planners are seeking.

Despite the perceived benefits, the actual near-term performance of fuel cell powered UAVs is unknown. Until the auto industry began spending billions of dollars in research, fuel cell systems were too heavy for useful flight applications. However, the last decade has seen rapid development with fuel cell gravimetric and volumetric power density nearly doubling every 2-3 years. As a result, a few design studies and demonstrator aircraft have appeared, but overall the design methodology and vehicles are still in their infancy.

The design of fuel cell aircraft poses many challenges. Fuel cells differ fundamentally from combustion based propulsion in how they generate power and interact with other aircraft subsystems. As a result, traditional multidisciplinary analysis (MDA) codes are inappropriate. Building new MDAs is difficult since fuel cells are rapidly changing in design, and various competitive architectures exist for balance of plant, hydrogen storage, and all electric aircraft subsystems. In addition, fuel cell design

and performance data is closely protected which makes validation difficult and uncertainty significant. Finally, low specific power and high volumes compared to traditional combustion based propulsion result in more highly constrained design spaces that are problematic for design space exploration.

To begin addressing the current gaps in fuel cell aircraft development, a methodology has been developed to explore and characterize the near-term performance of fuel cell powered UAVs. The first step of the methodology is the development of a valid MDA. This is accomplished by using propagated uncertainty estimates to guide the decomposition of a MDA into key contributing analyses (CAs) that can be individually refined and validated to increase the overall accuracy of the MDA. To assist in MDA development, a flexible framework for simultaneously solving the CAs is specified. This enables the MDA to be easily adapted to changes in technology and the changes in data that occur throughout a design process. Various CAs that model a polymer electrolyte membrane fuel cell (PEMFC) UAV are developed, validated, and shown to be in agreement with hardware-in-the-loop simulations of a fully developed fuel cell propulsion system. After creating a valid MDA, the final step of the methodology is the synthesis of the MDA with an uncertainty propagation analysis, an optimization routine, and a chance constrained problem formulation. This synthesis allows an efficient calculation of the probabilistic constraint boundaries and Pareto frontiers that will govern the design space and influence design decisions relating to optimization and uncertainty mitigation.

A key element of the methodology is uncertainty propagation. The methodology uses Systems Sensitivity Analysis (SSA) to estimate the uncertainty of key performance

metrics due to uncertainties in design variables and uncertainties in the accuracy of the CAs. A summary of SSA is provided and key rules for properly decomposing a MDA for use with SSA are provided. Verification of SSA uncertainty estimates via Monte Carlo simulations is provided for both an example problem as well as a detailed MDA of a fuel cell UAV.

Implementation of the methodology was performed on a small fuel cell UAV designed to carry a 2.2 kg payload with 24 hours of endurance. Uncertainty distributions for both design variables and the CAs were estimated based on experimental results and were found to dominate the design space. To reduce uncertainty and test the flexibility of the MDA framework, CAs were replaced with either empirical, or semi-empirical relationships during the optimization process. The final design was validated via a hardware-in-the loop simulation. Finally, the fuel cell UAV probabilistic design space was studied. A graphical representation of the design space was generated and the optima due to deterministic and probabilistic constraints were identified. The methodology was used to identify Pareto frontiers of the design space which were shown on contour plots of the design space. Unanticipated discontinuities of the Pareto fronts were observed as different constraints became active providing useful information on which to base design and development decisions.

CHAPTER 1

INTRODUCTION

With its first successful proof of concept demonstration in 1838 [1], the fuel cell is one of the oldest power generation devices proceeding many common devices such as the Otto cycle engine [2], diesel engine [3], and gas turbine [4]. Despite its early invention, fuel cells did not find a mainstream application until the 1960's when the long duration flights of the US Gemini and Apollo space programs required a long duration power source [5]. Despite widespread use in manned spaceflight, fuel cells were of little interest for atmospheric flight applications, primarily due to their historically low specific power and the dominance of combustion based engines. However, over the past two decades, fuel cells have received renewed interest and billions of dollars in funding, primarily fostered by the auto industry who view hydrogen fueled fuel cells as one of the least disruptive, sustainable, and clean technology alternatives to the internal combustion engine [6]. During the same period, development in unmanned aerial vehicles (UAVs) has drastically increased placing an emphasis on endurance, noise, and decreased size over traditional aircraft metrics such as speed and maneuverability. The intersection between increased fuel cell performance and the need for endurance and reduced noise in UAVs has made fuel cells appropriate for consideration in aviation applications.

1.1 Introduction to Unmanned Aerial Vehicles

The first vehicles to achieve controlled powered flight were unmanned. In 1896, Samuel Pierpont Langley launched Number 5, a small steam engine powered aircraft that

successfully flew nearly ¾ of a mile after a catapult launch from a boat on the Potomac River [7]. From Number 5, unmanned aerial vehicles developed as both models used to study flight, as well as military weapons such as the aerial torpedo developed in World War I [8], and the Vergeltungswaffe 1 (V-1) flying bomb used in World War II [9]. Up until the first operational reconnaissance UAVs were fielded in the Vietnam war [10], the majority of military UAVs were largely target drones and remotely piloted vehicles including many converted manned vehicles [8]. With increases in autonomous capability and the miniaturization of useful sensor payloads, UAVs have rapidly increased in military importance. In the 2003 invasion of Iraq, only a handful of UAVs were available. In 2008, the number of UAVs in the US military service grew to well over 1,000 and is expected to exceed 5,000 over the next 5 years [11]. As of 2009, the air force is training more UAV pilots than manned aircraft pilots [12] and industry giant Boeing is delivering more Scan Eagle UAVs then any other aircraft in their product line [13].

The primary reason for the rapid popularity of UAVs is their ability to provide increased levels of situational awareness in military operations. The primary role of UAVs to date have been to perform intelligence, surveillance, and reconnaissance (ISR) missions that allow commanders and soldiers alike to determine what is over the hill or around the corner. As reported by Lieutenant General Mark Curran [14], "[UAVs] enable ground forces to see first, understand first, act first, and then finish decisively." Unlike manned aircraft, UAVs can perform these ISR missions without risking the pilot or being constrained by human limitation such as food, sleep, heat, oxygen, or acceleration forces. As emphasized by Capps [15], "accessibility, in other words, has

become a dominant aircraft value—prized as much as, and sometimes more than, speed, altitude, and armament."

The primary UAV attribute that facilitates the valuable situational awareness and accessibility is endurance. UAVs such as the General Atomics Predator or the Northrop-Grumman Global Hawk can be configured to fly for more than 24 hours unrefueled. As pointed out by Eric Mathewson, director of the Air Force Unmanned Aircraft Systems Task Force, "sustaining the sorts of operations we conduct with the Predator used to be virtually impossible, the idea of putting an aircraft over an area of interest 24 hours a day, 365 days a year, was simply unsustainable. We're now looking at aircraft capabilities for the future that are even more persistent[15] ." In addition, Lt. Mark Roosz, of the U.S. Air Force Research Laboratory has stated that "on today's battlefield, information is key, and by enabling longer missions, we increase the amount of information available to friendly forces[16]."

According to Lieutenant General Mark Curran, in addition to increased endurance, layered employment will be needed [14]. In other words, a network of both small and large UAVs will ultimately be needed to provide the situational awareness that battlefield commanders' desire. Curran quotes a commander in Iraq as saying that "my #1 irritant as a Division Commander is not having UAV assets to execute my mission [14]." The current solution to making UAVs more accessible to commanders and troops alike is to decrease their size so that they can be easily transported, launched, and supported. However, decreasing the size of a UAV comes with both propulsion and stealth penalties.

For conventional based propulsion, Drela et al. [17] shows that the ideal power to mass ratio decreases and the power specific fuel consumption increases as the propulsion

system becomes increasingly small (see Figure 1.1). The small scale propulsion limitations at present are actually more severe than the idealized representation shown in Figure 1.1. Roy Braybrook, a UAV reporter and historian for Armada International, points out that current small UAVs suffer from a lack of specific propulsion development and have relied on low technology solutions including the adaptation of existing snowmobile and lawnmower engines [18].

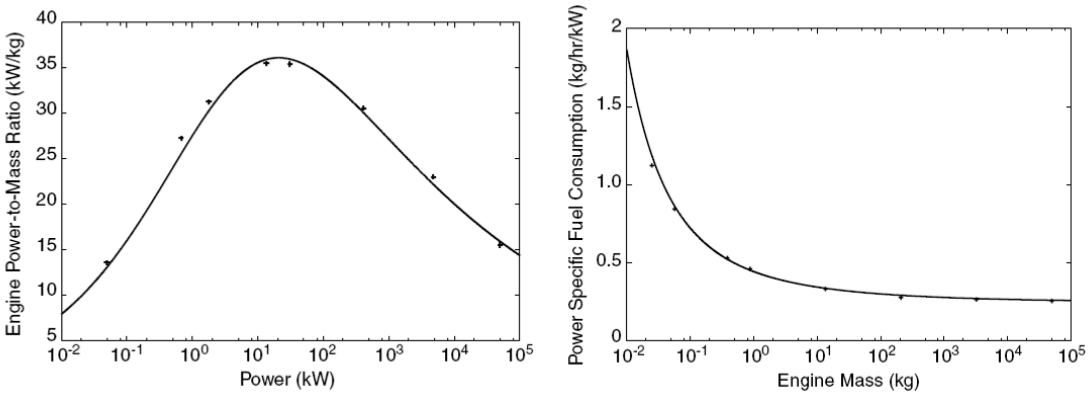

Figure 1.1: Power to mass (left) and power specific fuel consumption (right) trends for conventional combustion based propulsion [17].

Increases in power specific fuel consumption is detrimental to both range and endurance. Limits in propulsion power will decrease climb rates and maximum service altitudes. In addition, a lack of available payload power will put transmission and resolution constraints on payloads that with further decrease operational altitudes. This reduction in altitude is critical as large UAVs such as the Global Hawk and Predator have relied on altitude to mask their acoustic signatures.

Small UAV industry leader Israel Aerospace Industries (IAI) has emphasized that " [UAV] acoustics are very important today with anti-terror warfare [19]." This emphasis on acoustics has driven smaller UAVs to rely on battery electric propulsion

which is relatively free of noise and thermal signature [20]. However, battery electric UAVs have very poor payload and endurance capacity. Current state of the art vehicles like the AeroVironment Puma [21] can only stay aloft for approximately 2 hours which is an order of magnitude lower endurance than similarly sized conventional but noisy UAVs like the AAI Aerosonde [22].

Electrically powered UAVs can have more tactical utility if endurance can be increased [20]. Small military UAVs designed for surveillance, chemical-biological monitoring, border patrol, and other specialty missions are demanding extended flight times that cannot be achieved with battery power [23]. The US Office of Naval Research has even suggested a target by stating that a "24-hour endurance flight, with a 5 pound payload, [is] something nobody can do right now [24]."

Several approaches are underway to address the conflicting UAV drivers of small size, low acoustic signature, and long endurance. Advances in photovoltaic cells and battery technology have made solar powered long endurance vehicles like the QinetiQ Zephyr feasible [25], but reducing size to a reasonable level is still beyond current technology readiness levels. Researchers such as Rick Gaeta at the Georgia Tech Research Institute are studying "radical reductions from the [traditional internal combustion engine] baseline … to create a truly undetectable UAV [26]" while other companies such as GEOCEAN are proposing tethered UAVs [27] . Despite the alternatives, there is a growing consensus among the UAV industry that fuel cell based propulsion may be the most pragmatic solution to the conflicting requirements of small size and long endurance [28, 29].

1.2 Introduction to Fuel Cells

Fuel cells are electrochemical devices that convert chemical energy of the reactants directly into electricity and heat [30]. A fuel cell consists of an electrolyte layer in contact with a porous anode and cathode on either side as shown in the schematic in Figure 1.2. Gaseous fuel is fed to the anode while an oxidant is fed to the cathode. An electrochemical reaction takes place causing ion conduction through the membrane and produces an electric current as shown in Figure 1.2.

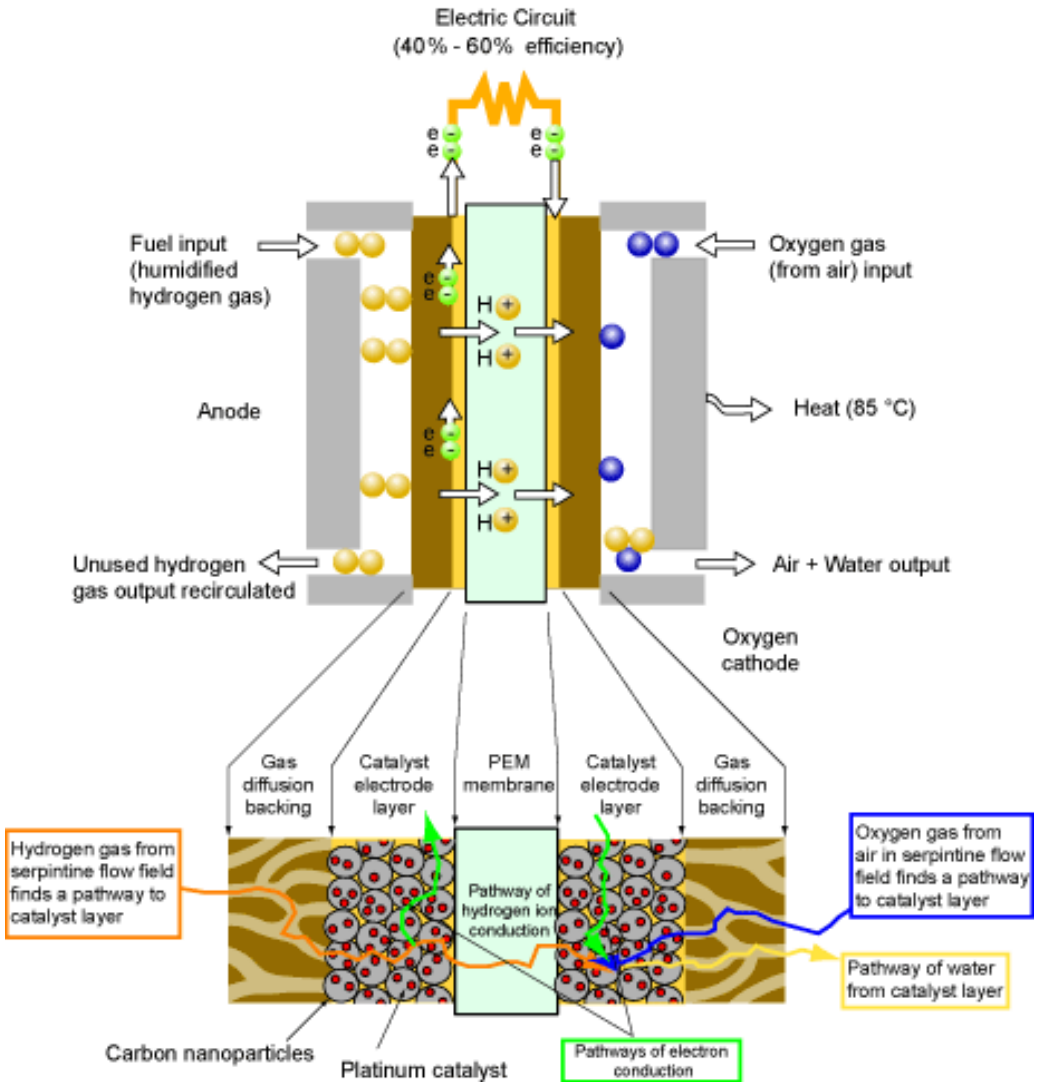

Figure 1.2: Basic fuel cell schematic [31].

Fuel cells have many advantages vs. conventional sources for generating electricity. As an electrochemical device, fuel cells are not limited by Carnot efficiency and have much higher potential efficiencies than heat engines. By themselves, fuel cells have no moving parts and are silent although minimal external devices such as blowers and pumps are typically required to deliver the reactants and manage the temperature. The basic design allows fuel cells to be highly scalable and a number of potential fuel sources are available that produce zero or near-zero regulated emissions.

For UAV applications, the primary benefits of fuel cells are high efficiency, quiet operation, the lack of a generator needed to produce electricity, and ease of scalability. The primary disadvantages are weight, cost, and degradation over time. Fuel cells typically require metals such as graphite aluminum that contribute to reduced power to mass ratios. In addition, fuel cells are currently not mass produced and require a significant amount of platinum which increases their cost relative to batteries and internal combustion powerplant.

1.3 Introduction to Hydrogen

Hydrogen and oxygen gas are the reactants required by a fuel cell. Oxygen is usually provided from ambient air while hydrogen must be carried with the fuel cell or reformed from another fuel. Hydrogen is the lightest and most abundant known element in the universe. Although it rarely exists in elemental form on Earth, hydrogen can be produced in a variety of ways. Most hydrogen on earth is stored in water and can be produced without harmful emissions from electrolysis using a clean power source,

although today most hydrogen is produced using fossil fuels and the reaction of hydrocarbon chains ($-CH_2-$) with H_2O [32].

Hydrogen has more energy per unit mass than any other fuel. As shown in Table 1.1, hydrogen has more than two times the lower heating value as either Jet A or gasoline [33-35]. This energy content gives fuel cells their primary benefit of increased energy to weight over traditional powerplants. Despite this benefit, hydrogen has very low density compared to other fuels, especially since it exists as a gas at standard pressure and temperature. Even if cryogenically cooled to a liquid, hydrogen still has a density that is several times lower than conventional fuels. As a result, to provide a given amount a power, hydrogen fuel will have less mass but more volume vs. conventional fuels.

Table 1.1: Properties of common fuels.

	Hydrogen	Methane	Jet A	Gasoline
Molecular Weight (g/mol)	2.016	16.04	168	107
Lower Heating Value (kJ/g)	120	50	42.8	44
Density 293 °K and 1 atm (kg/m3)	0.08375	0.6682	811	751
Liquid Density at 283 °K (kg/m3)	71	423	811	751
Boiling point at 1 atm (°K)	20.35	112	440-539	300-498

Storing hydrogen is much more involved than storing other fuels. Hydrogen is most commonly stored as a high pressure gas or as a cryogenic liquid. Hydrogen can also be stored through adsorption on activated carbon and carbon nanotubes, or in a hydrogen-storing alloy such as sodium borohydride or lithium borohydride. Figure 1.3

shows the relative volumes for storing 4 kg of H_2 in various methods [32]. Despite the smaller volumes, the two hydride storage on the right typically can only store a few percent of hydrogen by total tank mass and usually require heat input to release hydrogen at an acceptable flow rate. The compressed hydrogen storage offers quick refueling, in practice is lighter than hydride storage, but takes up a large volume and has potential safety issues. Although liquid storage usually provides the highest percentage of hydrogen stored by weight, cryogenic temperatures, heat transfer, boil off rates, and volume are potential issues. Regardless of the storage technique, storing hydrogen is more complex and requires a higher amount of storage mass per mass of fuel than conventional aviation fuels such as gasoline or Jet-A.

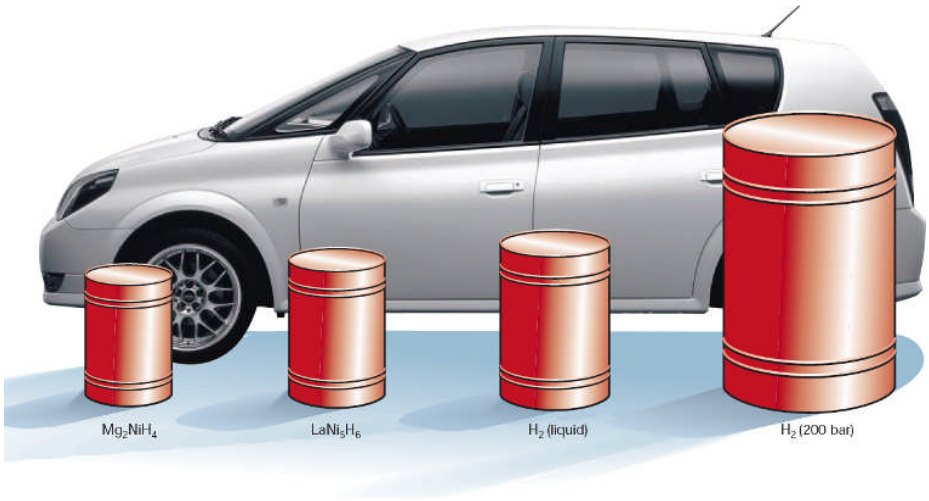

Figure 1.3: Volumes for storing 4 kg of H_2 for an automotive application [32].

1.4 Motivation

1.4.1 Improved Endurance

The primary benefit of a fuel cell system (fuel cell stack + balance of plant + hydrogen storage) is the potential to have increased specific energy versus conventional

powerplants. This advantage is evident through a rudimentary power and energy analysis. Using commercially available powerplant performance data (see Table 1.2), the total system mass of a powerplant versus required endurance is shown in Figure 1.4.

Table 1.2: Powerplant performance parameters of current state-of-the-art systems.

	Specific Power	Efficiency	Energy Storage	Respective Efficiency and Storage References
PEMFC	364 W/kg	0.55	0.605 kg/L	[36, 37]
SOFC	110 W/kg	0.3	0.006 kg/L	[38, 39]
ICE	2810 W/kg	0.13	0.006 kg/L	[38, 40]
Li-Ion Batteries	1000 W/kg	0.99	150 W-hr/kg	[41]

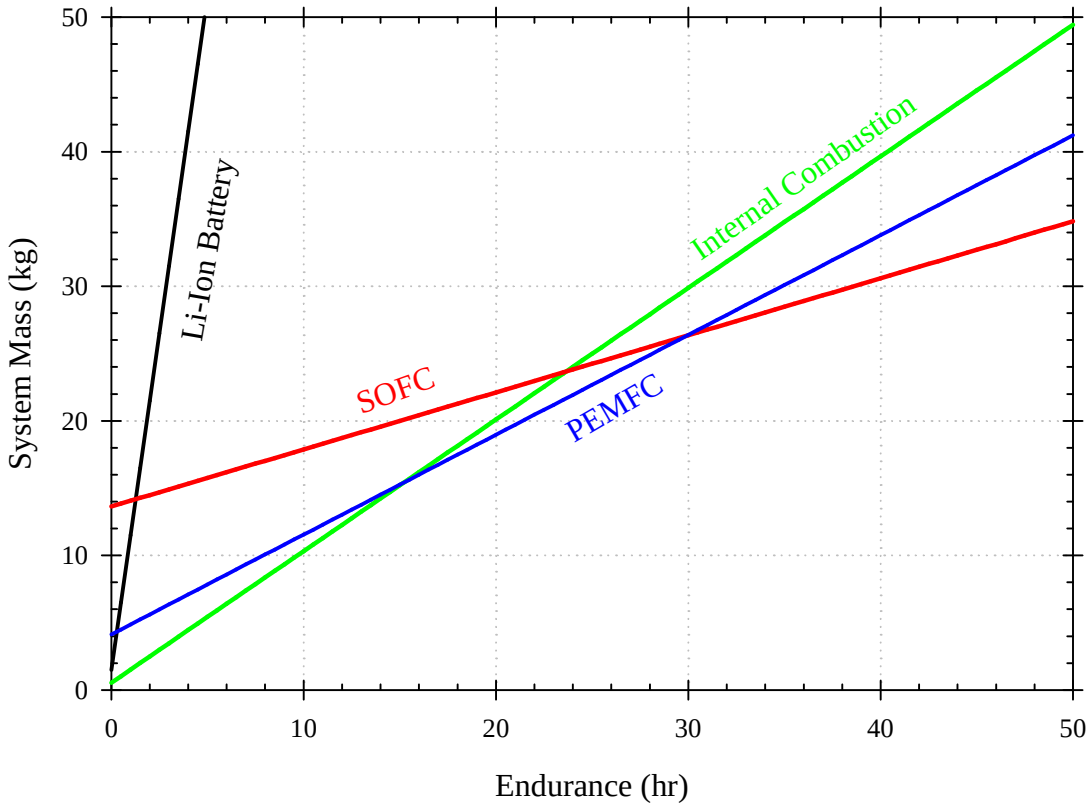

Figure 1.4: System mass for 1.5 kW powerplants as a function of endurance.

At very low endurances, the mass necessary to generate 1.5 kW drives the system mass making internal combustion engines (ICEs) or even batteries the clear winner. However, the slope of the lines in Figure 1.4 is related both to the energy storage content and the efficiency of the powerplant. For solid oxide fuel cells (SOFC) reforming hydrocarbon fuels, the specific energy of the fuel storage would be equivalent to an ICE. However, the SOFC efficiency is much higher than an ICE resulting in the reduced slope and eventual lower system mass at high endurances. For the PEMFC system, the higher specific power provides a distinct advantage versus SOFC at low endurances, but the increased mass of the hydrogen storage system eventually causes more system mass at high endurances. Overall, the potential high efficiency and specific energy of fuel cell systems will result in lower mass systems for long endurance applications.

1.4.2 Acoustic and Thermal Signatures

Fuel cells systems provide electrical current that can be used with the same small electric motors that are used on current small UAVs. The fuel cell itself is silent although a balance of plant (BOP) will typically contain pumps, fans, compressors, and valves that will provide minimal noise. Simplified systems have been demonstrated that reduce the BOP to a single pump [42] or a set of quiet fans [43]. Even with BOP noise, the fuel cell system would maintain similar levels of acoustic stealth as current battery electric UAVs.

The operating temperatures of fuel cell powerplants can greatly reduce the thermal signature of a UAV. Polymer electrolyte membrane fuel cell (PEMFC) systems operate at temperatures below 100 C [44] which greatly reduces their signature versus ICEs. Solid oxide fuel cells (SOFCs) operate at a much higher temperature but would still maintain a lower thermal signature than a gas turbine.

1.4.3 Scalability

Fuel cell stacks are more readily scaled then internal combustion engines. The active area and number of fuel cells in a stack can be varied to match current and voltage requirements and in general, the overall power to weight and efficiency do not drastically change with size or power. Fuel cells can be added or subtracted from a current stack to change the power and weight to meet evolving aircraft power requirements.

1.4.4 Rapid Rechargeability

Fuel cells can operate as long as they have reactants. For a typical hydrogen/air system, the limiting factor for recharging a fuel cell would be the time it takes to refill the hydrogen storage system. Both compressed and liquid hydrogen tanks can be refueled in comparable times to refilling a hydrocarbon fuel tank. This provides a very clear advantage over battery systems which are either single use or suffer from long recharge times.

1.4.5 Emissions

The only byproducts of a PEMFC are heat and water/steam if hydrogen and air are the reactants. Other hydrogen rich fuels can be reformed and used in some fuel cell but will resort in carbon dioxide byproducts and leftover lower forms of hydrocarbons [45]. Since water is not a regulated emission, fuel cells will satisfy existing and future emission regulations.

Although emissions may not be an issue for military UAVs, emissions are the core driver for fuel cell development in the automotive industry. This is logical since automobiles consume around 60% of the total energy used in US transportation [46] and

produce roughly 10% of global carbon dioxide emissions [47]. In comparison, aviation accounts for around 10% of the total US transportational energy and only about 2% of worldwide carbon dioxide emissions [48]. Legislation such as California's zero emission vehicle mandate has forced automakers to develop vehicles with no regulated emissions resulting in drastically increased fuel cell powerplant research and the building of fuel cell demonstrator vehicles [49]. This automotive research is providing the state of the art technology that is needed for aviation applications. To date, at least sixteen different auto manufacturers have demonstrated working fuel cell prototype vehicles [50-52] with Honda even offering a low volume production model for lease in limited areas of the United States [53].

1.4.6 Sustainable Alternative Fuel

Another driver for fuel cell research has been the potential of using hydrogen as the primary fuel. Hydrogen is a renewable fuel source that can be generated by a variety of different processes and doesn't require a limited natural resource like crude oil or natural gas. This makes hydrogen especially attractive to most industrialized nations that currently import large amounts of the oil they use. Recent years have seen demand for petroleum outgrow supply which has caused a drastic increase in the price of oil [54] (see Figure 1.5). In addition, events such as extreme weather or political unrest can cause significant fluctuations in the price of oil even if there direct impact on oil supply is minute. With oil prices reaching historic levels during the summer of 2008, public and political support for moving to alternative fuels for transportation has drastically increased.

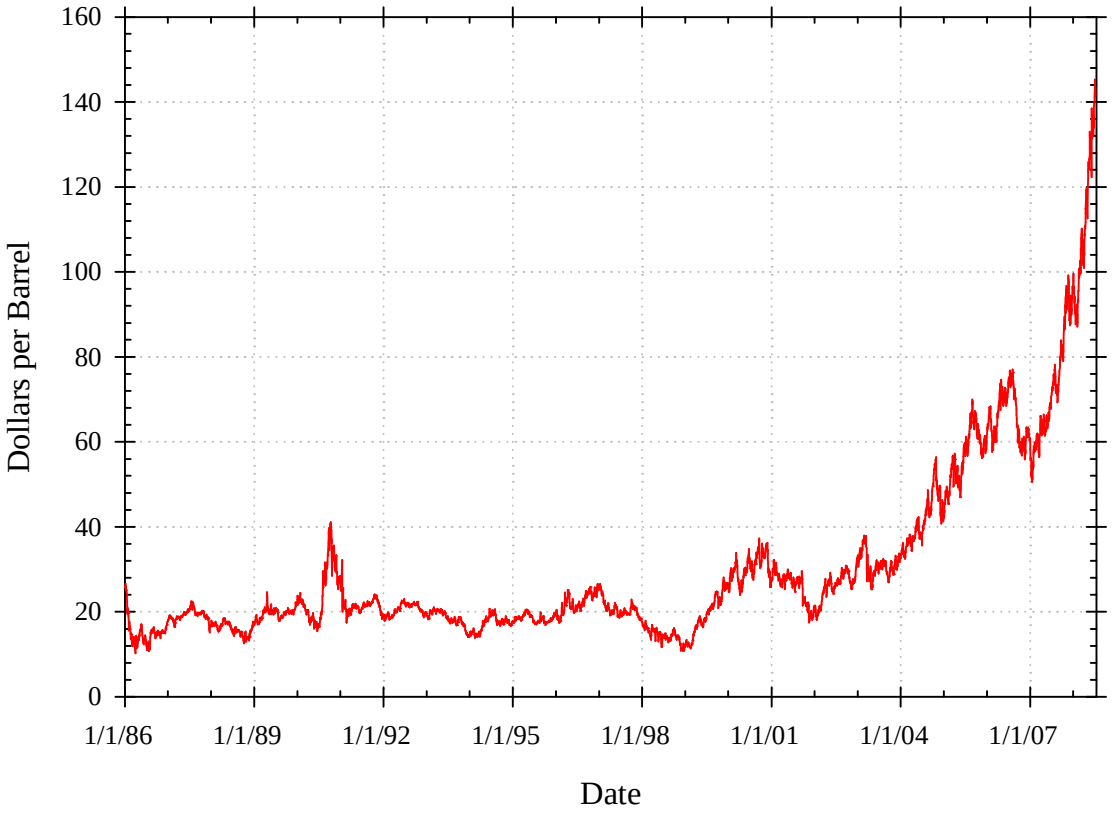

Figure 1.5: Timeline of oil prices over the last two decades [55, 56].

1.5 Research Motivation

Fuel cell systems have great potential to enable long endurance flight with a low acoustic and thermal signature. Also, the scalability of fuel cells can enable a truly "rubberized" propulsion system that can be sized and integrated to maximize overall vehicle metrics. The performance benefits are clearly in line with current military needs and the large investment by governments around the world in UAVs creates a desirable business case. In addition, fuel cell technology will only continue to improve as the automotive industry continues to make a substantial investment in fuel cell system research and development.

Despite the clear performance advantages, the capabilities of fuel cell powered aircraft are still largely unknown. Simplified analyses such as presented in Figure 1.4 show a clear performance benefit but do not capture subsystem interactions and vehicle level design constraints that will undoubtedly affect the design. The design framework to capture these interactions and constraints has not been adequately developed as a lack of fuel cell data, validated fuel cell performance models, and appropriate aircraft sizing routines have not been fully developed and documented. In addition, the low specific power of fuel cell systems will create a more highly coupled design space than has existed with the more mature ICE technology. Coupled with the performance uncertainty that accompanies any new technology, this design space will likely be problematic for traditional design methods and will require a new methodology.

1.5.1 Georgia Tech Fuel Cell Project

To begin developing fuel cell aircraft, a research and development project was started in 2004 as a collaboration between the Aerospace Systems Design Laboratory (ASDL) at the Georgia Institute of Technology and the Georgia Tech Research Institute (GTRI). The primary research objectives were to develop the design tools and methodologies needed to study and develop fuel cell aircraft designs, and to use these tools and methodologies to develop and test a series of UAVs as well as gaining insight into the potential performance benefits of fuel cell aircraft. Partial funding of this project was provided by the NASA University Research Engineering Technology Institute (URETI) grant to the Georgia Institute of Technology. Materials, funding, and manpower were also provided by ASDL and GTRI.

The research began with the development of demonstrator aircraft referred to as the Georgia Tech Fuel Cell UAV (GT FCUAV). The main goal of the GT FCUAV development was to achieve flight solely under fuel cell power and begin to understand the challenges and opportunities associated with fuel cell aircraft. Development of this

vehicle was based on a combination of design methodologies pioneered by ASDL, and UAV design techniques learned through modeling and developing remote control aircraft. After nearly a 2 year development period, the GT FCUAV was successfully flight tested in 2006. The design process, aircraft description, and test data obtained from the GT FCUAV were documented in [57-60].

The experience with the GT FCUAV provided the necessary background and experimental data to begin developing and refining a design methodology. As part of the process, several design studies were conducted to help explore the design space of various fuel cell UAV concepts including aircraft with transatlantic range and 24 hours of endurance (see references [58, 61, 62]). The research also sought to obtain results that could identify and inform the explanation of key fuel cell aircraft behaviors and design rules.

The culmination of the project resulted in the development of a 2nd generation fuel cell powered aircraft meant to demonstrate 24 hours of endurance using primarily off-the-shelf components.

1.5.1.1 Collaboration Efforts

Addressing the research goals of the Georgia Tech fuel cell project required a collaboration effort between several individuals. Undergraduate students, graduate students, research engineers, and professors were involved with various stages, especially during the development of the GT FCUAV. Following the GT FCUAV development, the project mainly became a collaboration between the author and Thomas Bradley, a PhD student in the Mechanical Engineering department at Georgia Tech and an employee of the Georgia Tech Research Institute. The research ultimately resulted in this dissertation as well as the dissertation of Thomas Bradley [63].

Both the author and Thomas Bradley worked to develop sizing and synthesis models of various components of a fuel cell aircraft. Thomas Bradley focused on

developing the fuel cell system models while the author focused primarily on the aerodynamic and propeller/motor propulsion models.

After modeling was completed, the research for this dissertation focused on developing the multidisciplinary design analysis framework as well as the design methodology to estimate sources of uncertainty and explore and optimize a design under the effects of uncertainty. Thomas Bradley focused on the modeling, design, and energy management of fuel cell powerplants for aircraft. As part of his research, Bradley performed nearly all of the experimental work that was necessary to develop, inform, and validate models. Bradley's work culminated with a hardware-in-the-loop setup that explored and tested the propulsion design of the 24 hour endurance aircraft.

1.6 Document Overview

This chapter (Chapter 1) provided an introduction to UAVs, fuel cell systems, and hydrogen storage systems. The general motivation for developing fuel cell powered UAVs is discussed and a brief background of the Georgia Tech fuel cell aircraft research project of which this dissertation is an integral part is given.

Chapter 2 provides a literature search relating to fuel cell and hydrogen storage systems. A survey of fuel cell design studies in the literature is covered and a description and discussion of fuel cell aircraft that have achieved flight is provided. A summary of the design process implemented for the Georgia Tech FCUAV is also given. Chapter 2 culminates with a discussion of the research gaps that informed the development of this dissertation.

Chapter 3 introduces research questions that resulted from the literature search and the development of the Georgia Tech FCUAV. A methodology is then proposed and

detailed steps to this methodology are outlined. Hypotheses that are an integral part of the methodology are also introduced. A research plan to test these hypotheses is outlined.

Chapter 4 introduces uncertainty propagation and documents the systems sensitivity analysis (SSA) technique used in this dissertation. A simplified example problem on uncertainty propagation is studied resulting in the development of a set of rules that dictate how the multidisciplinary analysis (MDA) must be constructed to remain within the underlying assumptions of the SSA technique.

Chapter 5 begins with the selection and discussion of the baseline architecture of a fuel cell aircraft. A high level sensitivity analysis is then used to guide decomposition of the analysis into more manageable contributing analyses. Further decomposition is also performed that allow for specific tests to be simulated for purposes of verification and validation. The chapter ends with a discussion on the development of surrogate models that were implemented to improve the speed of the most computationally intensive analyses and help smooth the behavior of the wing and tail sizing model.

Chapter 6 discusses the development of an automated flexible design framework for bringing together the various contributing analyses into a multidisciplinary design analysis (MDA). Results of the MDA are validated using experimental data obtained from hardware-in-the-loop tests. Different mathematical techniques were tested to find a robust solution process for the MDA.

Chapter 7 sets up the optimization formulation to be used in conjunction with the MDA. A procedure for calculating Pareto frontiers is introduced and several optimization algorithms were tested.

Chapter 8 provides two major implementation studies. The first is designed to develop a 24 hour endurance fuel cell aircraft. An iterative process that identifies key components of uncertainty and then reduces this uncertainty through the introduction of high order analyses is presented. Using the results from the first implementation study, a detailed study of the design space around an optimum endurance solution point is studied. The effects of uncertainty around the optimum solution are shown graphically and the design framework is used to identify the Pareto frontier that trades endurance versus climb rate performance.

Chapter 9 provides a summary of the lessons learned and introduces some future work ideas. Concluding remarks on this research are also provided.

CHAPTER 2

LITERATURE REVIEW

Fuel cell systems have the potential to increase endurance for UAVs while maintaining the low acoustic signature of an all-electric aircraft. Enhanced endurance and reduced acoustic signature are key attributes that are currently driving the thriving military UAV market. Despite the potential benefits, fuel cell powered aircraft are in their infancy and the methodology for their design has yet to be established and accepted in the aerospace community. To assist the development of this methodology, this chapter provides a review of the current literature. The review begins by covering the basics of fuel cell and hydrogen storage systems. A comparison of fuel cell systems to existing UAV propulsion is then discussed. Following this comparison, a brief history of fuel cell aircraft is given. This history is then followed by a summary of the design processes and methodologies that have been applied to fuel cell aircraft. The design process and results of the Georgia Tech fuel cell UAV are also presented. The chapter concludes by summarizing the shortcomings of current fuel cell UAV design methodologies.

2.1 Fuel Cells

Fuel cells are electrochemical devices that convert chemical energy of the reactants directly into electricity and heat. In basic, a fuel cell consists of an electrolyte layer in contact with a porous anode and cathode on either side. Gaseous fuel is fed to the anode while an oxidant is fed to the cathode. An electrochemical reaction takes place causing ion conduction through the membrane and produces an electric current.

2.1.1 Theoretical Efficiency

Since fuel cells are electrochemical devices, they are not governed by the same efficiency limits as heat engines. The basic fuel cell reaction is given in Eq. (2.1).

$$H_2 + ½\ O_2 \leftrightarrow H_2O \qquad (2.1)$$

At standard conditions, the free energy ($\Delta G = \Delta H - T\Delta S$) is equal to -237.3 kJ/mol while the enthalpy is equal to ΔH = -285.8 kJ/mol. Using a definition of efficiency as the maximum work out divided by the enthalpy input,

$$\eta_{fc} = \Delta G / \Delta G, \qquad (2.2)$$

the maximum thermodynamic efficiency at standard conditions is 83 percent. Likewise, using Faraday's constant (F), and the number of moles of electrons transferred per mol of fuel consumed (n_e), the maximum cell potential at standard conditions is

$$E_r = -\frac{\Delta G}{n_e F} = 1.229 \text{ V}. \qquad (2.3)$$

Although the values of 83% efficiency and 1.229V are shown for the simpler hydrogen and pure oxygen reaction shown in Eq. (2.1), these values are comparable to the more commonly used hydrogen air reactions. Even including the power to operate the balance of plant, commercially available small fuel cell systems typically show >40% efficiency, even at high power levels [43, 64] . Current generation automotive fuel cell systems are able to achieve up to 60% efficiency [65].

2.1.2 Types of Fuel Cells

Many types of fuel cells have been researched. Fuel cells are differentiated from one another on the basis of the electrolytes and/or fuel used with that particular fuel cell

type [30]. Although not an exhaustive list, six different fuel cell types that appear frequently in fuel cell research literature are given in Table 2.1.

Table 2.1: Fuel cell types [45].

	PEMFC	DMFC	AFC	PAFC	MCFC	SOFC
Primary applications	Mobile and stationary power	Portable power	Space vehicles and drinking water	Stationary power	Stationary Power	Stationary Power, vehicle auxiliary power
Electrolyte	Polymer (plastic) membrane	Polymer (plastic) membrane	Concentrated (30-50%) KOH in H_2O	Concentrated 100% phosphoric acid	Molten Carbonate retained in a ceramic matrix of $LiAlO_2$	Yttrium-stabilized Zirkondioxide
Operating temperature range	50-100 °C	0-60 °C	50-200 °C	150-220 °C	600-700 °C	700-1000 °C
Charge carrier	H^+	H^+	OH^-	H^+	$CO_3^=$	$O^=$
Prime cell components	Carbon-based	Carbon-based	Carbon-based	Graphite-based	Stainless steel	Ceramic
Catalyst	Platinum	Pt-Pt/Ru	Platinum	Platinum	Nickel	Perovskites
Primary fuel	H_2	Methanol	H_2	H_2	H_2, CO, CH_4	H_2, CO
Star-up time	Sec-min	Sec-min		Hours	Hours	Hours
Power density (kW/m3)	3.8-6.5	~0.6	~1	0.8~1.9	1.5-2.6	0.1~1.5

2.1.2.1 Stationary Fuel Cell Types

Fuel cells are inherently heavy and thus tend to be most appropriate for stationary applications. The most mature technology is the phosphoric acid fuel cell (PAFC) which has been used in small powerplants for over a decade [30]. In addition, molten-carbonate fuel cells (MCFC) and solid oxide fuel cells (SOFC) have also been researched and have applications to stationary power. These fuel cells all operate at higher temperatures which translates to higher efficiencies when the waste heat is used in cogeneration and are adaptable to use with more readily available fuels [30].

2.1.2.2 Mobile Fuel Cell Types

Mobile applications are much more weight sensitive than stationary applications and thus require higher power density cells like polymer electrolyte membrane fuel cells (PEMFC*), direct methanol fuel cells (DMFC), alkaline fuel cells (AFC), or solid oxide fuel cells (SOFC). Both PEMFCs and DMFCs use the same perflourosulfonic acid membrane and can operate at low temperatures [45]. The primary difference is that PEMFCs use pure hydrogen whereas DMFCs operate on liquid methanol. Direct methanol fuel cells suffer from high crossover of the methanol through the electrolyte which compromises power [66]. Alkaline fuel cells use an aqueous solution of alkaline potassium hydroxide for the membrane and represent one of the oldest technology fuel cells [67]. Alkaline fuel cells are extremely efficient but require pure reactants. Solid oxide fuel cells use a non-porous solid membrane and operate at very high temperatures. The ability to easily adapt SOFCs to operate on conventional hydrocarbon fuels and the potential for high specific energy have allowed SOFCs to be considered for mobile applications [68, 69].

2.1.2.3 Aerospace Fuel Cell Types

The first fuel cells to be used in a mainstream aerospace application were PEMFCs which were initially chosen for the Gemini space program. However, after several difficulties, AFCs were selected to replace PEMFCs for the Apollo and later the space shuttle program [1]. Alkaline fuel cells have performed well for the space program

---

* Many sources also refer to the polymer electrolyte membrane fuel cell as a proton exchange membrane fuel cell using the same acronym PEMFC.

achieving high efficiencies and showing high reliability. However, AFCs are susceptible to carbon contamination, so they require pure hydrogen and oxygen [70]. This is not a problem for space applications where the environment can be easily controlled, but terrestrial applications are limited.

For aviation applications, PEMFCs and SOFCs are the main fuel cells considered [71]. PEMFCs have quick start up times and higher specific power as compared to other fuel cell systems which make them more applicable for primary power. Solid oxide fuel cell systems operate at high temperatures and can be operated on current aviation logistical fuels [72]. The high temperature allows for higher efficiency as the waste heat can be used for heating while using logistical fuels can potentially provide very high system specific energy and energy density. However, the low specific power of almost all current SOFC systems makes them more appropriate for auxiliary rather than primary power in regard to aviation applications.

2.1.2.4 Technology Development

Although fuel cells predate modern UAV propulsion systems, their performance didn't reach levels appropriate for aerospace applications until recently. The trends of fuel cell development are evident in the number of patent applications. Figure 2.1 shows the number of patent applications filed per year. The first major boom in fuel cell development was galvanized by spacecraft applications in the 1960's. During this time, AFCs emerged as the fuel cells of choice due to their reliability and success with the Apollo and space shuttle programs. The recent increase in patent activity is evident of a shift toward cleaner forms of energy. The surge in PEMFC patents over other fuel cell types is driven by the substantial research and development of the automotive industry.

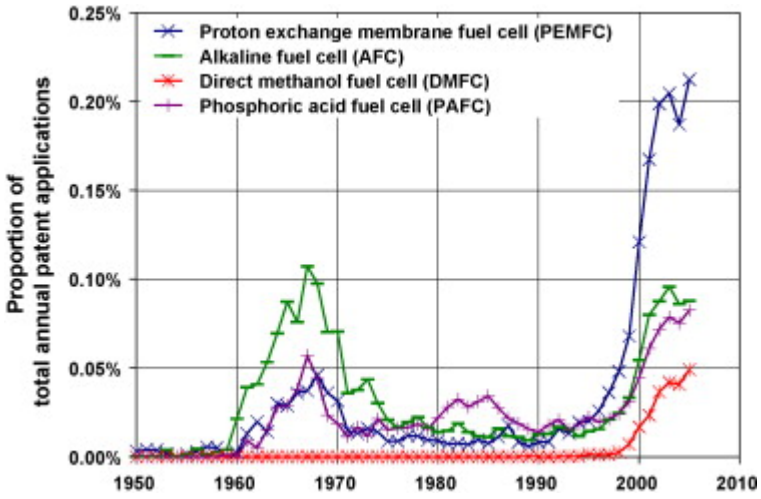

Figure 2.1: Worldwide annual patent applications for various fuel cell types [73].

The research and development efforts focused on PEMFCs have resulted in substantial increases in performance. Figure 2.2 shows the power density improvements that have been made with PEMFCs since their initial development. Most notably, Honda and Ballard have been successful at drastically improving power density over a few short years. Based on this trend, both Ballard and Honda expect to exceed DOE targets for 2010 [73].

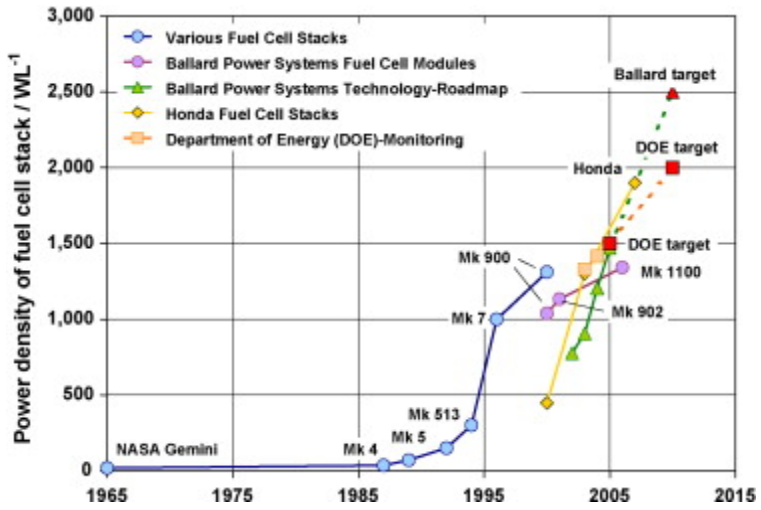

Figure 2.2: Power density development of PEMFCs [73].

In addition to power density increases, fuel cell manufacturers have also made drastic improvements in specific power. Figure 2.3 shows both the specific power and power density of three generations of Honda fuel cell stacks. Honda's current generation fuel cell stack has changed from the horizontal cell configurations shown in Figure 2.3 to a vertical flow stack design. As a result, the specific power has increased by 67% and power density has increased by 50% relative to the values shown in Figure 2.3 [65].

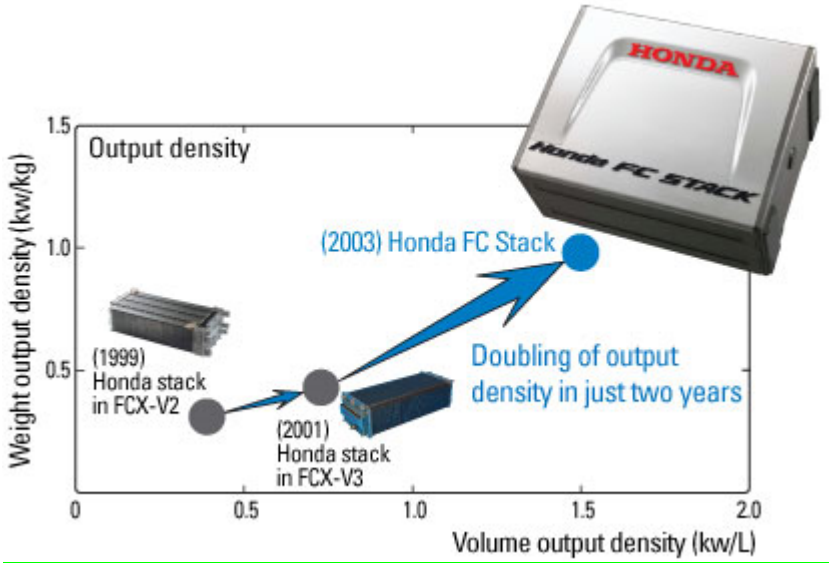

Figure 2.3: Honda fuel cell specific power and power density development over three generations [74].

In addition to Honda, other manufacturers have made similar rapid progress with fuel cell development [44]. General Motors has reported achieving a stack specific power of as high as 1570 W/kg [75] while the United Technologies Research Center and the Technical University of Berlin have reached specific power levels capable of facilitate rotary wing aircraft [76, 77] . General Motors 5th generation fuel cell stacks have reportedly also increased the service life of their fuel cell stacks while improving the manufacturability and decreasing the amount of expensive platinum required [78]. In

addition, General Motors has drastically reduced the part count and volume of their fuel cell systems and reportedly achieve a system specific power of 600 W/kg and a power density of 408 W/L [79].

The capabilities of most technologies tend to follow an S curve shape over time (see Figure 2.4). In the early development phase, increases in capability may take years as researchers begin understanding the new technology. Following this early development phase, the technology will generally increase in capability rapidly as the technology becomes better understood and investment in the technology is increased. Eventually the technology will begin reaching a physical limit in capability where it becomes much more difficult to increase capability over time.

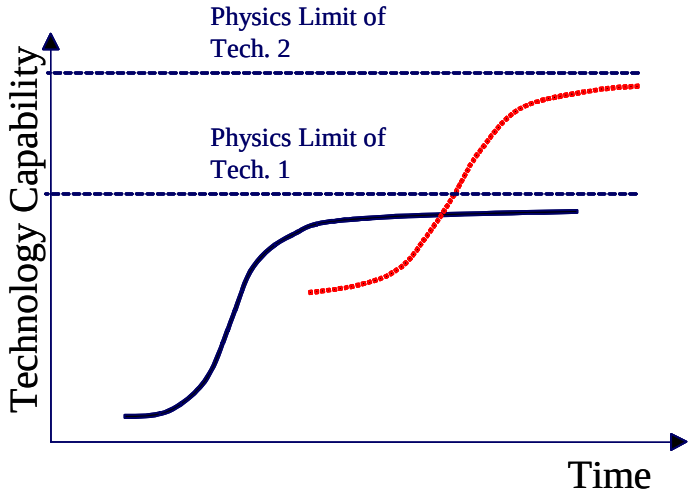

Figure 2.4: Technology S-curves.

New technologies will often follow a different S curve shape and will have different physical capability limits. Often, as is the case in Figure 2.4, a new technology may not be able to exceed the capability of an existing technology when first introduced, but has the potential to surpass the physics based limits of the existing technology. At

current, fuel cells surpass conventional aircraft powerplants in terms of efficiency, noise, and emissions. Fuel cells currently trail behind conventional propulsion in terms of specific power but may approach or surpass the specific power levels of internal combustion engines if the technology trends continue to increase at their current pace.

By comparing Figure 2.2 and Figure 2.4, fuel cells are currently following the steep slope part of the technology capability S curve. Fuel cells also appear to be far from their current specific power and specific volume limits. With a the current worldwide focus on clean energy, investment in fuel cell systems will likely continue and it is reasonable to assume that fuel cells will continue to rapidly increasing in capability over the next few years. This rapid increase in capability presents a challenge for aviation applications as capability is expected to rapidly increase over the time scale of a typical aerospace design cycle.

2.2 Hydrogen Storage

Hydrogen and oxygen gas are the reactants required by a fuel cell. Oxygen is usually provided from ambient air to eliminate providing onboard storage while hydrogen must be carried with the fuel cell or reformed from another fuel.

Hydrogen contains the most energy per unit mass of any known fuel with over 2.5 times the lower heating value (LHV) as common hydrocarbon fuels. It is precisely this high LHV that allow fuel cell systems to demonstrate high specific energies. However, hydrogen has very low density and exists as a gas except at cryogenic temperatures. As a result the storage of hydrogen is more involved than conventional fuels. The most common storage techniques include using pressure vessels to store gaseous hydrogen, storing hydrogen in alloys such as sodium borohydride or lithium borohydride, and

storing hydrogen as a cryogenic liquid. Each technique has advantages and disadvantages, however, the primary metric concerning aviation applications is the weight percent as defined in Eq. (2.4) where W_{H2} and $W_{storage}$ are the respective weights of hydrogen and the storage system.

$$W_{\%H2} = \frac{W_{H2}}{W_{Storage} + W_{H2}} \qquad (2.4)$$

2.2.1 Compressed Hydrogen Storage

The most straightforward method of storing hydrogen is using a pressure vessel to store hydrogen in gaseous form. However due to the properties of hydrogen, high pressures are required to store significant amounts of hydrogen. Hydrogen is typically stored at pressures up to 35 MPa although automotive industry leaders like Toyota have been pushing operating pressures up to 70 MPa [80].

To date, the lightest compressed hydrogen tanks are manufactured using composite materials. Department of transportation (DOT) rated tanks typically contain 3-6% hydrogen by weight [81]. Lightweight designs used for aerospace and automotive applications store between 7-10% hydrogen by weight [82] with the current maximum of 11.3% demonstrated by a 35 MPa cylinder built by Quantum Technologies [37, 83].

High pressure hydrogen storage is problematic primarily in terms of safety. Compressing and storing any high pressure gas poses safety risks. In Japan, certain high pressure vessels are prohibited on the roads in automobiles [32]. Jean Botti, the chief technical officer at The European Aeronautic Defense and Space Company (EADS) Defense and Security Unit has stated that “we need to do more research to store hydrogen at low pressure, certifying an aircraft with high-pressure hydrogen storage could be a showstopper [84].”

2.2.2 Adsorption Hydrogen Storage

To avoid the potentially dangerous high-pressures of compressed hydrogen storage, hydrogen is also commonly stored using alloys such as sodium borohydride [85, 86] or lithium borohydride [87]. Commercially available storage tanks of this type currently only hold about 1-2% hydrogen by weight although active heating can increase the percentage to 5%-7% [83]. Current research is also looking into storing hydrogen by adsorption with various materials [87-90] including activated carbon and carbon nanotubes [91, 92]. Although 'fantastic' results for carbon nanotubes such as over 60% hydrogen storage by mass have been reported by a Northeastern University group [93], these results have not been reproduced [32].

Various adsorption techniques have the advantage of low pressures and lower volumes versus other storage methods. However, the recharge times for the tanks are longer and heat input is typically needed to provide an adequate flow rate for high power applications.

2.2.3 Cryogenic Liquid Hydrogen Storage

By far the most successful method at storing a high percentage of hydrogen by weight is liquid hydrogen storage. However, liquid storage isn't straightforward as hydrogen has an extremely low boiling point of 20 degrees K. Even when stored cryogenically at or below 20 degrees K, liquid hydrogen containers typically have to be open systems since heat transfer with the environment can lead to boil off that can result in very strong overpressure. As a result of the open system design, a certain amount of liquid hydrogen will be lost to the surroundings causing the tank to empty even if not in use. This loss rate requires thermal management to become a major player in liquid hydrogen storage and strongly dictates the mass of the tank. Hydrogen storage systems that are well insulated and designed with very low leak rates can achieve 19% hydrogen by weight [94], whereas shorter endurance applications such as high speed aircraft [95]

and the space shuttle hydrogen tank [96, 97] can obtain hydrogen weight percentages as high as 85% and 89% respectively. Due to common use in launch vehicle and satellite operations, most of the details of liquid hydrogen storage are understood. Design tradeoffs and details are contained in extensive studies such as provided by Brewer [33] and Sullivan et al. [98].

2.2.4 Other Hydrogen Storage Methods

Other methods for storing hydrogen including hydrogen rich fuels, and solid hydrogen. Hydrogen rich fuels such as gasoline, kerosene, and propane can also be used to store hydrogen. To generate the hydrogen, a reformer is needed which can significantly add to the storage system mass and reduce overall system efficiency [99]. Reforming is typically more applicable to higher temperature fuel cells such as SOFCs.

At very low temperatures (< 14 deg K) and pressures, hydrogen can be stored as a solid. Although not common, solid hydrogen has been successfully used for cooling instruments on satellites. The few solid hydrogen storage designs that exist are designed to minimize losses due to heat leakage in a space environment [100, 101]. The weight percent of hydrogen storage for an aircraft application is unknown as no designs exist for the type of heat leakage rate that would be required to power a fuel cell.

2.2.5 Comparison of Developed Hydrogen Storage Systems

A comparison of commercially available hydrogen storage systems is given in Figure 2.5. The different storage systems fall into fairly clear regions of stored hydrogen mass. For very low amounts of hydrogen, adsorption storage using metal hydrides is common; however the weight percent of hydrogen for these systems is only about 1%. From approximately 50 g up to 1 kg of H_2, lightweight compressed systems have been

designed. These designs are catered mainly to the space industry. From 1 to 10 kg, several DOT rated compressed hydrogen tanks exist. These tanks have higher safety factors than the lighter weight tanks and are certified to more pressurization cycles. At the high end of the DOT rated compressed tanks is the Quantum Technologies automotive tank that pushes the limits of hydrogen storage to 11.3% hydrogen by weight.

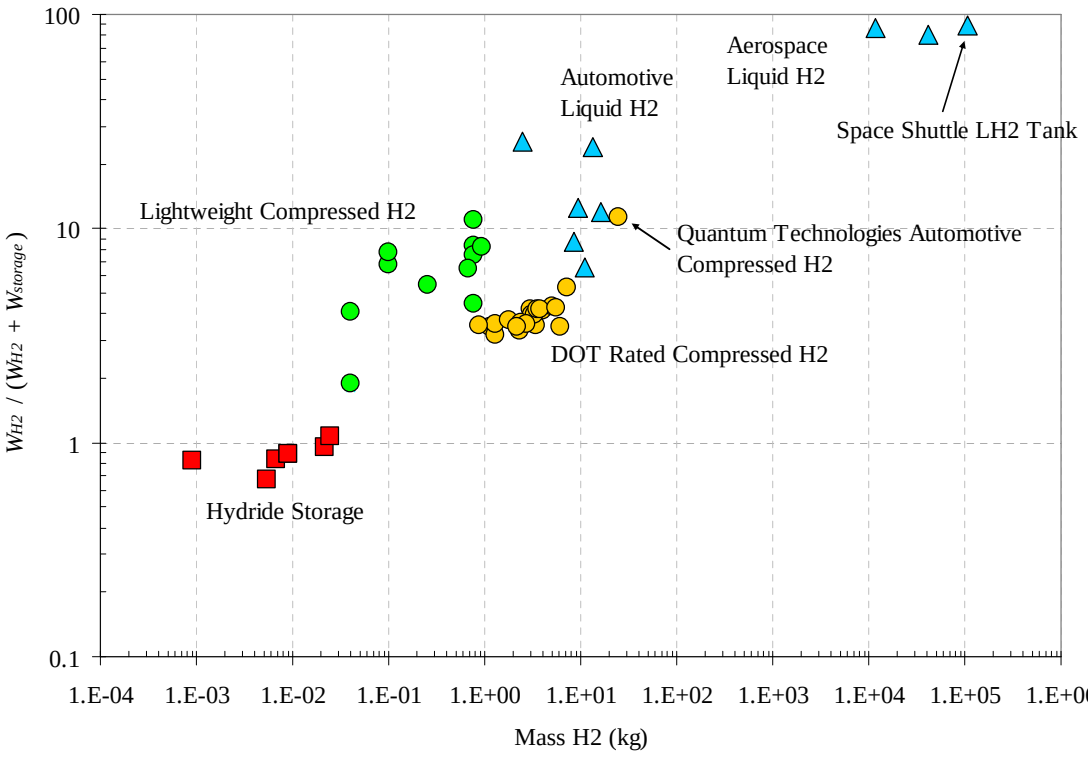

Figure 2.5: Percent of hydrogen storage by weight for various conventional storage techniques.

Several liquid hydrogen tanks have been developed for automotive applications. With the exception of the Quantum Technologies tank, they have a higher weight percent of hydrogen stored versus compressed tanks. However, the automotive application limits the design since extremely low leak rates are desired.

The only historical applications requiring lightweight tanks that can store large masses of hydrogen are aerospace applications. In the early 1950s, liquid hydrogen was studied as a possible combustion based fuel for increasing speed and altitude performance [95]. More recently, liquid hydrogen has been studied to reduce the weight of the United States Navy P-3 aircraft [102], and to enable a new large aircraft with multi-day endurance [103].

2.3 Comparison with Conventional Propulsion

The two performance metrics most often used to describe aviation propulsion systems are specific power and power specific fuel consumption. Specific power is defined as the maximum rated power of the propulsion system divided by the mass of the propulsion system. The mass includes the engine and all auxiliary systems needed to operate the engine with the exception of the fuel storage system. Power is typically measured as the brake power or rotating power provided by the motor shaft. For aircraft systems, high specific power is desirable in order to reduce the weight of the propulsion system. Power specific fuel consumption (SFC) is defined as the mass of fuel required per unit power per unit of time. Using the units of g/kW/hr, SFC specifies the mass of fuel (in grams) required to produce one kW of power for 1 hour. Low SFC is desired in order to reduce the amount of fuel that must be carried onboard an aircraft to fulfill a given mission.

Figure 2.6 shows the specific power and specific energy of several aircraft propulsion systems. With exception of the gas turbine engines, the area for each circle in Figure 2.6 is related to the maximum rated power for the device. Gas turbine engines are represented using gray squares since their power ratings are orders of magnitude larger than the majority of propulsion systems included.

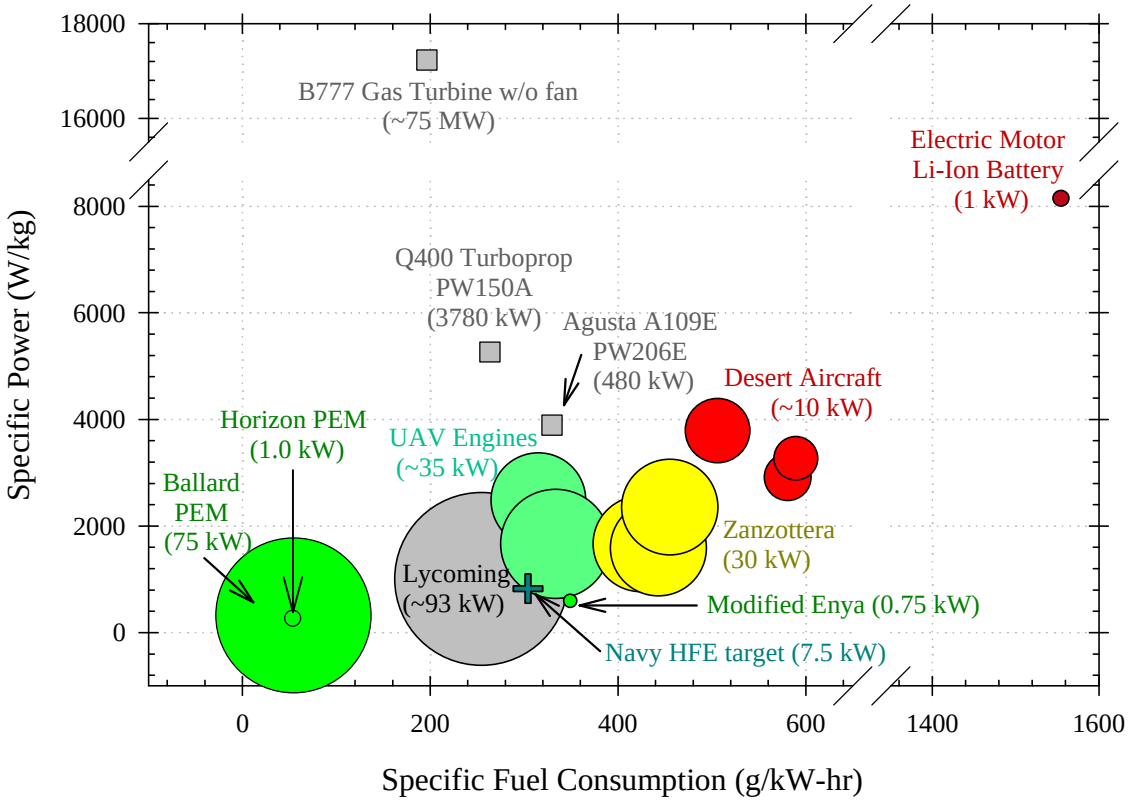

Figure 2.6: Specific power and fuel consumption for aerospace applicable propulsion systems.

Propulsion systems common in larger manned aircraft are shown in gray on Figure 2.6. The Lycoming O-235 series [104] engine shown is common for general aviation applications and represents the moderate specific power and very low SFC that has resulted from over a century of engine development. The PW206E and PW150A engines represent a respective low and high power range that is common for available shaft power gas turbine engines used in both turbo-prop and rotary wing aircraft. Both of these gas turbines engines provide several times the specific power of the Lycoming engine at a cost of slightly higher fuel consumption, although fuel consumption tends to decrease with increasing rated power. At the high end of available gas turbine engines is an estimate of the shaft power of a typical B777 engine. NASA correlations [105] to remove the weight of the fan and estimate the shaft power for the B777 engine were used to allow this engine to be properly compared to the others in Figure 2.6. For high power

applications, gas turbine engines offer unparalleled specific power as well as excellent SFC. Although much smaller gas turbines have been developed, they are limited to much lower specific power and higher SFC [106].

At the right side of Figure 2.6, an extreme in specific power is representative of the small electric motors that are commonly used on man portable electric UAVs similar to the RQ-11 Raven [107, 108] . Although these electric motors have efficiencies near 90%, they require heavy batteries. For Figure 2.6, a pack of 4 lithium-ion 18650 battery cells appropriate for a 1 kW peak power system were used to calculate a comparative SFC. However, this SFC value may be misleading as SFC typically does not include the weight of the energy storage device.

Aircraft requiring less than ~90 kW have historically been lightweight experimental aircraft or unmanned aerial vehicles. Since the majority of users are hobbyists developing low cost vehicles, development has been limited. Most engines at this scale run on simple 2-stroke cycles and burn a fuel oil mixture [18] . Although specific power is generally higher than for general aviation engines like the Lycoming in Figure 2.6, SFC is poor. The Desert Aircraft engines which are representative of typical high power 2 stroke engines have a minimum SFC of over 500 g/kW-hr and a efficiency of only 13-14% [109].

A general trend among smaller engines is that as fuel consumption is decreased and engines become more efficient, they sacrifice specific power. This is represented by the Zanzottera engines [110] as compared to the Desert Aircraft Engines. The current state of the art fuel consumption for a small engine is represented by the 4-stroke modified Enya engine which includes spark ignition, a carburetor, and an oil circuit [111]. The Navy is currently trying to improve performance through the Ultra Endurance Unmanned Aerial Vehicle (UE-UAV) heavy fuel engine (HFE) program [112]. Goals of the UE-UAV are for a SFC of around 300 g/kW-hr which corresponds to an efficiency of 27%. To meet the Navy's goals, manufacturers are modifying

engines to run on kerosene based fuels [113] as well as examining Wankel rotary cycles such as the UAV Engines LTD [114] shown in Figure 2.6.

Even with serious development, small internal combustion engines (ICEs) have matured to a point where efficiency gains are limited to only a few percent at best with a maximum obtainable efficiency likely around 30%. As electrochemical devices, fuel cell powerplants are not governed by the same Carnot efficiency limits as ICEs allowing theoretical efficiencies of up to 83%. System efficiencies >40% efficiency are normal for fuel cell systems, even at high power levels [43, 64]. In Figure 2.6, a 75 kW Ballard PEM [115] system is shown that is typical of the technology used in the Honda FCX V3 demonstration automobile [116, 117]. At normal power levels running on hydrogen and air, Honda reports that their FCX V3 has a system efficiency of 55% which results in a SFC of 55 g/kW-hr [74]. This SFC is over 33% lower than what could be achieved by a hydrocarbon fuel engine if it violated thermodynamic laws and operated at 100% efficiency!

Fuel cell units with rated power at or below 1 kW are also commercially available. Horizon Fuel Cell Technologies offers a series of small portable fuel cell systems that range from 12 to 5000 kW [118]. Figure 2.6 shows the SFC and specific power of a 1 kW Horizon system suitable for a small UAV. Note that the concentricity of the Horizon and Ballard PEM fuel cell stacks in Figure 2.6 shows that fuel cell systems can generally be scaled to various sizes while maintaining similar specific power and SFC.

2.4 History of Fuel Cell Flight

Atmospheric flight using fuel cells is a recent development. Atmospheric flight using fuel cells first began to appear in academic literature as a means for enabling multi-day unrefueled endurance. The idea of multi-day endurance was born out of solar

powered aircraft development such as the Advanced Research Project Agency (ARPA) Sunrise project [119] and later the NASA Environmental Research Aircraft and Sensor Technology (ERAST) program [120]. Researchers at both NASA Langley [121] and NASA Glenn [122] began promoting fuel cells as an alternative to batteries or gliding/thermalling as a means to maintain flight when adequate solar power was unavailable. As the crowning act of the ERAST project, NASA developed a fuel cell system to extend the endurance of its solar powered Helios vehicle. However, failure to anticipate the aircraft dynamics due to the weight of the fuel cell system resulted in the loss of the vehicle before it could be flown under fuel cell power [123].

At the time of the Helios accident in 2003, small battery powered UAVs such as the AeroVironment Wasp and Dragoneye were proving to be very valuable at providing close battlefield support despite their limited endurance. Fueled in part by renewed research and excitement in fuel cells as a result of the auto industry, applying fuel cells to small UAVs seemed a logical next step. The first fuel cell powered aircraft flight was accomplished by Lynntech under the Defense Advanced Research Projects Agency's (DARPA's) Synthetic Multifunctional Materials program [42]. Using a modified Wasp renamed Hornet, Lynntech sought to double the 100 minute endurance of the battery powered vehicle. Despite achieving over 2.5 times the energy of the Wasp's lithium-ion polymer battery in laboratory conditions, the Hornet was only able to fly for about 5 minutes before the fuel cells became too dry to operate. Despite achieving a first flight under fuel cell power, the difference in achieved vs. potential endurance of the Hornet emphasized the need for further fuel cell design and development work.

Figure 2.7: Lynntech/AeroVironment Hornet fuel cell UAV [124].

Between the 2003 flight of the Hornet and the year 2009, there have been at least 19 documented fuel cell aircraft that have achieved flight. Table 2.2 gives a brief summary of publically available statistics on each one of these aircraft.

2.4.1 System Integrators

The main groups who have flown fuel cell aircraft consist of small companies, research organizations, and universities. AeroVironment has been involved with several projects and has been able to leverage their experience with solar and battery electric aircraft to take a leading role. The AeroVironment Global Observer is arguably the most advanced and capable fuel cell UAV that has been flight tested. Other small companies such as Protonex, Horizon Fuel Cell Technologies, Adaptive Materials Inc. (AMI), and Lynntech have been involved with multiple demonstrations. More recently, BlueBird Aero Systems has partnered with Horizon Fuel Cell Technologies to offer the first commercially available fuel cell powered aircraft. Universities such as the Georgia

Table 2.2: Published fuel cell powered aircraft demonstrations.

System Integrators	Aircraft Name	Type	Fuel Cell Manufacturer	Fuel Storage	Wingspan (m)	GTOM (kg)	Max Power (W)	Endurance (hr)	Year	References
Lynntech/AeroVironment	Hornet	PEM	Lynntech	H_2 Sodium Borohydride	0.381	0.17	-	0.25	2003	[42]
AeroVironment	Global Observer	PEM	-	Liquid H_2	15.24	-	-	24	2005	[125]
FH-Wiesbaden	Hy-Fly	PEM	Heliocentris	Gaseous H_2	2	1.75	65	0.025	2005	[126]
Naval Research Lab	Spider-Lion	PEM	Protonex	Gaseous H_2	2.2	3.1	115	3.3	2005	[127]
Adaptive Materials (AMI)	-	SOFC	AMI	Propane	-	-	60	4.3	2006	[128]
Georgia Inst. of Tech.	-	PEM	BCS	Gaseous H_2	6.58	16.4	550	0.75	2006	[58, 59]
Cal State LA	-	PEM	Horizon	Gaseous H_2	5.49	12.9	513	0.25	2006	[129]
SmartFish/DLR	HyFish	PEM	Horizon	Gaseous H2	1	6.1	1300	0.25	2007	[130, 131]
AFRL/AeroVironment	Puma	PEM	Protonex	Sodium Borohydride	2.6	6.5	-	9	2007	[28, 132]
Cal State LA/Oklahoma State Univ.	Pterosoar	PEM	Horizon	Gaseous H_2	4	5	150	12	2007	[133, 134]
Korea Advanced Institute of Science and Tech.	-	PEM	-	Sodium Borohydride	1.2	2	-	10	2007	[135]
Boeing	Dimona	PEM	Intelligent Energy	Gaseous H_2	16.3	841		0.5	2008	[136-138]
AMI/AeroVironment	Puma	SOFC	AMI	Propane	2.6	-	-	7	2008	[139]
United Technologies Research Center	FC Helicopter	PEM	UTRC	Gaseous H_2	-	-	-	-	2008	[76]
Adaptive Materials/U. of Michigan	Endurance	SOFC	Adaptive Materials	Propane	1.524	5.3		10.25	2008	[140]
DLR	Antares	PEM	BASF	Gaseous H_2	20	660	25000	5	2009	[141-143]
BlueBird Aero Systems	Boomerang	PEM	Horizon	H_2 Hydride	2.75	9	500	9	2009	[144-146]
Naval Research Lab	XFC	PEM	Protonex					6	2009	[147]
Naval Research Lab	Ion Tiger	PEM	Protonex	Gaseous H_2			500	24	2009	[148]

Institute of Technology, California State University Los Angeles, and the University of the Michigan have taken a lead in using student led projects to both design and build proof of concept aircraft [149, 150]. Government research organizations such as the Deutschen Zentrums für Luft und Raumfahrt (DLR), the Air Force Research Lab (AFRL), the Naval Research Lab (NRL), and NASA have been actively involved in multiple flight demonstrations [28]. Additionally, research arms of large aerospace corporations like Boeing and United Technologies have flown demonstrators [76]. Overall, the 19 known flight demonstrations of fuel cell UAVs represent a diverse group of at least 25 different organizations.

2.4.2 Size

The size and investment in each of the successful aircraft has greatly varied. Many of the aircraft designed and built by universities had very low budgets and relied on donated and off the shelf components. Many of the projects related to DLR, AFRL, and NRL received more moderate funding [151-153].

2.4.3 Airframe

Airframes of fuel cell aircraft have varied from low aspect ratio high wing loading designs like the biologically inspired HyFish to high performance motor gliders like the Antares (see Figure 2.8). Most aircraft have tended toward high aspect ratio low wing loading designs to improve endurance and compensate for low specific power. A few aircraft such as the FH-Wiesbaden Hy-Fly and the Korean Advanced Institute of Science and Technology (KAIST) aircraft have chosen flying wing configurations. United Technologies Research Center is the first known organization to successfully fly a rotary

wing configuration [76]. A European Union research project called the Fully Autonomous Micro Helicopter flew a 350 g quadrotor helicopter in 2009 [154].

Most of the fuel cell aircraft have used existing airframes. Boeing chose to modify the Diamond Aircraft Dimona motor glider while DLR selected a similarly designed Lange Aviation Antares 20E. The NRL Spider Lion and FH-Wiesbaden Hy-Fly used existing model airplane kits. The Lynntech/AeroVironment Hornet used the Wasp airframe. The AeroVironment Puma has been used as the base airframe for two different fuel cell demonstrations. AFRL and Protonex used the Puma to make a PEMFC powered flight and Adaptive Materials used the Puma to house their portable SOFC stack for a similar flight demonstration.

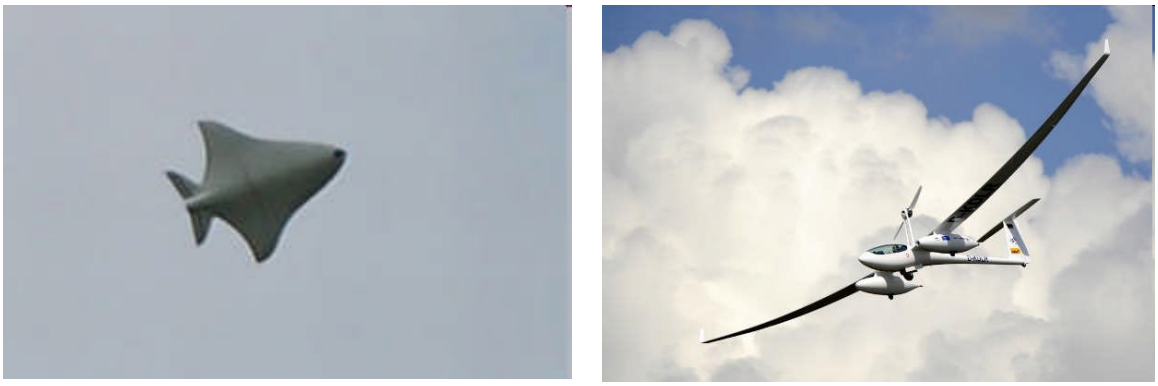

Figure 2.8: DLR/Smartfish HyFish (left) [155] and DLR Antares (right) fuel cell aircraft [156].

Universities such as the Georgia Institute of Technology, California State University Los Angeles, Oklahoma State University, and the University of Michigan have all developed custom airframes designed around specific fuel cell systems. The designs have all featured sailplane like wing designs with oversized fuselages designed to house the fuel cell and hydrogen storage systems. Each of the university designed

aircraft used very low specific power fuel cell stacks and chose to size the aircraft to meet the power of the propulsion system.

Many of the aircraft feature no landing gear and require assistance at launch. Some are light enough to be hand launched while others such as the KAIST demonstrator and the DLR HyFish have used special catapult launching systems [157].

Figure 2.9: Oklahoma State/Cal State LA Pterosoar (left) [158] and Georgia Tech (right) fuel cell aircraft.

More recently, development work by Protonex, Horizon Fuel Cell Technologies, the United Technologies Research Center, and Adaptive Materials Inc. have produced advanced fuel cell units tailored toward the specific power needs of UAVs. As a result, custom designed airframes for various missions are appearing. The Naval Research Laboratory has developed the Ion-Tiger PEM powered UAV designed to demonstrate 24 hour endurance carrying a 2.3 kg (5 lb) payload. The Naval Research Laboratory also recently announced the XFC which is an expendable portable UAV with foldable wings (see Figure 2.10). At the Paris Air Show in 2009, BlueBird Aero Systems and Horizon Fuel Cell Technologies displayed the Boomerang (see Figure 2.10). The Boomerang is the first commercially available fuel cell powered UAV.

2.4.4 Fuel Cell Powerplant

Of the 19 different aircraft that have flown, nine different fuel cell manufacturers have participated. The manufacturers vary from large corporations like United Technologies and BASF that have years of experience with fuel cell development, to small companies like Protonex and Horizon Fuel Cell Technologies that are focusing on the portable power market. With the exception of the SOFC units provided by Adaptive Materials Inc., all of the known fuel cells to achieve flight have been PEMFC.

Figure 2.10: BlueBird Boomerang (left) [159] and NRL XFC (right) fuel cell aircraft [147].

The architectures of the different fuel cell systems are largely unknown. Diagrams and detailed descriptions of the fuel cell systems are only available for a few of the aircraft. Companies such as Protonex and Adaptive Materials Inc. surround their fuel cell and balance of plant in an enclosure making the architecture difficult to determine. Of the systems that are in the public domain, the fuel cell and balance of plant architecture varies. Traditional PEMFC systems with a coolant loop composed of pumps and radiators, an air management system with compressors and humidifiers, and a hydrogen system with valves and regulators have been used on aircraft such as the NRL

Spider Lion [127] and the GT FCUAV [58]. Simplified systems such as the Horizon Pterosoar fuel cell [133] that achieve both the cooling and air delivery with a single axial fan have also been used (see Figure 2.12).

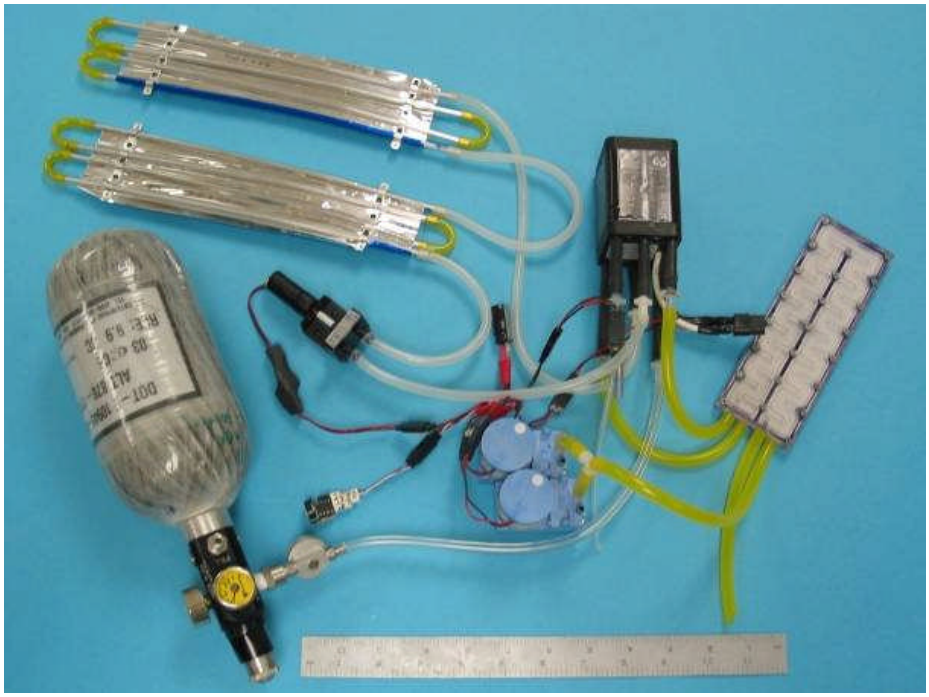

Figure 2.11: Protonex/NRL fuel cell system on the Spider Lion UAV [127].

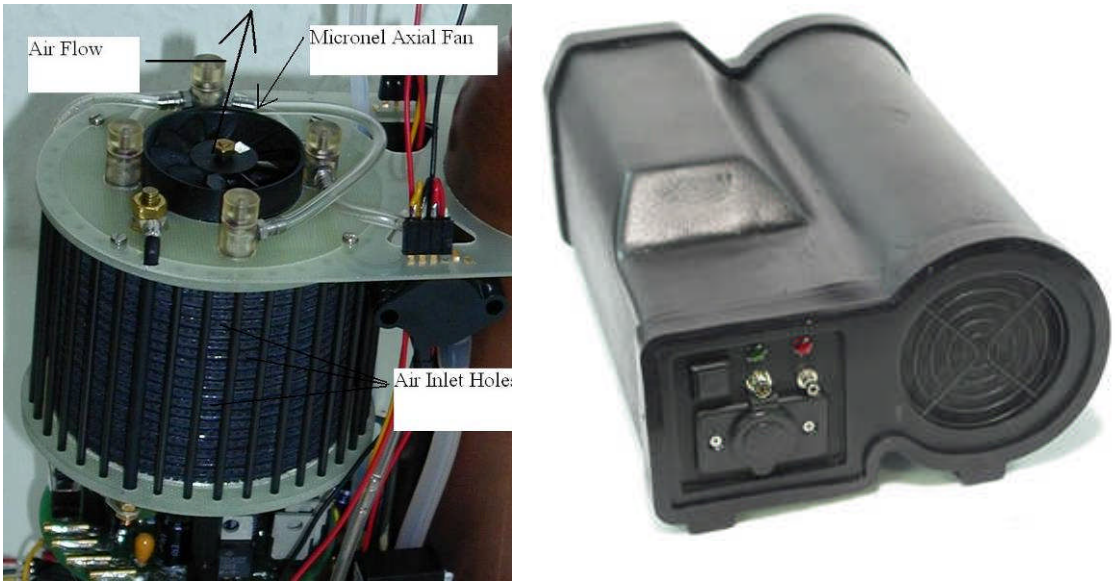

Figure 2.12: Horizon fuel cell (left) [133] and Adaptive Materials Inc. SOFC (right).

Some of the aircraft, including the Boeing Dimona, the AFRL/AeroVironment Puma, and the Cal State LA/Oklahoma State Pterosoar have augmented their fuel cell systems with batteries for high power conditions such as takeoff and climb [133, 136]. Other aircraft such as the GT FCUAV and the DLR Antares have chosen to use only fuel cell power over the whole mission including takeoff and climb.

2.4.5 Hydrogen Storage

Storing the hydrogen has been accomplished in various forms. Most aircraft store hydrogen either as a compressed gas in a pressure vessel, or through a chemical reaction in sodium borohydride tanks. The exceptions are the Adaptive Materials system which reforms hydrogen for their SOFC from standard propane tanks and the AeroVironment Global Observer which stores hydrogen as a liquid at cryogenic temperatures.

2.4.6 Performance

Performance specifications differ widely from aircraft to aircraft. Some aircraft have reported endurance values from actual flight tests while others have extrapolated based on flight results. Most organizations have chosen to publish only limited data related to performance of the actual test aircraft. Some of the early aircraft could only fly for a few minutes while some have estimated flight times of up to 24 hours. As of late 2009, the longest reported flight test has been 26 hours for the NRL Ion Tiger [160]. The next best reported flight endurances have been 9 hours for the Protonex/AeroVironment Puma [132] and 10.25 hours for the Adaptive Materials Inc./University of Michigan Endurance [140].

With the exception of the BlueBird, all of the aircraft have been proof-of-concept prototype vehicles. Most of the vehicles including the Boeing Dimona, GT FCUAV, Cal State LA demonstrator, FH-Wiesbaden Hy-Fly, and the DLR Hy-Fly were designed to achieve flight as the primary objective. In contrast, aircraft such as the NRL Ion Tiger and the Cal State LA Pterosoar have been specifically designed and flight tested to maximize endurance.

With the exception of the AeroVironment Global Observer, the highest endurance values have been reported for the lighter aircraft that have a total mass under 10 kg. Larger manned aircraft such as the Antares and Dimona have had more limited endurance despite their highly efficient aerodynamic designs. The Global Observer is likely an exception primarily due to its liquid hydrogen tank which could carry a much higher percentage by mass of hydrogen as compared to compressed tanks [103]. The Global Observer also had a custom designed airframe vs. the modified existing airframes used on other heavier fuel cell aircraft.

2.4.7 Summary of Flight Demonstrations

As of December 2009, only 19 aircraft are known to have flown under fuel cell power. These aircraft have been developed by various organizations with drastically varying budgets and performance. Both PEMFC and SOFC aircraft have flown and various fuel cell system architectures have been used. Aircraft design has varied and many configurations have been successfully used. Aircraft have varied in size from small hand launched UAVs to manned motor gliders. Information on the different aircraft is contained almost entirely in press releases. For many aircraft, fundamental data on size, mass, and power are unavailable. Of the many companies, research institutions, and

universities that have been involved, only a few such as Georgia Tech, Cal State LA, NRL, DLR, and Boeing have chosen to publish reports or presentations that give details of the design. Of all the 19 aircraft, only Georgia Tech has actually published any experimental flight data [59]. Despite the growing number of successful flight demonstrations, the basic design rules and lessons learned from a successful demonstration remain out of the public domain.

2.4.8 Aircraft in Development

In addition to the fuel cell aircraft that have achieved flight, several aircraft are known to exist or to be in development. One of the earliest planned fuel cell aircraft was a manned design using a modified DynAero Lafayette III [161]. A patent was filed on the design in 2001 [162] and a goal flight date set for 2004, but no press release has been made of a successful flight. A similar aircraft in development is the Environmentally Friendly Inter City Aircraft powered by Fuel Cells (ENFICA-FC). The ENFICA-FC project consists of several European companies and universities that are converting a two seat manned Jihlavan Rapid 200 aircraft to operate on a fuel cell system [163]. An additional manned fuel cell aircraft termed the SkySpark is also under development in Europe. The goal of the SkySpark is to achieve a 300 km/hr speed record in an environmentally friendly aircraft. On June 12, 2009, the SkySpark aircraft achieved 250 km/hr in a flight powered by batteries. The project is now working on the fuel cell powerplant system for the aircraft [164].

BlueBird AeroSystems is currently developing a small UAV called the Thunderbird. The goal of the Thunderbird is to achieve 10 hours of endurance aided by a fuel cell with a specific power of 500 W/kg [165].

2.5 Fuel Cell Aircraft Design

As fuel cell and hydrogen storage have developed to technological readiness levels appropriate for flight, a relatively small group of researchers have begun to look into fuel cell aircraft design. Most design studies have followed a simple methodology where an existing aircraft design is chosen and compared to the same airframe retrofitted with a fuel cell propulsion system. A few studies have built multidisciplinary analyses and have used optimization to size the vehicle and propulsion system. More recently, probabilistic design methodologies have been formulated that are applicable to fuel cell aircraft design.

2.5.1 Retrofit Design Studies

The vast majority of published fuel cell design studies have been based on the concept of retrofitting an existing airframe with a fuel cell based propulsion system. Researchers have chosen to focus primarily on the subsystem level sizing and synthesis of the propulsion system subject to a mature airframe design with known performance characteristics. A notional methodology process chart with a general aviation aircraft design presented in Wentz et al. [166] is shown in Figure 2.13. The basic concept is to take a mature aircraft design with known performance and remove the propulsion system. The design then seeks to optimize a fuel cell propulsion system subject to various constraints such as mass, power, and volume that are related to the airframe. The resulting design is then compared to the mature existing aircraft and any technology gaps needed to match existing performance are noted.

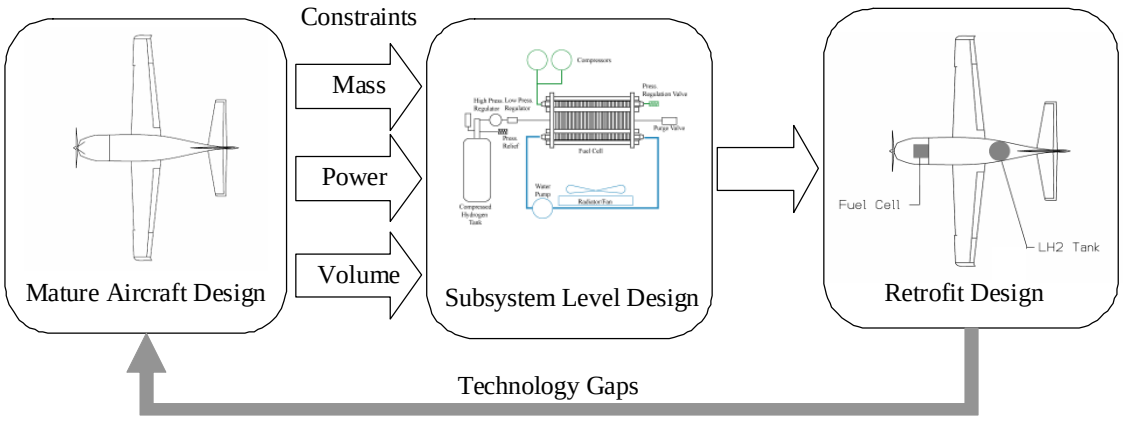

Figure 2.13: Retrofit aircraft design methodology.

Kohout, et al. [167]**,** Wentz and Mohamed [166]**,** Romeo [163]**,** and Berton et al. [168] have all examined retrofitting light general aviation aircraft while maintaining the initial takeoff gross weight as a constraint. The results of each study conclude that although the retrofitted aircraft may be capable of flight, none could match the performance of its internal combustion counterpart. Each report then proposed various improvements needed to bridge the gap in performance with ideas ranging from using an advanced SOFC with a turbine [167], to a PEMFC and liquid hydrogen system with an efficiency > 60% and a propulsion specific power of 625 W/kg [166]. This same retrofit based approach has also been applied to larger transport planes resulting in an even larger technological performance gap between the existing and retrofitted aircraft as well as the need for additional volume for fuel storage [169].

All retrofit design studies have focused almost entirely on sizing the fuel cell propulsion system. Wentz and Muhammed [166] chose to simply model the fuel cell using assumed values for specific power, power density, and efficiency of the fuel cell system. This conceptual approach allowed them to quickly analyze the mass breakdown and range of several vehicles. Although very high level, the study allowed Wentz and

Muhammed to conclude that a general aviation aircraft would be most accommodating for a fuel cell retrofit. Larger aircraft would require configuration changes to account for increased volume requirements due to the low-density of hydrogen.

Conceptual studies like those of Muhammed and Wentz do not provide a path to achieving their assumed fuel cell metrics, and their assumed efficiencies are much higher than what has been reported for state of the art fuel cell systems. To achieve better fidelity, researchers at NASA have built more detailed fuel cell system models that attempt to include the weights, volumes, efficiencies, and power requirements of the balance of plant. A NASA study performed by Berton and Freeh [168] built a propulsion model based on the diagram shown in Figure 2.14 to model the performance of a small light general aviation aircraft. The Numerical Propulsion System Simulator (NPSS) code was used [170] to model the solid shaped components shown in Figure 2.14 while the dashed shapes were modeled using either data or available performance models. The propulsion model would minimize hydrogen flow for a given thrust. The results from the propulsion model were then used in NASA's Flight Optimization System (FLOPS) computer code to compute aircraft mission performance. The use of legacy codes and experimental data provide a sense of credibility to the analysis, however, no estimates of uncertainty or validation were provided.

Analysis of Berton and Freeh's model suggested that flight was possible using existing off-the-shelf technology but would require reduced speed, climb rate, payload, and range. However, the detailed analysis did reveal that the fuel cell propulsion system could perform low propeller shaft speed takeoffs with considerable noise loss and improved field length and climb compared to conventional propulsion.

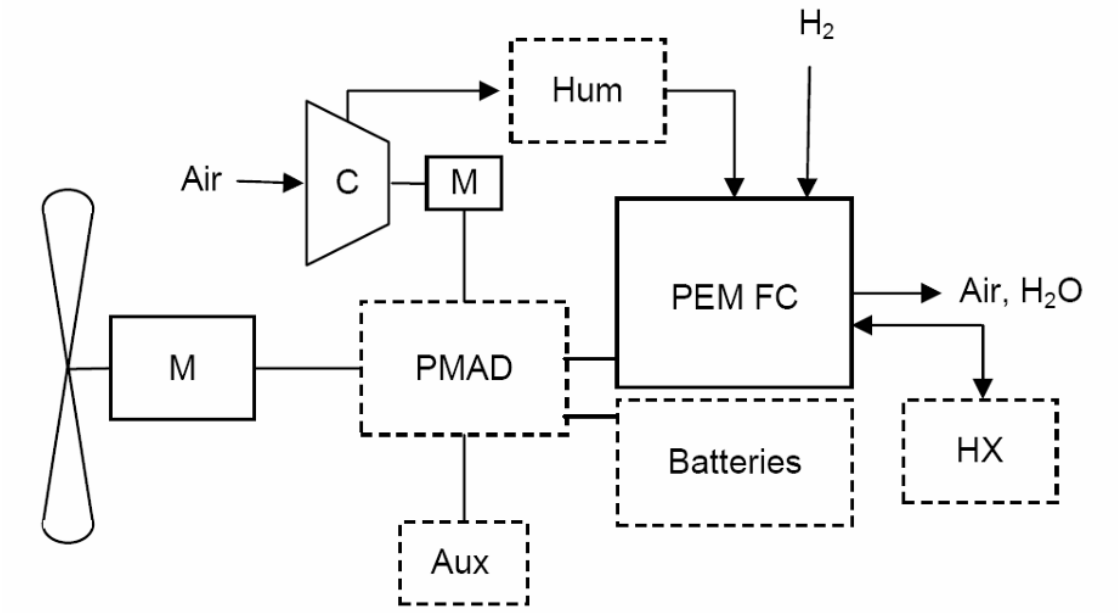

Figure 2.14: Fuel cell propulsion system proposed by Berton and Freeh [168].

Overall, retrofit design studies are useful in that they provide a direct comparison of fuel cell vs. conventional propulsion performance for a common platform. With a mature airframe, overall analysis is simplified and little uncertainty exists relating to the airframe weight and aerodynamic performance. The sizing of the fuel cell system is simplified as the vehicle provides hard constraints that do not vary with fuel cell sizing variables. Despite these advantages, the results will always be suboptimal as the airframe has been previously optimized for a propulsion system with characteristics that vastly differ from a fuel cell powerplant system. In addition, despite the best effort of researchers to estimate the performance of a future system, uncertainty will be high until hardware is actually developed and tested. As an example, Boeing engineers have noted that retrofitting a Dimona aircraft with a PEMFC system has been difficult due to volume, weight, power management, and thermal interactions that evidently were not fully appreciated until hardware was developed [171].

2.5.2 Multidisciplinary Based Design Methodology

To move beyond the limitations of existing airframes, many researchers have replaced the subsystem specific design environment of the retrofit methodology with a multidisciplinary design environment that includes sizing of both the aircraft as well as the propulsion system. The methodology that has resulted is generalized in Figure 2.15. Similar to the methodology in Figure 2.13, the design begins with a notional concept. Rather than using fixed constraints provided by an existing airframe, a multidisciplinary design analysis is used where the propulsion and airframe are coupled. An optimization is then performed subject to constraints that represent a given mission. Typical mission analyses often include very optimistic performance levels that cannot be achieved with current propulsion technology. Therefore, results often include feasibility studies that determine the technological gaps that are required to satisfy the mission constraints.

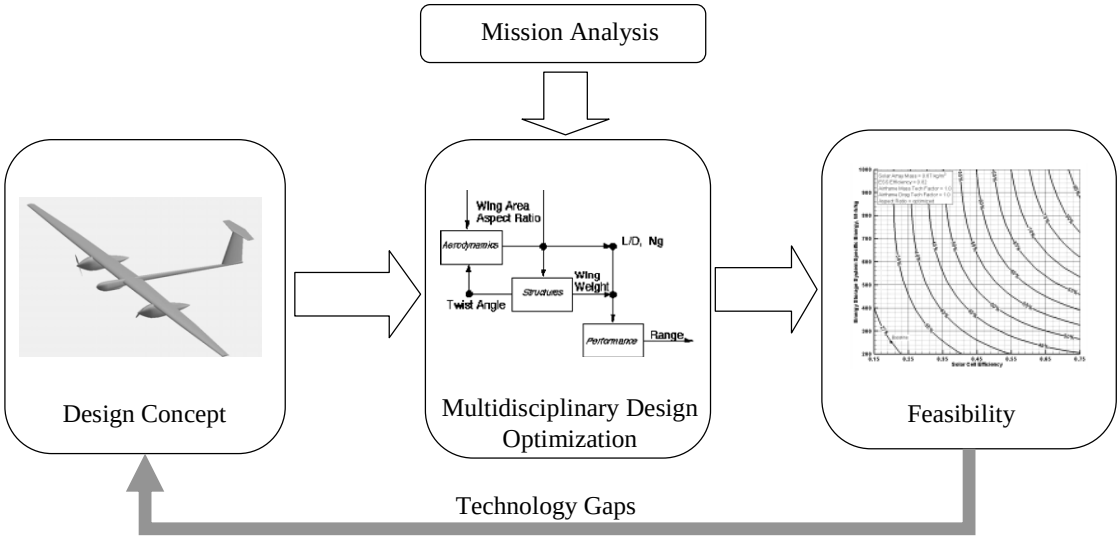

Figure 2.15: Multidisciplinary based design methodology [172].

Several implementations of the methodology shown in Figure 2.15 have been published. A NASA study performed by Nickol et al. [172] examined several design concepts for a HALE mission. The multidisciplinary analysis was accomplished using a

HALE Multi-disciplinary Design Optimization (MDO) code developed by AeroVironment. The code provides high-level conceptual analysis and sizing of lightweight low wing loading aircraft specifically for HALE missions. The code was calibrated by NASA to the Scaled Composites Voyager aircraft, the Boeing Condor HALE UAV, the AeroVironment Pathfinder, and the AeroVironment Helios aircraft using calibration factors to account for any significant discrepancies between predicted and actual performance. The missions involved hurricane science and communications relay missions with an endurance up to 180 days, payload mass of at least 136 kg, and altitude of 18-21 km. None of the fuel cell aircraft concepts could meet all of the performance targets and the study concluded that the missions would be best served in the near-term by a fleet of smaller diesel fueled aircraft with endurance on the order of four days.

Another NASA study performed by Guynn et al. [173] extended the NPSS and FLOPS based model to a blended wing body aircraft designed for utility similar to a Boeing 767. The fuel cell system was implemented in this system to both reduce noise and emissions. The blended wing body design was chosen since it had been studied in detail previously; however, the analysis did allow the design to be scaled to meet the volume requirements of the fuel cell propulsion system. The study concluded that even with optimistic advances in technology, the aircraft was not feasible using the fuel cell propulsion system.

Similar to the decomposition and modeling approach of the NASA studies, is an approach employed by Choi et al.[174]. Choi focused most of his effort on developing a notional fuel cell based propulsion architecture. To build the MDO, energy and power

relationships were derived. Both an on-design and off-design analysis sequence for determining performance were constructed. Figure 2.16 shows the decomposition as well as data exchange in the model proposed by Choi. The primary difference between Choi and NASA was the choice of analysis tools. Rather than using NPSS and FLOPS, each of the component blocks in Figure 2.16 were modeled using primarily in-house codes developed by the Georgia Institute of Technology. As many of these codes existed in different programming languages, Choi used Phoenix Integration's ModelCenter to integrate all of the codes and calculate the system level solutions.

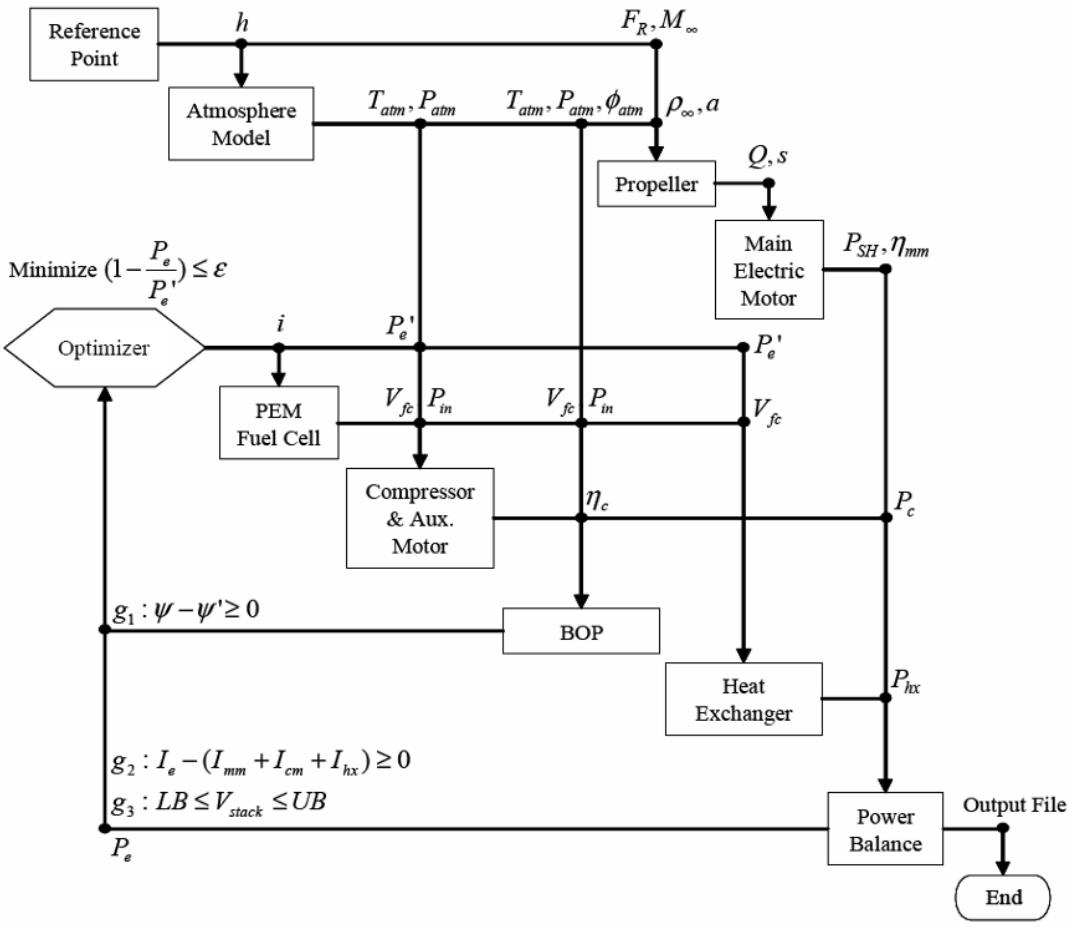

Figure 2.16: Fuel cell propulsion system model proposed by Choi et al. [174].

Using a general aviation propulsion system power requirement, Choi noted that the fuel cell propulsion system did not have as drastic of a power-lapse effect with increasing altitude as conventional propulsion systems. The hydrogen flow rate was also found to increase with altitude due to pressurization requirements of the fuel cell stack and component efficiencies were found to be relatively independent of Mach number.

In a separate study, Choi et al.[175] used the propulsion system in Figure 2.16 to study the design of a HALE aircraft to perform the same mission as the Global Hawk UAV. The resulting fuel cell powered HALE aircraft proved to be much larger and nearly three times heavier than a gas turbine powered Global Hawk although Choi did calculate that future improvements in technology could make the fuel cell aircraft comparable in weight.

Another approach to multidisciplinary design was published by Ofoma and Wu [150]. Ofama and Wu concluded that fuel cell aircraft design will be dominated by the selection of a fuel cell. They choose to use energy to size the fuel cell system and recommended an iterative process based on fuel cell selection. This provided a straightforward although iterative process to design a fuel cell aircraft. A similar approach was taken by Chiang et al. [133]. In Chiang, an energy requirement was used to specify a fuel cell system for an aircraft and a battery was chosen to supplement that system to meet a power requirement. An airframe was then sized based on a combination of constraints provided by the fuel cell as well as an overall limit on take off mass. The resulting aircraft flew in 2007 and is slated to make a future 16 hour endurance flight.

One of the challenges for most design methodologies has been developing adequate aircraft performance relationships within the multidisciplinary analysis.

Researchers have often noted that traditional sizing relationships are not applicable for fuel cell aircraft design. As a result, a few researchers have focused on defining the sizing and performance relationships of fuel cell propeller aircraft. Colozza [122] used power conservation to develop a relationship for the necessary wing area and aspect ratio needed for a fuel cell/solar cell aircraft and concluded that specific energy of the fuel cell system substantially effected aircraft size. Nam [176] developed fundamental energy and power based relationships that are applicable to the design and performance estimation of virtually any type of propulsion system. Deemed the Architecture-Independent Aircraft Sizing Method (AIASM), the method provides relationships for generalized constraint analysis, mission analysis, and weight estimation for any aircraft regardless of its chosen power source. Nam performed design examples for conventional, fuel cell, and solar cell powered aircraft.

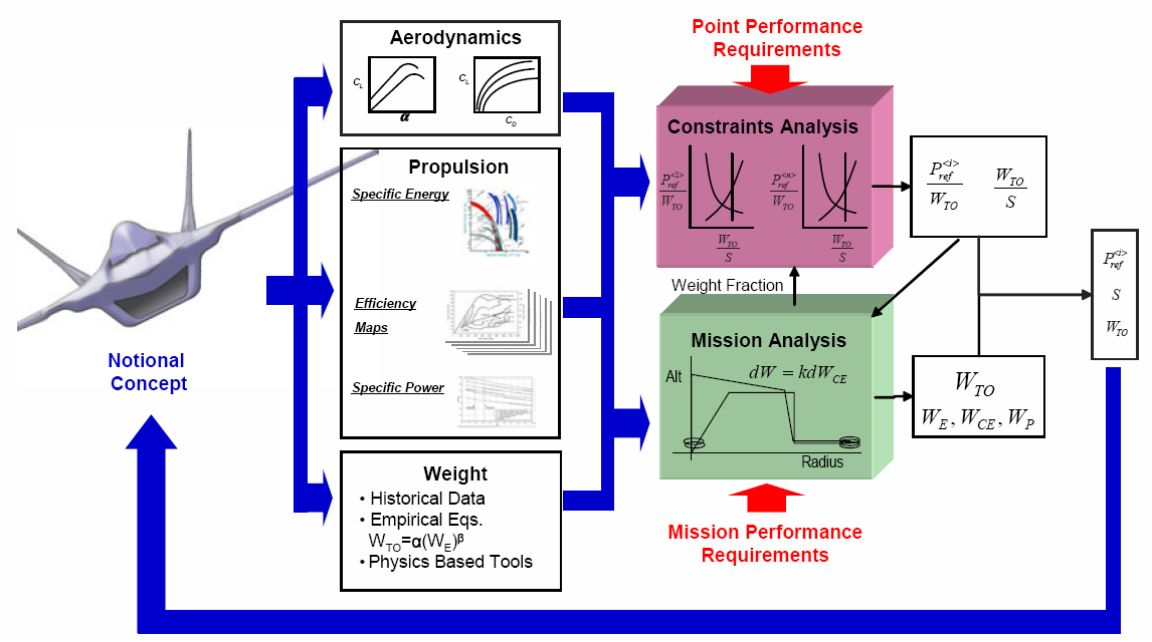

Figure 2.17: Overview of AIASM [176].

2.5.3 Technology Mapping Methodology

Both the retrofit and multidisciplinary based design methodologies have largely resulted in aircraft design studies where the final aircraft can either not meet mission requirements or cannot meet or exceed the performance of a similar vehicle powered by conventional propulsion. This has led researchers such as Soban and Upton [177] to apply a technology mapping methodology aimed at identifying a vehicle to capitalize on the unique features of fuel cell propulsion. Figure 2.18 shows the flow chart that summarizes the technology mapping methodology.

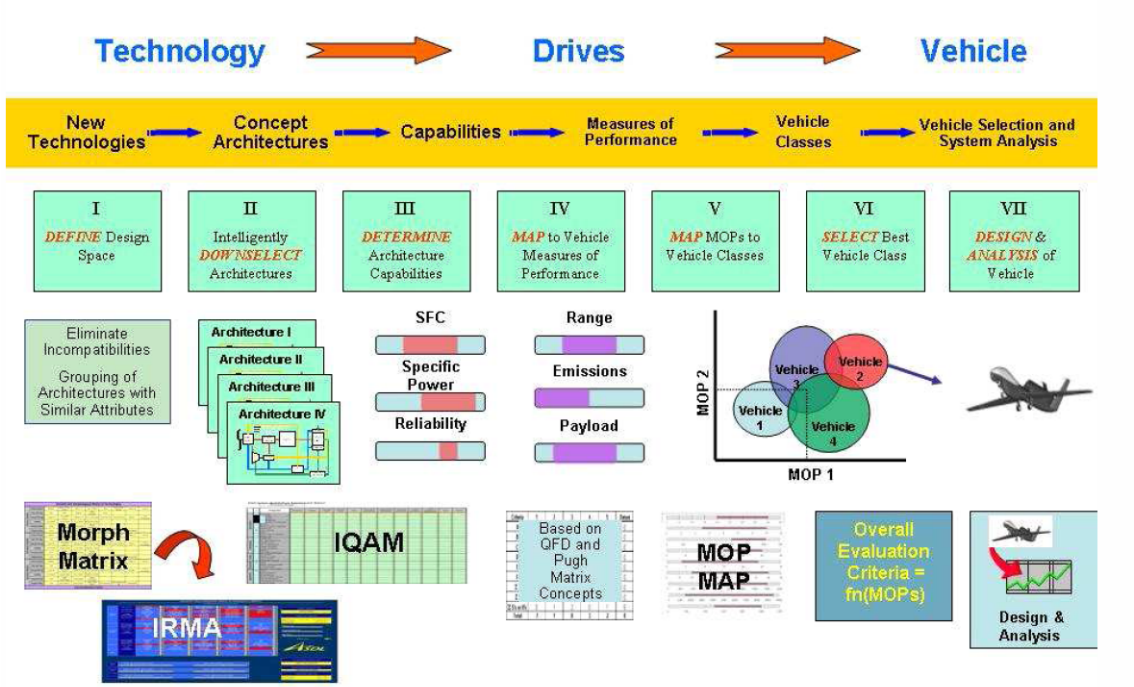

Figure 2.18: Technology mapping methodology [177].

Soban and Upton used the technology mapping methodology to study both the near-term and future performance of both PEMFC and SOFC powered aircraft. They concluded that fuel cell systems are most appropriate for long-endurance low-power missions such as a long-endurance low-altitude ISR UAV. At current technology levels,

fuel cell systems did not compete well against conventional propulsion but technologies such as SOFC showed potential at future technology levels.

2.5.4 Probabilistic Design Methodologies

Most fuel cell researchers have noted the high uncertainty associated with the design of any fuel cell system. Since very few fuel cell vehicles have been developed and most state-of-the-art fuel cell performance data is proprietary, verification and validation of fuel cell aircraft designs are lacking. Although not directly accounting for uncertainty, most studies have attempted to use mature airframe designs and legacy design tools when appropriate to help support the validity of the results. To further fuel cell aircraft design, a few researchers have begun applying probabilistic design methodologies to fuel cell aircraft design.

Probabilistic design methodologies have received significant research and development over the last two decades. In particular, universities such as the Georgia Institute of Technology have set up specific laboratories such as the Aerospace Systems Design Laboratory (ASDL) to develop, advance, and apply probabilistic design methodologies. On of the earliest methodologies was an approach deemed Robust Design Simulation (RDS) [178]. Robust Design Simulation was developed to identify designs that are most insensitive to noise variables. The methodology is highly based on Response Surface Methodology (RSM) which is needed to develop efficient surrogate models that can be used in a Monte Carlo Analysis. The method has been applied to many design problems including several conceptual design studies of a high-speed commercial transport. The basic steps of RDS are shown in Figure 2.19.

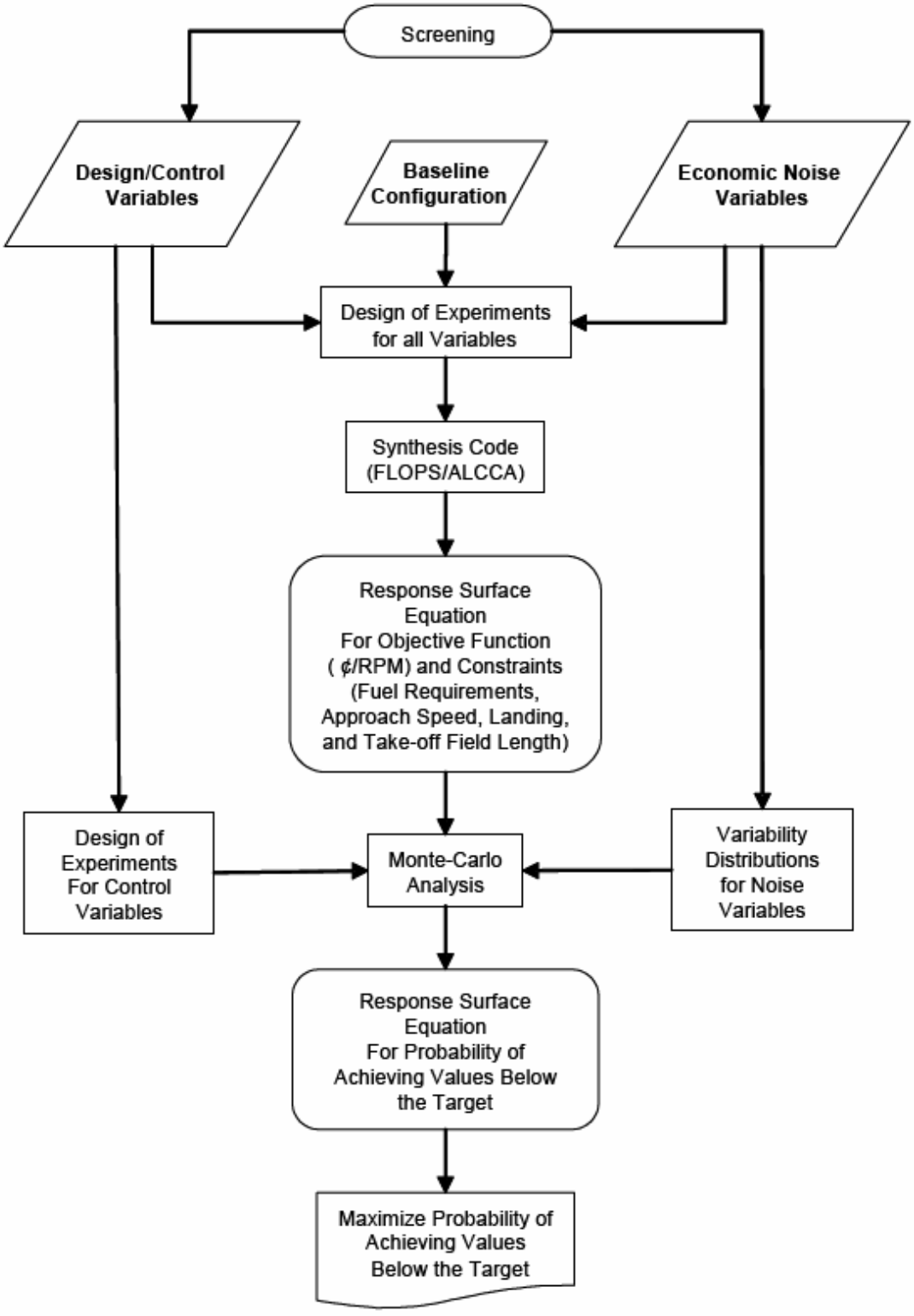

Figure 2.19: Robust design simulation [178].

The RDS method sizes an aircraft deterministically using existing design tools and then seeks to calculate the impact on system level metrics due to the variability of noise variables. As implemented, RDS does not size an aircraft subject to probabilistic constraints and seeks a solution that maximizes the probability of meeting a single overall evaluation criterion. This makes the method less appropriate to fuel cell aircraft where many independent probabilistic constraints will influence aircraft sizing.

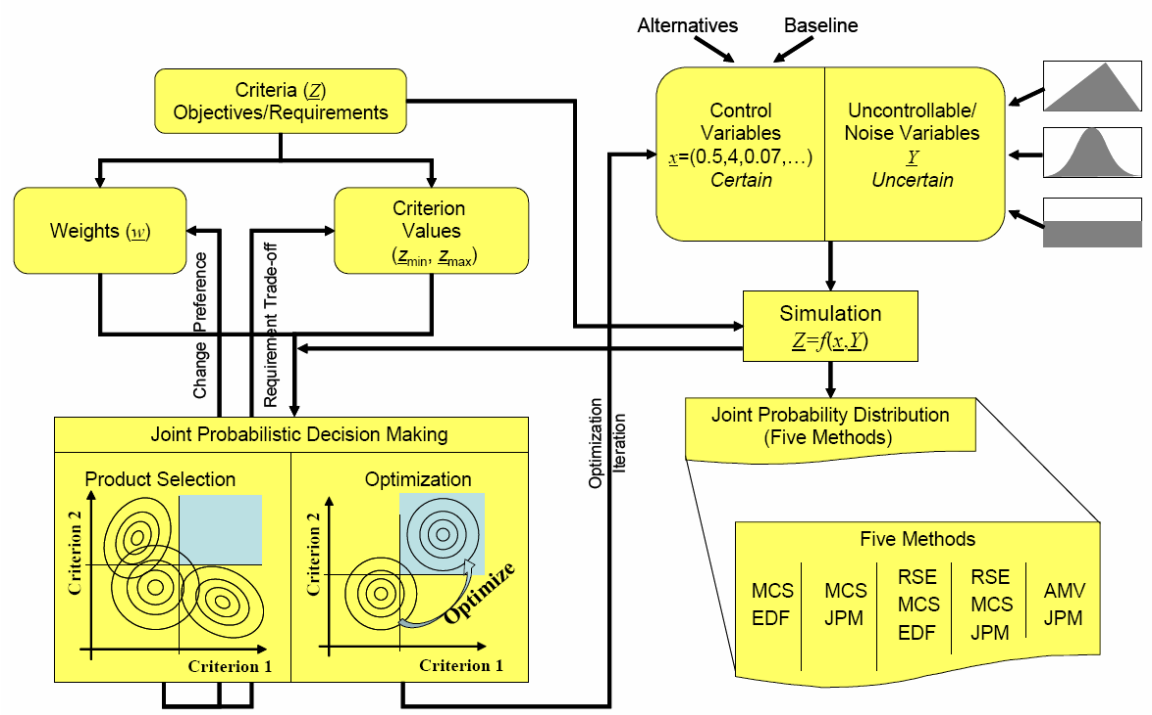

Figure 2.20: Bandte's JPDM process [179].

Another proposed probabilistic based methodology is the Joint Probabilistic Decision Making (JPDM) method proposed by Bandte [179]. This method is similar to RDS and also uses RSM and Monte Carlo analysis to facilitate the probabilistic analysis. This method is designed to facilitate designs that can meet the joint probability of multiple design criterion. The JPDM method has been applied to various aircraft designs including a high-speed commercial transport. In the JPDM method, the probability of

success is evaluated at fixed values. This does not facilitate probabilistic constraints that are multivariate functions of aircraft design variables.

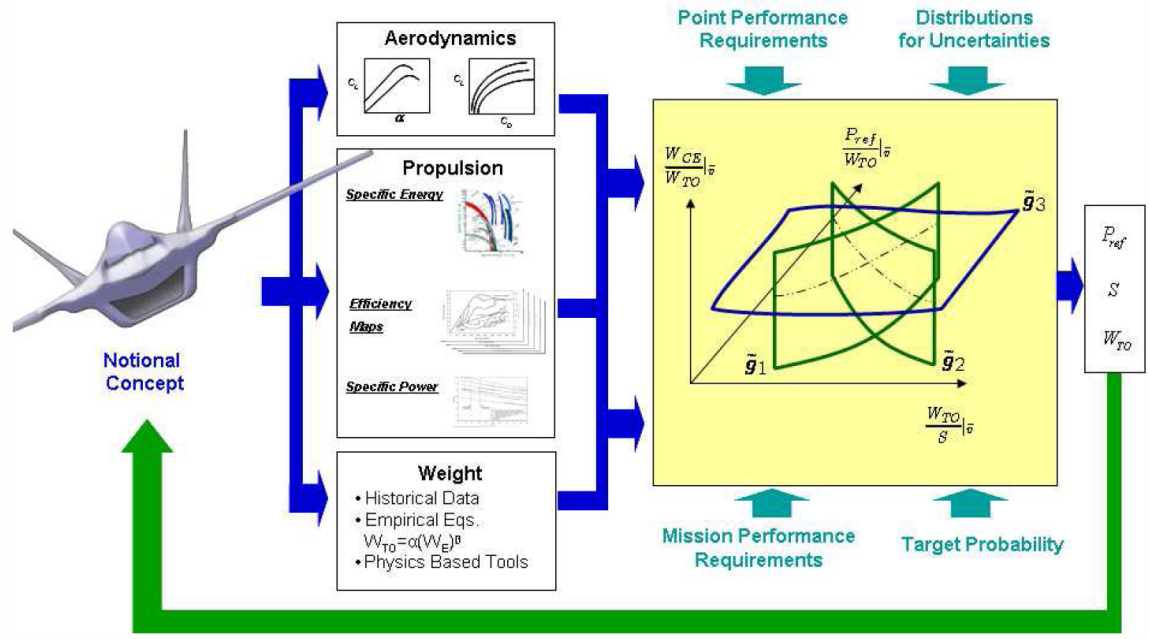

Figure 2.21: Probabilistic aircraft sizing method [176].

Based on the limitations of RDS and JPDM, Nam formulated the Probabilistic Aircraft Sizing Method (PASM) [176]. The goal of PASM is to allow adequate design margins in a design to account for the various sources of uncertainty. Nam accomplishes this by formulating a methodology based on the application of change-constrained programming (CCP). The method allows a design to be optimized within a probabilistically feasible space that is constrained by probabilistic constraints that are multivariate functions of the system design variables. A diagram outlining PASM is shown in Figure 2.21.

In PASM, uncertainty is captured through both probabilistic constraints and probabilistic evaluation criteria. Choi [180] has noted that this may prove to be overly

conservative for a new and revolutionary technology with high uncertainty. Choi notes that in practice, as hardware is developed or better analytical tools are developed, design cycles often use recourse as a method to update a design.

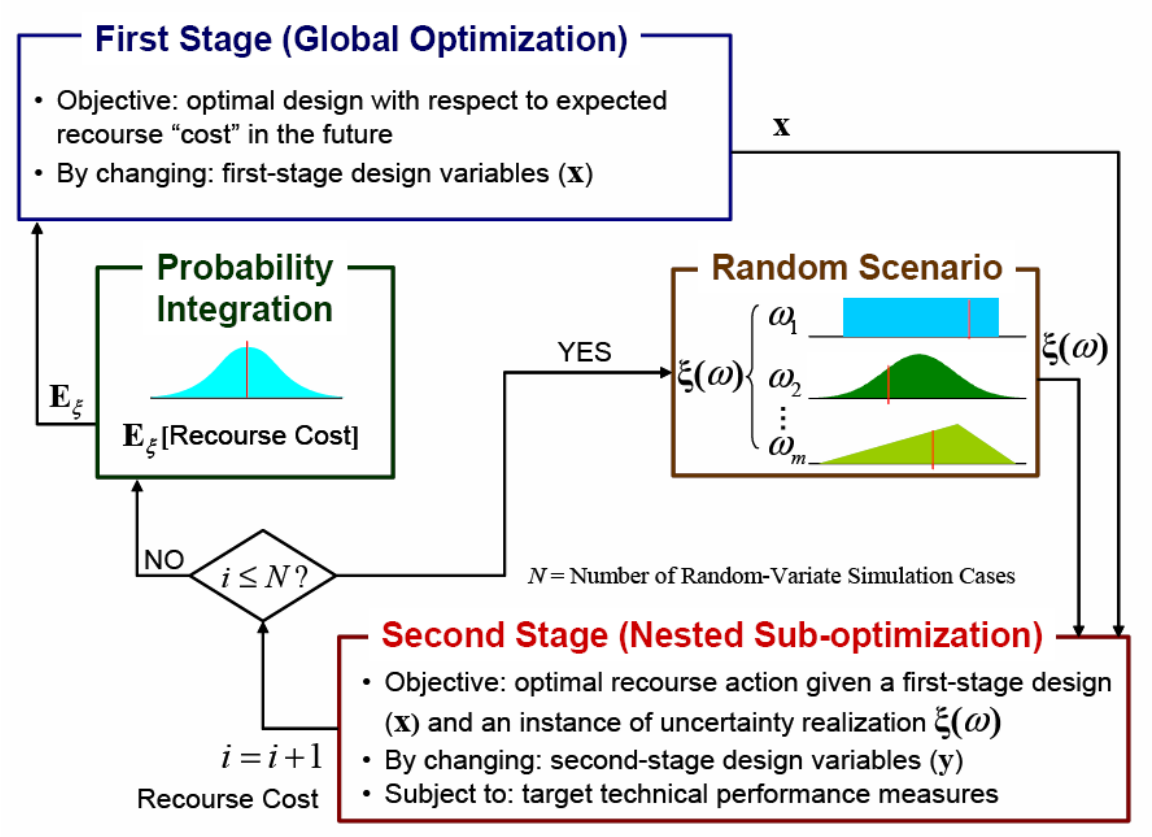

Figure 2.22: Recourse based design methodology [180].

Choi proposed a recourse based design methodology (see Figure 2.22) where the design process is composed of two stages. The first stage is composed of identifying a design before adequate estimates of uncertain parameters are known. Assuming that the realization of uncertain parameters will affect the feasibility of the design, a second design stage is implemented using an *a posteriori* correction to the first stage design. A penalty is imposed to the second-stage design to account for the increased costs that occur with having a multi-stage design. Choi proposes embedding the multi-stage

recourse based analysis inside a larger design loop to study the costs of numerous recourse scenarios in an attempt to provide a more balanced solution than robust, probabilistically maximized, or chance-constrained solutions. Choi tests the approach using multidisciplinary design analyses based on both PEMFC and SOFC UAVs.

2.6 Georgia Tech Fuel Cell UAV Design

In addition to the fuel cell aircraft design studies in the literature, an important foundation that provided background to this research was the development of the Georgia Tech Fuel Cell UAV (GT FCUAV). The GT FCUAV provided valuable experience in all phases of design, hardware development, and experimental testing. A brief summary of the GT FCUAV is provided. Further documentation of the design and testing of the GT FCUAV is available in references [57-60].

The GT FCUAV originated in the summer of 2004 with the hypothesis that using primarily off-the-shelf technology, a fuel cell aircraft could be designed and constructed to achieve flight. At the time, this was a very ambitious hypothesis to test as the budget and timeframe constraints of the project limited fuel cell selection to a handful of fuel cells stacks designed for a laboratory type testing environment. These fuel cells were not optimized for weight or power and were reminiscent of specific power levels that had not limited aircraft design since the Wright Flyer. In addition, the original team of students had never worked with an actual fuel cell and were not aware of a successful fuel cell powered flight attempt.

The GT FCUAV was developed in 2 major design phases. The first stage was referred to as a high level design. This design phase selected the basic configuration,

size, and power requirements of the aircraft. The second design phase referred to as the low level design included all of the decisions to move from the conceptual design to the actual hardware of the aircraft.

2.6.1 High Level Conceptual Design

The primary purpose of the high level design was to produce a feasible fuel cell aircraft design using an off-the-shelf fuel cell and hydrogen storage system that could be easily acquired. The approach to achieving this goal was to develop a multidisciplinary design analysis of a fuel cell UAV and then run a large grid search of the design space to identify and rank any feasible solutions. Apart from identifying 6 fuel cells and a number of metal hydride hydrogen tanks that fit within the project constraints, very few assumptions were made about the design.

The multidisciplinary design analysis (MDA) is summarized in Figure 2.23. The analysis was decomposed into five separate contributing analyses (CAs). These CAs were arranged into a design structure matrix (DSM) that was solved using fixed point iteration.

The design space for the high-level design was far from continuous. Several discrete variables were used that represented different fuel cells, hydrogen storage tanks, aircraft configurations, and aircraft shape. For this reason, no initial optimization scheme was used. Instead, a grid search of the entire design space was performed and the best designs were selected through a filtering of the results.

Over 15.2 million combination of design variables were executed in the MDA resulting in only ~2000 feasible designs. The feasible design space as a function of thrust margin ratio (Thrust Available/Thrust Required) is given in Figure 2.24.

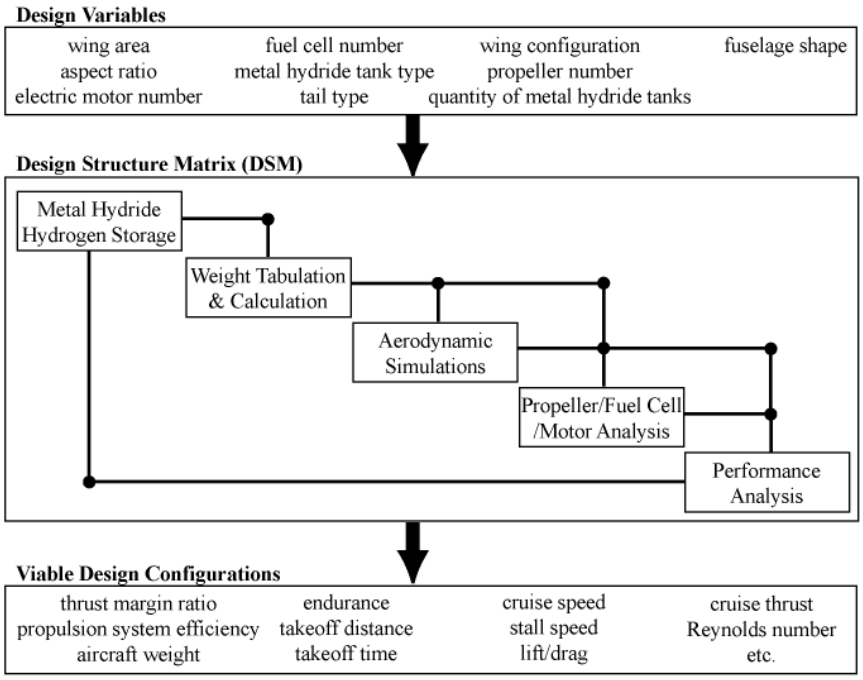

Figure 2.23: Multidisciplinary analysis for the GT FCUAV low level design.

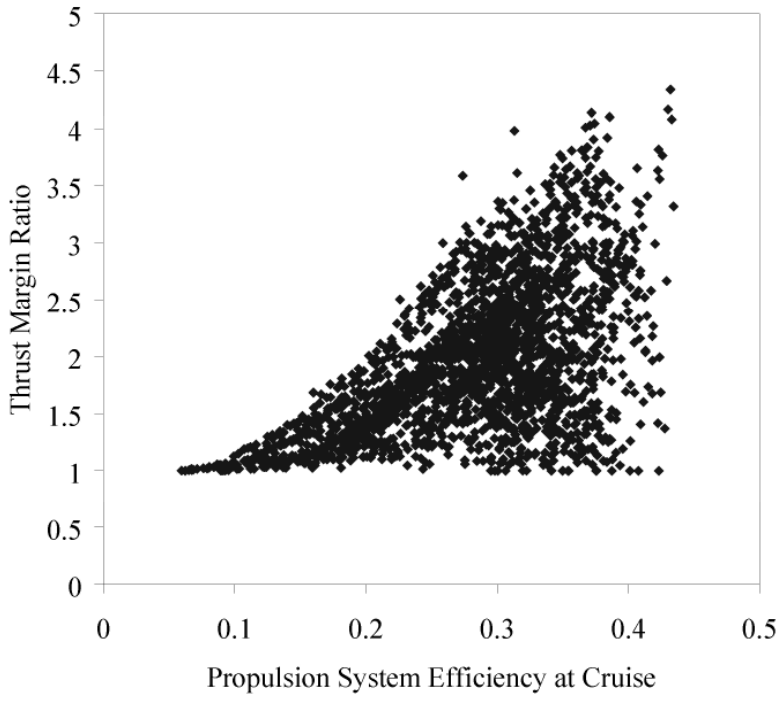

Figure 2.24: Propulsion efficiency and thrust margin ratio for feasible high level GT FCUAV designs.

The results shown in Figure 2.24 contain various fuel cells, hydrogen storage tanks, and aircraft configurations. Rather than having a clear Pareto front between the thrust margin ratio and propulsion efficiency, certain combinations of the design variables could provide high thrust and propulsion efficiency. Studying the results revealed that designs were highly sensitive to the fuel cell/electric motor/propeller combination. Only designs that found a good match of the fuel cell, motor, and propeller could achieve reasonable propulsion system efficiency and produce enough thrust for flight. Apart from the propulsion system, all of the best designs occurred at maximum wing area and aspect ratio wings.

Based on the high level design results, a 500W fuel cell from BCS Fuel Cells Inc. and a set of three 20L $MmNi_{4.1}Fe_{0.9}$ metal hydride tanks were purchased. The detailed design was then based on refining the design around this propulsion system.

2.6.2 Low-Level Detailed Design

The high-level design suggested that the propulsion system and airframe design could be decoupled and performed in parallel as optimizing the power to weight of the propulsion system and the efficiency of the aircraft would lead to designs that had the best chance of achieving flight.

The initial powerplant system for the GT FCUAV is shown in Figure 2.25. The design consisted of selecting balance of plant components that would minimize the weight of the system and provide the necessary power. This system used two compressors for air management and consisted of a cooling loop that rejected heat to the metal hydride tanks and a radiator.

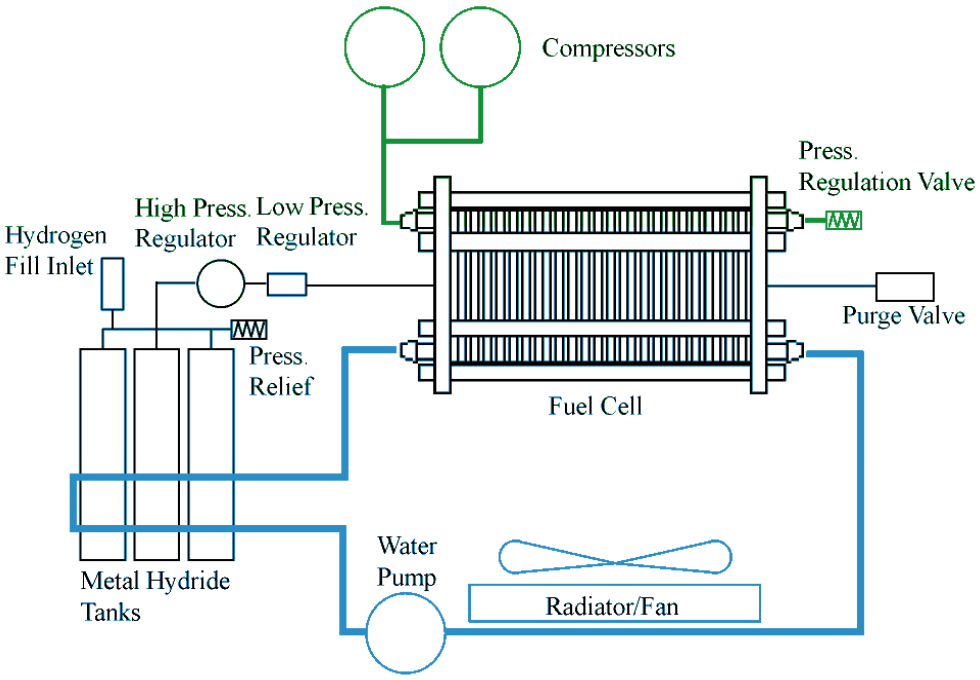

Figure 2.25: Initial GT FCUAV powerplant system.

The resulting polarization curve of the BCS fuel cell powerplant system is given in Figure 2.26. The measured performance differed significantly from the values used in the high-level design analysis. Most notably, the voltage dropoff occurred at a much lower current than originally expected reducing the maximum power output of the fuel cell stack. A portion of the discrepancy in the polarization curves was due to neglecting the power requirements of BOP components in the high-level design. However, subsequent analyses showed that even with BOP power requirements included, there was still a significant difference in the polarization curves.

Detailed sizing of the airframe was accomplished by using the same MDA structure as in the high-level design, but with updated models of the propulsion system and the aerodynamics of the aircraft. The general approach was to build response surface equations of regions of interest within the design space. The response surfaces could

then be used to study the design space to easily identify constraint boundaries and design tradeoffs. Based on the initial predicted performance of the fuel cell powerplant system, Figure 2.27 shows how the wing area and aspect ratio affect the Reynolds number and thrust margin of the aircraft. By defining a thrust margin constraint of 4 and a Reynolds number constraint of 250,000, the feasible space in Figure 2.27 is shown in white.

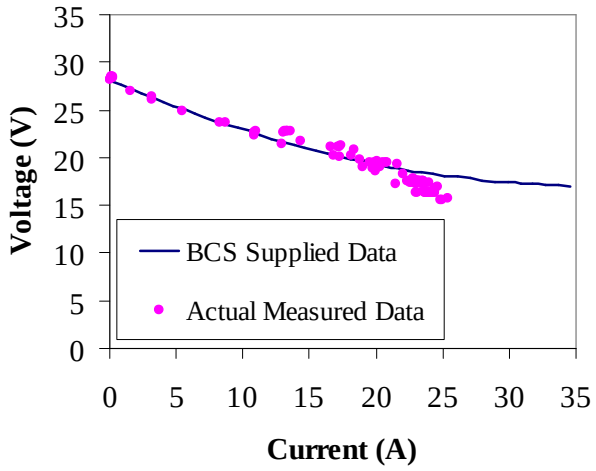

Figure 2.26: GT FCUAV fuel cell actual and predicted polarization curves.

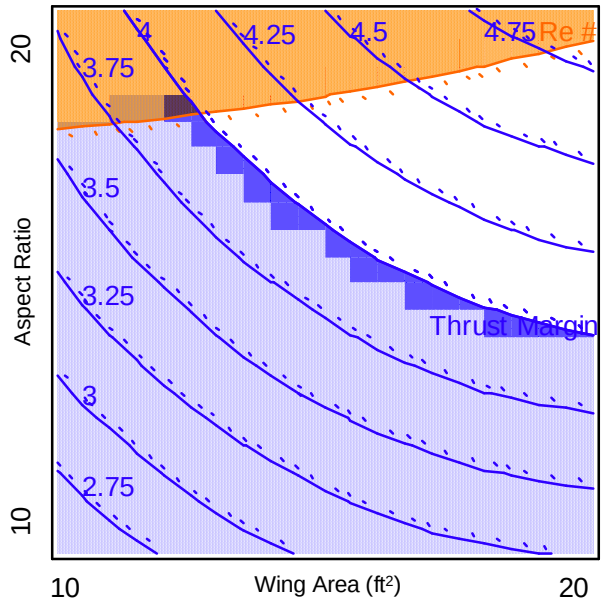

Figure 2.27: GT FCUAV initial wing design contour plot.

2.6.3 Iterations in Design

In addition to the discrepancies in predicted versus measured fuel cell performance, discrepancies in the propeller modeling, motor modeling, and weight estimation were observed as the actual hardware was developed and tested. In addition, as a more detailed aerodynamic analysis was performed and static stability constraints were included in the analysis, the lift/drag performance of the aircraft decreased with respect to what was predicted in the high-level design. The overall effect of discrepancies in actual versus predicted performance was to degrade predicted performance to levels where it was questionable whether the aircraft would be able to takeoff and climb under fuel cell power. To improve the design, the fidelity of the CAs was continually improved by either including a more detailed analysis, or including calibration factors that were informed by experimental testing. The remaining design variables could then be varied to improve the overall design. However, since experimental data was not gathered simultaneously, the MDA was constantly being updated as new data became available.

The final design of the GT FCUAV is shown in Figure 2.28. The final aircraft design drastically changed from the results of the high level conceptual design. Most notably was a change in the fuel cell powerplant system. The metal hydride storage system proved to be heavier and more difficult to analyze than was evident in the high-level design. As a result, a compressed hydrogen storage solution was implemented. This design also caused changes in the BOP as the heat could no longer be transferred to the metal hydride tanks to facilitate the release of hydrogen. A larger custom radiator was developed to account for the additional cooling requirements (see Figure 2.29).

Figure 2.28: Georgia Tech fuel cell UAV.

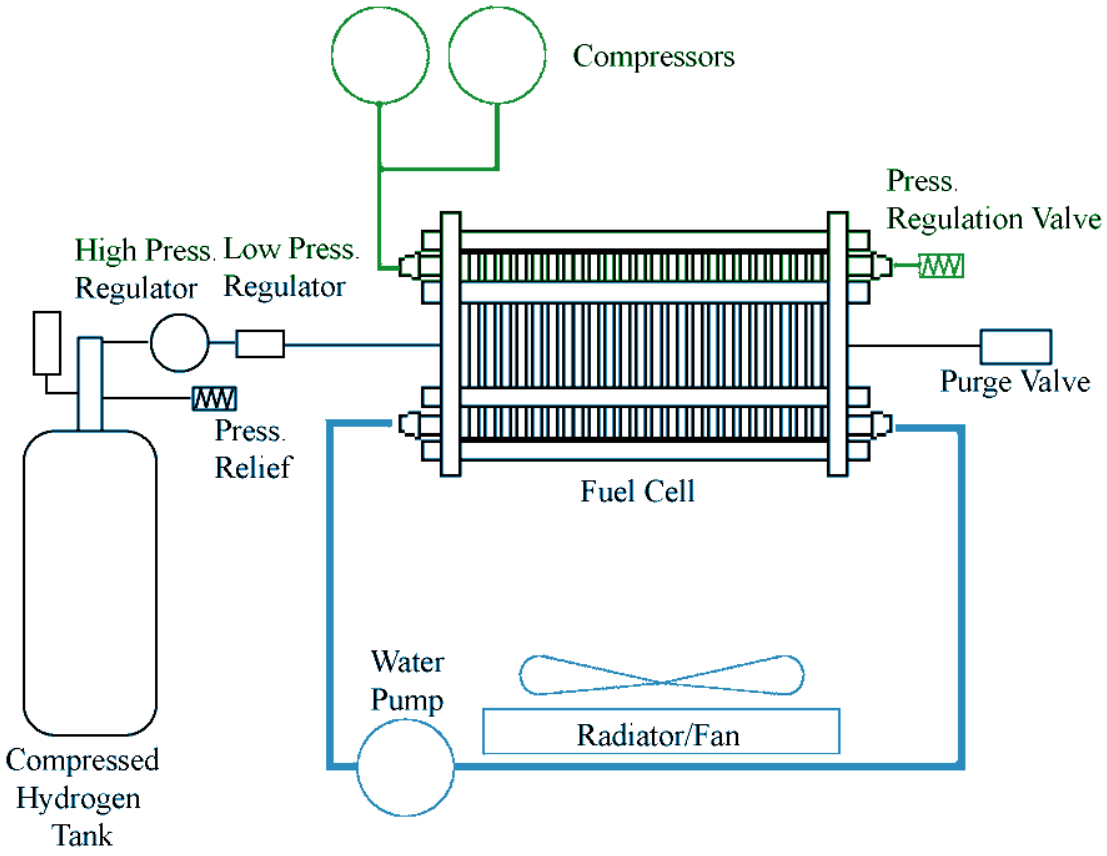

Figure 2.29: Final design of GT FCUAV fuel cell powerplant system.

The final airframe design also drastically changed from conceptual to final design. After improving the weight estimates by building two complete prototype airframes, and using improved analyses for the aerodynamics, propeller, motor, and fuel cell performance, the final airframe was optimized using response surface equations regressed to results of the MDA.

The improved MDA revealed that the design space was more constrained than estimated during the conceptual design. Apart from thrust margin and Reynolds number constraints, turn bank angle, turn thrust margin, and stall constraints[†] also affected the design. Figure 2.30 shows the design space as a function of wing planform variables using the final developed MDA. A comparison of the wing planform design space shown in Figure 2.27 and Figure 2.30 reveals that the stall and turn constraints decreased the feasible region of the design space.

The final aircraft design resulted in a higher wing area, a higher aspect ratio wing, and taper and dihedral in order to compensate for the reduced power of the fuel cell. The lift distributions and planform wing and tail geometry for both the conceptual and final designs are shown in Figure 2.31.

2.6.4 Results and Lessons Learned

The GT FCUAV flew under fuel cell power for the first time on June 14, 2006. In all, a total of 10 test flights were conducted. The design and development of the GT FCUAV resulted in lesson learned about the dominance of the fuel cell and hydrogen

[†] The stall constraint was implemented by making sure the design angle of attack was below the onset of stall. The design α in Figure 2.30 represents the maximum angle of attack allowed for cruise to be below the predicted onset of stall.

storage system, the value of an accurate multidisciplinary design environment, and the importance of uncertainty.

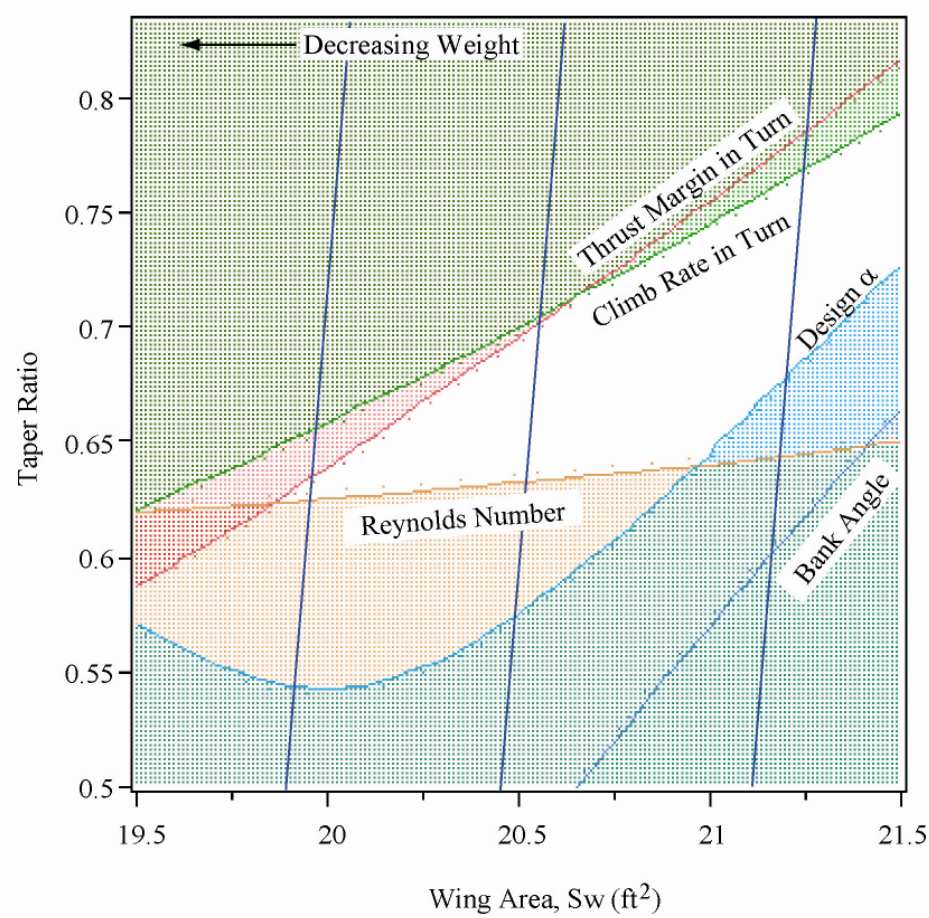

Figure 2.30: GT FCUAV design space as a function of wing planform.

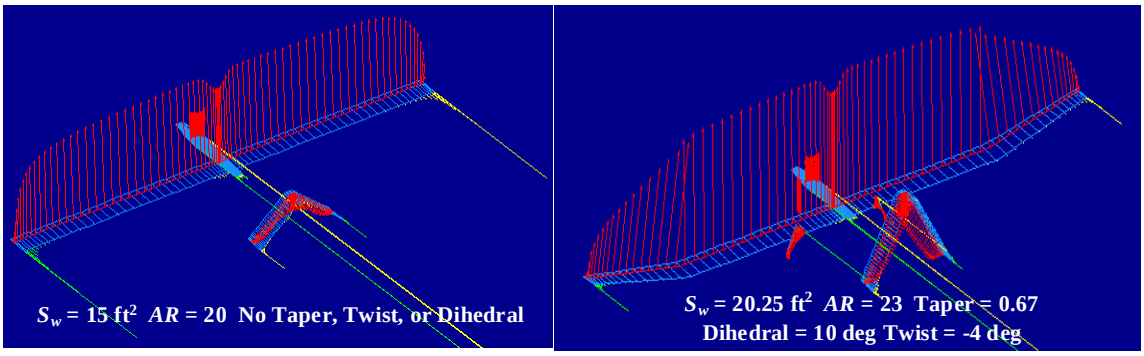

Figure 2.31: Conceptual (left) and final (right) aerodynamic designs of the GT FCUAV.

2.6.4.1 Fuel Cell Dominated Design

The dominance of the fuel cell was understood from early on in the high level design phase. Only the fuel cell stacks with a higher power to weight ratio were able to produce feasible designs although millions of cases were studied. The final aircraft weight breakdown in Figure 2.32 shows that the fuel cell, balance of plant, and hydrogen storage system represent over half the weight of the aircraft. As a result, the aerodynamics, weight, and propulsion had to be optimized to make the aircraft feasible.

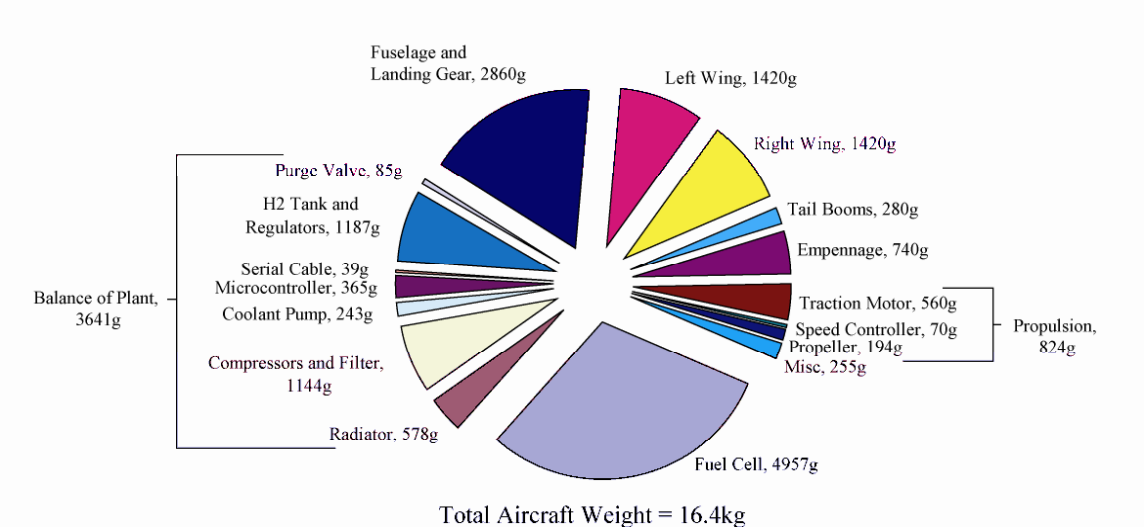

Figure 2.32: Weight breakdown of the GT FCUAV.

Figure 2.32 shows that the balance of plant represents a significant portion of the total mass of the aircraft. Fuel cell manufacturers report performance either on a cell or stack level and rarely include the performance or mass of the balance of plant. As a result, the mass and power requirements of the balance of plant were underestimated during the conceptual design.

The flight tested power breakdown of the entire powerplant and propulsion system is shown in Figure 2.33. Despite losses due to fuel cell irreversibilities, balance

of plant inefficiencies, electric motor inefficiencies, and speed controller inefficiencies, the final aircraft was able to achieve 33% efficiency at converting hydrogen to net electrical power, and 22% efficiency at converting hydrogen to rotating shaft power. This represents a significant improvement over gasoline engines in this same power class that have been shown to have efficiencies as low as 3.5% [181].

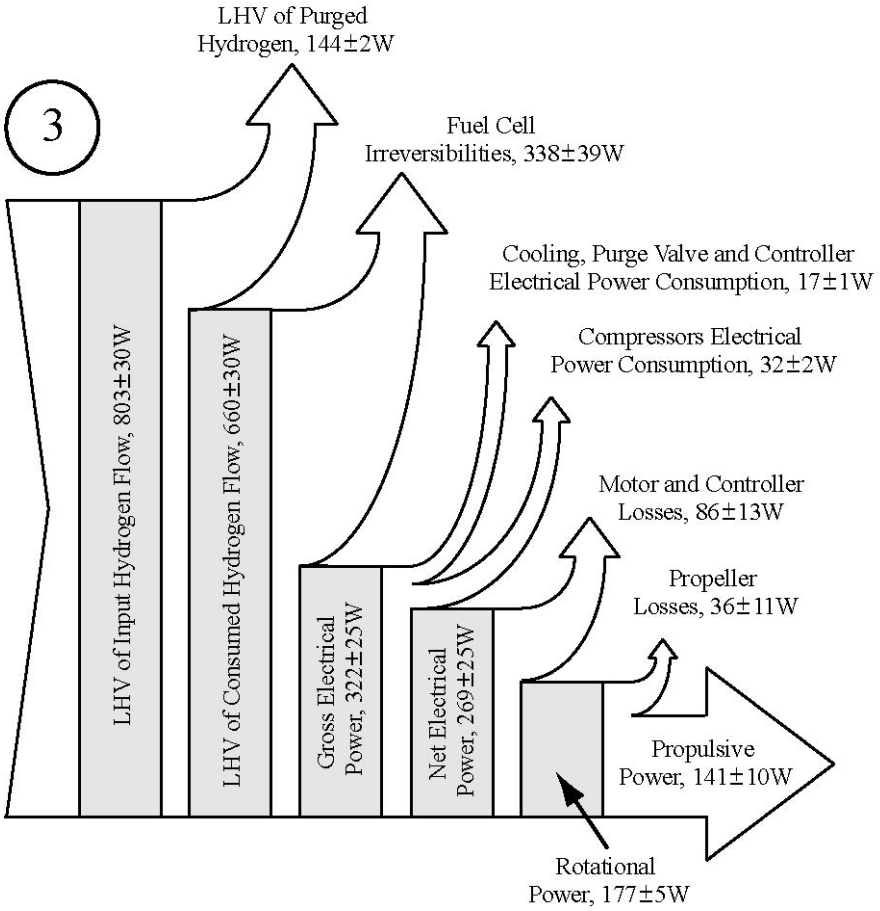

Figure 2.33: Propulsion system power breakdown at the cruise condition.

2.6.4.2 Highly Constrained Design Space

Throughout the design and testing, an emphasis on the highly constrained nature of the design space was evident. The design effort was much more involved than a

conventional UAV because the design was very close to critical performance constraints (see Figure 2.30). Initially, it was hypothesized that meeting a certain thrust margin would be sufficient for a demonstrator flight but testing of prototype aircraft under battery power quickly proved that climb, turn, and stall effects would also limit the design. For the GT FCUAV, the primary source of all of the constraints was the high mass and low power of the fuel cell system. This high mass to power of the fuel cell system resulted from using a fuel cell designed for stationary applications. State of the art fuel mobile cell systems would not be nearly as constrained for simply demonstrating the feasibility of flight. However, fuel cells will not be of considerable use in UAV applications unless they can enable increased endurance over conventional propulsion. As endurance is maximized to values beyond what can be accomplished with existing propulsion, the design space will continue to be constrained similarly to the GT FCUAV.

2.6.4.3 Multidisciplinary Design Analysis

Designing within the highly constrained design space required an accurate multidisciplinary design analysis of the vehicle. Sizing the aircraft would have been extremely difficult without the MDA as the aircraft design strayed considerably from conventional designs. Most notably, experts cautioned that the aspect ratio, wing area, and propeller pitch were too high for this type of design. However, experimental bench top and flight tests supported the analysis. Figure 2.34 shows that the MDA properly captured the highly interdisciplinary behavior of fuel cell power, voltage, and motor speed as a function of fuel cell current during a bench top test. Test data in Figure 2.35 show that the MDA also was able to reasonably predict the thrust and motorspeed for a sample test flight.

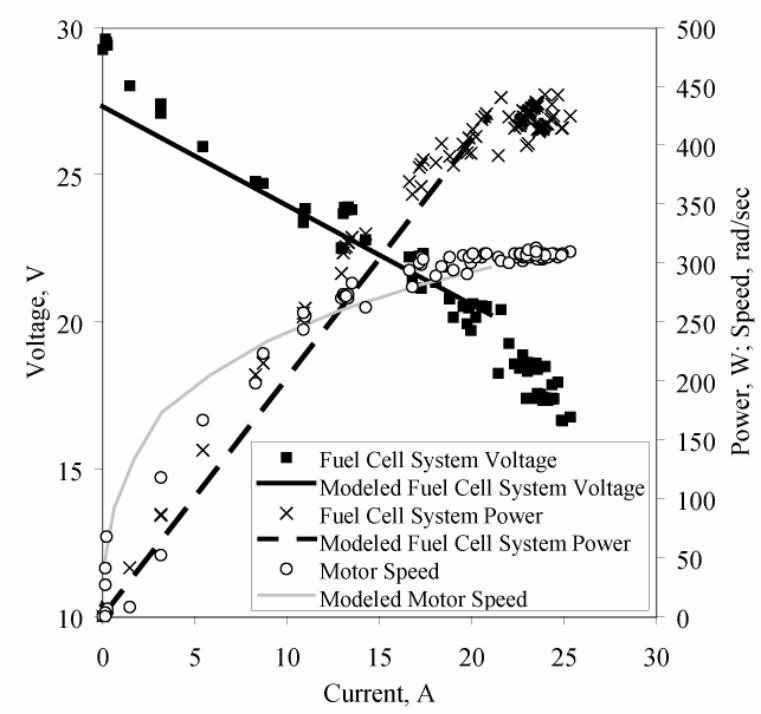

Figure 2.34: Propulsion system test of the GT FCUAV.

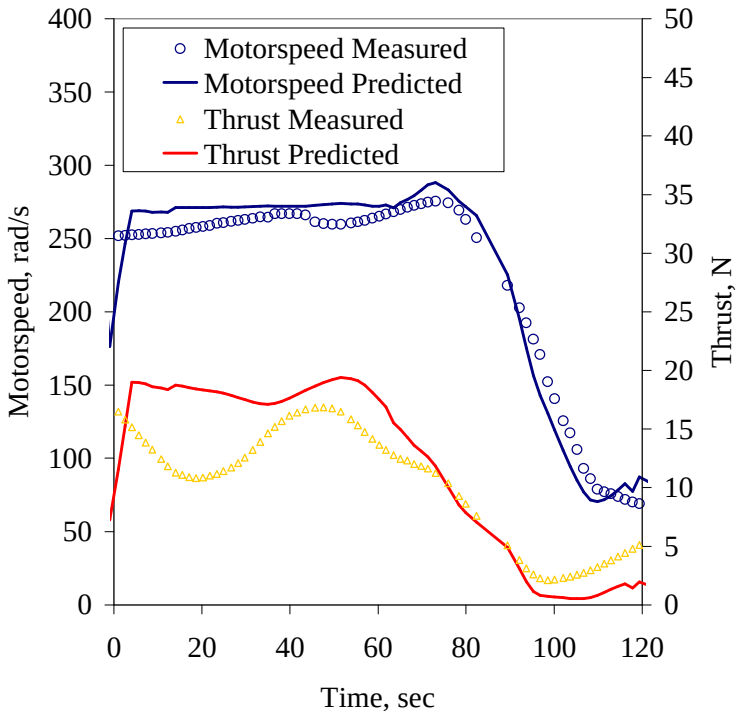

Figure 2.35: Flight test results of motorspeed and thrust for the GT FCUAV.

The MDA was updated and improved throughout the design as more information was learned and more fidelity was needed. As discrepancies were found between predicted and measured component performance, the MDA was crucial in estimating the system level performance implications. The MDA also proved valuable when redesign was necessary to maintain feasibility of the aircraft design.

2.6.4.4 Uncertainty Effects

The need to estimate the effects of uncertainty became apparent throughout the development process. Since the design was highly constrained, any variations in actual versus predicted performance tended to cause constraint violations. Had the level of uncertainty in the fuel cell models, balance of plant, weight estimations, electric motor, and propeller performance models been known *a priori*, a better design point could have been selected earlier in the design process eliminating several design iterations.

However, with any new technology, uncertainty in performance predictions will be largely unknown until validated performance models are produced and commonly accepted. Therefore, design iterations will likely be necessary. In this case, a more flexible MDA would be valuable. As higher fidelity contributing analyses and/or test data was included in the MDA, a significant effort was needed to reorganize inputs and outputs and assure that the DSM was being properly solved.

2.7 Deficiencies in Current Design Methodologies

The study of fuel cell aircraft has only recently begun. Although researchers have noted that the design of fuel cell aircraft is fundamentally different from conventional propulsion based aircraft, only a few design methodologies have emerged with most

designs following traditional aircraft design methods. As with any emerging research area, there are several deficiencies in current approaches requiring consideration. These include the lack of a validated multidisciplinary design analysis, the inflexibility of the design environment for adapting to change, and the failure to account for uncertainty.

2.7.1 Lack of Validated Multidisciplinary Analysis

The fundamental limitation of the current methodologies proposed for fuel cell aircraft is the development of a multidisciplinary design analysis. No method specifically defines how to build a validated multidisciplinary analysis for a revolutionary new technology. Most fuel cell aircraft have been designed at a very high level of conceptual design where simplifying assumptions were made about the weight and power of the fuel cell powerplant. These assumptions are usually based on automotive or department of energy targets [182] and are difficult to validate since similar fuel cell systems either do not exist or their design and performance are closely protected by their manufacturers. Additionally, many of the high level designs are based on simple weight and power estimates of the fuel cell system do not capture key interdisciplinary relationships between the propulsion and airframe systems. However, fuel cells systems effect more than just the weight and power of an aircraft. Boeing engineers have noted that the integrating the different fuel cell subsystems in their Dimona aircraft has been difficult due to volume, weight, power management, and thermal interactions [171].

Some of the more detailed design studies have proposed more complex MDAs that attempt to use legacy codes or limited experimental data. However, no mention is made of how to build these MDAs, what level of modeling fidelity is required, and what

level of uncertainty is associated with the results. In addition, with exception of the GT FCUAV, no MDA has been validated against an actual aircraft system.

Most MDA used in fuel cell design studies have had incomplete validation. Nam performed validation of AIASM using a conventional mission but did not validate any fuel cell powered designs as adequate data was not available [176]. Similarly, Nickol [172] used calibration factors to modify a MDA to match results of several long endurance high altitude vehicles, however none of these vehicles were flight tested with fuel cell propulsion systems. Choi et al. performed validation at the component level [174]. To lend credibility to their analyses, researchers such as Berton et al. [168] and Guynn et al. [173] , and Alexander [183] have used legacy codes such as FLOPS and NPSS to model the aircraft and propulsion system and have generated subsystem results to show that accepted component trends are being captured. However, both FLOPS and NPSS have been historically validated against aircraft powered by conventional propulsion and their ability to capture multidisciplinary aspects of fuel cell aircraft design is still unproven. Overall, nearly all of the design studies are conceptual and have not resulted in any significant hardware development and experimental testing. Although many of the MDAs in these studies may provide an accurate evaluation of a fuel cell powered aircraft, they remain unvalidated at the aircraft level. Furthermore, difficulties experienced by Boeing [171] and Georgia Tech [60] demonstrate that estimating the weight and power of the fuel cell system is difficult without a detailed knowledge of the system gained through hardware development.

Since 2003, several demonstrator aircraft have flown under fuel cell power. With the exception of the GT FCUAV, only a few details have been published on the analysis

behind these designs and no flight test data or validation exercises exist in the public domain. Many of the designs are retrofits of existing aircraft. Available details suggest that the retrofit designs focused on developing a fuel cell system to closely resemble the power output and weight of the original propulsion system. As a result, the multidisciplinary relationships between the powerplant, propulsion, and airframe are not fully captured and the aircraft is not sized to extract the maximum potential of the fuel cell powerplant. A few of the designs such as the AeroVironment Global Observer prototype, and the Bluebird Aero Systems Boomerang have impressive performance specifications and are likely based on a more mature MDA. However, these designs have been developed as potential commercial products and are not publically available.

2.7.2 Lack of Flexibility in the Sizing Environment

Most analysis tools are based on existing design paradigms for aircraft powered by conventional propulsion [184]. Since the underlying physics varies for fuel cell aircraft vs. combustion based propulsion, different analyses and different solution procedures are needed.

Many researchers have chosen to derive design relationships using basic energy and power balance equations. Colozza [122] developed specific sizing relationships for a fuel cell/solar cell aircraft. Smith et al. proposed a similar analysis for a purely electric vehicle [185] and Harmats and Weihs developed relationships for a solar cell/ICE hybrid aircraft [186]. Nam developed a set of more general relationships (termed AIASM), which are independent of the energy-propulsion system architecture of an aircraft [176]. Regardless of the sizing relationships, a sizing procedure is needed. Examples provided

in Colozza and Nam arrange the set of applicable equations into an iterative sizing routine that is largely customized for a given example.

None of the existing sizing environments allow the user to easily delete, insert, or modify portions of the analysis. Doing so would require adjusting the iterative routines to ensure that a solution could be reached. Since setting up the sizing environment is largely a labor intensive process, this can require significant rework if fundamental analysis changes are needed.

Creating a flexible design environment is critical for a fuel cell aircraft because fuel cells are easily equipped to provide electrical power to all subsystems of the aircraft [69]. Traditional aircraft have tied pneumatic, hydraulic, and electrical power to the mechanical power of the engine which both provides a more rigid subsystem architecture and reduces engine efficiency. With an all electric system, aircraft have much more freedom in the way they power and integrate their various subsystems. Breit and Szydlo-Moore of the Boeing Company have noted that a key enabler of more electric aircraft (MEA) powered by either fuel cells or conventional propulsion is a design framework with "an open architecture that is easily able to accept new components or sub-systems [69]."

Another important motivation for a flexible design environment is the need to easily update the analysis as better models become available. Since fuel cells systems are rapidly improving in performance and various configurations are appearing from one generation to the next, updated performance models that require different inputs and outputs will constantly be in development. In addition, updating or replacing models with experimental results will be valuable during the design process to help mitigate the

effects of uncertainty. Rather than manually reconfiguring the sizing environment each time a new performance model becomes available, a flexible automated solution procedure is desirable.

2.7.3 Unknown Effects of Uncertainty

Uncertainty is greatest during the conceptual design phases due to the scarcity of information about the new product being designed [187]. For fuel cell aircraft, uncertainty is generally more prevalent as most engineers have little experience working with actual fuel cell systems, and fuel cell systems are rapidly evolving. Although most fuel cell aircraft design studies have noted that uncertainty effects are significant [173], only a few researchers have addressed its effects in their design methodologies.

One of the primary difficulties that hinders including uncertainty in fuel cell aircraft design, is that uncertainties are generally unknown. State of the art fuel cell technology has been developed by companies that closely protect their designs and experimental data. Researchers such as Nam [176] and Choi [180] have proposed different design methodologies to include the effects of uncertainty, but both were forced to make arbitrary estimates of uncertainty as information was not available to make more adequate estimates.

2.8 Chapter Summary

Many different types of fuel cells are being developed. The most promising technologies for aircraft applications are PEMFCs and SOFCs. Polymer electrolyte membrane fuel cells are desirable due to specific power, fast startup times, and low operating temperatures while SOFCs can demonstrate higher efficiencies and can be

more easily adapted to operating on logistical fuels. At current levels of technology, PEMFCs are more appropriate for consideration in UAVs as they have superior specific power, rapid startup times, and are more commercially available. Fuel cell technology is developing rapidly due to a substantial investment by the automotive community. Fuel cells specific power and power density are nearly doubling every 3-4 years as automakers have experimented with different configurations.

Despite development, fuel cells have much lower specific power than conventional gas turbine propulsion and are not expected to be applicable to large passenger aircraft in the near future. However, at the lower power levels required by UAVs, fuel cell powerplants have high efficiency with comparable specific power.

Various methods for storing hydrogen exist. For small amounts of hydrogen, adsorption based storage in metal hydride tanks is prevalent whereas compressed gaseous storage has better performance for medium amounts of hydrogen. For medium to large masses of hydrogen, liquid storage systems can store a large percentage of hydrogen by weight but are more complex due to cryogenic temperatures.

Since 2003, a number of fuel cell powered aircraft have flown. Various universities, research organizations, and companies have developed demonstrator aircraft. Most aircraft have been small UAVs with large aspect ratio wings optimized for long endurance applications. The fuel cell and hydrogen storage systems have been fundamentally different for many of demonstrator aircraft and various fuel cell suppliers have been used. Although most fuel cell aircraft to date have been demonstrators, at least one company is currently developing a commercial UAV.

Despite the emergence of demonstrator aircraft, little has been published about methodologies relating to the design of fuel cell aircraft. Only one of the demonstrator aircraft developers has published flight data and documented the design methodology. Most design studies in the literature have focused on the performance of existing aircraft retrofitted with fuel cell propulsion systems. These design studies do not capture the interdisciplinary sizing relationships between the airframe and propulsion system and typically result in suboptimal performance. More recently, researchers have begun to develop multidisciplinary design analyses based on power and energy balances of fuel cell aircraft systems. Most studies have been at a high conceptual level although more integrated design frameworks using legacy codes have also appeared.

A summary of the GT FCUAV design showed that the fuel cell design space is highly constrained. Uncertainties in analysis resulted in several iterations during the development cycle that were necessary to maintain a feasible design of the vehicle. As a result, the hydrogen storage system, balance of plant, and airframe underwent significant changes from conceptual to final design. Successful flight and bench tests of the aircraft were in agreement with predictions from the final version of the multidisciplinary analysis.

Based on the literature and the experience of the GT FCUAV, three major deficiencies in current design methodologies were noted. The first deficiency is a lack of a validated multidisciplinary design analysis (MDA). Many of the analyses in the literature do not capture many of the interdisciplinary couplings between the various subsystems that compose a fuel cell aircraft. In addition, MDAs that include more of these interactions have only been partially validated at the component level.

The second deficiency is the lack of a flexible design framework. Existing designs have relied on the heavy modification of legacy codes or the development of application specific design relationships. With the rapid development of new fuel cell architectures and the design freedom afforded by an electric subsystem architecture, a flexible design framework is necessary to both evolve with fuel cell development, and allow various architectures to be evaluated.

The final deficiency is the inability of design methodologies to quantify the effects of uncertainty. Despite acknowledging that uncertainty is significant, almost all fuel cell design studies have ignored its effects. Two recent methodologies that include uncertainty are an exception, but a lack of available data in these studies led to arbitrary estimates of key uncertainty parameters.

CHAPTER 3

RESEARCH QUESTIONS AND HYPOTHESES

Fuel cell systems have made great technological advances over the past few years. These advances coincide with an increasing need for UAVs that improve their utility through decreased size, reduced thermal signature, and long endurance. Although fuel cells have favorable attributes that address the emerging UAV needs, the near-term potential of fuel cell powered UAVs has yet to be fully established. To date, only a limited number of design studies have been performed and relatively few demonstrator aircraft have flown. A review of the literature has identified key deficiencies in current design methodologies for fuel cell aircraft that has led to the research objective of this dissertation. A summary of the research questions, hypotheses, and tasks that support the research objective are presented.

3.1 Research Objective

The research objective of this dissertation is the creation of a design methodology that will enable the near-term performance of fuel cell UAVs to be determined. In order to achieve this objective, the methodology will need to provide a means to explore the design space of a fuel cell UAV while addressing the key deficiencies that were identified in the literature review. These key deficiencies include the lack of a clearly defined method to develop a validated multidisciplinary analysis, the lack of a flexible design framework, and an incomplete quantification of the effects of uncertainty.

3.2 Research Questions

The research objective can be decomposed into a series of research questions. Solutions to these research questions will enable the fulfillment of the research objective. The research questions are posed to provide solutions that will address the key deficiencies described in the literature review and provide key steps in the overall design methodology.

Research Question 1: *How can a validated multidisciplinary design analysis be created for a fuel cell powered UAV?*

The first research question addresses the multidisciplinary analysis (MDA) which is the core of any design space exploration. A MDA is needed to predict how all systems will perform when fully interacting with each other so that the system level vehicle performance can be obtained. For conventional propulsion, a wealth of legacy codes, semi-empirical, and empirical relationships exist that have been both validated and successfully used for multidisciplinary analysis. Fuel cell aircraft however have fundamentally different power, weight, and volume attributes that will exclude the applicability of many existing codes and design relationships and require the development of a new multidisciplinary analysis. Developing a MDA for a fuel cell powered aircraft in not a novel idea and has been addressed in the literature. However, the additional requirement that the MDA be validated is both unique and challenging. System level validation is difficult for aerospace systems due to the time, cost, and complexity of developing and testing a full system. Regardless, without a validated analysis, results will always be in question.

Research Question 2: *How can the framework for a MDA be created that is flexible enough to adapt to various powerplant architectures?*

A framework consists of the organizing and joint-solution-technique of the various contributing analyses (CAs) that make up a MDA. For conventional propulsion, the interdisciplinary relationships between the various aircraft subsystems have been studied and frameworks have been developed that specify the order in which analyses should be conducted as well as methods to assure convergence [188]. Most advances in conventional propulsion technology have been at a component level as opposed to the system level and fall within the applicability of traditional frameworks. However, fuel cells systems are rapidly developing and the basic architecture often changes throughout development. A clear example is the development of Honda's FCX Clarity fuel cell stack which introduced vertical rather than horizontal flow of the reactants and relies on gravity as opposed to purging to remove water [65, 189]. The analysis of this type of design would have fundamentally different inputs, outputs, and constraints compared to the previous Honda fuel cell stack design and would require a significant reworking of the MDA framework. Likewise, various hydrogen storage systems would require a flexible framework as the volume, mass, and thermal requirements and constraints drastically vary from system to system. Finally, fuel cell powerplants enable an all electric architecture to supply power to various aircraft subsystems. This all electric architecture allows for increased integration of subsystem functionality and substantially more feasible architecture choices than traditional systems that have relied on mechanical, pneumatic, and hydraulic forms of power distribution. Overall, flexibility in

the design framework is a necessary component to facilitate any exploration of the design space.

Research Question 3: *What generalized method will allow the determination of an optimal solution under the effects of uncertainty?*

A flexible framework and validated MDA are of limited use without a method for exploring the design space and determining an optimal solution. In addition, uncertainties associated with any unproven and rapidly advancing technology will be significant. The real term performance of a fuel cell powered UAV can therefore not be fully determined without specifying a design that has adequate margins that ensures a high probability that constraints will be satisfied.

3.3 Hypotheses

Answers to the research questions are posed as three distinct hypotheses. The hypotheses will form the basis of the proposed design methodology.

Hypothesis 1: *By using uncertainty propagation to guide decomposition, a fuel cell propulsion system can be decomposed into validateable contributing analyses that will facilitate a multidisciplinary design analysis that will agree with system level performance.*

It is a common practice in engineering to decompose a complex system into more tractable contributing analyses (CAs). Proving that this is true is not the fundamental purpose of Hypothesis 1, rather the goal is decompose the design into CAs that have sufficient detail as to capture key aspects that dominate system level performance. A reoccurring problem in design is the level of detail at which decomposition should occur.

With aircraft design based on traditional propulsion, over 100 years of design experience including data on fully developed systems has helped distinguish the level of detail required to provide reasonable system level performance predictions. However, for fuel cell powered aircraft, design experience and experimental data are currently limited and a validated analysis has yet to be established. In addition, in order for a design to be validated, it must have sufficient detail to mimic either an experiment, higher fidelity analysis, or some other method of analysis. The UAV platform offers an unique opportunity as UAV subsystems can be rapidly developed with much less cost than traditional aerospace subsystems making decomposition for verification and validation feasible.

Hypothesis 2: *By specifying the MDA as a function of the hierarchy, inputs, and outputs of each contributing analysis, an automated procedure can be developed to transform the system into a set of solvable compatibility equations.*

The goal of Hypothesis 2 is to automate the process of using the contributing analyses to find a system level solution. For simple design problems, contributing analyses may be formulated and arranged so that a simple execution of each analysis in a given order will result in the system level solution. This forms the classic textbook type design problem. For more complex aircraft design problems, contributing analyses will be cross coupled resulting in feedback loops that require iteration to reach a system level solution. Traditional aircraft design problems often formulate the contributing analyses and their hierarchy so that iterations on a key variable such as gross takeoff weight are all that is needed to identify a converged system level solution. However, this approach is

based on a rigid design framework and will require a reformulation if the addition of new contributing analyses offer non-traditional interdisciplinary couplings.

Hypothesis 2 is based on the idea that a set of contributing analyses can be transformed into a set of compatibility equations that when solved will result in the system level solution. To formulate the compatibility equations, an automated procedure is needed. The fundamental idea is that by specifying an arbitrary hierarchy of CAs, as well as the input and output variables of each CA, a parsing type routine can be developed to automatically identify the compatibility equations and format these equations for solution via a non-linear equation solving routine.

Hypothesis 3: *An optimal solution under the effects of uncertainty can be obtained by using system sensitivity analysis to calculate the probabilistically feasible space and inform optimization via a robust optimization scheme.*

The ability to explore a design space is enabled by obtaining an efficient method to explore the design space. Unfortunately, calculating the probabilities of meeting the design space requires uncertainty propagation which can be computational prohibitive. Hypothesis 3 addresses this applying a single technique for both uncertainty propagation and system level gradient calculation.

System sensitivity analysis (SSA) was originally developed as a method to provide an efficient parallel scheme to calculate system level gradients needed for optimization without requiring finite differencing of the entire system level analysis [190]. The SSA method of determining sensitivity has also been successfully used to propagate uncertainty from design variables and contributing analyses to system level metrics [191, 192]. The estimates of uncertainty propagation will allow the probability of

satisfying design constraints to be calculated. The system level gradient information provided by SSA will also be of aid in gradient based optimization schemes such as sequential quadratic programming (SQP).

An important part of Hypothesis 3 not yet addressed is the term "optimal solution." For complex design problems, the optimal solution is often a tradeoff of several performance metrics rather than a single scalar value as often seen in optimization studies. The use of an efficient optimization scheme can rapidly allow the determination of the Pareto frontiers within the design space [193]. From this frontier, designers can make decisions to determine an optimal solution for a given application.

3.4 Overview of Methodology

The overall methodology is summarized in Figure 3.1. The methodology is very similar to Nam's PASM [176] in structure (see Figure 2.21). However, the method seeks to improve upon PASM by providing a methodology to obtain the MDA (see Hypotheses 1 and 2) as well as a methodology to efficiently determine the Pareto frontiers of the design space (see Hypothesis 3). The design starts with a notional concept aircraft. The design is then decomposed and modeled just as in PASM. However, the difference is that the decomposition should be informed by expected uncertainty in the problem as well as what will be required to validate the decomposition. Therefore, the fidelity of the decomposed CAs is based on how sensitive the overall design is to any uncertainty in their calculation as well as what type of data would be needed to both verify and validate the CA. It is assumed that creating a validated MDA will be akin to chasing a moving target as fuel cell technology will continue to improve and analysis methods will improve

as the design process progresses. Therefore, to minimize rework, a flexible MDA structure is needed that can easily adapt to changes in decomposition.

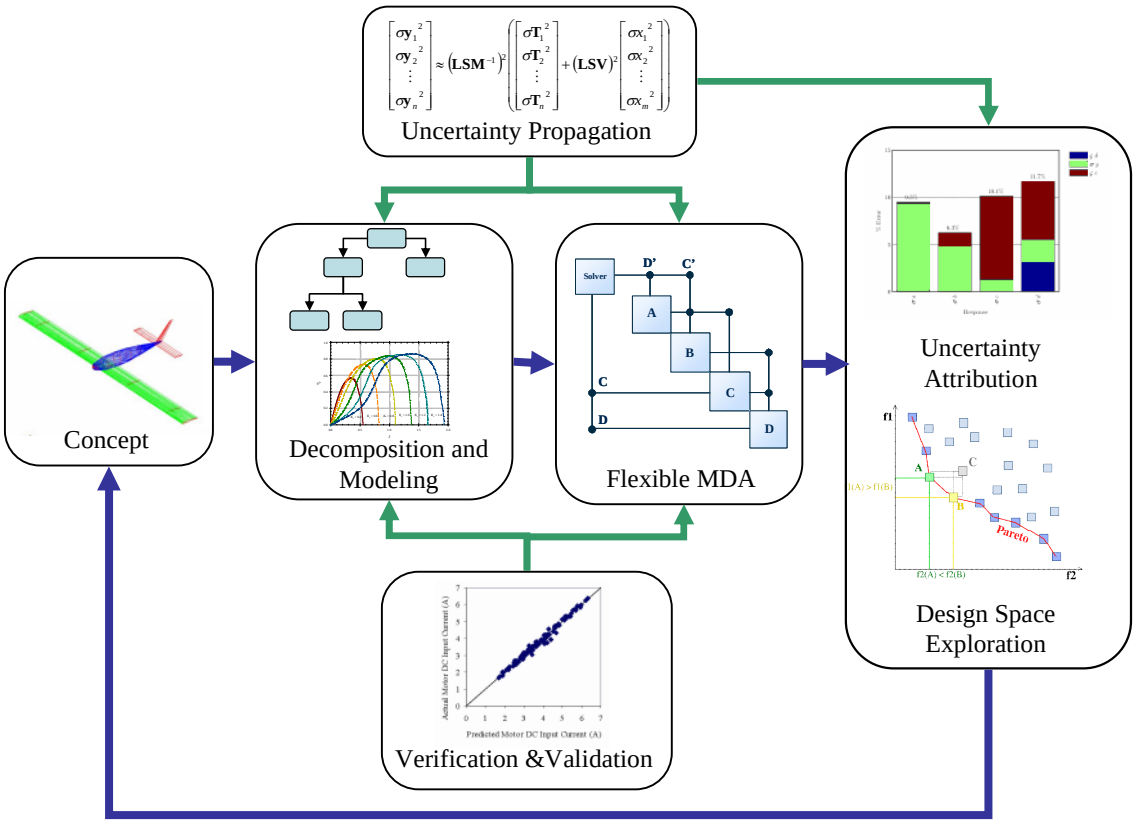

Figure 3.1: Design methodology overview.

Finally, Hypothesis 3 was formulated to define how to implement a probabilistic design optimization once a validated MDA has been created. It is hypothesized that SSA be employed to assist in the optimization process by providing gradient estimates as well as providing estimates of the propagated uncertainty in both performance metrics and design constraints. If SSA can be executed robustly throughout the design space, the Pareto frontiers of the design can be efficiently located and be used to drive design decisions.

3.5 Research Tasks

To address each hypothesis, a number of research tasks are necessary. For clarity, the research questions and hypothesis are repeated as a precursor to stating the research tasks.

Research Question 1: How can a validated multidisciplinary design analysis be created for a fuel cell powered UAV?

Hypothesis 1: By using uncertainty propagation to guide decomposition, a fuel cell propulsion system can be decomposed into validateable contributing analyses that will facilitate a multidisciplinary design analysis that will agree with system level performance.

Task 1.1: Use uncertainty propagation to guide problem decomposition.

Task 1.2: Seek out modeling techniques and data to be used for validation.

Task 1.3: Acquire and/or code contributing analyses.

Task 1.4: Verify and validate results using data gathered from either the literature or experiments.

Task 1.5: Validate system level propulsion solution against a hardware-in-the-loop simulation.

The first hypothesis addresses the challenge of developing a validated multidisciplinary design analysis and is the primary subject of Chapter 5. Task 1.1 will tests the effectiveness and efficiency of using uncertainty propagation to guide problem decomposition. Task 1.2 will seek out modeling techniques that will help influence Task 1.3 and will identify data that can be used for validation. In the case where data is unavailable, experiments will be specified to gather the appropriate data. Task 1.3

consists mainly of developing mathematical models for the contributing analyses if existing codes are inappropriate or unavailable. Tasks 1.4 offers a unique research challenge as all contributing analyses must either be based on appropriate empirical relationships, or validated using experimental data. The primary challenge in Task 1.4 is obtaining validation data. Apart from a lack of data on fuel cell systems, very little data exists in the public domain about the performance of small UAVs. As a result, where literature data is unavailable, experimentation will be performed. Task 1.5 is used as the primary test of the hypothesis. Using a hardware-in-the-loop setup of an entire fuel cell propulsions system, validation of the MDA will be performed. As a point of clarity, experimental data for validation and the hardware-in-the-loop testing was provided under the overall fuel cell UAV research effort by Bradley [63].

Research Question 2: How can the framework for a MDA be created that is flexible enough to adapt to various powerplant architectures?

Hypothesis 2: By specifying the MDA as a function of the hierarchy, inputs, and outputs of each contributing analysis, an automated procedure can be developed to transform the system into a set of solvable compatibility equations.

Task 2.1: Build an automated parsing code that uses the inputs, outputs, and hierarchy of the contributing analyses to define compatibility equations.

Task 2.2: Using the MDA developed from Task 1, compare multiple non-linear equation solving routine to identify a robust and efficient method for addressing the compatibility equations.

Task 2.3: Verify the results of the automated process by examining different CA organizations and comparing results to a more traditional nested solution framework.

Building a flexible framework for solving the MDA is the primary goal of Tasks 2.1 - 2.3 and forms the basis of Chapter 6. Task 1.1 focuses on the development of a parsing code that will scan through the inputs, outputs, and hierarchy of each contributing analyses to determine where feedback loops exist and automatically formulate compatibility equations based on these feedback loops. The compatibility equations will then be formatted for use in a nonlinear equation solver. To be useful, the full automated procedure must be robust and efficient for a variety of compatibility equations. To test this, Task 2.2 will compare several non-linear equation solving routines based on execution time and robustness. As a test of whole process, Task 2.3 will compare the results against a more traditional rigid framework that uses a series of nested analyses to solve each CA. Slight changes in the CAs will also be used to test that automated routine can properly identify and solve the compatibility equations.

Research Question 3: What generalized method will allow the determination of an optimal solution under the effects of uncertainty?

Hypothesis 3: An optimal solution under the effects of uncertainty can be obtained by using system sensitivity analysis to calculate the probabilistically feasible space and inform optimization via a robust optimization scheme.

Task 3.1: Develop a SSA code that can be used with the MDA developed in Task 1.

Task 3.2: Verify the SSA using a Monte Carlo simulation as well as results published in the literature.

Task 3.3: Integrate SSA into MDA for use with an optimization algorithm.

Task 3.4: Test performance of several optimization routines for robustness across a given design space.

Task 3.5: Study a baseline aircraft designed to maximize endurance subject to probabilistic constraints.

Much of the practical implantation of the method is contained within the tasks that support Hypothesis 3. Tasks 3.1 and 3.2 will develop the SSA code and verify that results in the literature can be duplicated. To provide confidence that the SSA method can be extrapolated to a more complex system, a Monte Carlo simulation will be used to verify the results of the SSA for the full propulsion system of the baseline fuel cell UAV. Tasks 3.3 will implement gradients calculated by SSA as well as propagated uncertainty estimates into an optimization routine. To ensure that the optimizations can be robustly carried out within the fuel cell UAV design space, several optimizers will be compared. Task 3.5 is designed to implement the methodology into the study of a near-term fuel cell UAV designed to maximize endurance. The baseline aircraft will be based on the validated MDA developed in Task 1 and will implement the flexible design framework of Task 2 to implement updates in the CAs as more information is gained throughout the design process. The optimization under uncertainty routine using SSA will then be used to locate optima in the design space and identify Pareto fronts.

CHAPTER 4

UNCERTAINTY PROPAGATION

The lack of accounting for the effects of uncertainty was a common gap in many fuel cell UAV design methodologies. Uncertainty is high in fuel cell systems due to a lack of available data as well as the rapid pace at which fuel cell systems are developing. In addition, the desire for maximizing endurance coupled with reduced specific power of fuel cells as compared to conventional propulsion provides a highly constrained design space. In order to estimate an adequate design that lies within a probabilistically feasible design space, a method for efficient uncertainty propagation is needed. In addition, uncertainty propagation is key to the proposed methodology for decomposition. This chapter provides a brief introduction to uncertainty and then derives the SSA approach to propagating uncertainty that was included as part of Hypothesis 3. A simple example problem is given to verify the results of the SSA approach. The derivation and implementation of the SSA approach also leads to three different design rules that inform the construct of the MDA.

4.1 Uncertainty Classification

Uncertainty is often a term that is used loosely in design. As uncertainty analysis has become more prevalent among engineering design, more common definitions are becoming standard. In general, there are three classifications of uncertainty: aleatory, epistemic, and numerical.

Aleatory uncertainty is a term to describe inherent random variations in the physical system. Aleatory uncertainty is also referred to as variability, stochastic uncertainty, inherent uncertainty, and irreducible uncertainty [194]. In the introduction, aleatory uncertainty was referred to as an external source of uncertainty and material properties, part dimensions, and actual operating conditions were given as examples.

Epistemic uncertainties are due to ignorance, lack of knowledge, or incomplete information [195]. Epistemic uncertainties can be classified as either parametric or model-based. Parametric epistemic uncertainty is associated with parameters used in engineering models that cannot be exactly estimated usually because of sparse or inadequate information. In the introduction, the actual value of the gravitational constant was given as an example of a parametric uncertainty because researchers have yet to set up experiments that will allow its measurement with an uncertainty of less than 1.5 parts in 1000 [196]. Model-based uncertainty is due to improper and inadequate modeling of a physical system. When mathematical models are developed, there is always model-based epistemic uncertainty associated with how well the model will actually predict observed behavior. Typically, epistemic uncertainty is reducible since a better knowledge of the physics of the problem can enable a better mathematical model. Additionally, experimental data can be used to calibrate mathematical models to improve their predictive ability and thus reduce their epistemic uncertainty.

Numerical uncertainty is commonly associated with numerical models used in modeling and simulation [195]. Computer round off errors, or errors due to the number of digits of precision that can be used in a calculation are example of numerical uncertainty. Also, since many models require numerical iterative methods to obtain a

solution, there will be numerical uncertainty associated with tolerances used to define convergence criteria.

4.2 Uncertainty Propagation

In order to determine its cumulative effects, all sources of uncertainty must be modeled and propagated through all contributing analyses that compose a complex system. A number of probabilistic techniques exist including simulation methods, importance sampling techniques, first-order reliability methods, second-order reliability methods, response surface methods, and method of moments techniques [197]. Perhaps the most widely used and understood method is the Monte Carlo simulation (MCS). Monte Carlo simulation is widely used because it is easy to accommodate to existing MDAs and it is also parallelizable. Monte Carlo simulation samples uncertain variables from a probability density function that models the variable's uncertainty. A large number of simulations are typically executed and results are tracked and used to estimate statistical parameters of the system uncertainty. Although MCS is typically the method of choice since it is based on the least number of simplifying assumptions, it is often too costly for widespread use in early design. Reduced sampling techniques [198] such as Latin hypercube sampling, importance sampling, and Taguchi orthogonal arrays may be used to improve computational efficiency but may not always be appropriate depending on the structure and complexity of the design. Response surfaces have also been employed to provide regressed models of MDAs that can be economically used with MCS [178]. Another popular method is based on statistical moments. If the input variables are independent, random, and normally distributed, first and second-order

statistical moment matching has been shown to be an efficient method that agrees with MCS [199].

More recently, methods have also been proposed based on sensitivity analysis. One primary advantages of sensitivity analysis methods is that they tend to handle both aleatory and epistemic uncertainties, whereas many other methods focus mostly on propagating aleatory uncertainties. As a result, propagation techniques based on sensitivity analysis help designers to gain insights about complex model behavior and make informed decisions regarding where to spend engineering effort to reduce the variability of a system [200]. Gu et al. [192] has proposed a sensitivity method that has been validated against MCS for estimating the worst case uncertainty propagation based on bracketing the source uncertainties with intervals. Closely related is the work of McDonald who extends the same sensitivity approach to propagate indeterminate uncertainty [191].

This research is based upon uncertainty propagation using the systems sensitivity analysis (SSA) approach based on the work of Gu et al. [192] and McDonald [191]. The SSA approach was chosen primarily due to its synergy with other aspects of this research. The SSA approach provides system level gradient information which can be used to improve the efficiency of gradient based optimization. The SSA approach also requires a knowledge of the interdisciplinary couplings between various contributing analyses which is useful in developing the automated DSM solution framework presented in Chapter 6. In addition, uncertainty attribution can be estimated using SSA which will allow the designer to determine what sources of uncertainty have the largest impact on the overall uncertainty at a given location in the design space.

4.3 Systems Sensitivity Analysis

Systems sensitivity analysis is the basis for estimating the total derivatives of the performance metrics with respect to the design variables. These derivatives provide information for optimization and decision making as well as facilitating the efficient calculation of the system level uncertainty. The formulation of SSA is well described in several works by Sobieszczanski-Sobieski [190, 201-203]. The method is well suited for use in multidisciplinary design environments and has been shown to be useful in conceptual multidisciplinary design optimization problems [204].

The SSA formulation is centered on a multidisciplinary design environment as shown in Figure 4.1. For clarity in the formulation, a simple nomenclature is used where the design variables are contained in the vector **x**, **T** is the CA or tool used to perform a given analysis and produce an output vector **y**. Since there are multiple CAs, or tools, numbered subscripts are used to distinguish the order in which the CA resides in the MDA.

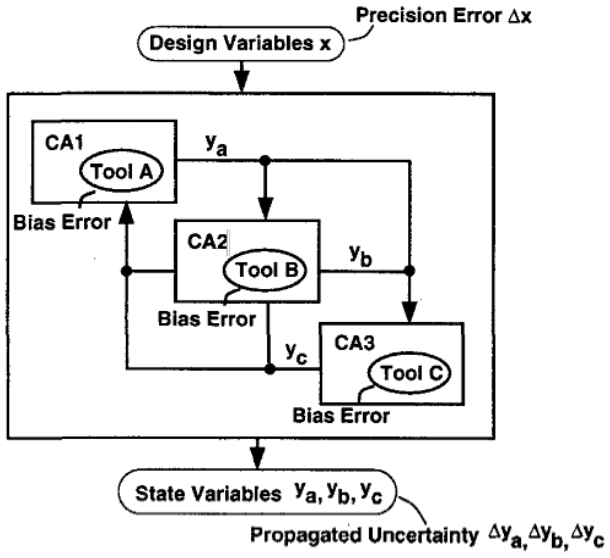

Figure 4.1: Multidisciplinary system analysis [192].

Using this notation, the basic mathematical equation for CA number 1 is as shown in Eq. (4.1). This equation shows that CA number 1 is a function of the design variables as well as outputs from various other CAs.

$$\mathbf{y}_1 = \mathbf{T}_1\left(\mathbf{x}, \mathbf{y}_1, \mathbf{y}_2, \ldots, \mathbf{y}_n\right) \tag{4.1}$$

Systems sensitivity analysis sets up a system of coupled equations that relates the total derivative of the CAs with respect to the input variables, to partial derivatives of the CAs with respect to both the design variables and other CA variables. The generalized SSA equation is given in Eq. (4.2).

$$\begin{bmatrix} \mathbf{I}_1 & -\frac{\partial \mathbf{T}_1}{\partial \mathbf{y}_2} & \cdots & -\frac{\partial \mathbf{T}_1}{\partial \mathbf{y}_n} \\ -\frac{\partial \mathbf{T}_2}{\partial \mathbf{y}_1} & \mathbf{I}_2 & & \vdots \\ \vdots & & \ddots & -\frac{\partial \mathbf{T}_{n-1}}{\partial \mathbf{y}_n} \\ -\frac{\partial \mathbf{T}_n}{\partial \mathbf{y}_1} & \cdots & -\frac{\partial \mathbf{T}_n}{\partial \mathbf{y}_{n-1}} & \mathbf{I}_n \end{bmatrix} \begin{bmatrix} \frac{d\mathbf{y}_1}{d\mathbf{x}} \\ \frac{d\mathbf{y}_2}{d\mathbf{x}} \\ \vdots \\ \frac{d\mathbf{y}_n}{d\mathbf{x}} \end{bmatrix} = \begin{bmatrix} \frac{\partial \mathbf{T}_1}{\partial \mathbf{x}} \\ \frac{\partial \mathbf{T}_2}{\partial \mathbf{x}} \\ \vdots \\ \frac{\partial \mathbf{T}_n}{\partial \mathbf{x}} \end{bmatrix}. \tag{4.2}$$

Equation (4.2) is called the global sensitivity equation (GSE). The GSE is composed of three matrices known as the local sensitivity matrix (LSM), the local sensitivity vector (LSV), and the sensitivity derivative vector (SDV). In comparison with Eq. (4.2), the GSE components are as shown in Eq. (4.3).

$$[\mathbf{LSM}][\mathbf{GSV}] = [\mathbf{LSV}] \tag{4.3}$$

The LSM is a matrix of partial derivatives of the CAs with respect to output values of other CAs in the DSM. Similarly, the LSV is a matrix of partial derivatives of the CAs with respect to the design variables. The GSV matrix contains the total derivatives, or system level sensitivity derivatives. The LSM and LSV can be directly populated using either finite difference methods or by taking the partial derivatives of the

CAs analytically. Once the LSM and LSV are calculated, Equation (4.3) can then be solved for the GSV.

A Matlab code was written to populate and solve the GSE. The code was purposely made very general so that it could easily be adapted to any DSM. The code simply requires a solution point of the MDA (values for $\mathbf{y}_1$ through $\mathbf{y}_n$ given $\mathbf{x}$) and an input file that lists the inputs and outputs of each CA as well as the design variables required by each CA. In general, many of the CAs may not be coupled or functions of the design variables which results is sparse matrices for the LSM and LSV. For efficiency, the code compares the inputs and outputs of the CAs as well as the input variables required by the CAs so that partial derivatives that are known to be equal to zero are not calculated.

To make the code more general, it was assumed that analytical partial derivatives would not be available. As a result, the code implements a central difference scheme with a user defined step size to estimate the values of the partial derivatives around the solution point.

Solving Eq. (4.3) involves taking the inverse of the LSM. Since CA outputs could theoretically vary by orders of magnitude (e.g. Range in km vs. a drag coefficient), it is likely that the LSM will be poorly conditioned in most real problems. To help improve the conditioning of the LSM, all values of the LSM are scaled with respect to a baseline. If baseline values are not input to the code, then the code will treat the current solution point as a baseline as suggested by Sobieszczanski-Sobieski [190]. To avoid divide by zero errors, all CA or design variables equal to zero are assigned a scaling value of unity.

4.4 Uncertainty Propagation

A paramount element of the proposed research is the efficient propagation of uncertainty. Uncertainty propagation must be accurate and yet computationally efficient in order to be used in a design space exploration. Two different uncertainty propagation techniques were chosen to assist in proposed research. Both techniques are based on SSA. The first technique calculates the bounded error based on defining bounds of the uncertainty of the input variables as well as the uncertainty bounds of resulting **y** vectors calculated by the CAs. The second technique propagates indeterminate uncertainty by defining variances of both the design variables as well as the CA's calculated **y** vectors. The uncertainty propagation results in an estimation of the system level uncertainty variance rather than just providing a bounded uncertainty. Both techniques are based upon SSA and computationally are dependent on the population of the LSM and LSV matrices as well as the calculation of LSM^{-1}. As a result, employing both methods is only slightly more computationally expensive than just employing one of the methods individually.

4.4.1 Bounded Uncertainty

Bounded uncertainty is based upon first defining uncertainty associated with input variables (design variables and/or constants) and bias errors or uncertainties related to the accuracy of the CAs. If an input variable or constant is uncertain, the relationship between the true value ($\mathbf{x}^{true}$) and the uncertain value **x** is given as

$$\mathbf{x}^{true} = \mathbf{x} + \Delta\mathbf{x} \qquad (4.4)$$

where $\Delta\mathbf{x}$ is a vector that describes the difference between the uncertain and the true values. Similarly, the uncertainty associated with a given CA, in this case CA_1, can be related to the true out put of the CA as shown in Eq. (4.5).

$$\mathbf{T}_1^{\,true} = \mathbf{T}_1\left(\mathbf{x}, \mathbf{y}_2, \ldots, \mathbf{y}_n\right) + \Delta\mathbf{T}_1 \qquad (4.5)$$

The term $\Delta\mathbf{T}_1$ represents the bias error or uncertainty of the CA and is a function ($\boldsymbol{\delta}_1$) of the CA inputs.

$$\Delta\mathbf{T}_1 = \boldsymbol{\delta}_1\left(\mathbf{x}, \mathbf{y}_2, \ldots, \mathbf{y}_n\right) \qquad (4.6)$$

In multidisciplinary analysis, $\mathbf{T}_1$ is dependent on various inputs $\mathbf{y}_2$, …, $\mathbf{y}_n$ that are calculated by other CAs. In Eq. (4.5), it is assumed that $\mathbf{x}$ and $\mathbf{y}_2$, …, $\mathbf{y}_n$ contain no uncertainty. However, since the CAs that calculate the respective values of $\mathbf{y}$ will have some uncertainty associated with their models**,** the actual output $\mathbf{y}_1^{\,\text{true}}$ will vary from the calculated value of $\mathbf{y}_1$ with propagated uncertainty $\Delta\mathbf{y}_1$ according to Eq. (4.7).

$$\mathbf{y}_1^{\,true} = \mathbf{y}_1 \pm \Delta\mathbf{y}_1 \qquad (4.7)$$

Using a derivation provided by Gu [192], the bounded propagated uncertainty $\Delta\mathbf{y}$ can be calculated as a function of $\Delta\mathbf{x}$ and $\boldsymbol{\delta}$ according to Eq. (4.8). It is important to note that the absolute value of $\Delta\mathbf{x}$ and LSM^{-1} are meant to be performed on a term by term basis.

$$\begin{bmatrix} \Delta\mathbf{y}_1^{\,2} \\ \Delta\mathbf{y}_2^{\,2} \\ \vdots \\ \Delta\mathbf{y}_n^{\,2} \end{bmatrix} = \begin{bmatrix} \left|\frac{d\mathbf{y}_1}{d\mathbf{x}}\right| \\ \left|\frac{d\mathbf{y}_2}{d\mathbf{x}}\right| \\ \vdots \\ \left|\frac{d\mathbf{y}_n}{d\mathbf{x}}\right| \end{bmatrix} |\Delta\mathbf{x}| + \left|LSM^{-1}\right| \begin{bmatrix} \left|\boldsymbol{\delta}_1\left(\mathbf{x}, \mathbf{y}_2, \mathbf{y}_3, \ldots, \mathbf{y}_n\right)\right| \\ \left|\boldsymbol{\delta}_2\left(\mathbf{x}, \mathbf{y}_1, \mathbf{y}_3, \mathbf{y}_4, \ldots, \mathbf{y}_n\right)\right| \\ \vdots \\ \left|\boldsymbol{\delta}_n\left(\mathbf{x}, \mathbf{y}_1, \mathbf{y}_2, \ldots, \mathbf{y}_{n-1}\right)\right| \end{bmatrix} \qquad (4.8)$$

In a real design problem, the exact value of $\Delta\mathbf{x}$ and the function values of δ would not be known to a designer. However, based on knowledge of the design variables and constants, the designer could use $\Delta\mathbf{x}$ to define a reasonable bound for **x**. Likewise, calibration of a CA or previous experience could provide an estimate of the accuracy of **T** and thus an estimation of δ could be made. In this case, Eq. (4.8) would provide a conservative estimate for the bounded uncertainty of **y**.

4.4.2 Indeterminate Uncertainty

A slightly different formulation is to treat uncertainty as a random variable. In this case it is assumed that the uncertainty varies about the expected value of the CA with a standard deviation $\sigma\mathbf{T}$. Thus the true value of CA_1 is related to the uncertainty as given in Eq. (4.9).

$$\mathbf{T}_1^{true} = \mathbf{T}_1\left(\mathbf{x}, \mathbf{y}_2, \mathbf{y}_3, \ldots, \mathbf{y}_n\right) \pm \sigma\mathbf{T}_1 \qquad (4.9)$$

Using the same argument as presented in support of Eq. (4.7), if we consider that the **y** values calculated by other CAs also contain uncertainty, then the actual output $\mathbf{y}^{true}$ will vary from the calculated value of **y** with propagated uncertainty $\sigma\mathbf{y}$ according to Eq. (4.10).

$$\mathbf{y}_1^{true} = \mathbf{y}_1 \pm \sigma\mathbf{y}_1 \qquad (4.10)$$

Using SSA, McDonald [205] shows that the total propagated uncertainty can be estimated by Eq. (4.11) where the square of the inverse of the LSM and the square of the LSV are performed on a term-by-term basis. Note that σx represents the corresponding uncertainty in the input variable **x** similar to the relationship shown in Eq. (4.10). Also

note that for Eqs. (4.9) and (4.11), *n* is the number of CAs and *m* is the number of input design variables.

$$\begin{bmatrix} \sigma \mathbf{y}_1^{\,2} \\ \sigma \mathbf{y}_2^{\,2} \\ \vdots \\ \sigma \mathbf{y}_n^{\,2} \end{bmatrix} \approx \left(\mathbf{LSM}^{-1}\right)^2 \left(\begin{bmatrix} \sigma \mathbf{T}_1^{\,2} \\ \sigma \mathbf{T}_2^{\,2} \\ \vdots \\ \sigma \mathbf{T}_n^{\,2} \end{bmatrix} + \left(\mathbf{LSV}\right)^2 \begin{bmatrix} \sigma x_1^{\,2} \\ \sigma x_2^{\,2} \\ \vdots \\ \sigma x_m^{\,2} \end{bmatrix} \right) \tag{4.11}$$

4.4.3 Uncertainty Attribution

One of the useful features of the uncertainty propagation techniques presented is that they capture the how each uncertainty in either the design variables or the CAs contribute to the overall propagated uncertainty. Equations (4.8) and (4.11) represent sums of the all of the individual propagated uncertainties that contribute to the overall propagated uncertainty. By expanding out the matrix multiplications in Eqs. (4.8) and (4.11), the contribution that each design variable and CA uncertainty has on the overall system level uncertainties can be calculated.

For indeterminate uncertainty, Eq. (4.11) represents a Pythagorean sum of the individual variance terms. However, it is typically easier for people to understand uncertainty in terms of standard deviation rather than variance. McDonald [191] suggests Eq. (4.12) as a valuable way to determine these contributions of uncertainty. Note that in Eq. (4.12), σ can represent either a propagated contribution of uncertainty due a specific CA or the propagated uncertainty due to uncertainty of the inputs.

$$\overline{\sigma}_j = \frac{\sqrt{\sum_{i=1}^{n+m} \sigma_i^{\,2}}}{\sum_{i=1}^{n+m} \sigma_i} \sigma_j \tag{4.12}$$

4.4.4 Uncertainty Propagation Validation

To verify the SSA code and the uncertainty propagation estimates, an example problem given by McDonald [191] was used. The problem is defined by Eqs.(4.13-4.16).

$$a = \frac{1}{40}\left(\begin{array}{l} 2.48374x + \dfrac{4.746265d^2}{x + 3.2874} + 3.23872dx + \left[y - 3.48572\right]x \\ + \dfrac{\left[d - 4.34721\right]y}{\left[x + 5.424\right]} 2.3421 + y \end{array} \right) \tag{4.13}$$

$$b = \frac{1}{40}\left(xac + \frac{a}{c^2 + 0.02375} \right) \tag{4.14}$$

$$c = 2 + \frac{1}{60}\left(x^2\left[x - 5.67834\right] + ax\left[a - 6.3432\right] \right) \tag{4.15}$$

$$d = \frac{1}{1200}\left(bc\left[c + 0.0345\right] + z^2\left[b^2 + 0.34721\right] \right) \tag{4.16}$$

There are several ways in which the sample problem can be organized into a design structure matrix (DSM). Figure 4.2 shows three different DSMs that vary by the degree in which the problem is decomposed into CAs. Similar decompositions are expected to be part of any more complex DSM. The most logical structure is to allow each equation in the sample problem to be its own CA. This would result in Decomposition 1 in Figure 4.2 where each CA has multiple input values but only calculates a single output value. A CA used in a practical design problem would likely have multiple inputs and outputs. To allow the sample problem to simulate this, Decompositions 2 and 3 in Figure 4.2 are used. In Decomposition 2 Eqs. (4.13) and (4.14) make up the CA labeled **AB**. Similarly, Decomposition 3 combines Eqs. (4.15) and (4.16) into the CA labeled **CD**.

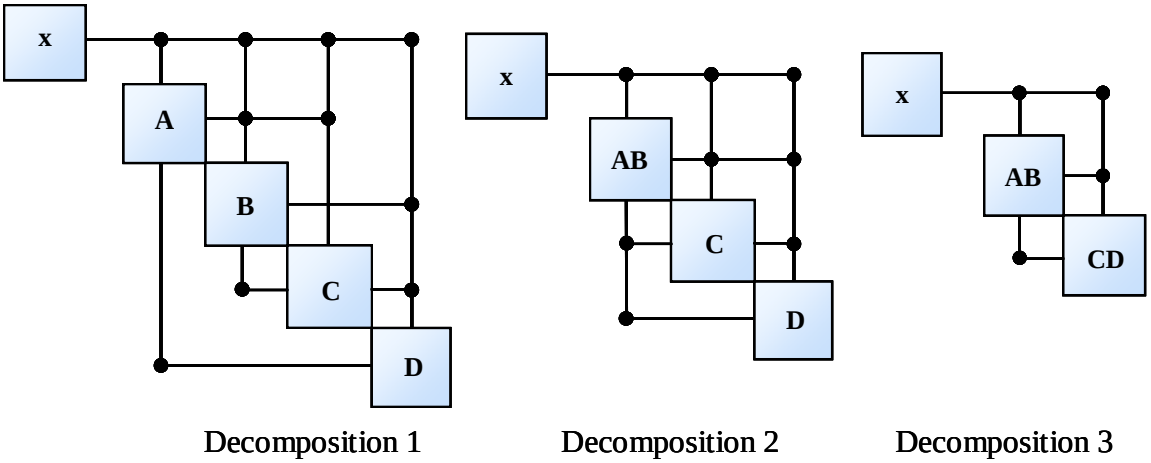

Figure 4.2: Different DSM structures for the sample problem.

To bring the CA variables into agreement, compatibility equations were written for each feedback loop in the DSM. Newton's method was employed to solve the resulting coupled system of nonlinear equations. The use of a solver such as Newton's method coupled with the DSM is referred to as an MDA throughout this dissertation. For the example problem, the values of the design variables can be found in Table 4.1 with the resulting values of the CA responses given in Table 4.2. In Table 4.2 the exact values of the CA responses were the values calculated using Newton's method. In addition, values calculated in reference [191] by developing a Gaussian process surrogate model of Eqs. (4.13-4.16) are also presented. Note that the surrogate model values for *b* and *d* vary significantly from the exact values.

Table 4.1: Example problem design variable inputs.

Design Variable	Value
x	5.0
y	5.0
z	5.0

Table 4.2: Example problem converged CA response.

CA Variable	Value Exact	Value Surrogate Model [191]
a	0.506	0.509
b	0.099	0.312
c	1.471	1.469
d	0.0076	0.0175

Using the variable values given in Table 4.1 and Table 4.2, the SSA code was used to populate the LSM and LSV matrices. For the central differencing scheme used to estimate the partial derivatives, a step size of 0.01% of the variable being differentiated was used. The resulting derivative calculations were compared to the analytical derivatives and found to be in agreement to at least 8 decimal places. The populated matrices of the GSE for the DSM Decompositions 1, 2, and 3 are shown respectively in Eqs. (4.17-4.19).

$$\begin{bmatrix} 1 & 0 & 0 & -0.4331 \\ -0.1953 & 1 & -0.0555 & 0 \\ 0.4443 & 0 & 1 & 0 \\ 0 & -0.0060 & -0.0003 & 1 \end{bmatrix} \begin{bmatrix} da/d\mathbf{x} \\ db/d\mathbf{x} \\ dc/d\mathbf{x} \\ dd/d\mathbf{x} \end{bmatrix} = \begin{bmatrix} 0.1123 & 0.1256 & 0 \\ 0.0186 & 0 & 0 \\ 0.2544 & 0 & 0 \\ 0 & 0 & 0.0030 \end{bmatrix} \tag{4.17}$$

$$\begin{bmatrix} 1 & 0 & 0 & -0.4331 \\ 0 & 1 & -0.0555 & -0.0846 \\ 0.4443 & 0 & 1 & 0 \\ 0 & -0.0060 & -0.0003 & 1 \end{bmatrix} \begin{bmatrix} d\mathbf{AB}/d\mathbf{x} \\ dc/d\mathbf{x} \\ dd/d\mathbf{x} \end{bmatrix} = \begin{bmatrix} 0.1123 & 0.1256 & 0 \\ 0.0405 & 0.0245 & 0 \\ 0.2544 & 0 & 0 \\ 0 & 0 & 0.0030 \end{bmatrix} \tag{4.18}$$

$$\begin{bmatrix} 1 & 0 & 0 & -0.4331 \\ 0 & 1 & -0.0555 & -0.0846 \\ 0.4443 & 0 & 1 & 0 \\ 1.1e-4 & -0.0060 & 0 & 1 \end{bmatrix} \begin{bmatrix} d\mathbf{AB}/d\mathbf{x} \\ d\mathbf{CD}/d\mathbf{x} \end{bmatrix} = \begin{bmatrix} 0.1123 & 0.1256 & 0 \\ 0.0405 & 0.0245 & 0 \\ 0.2544 & 0 & 0 \\ 6.2e-5 & 0 & 0.0030 \end{bmatrix} \tag{4.19}$$

The DSM for Decomposition 1 had the highest degree of decomposition out of the three DSM analyzed. Since the CAs were decomposed to a level where each CA only returned one variable, each one of the partial derivative submatrices as well as the identity submatrices in the LSM are 1x1 matrices. For Decomposition 2, the two variable output of CA **AB** results in 2x2 submatrices for all entries in row 1 of the LSM. Note that in Eq. (4.17), LSM(2,4) = 0 since $\partial \mathbf{B}/\partial d = 0$. However, in Eq. (4.18) LSM(2,4) $\neq 0$ since $\partial \mathbf{AB}/\partial d \neq 0$. This result is due to partial derivatives being calculated at the CA level. Since *a* is a function of *d*, and *b* is a function of *a*, and both calculations are carried out within **AB**, **AB**'s calculation of *b* is now a function of *a*. Similarly, in Eq. (4.18), LSV(2,2) $\neq 0$ since within *AB*, the calculation of *b* is now a function of *y*. The resulting changes in the LSM and LSV provide valuable information about executing SSA. Since a finite differencing scheme was used to calculate partial derivatives, and all of the partial derivatives were calculated at the CA level, the LSM and LSV were correctly populated. An alternate approach would be to use analytical derivates if they are available [204]. A typical mistake for Decomposition 2 might be to say that $\partial \mathbf{AB}/\partial d = 0$ since Eq. (4.14) is not a function of *d*. The correct approach for taking an analytical derivative for Decomposition 2 would be to substitute *a* in Eq. (4.13) into Eq. (4.14) and then take the partial derivate of the resulting equation.

When Eqs. (4.17-4.19) are solved for the GSV, all three equations provide the result shown in Eq. (4.20). Thus, if the partial derivatives are properly taken at the CA level, the calculation of the GSV will be correct regardless of the degree of decomposition within the DSM.

$$[GSV] = \begin{bmatrix} 0.1124 & 0.1257 & 0.0013 \\ 0.0519 & 0.0215 & 0.0002 \\ 0.2044 & -0.0558 & -0.0006 \\ 0.0004 & 0.0001 & 0.0030 \end{bmatrix} \tag{4.20}$$

Having solved the GSE, the bounded and indeterminate uncertainties were calculated. The source uncertainties are given in Table 4.3. For this example, the design variable *y* was assumed to be uncertain as was the calculation of *c* and *d*.

Table 4.3: Example problem uncertainty sources

Indeterminate Uncertainty Source Value (%)		Bounded Uncertainty Source Value (%)	
σy	0.05	Δy	0.05
σc	0.075	Δc	0.075
σd	0.1	Δd	0.1

The resulting propagated indeterminate uncertainties for each of the decomposition schemes are given in Table 4.4. To assist in verifying the results, two Monte Carlo simulations were also executed. Monte Carlo 1 solved the DSM 10,000 times with input uncertainty values sampled from a normal distribution. Monte Carlo 2 also solved the DSM 10,000 times but used samples from a uniform distribution to model the indeterminate uncertainties. In addition, the results from reference [191] using surrogate models rather than the actual equations are also given in Table 4.4.

Table 4.4: Propagated indeterminate uncertainty comparison

Response Uncertainty	Decomp. 1	Decomp. 2	Decomp. 3	Monte Carlo 1	Monte Carlo 2	Surrogate Models [191]
σy_a	0.093	0.093	0.093	0.094	0.093	0.095
σy_b	0.116	0.125	0.125	0.116	0.116	0.063
σy_c	0.101	0.101	0.101	0.099	0.102	0.101
σy_d	0.052	0.052	0.051	0.052	0.052	0.117

For Decomposition 1, all of the propagated uncertainties are in excellent agreement with both Monte Carlo simulations (see Table 4.4). For Decompositions 2 and 3, the indeterminate uncertainty of response *b* slightly increases from 11.6% to 12.5%. To help explain this change, it is useful to examine the uncertainty attribution as shown in Figure 4.3. Based on the data in Figure 4.3, the propagated uncertainty is virtually all due to the uncertainty in the design variable *y* and the uncertainty in the calculation of *c*. The effect of the uncertainty in the calculation of *c* is virtually unchanged for the three different decomposition schemes, however, combining Eqs. (4.13) and (4.14) artificially makes the propagated uncertainty more sensitive to uncertainties in *y*. The reason for the change in propagated uncertainty is that with Eqs. (4.13) and (4.14), there is no means at the CA level for propagating the uncertainty from *a* into *b*. Also, at the CA level in Decompositions 2 and 3, *b* effectively becomes a function of *y* and thus is directly sensitive to uncertainties in *y*. For Decomposition 1, *b* is only sensitive to *y* after the uncertainty of *y* has been propagated into the calculation of *a*, since *b* is a function of *a* and not *y*.

In addition, Figure 4.3 also shows the propagated uncertainty attribution for *d*. Even though the summed propagated uncertainty in d is relatively constant over the three different decomposition schemes, the error attribution slightly changes. Since *d* is a function of *c*, when Eqs. (4.15) and (4.16) are combined in Decomposition 3 and the distinction between *c* and *d* is lost at the CA level, *d* becomes less sensitive to *c*. However, since at the system level, *d* becomes a function of *a*, then more uncertainty in *d* that propagates to *a* will also be propagated back to *d* causing the slight increase in σy_d due to σd.

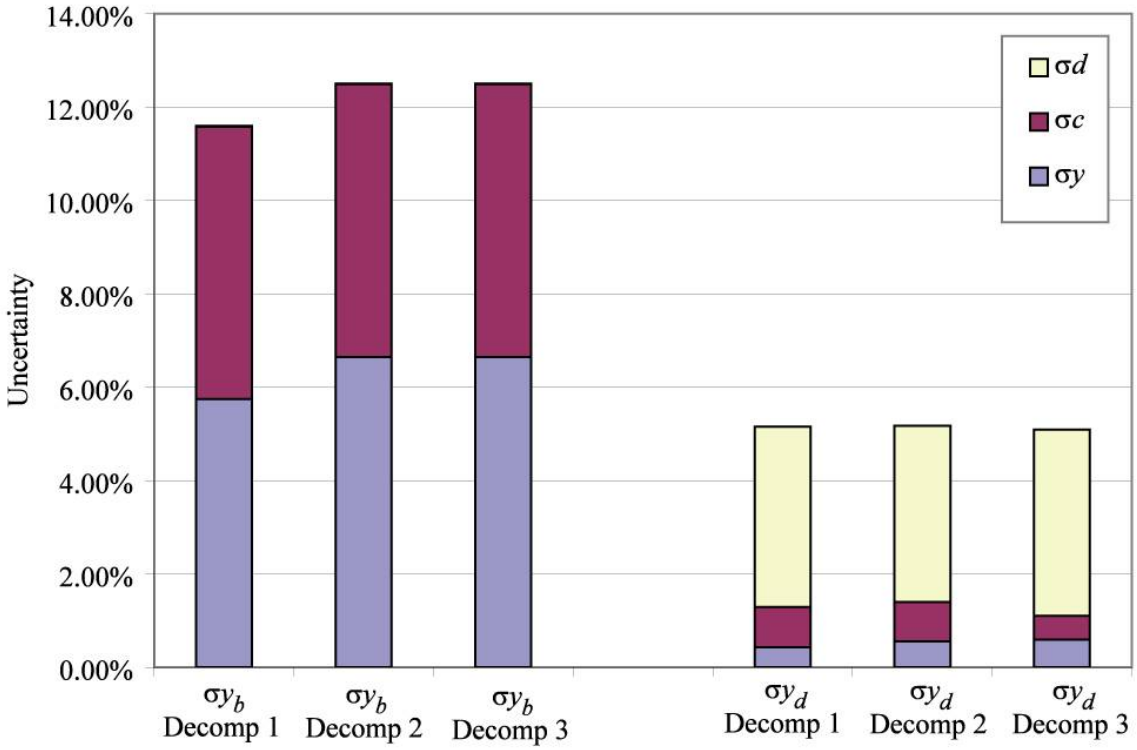

Figure 4.3: Uncertainty attribution for variables *b* and *d*.

The results for predicting the bounded uncertainty propagation for the three different decompositions are given in Table 4.5. For verification purposes, a Monte Carlo simulation was executed and compared to the results. A set of uniform distributions with boundaries defined in Table 4.3 were used to model the source uncertainties. For 10,000 cases, the DSM was brought to convergence. Out of the 10,000 cases executed, the maximum value of Δy was stored and is given in Table 4.5. Note that for each of the decompositions, the results for Δy_a, Δy_c, and Δy_d are in excellent agreement with the Monte Carlo simulation. For the same reasons as in the indeterminate uncertainty propagation results, Decompositions 2 and 3 result in slightly higher propagated uncertainty predictions for *b*.

Table 4.5: Propagated bounded uncertainty comparison.

Bounded Uncertainty	Decomp. 1	Decomp. 2	Decomp. 3	Monte Carlo
Δy_a	0.094	0.094	0.094	0.093
Δy_b	0.164	0.188	0.188	0.168
Δy_c	0.114	0.114	0.114	0.113
Δy_d	0.067	0.070	0.065	0.068

Overall, both the indeterminate and bounded uncertainty propagations provided results that agreed with Monte Carlo simulations. In addition, assuming that the bounds of the source uncertainties in the bounded uncertainty propagation are the same as the standard deviation values used for sources in the indeterminate uncertainty provided fairly consistent propagated uncertainty ranges between the two methods (compare Table 4.4 with Table 4.5).

4.5 Decomposition Rule

One of the key results was determining that the degree of decomposition has an effect on the calculation of the overall propagated uncertainty. When two values calculated in a CA are dependent on each other, there is no means for either uncertainty propagation method to directly capture this dependency since all partial derivatives in SSA are taken at the CA level. Thus a general rule that should be adopted for formulating problems for uncertainty propagation using SSA is that the problem should be decomposed to a point where no output of a CA is dependent on any other output of the same CA. In many multidisciplinary designs, the analysis is decomposed into CAs by discipline and many CAs will return a vector of outputs that are not independently calculated. For example, a typical propeller performance CA might have the propeller

geometry, rotational speed, and airspeed as inputs and might calculate the generated thrust and power as outputs. In this case, the propeller performance CA would likely first calculate the thrust and then simply calculate the available power as the thrust multiplied by the airspeed. In this case, the LSM will not capture the effect that available power is a function of available thrust since they are both outputs of the same CA, and thus no proper partial derivative will be calculated. However, the LSV will not change since available power is still a function of the input variables to available thrust and the resulting GSV will be correct. Despite this, when Eqs. (4.8) or (4.11) are calculated, the estimated propagated uncertainty will change since the formulation of Eqs. (4.8) or (4.11) will allow the uncertainty in available power to only be due to the propagated uncertainty in the inputs to the propeller CA and will not capture any uncertainty that may exist in the propeller performance CA's ability to model available thrust. In this case, the correct formulation is to decompose the propeller performance CA into two separate routines. The first would calculate available thrust, and the second CA could calculate available power as a function of available thrust. In this case, the SSA could correctly propagate any uncertainty in the thrust calculation into the available power.

4.6 Equality Constraint Rule

Another rule for implementing SSA for uncertainty propagation addresses equality constraints. A typical equality constraint would force the outputs of two different CAs to equal each other. The equality constraint would be forced by a solver that operates at a level just above the DSM. A typical example would be a propeller CA and a motor CA that both contain motor speed as an input and torque as an output. A

common formulation would be to use an equality constraint that states that the propeller torque must equal the motor torque. Under this formulation, uncertainty from either the motor or the propeller could not be propagated to the other as the SSA formulation does not account for couplings outside the DSM level due to equality constraints. Therefore, equality constraints must be eliminated by properly organizing the DSM and the CAs.

4.7 Design for Validation Rule

Ideally, the estimate of the uncertainty would be obtained from controlled experimental validation. However, to make a proper estimate that is useful for SSA, information must flow in terms of inputs and outputs through the CA just as it does in the controlled experiment. By decomposing the problem so that the a CA's input and output structure is similar to the input and output structure of controlled experiments makes replacing the CA with a regression or calibrated model based on experiment much simpler. Although this may seem straightforward, many CA formulations are actually based on computational efficiency and may not have the same structure of information flow as experiments used to estimate uncertainty.

As an example of a CA where uncertainty is present in the system, consider a multidisciplinary model of a propeller driven aircraft. This very simple model contains two CAs: *Propeller Performance CA* and *Aircraft Performance CA*. The *Propeller Performance CA* contains one equation (4.21) that describes the relationship between freestream velocity (V), thrust (T), and propeller rotational speed (ω).

$$C_T = C_T(\omega, V) = \frac{T}{\rho\left(\omega/2\pi\right)^2 d^4} \tag{4.21}$$

The relationship in Eq. (4.21) can be structured either as Eq. (4.22) or Eq. (4.23), depending on the inputs and outputs desired.

$$T = T(\omega, V) \tag{4.22}$$

$$\omega = \omega(T, V) \tag{4.23}$$

The *Aircraft Performance CA* contains the single equation given in Eq. (4.24).

$$m\frac{dV}{dt} = (T - D(V)) \tag{4.24}$$

Assuming that the *Aircraft Performance CA* is used to calculate conditions for steady level flight, Eq. (4.24) can be simplified as

$$T = D(V) = \frac{1}{2}\rho V^2 S_w C_D \tag{4.25}$$

which can be arranged so that $V = V(T)$.

For a single input, single output system, the DSM can be constructed in two different ways, shown in Figure 4.4 (a) and (b).

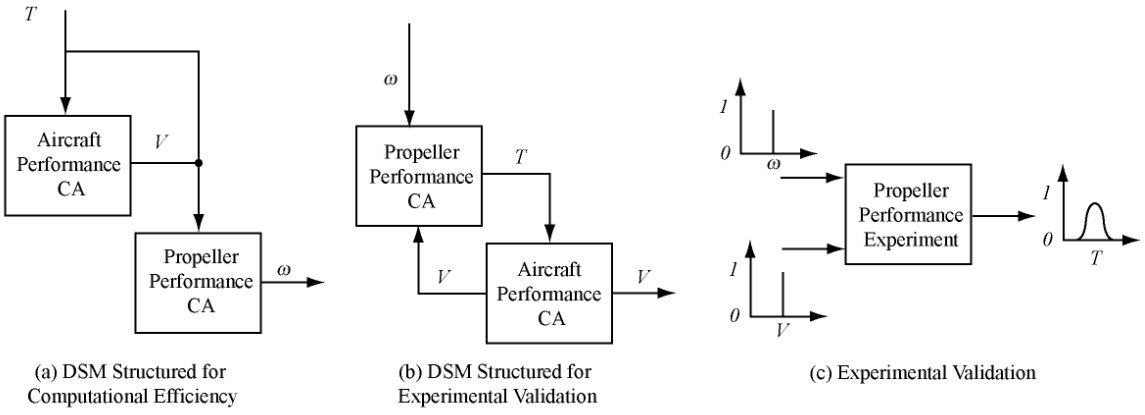

Figure 4.4: Comparison of DSM structures for computational efficiency and for experimental validation.

In Figure 4.4 (a), the DSM is constructed so that the input to the *Aircraft Performance CA* is T and the output is ω. Because this allows the DSM to be structured without feedback of CA output variables, the solution of the design problem can proceed in a computationally efficient manner without iteration. If the *Propeller Performance CA* is known to have some uncertainty associated with its mathematical models, then the uncertainty will be difficult to obtain by experiment assuming the DSM in Figure 4.4 (a). The DSM in Figure 4.4 (a) would require a difficult and unconventional validation experiment where the propeller thrust (T) and freestream velocity (V) are held constant and the propeller rotational speed (ω) is measured for its statistical distribution. Thrust is typically much more difficult to control and measure in an experiment introducing additional uncertainty into any measurement of rotational speed.

A schematic of the information flow in a prototypical validation experiment is shown in Figure 4.4 (c). In this experiment, a propeller is placed into a wind tunnel and the performance of the propeller is measured. Deterministic values of ω and V, which are typically easier to tightly control, are provided as inputs to the validation experiment and a statistical distribution of T is the output. In order for the uncertainty that is associated with the experimental validation data to be incorporated into the *Propeller Performance CA*, the *Propeller Performance CA* must have the same inputs and outputs as the validation experiment. This leads to the DSM that is shown in Figure 2 (b). In this case the DSM must incorporate feedbacks, compromising its computational efficiency.

For design problems where CA uncertainty is of interest, the DSM must be constructed to allow uncertainty data to be represented in the same way that it is gathered. For design problems where higher fidelity CAs are available, the low fidelity CAs must

be structured to emulate the data and uncertainty flow of the higher fidelity analyses. This hierarchy is based on the assumption that higher fidelity analyses, including experiments, are generally more costly and less structurally flexible.

4.8 Chapter Summary

The System Sensitivity Analysis formulation for obtaining system level gradients based on the partial derivatives of the CAs was given. The SSA formulation was then extended to provide an estimate of the propagated values of bounded and indeterminate uncertainty. A sample problem consisting of four coupled equations was given and formulated into various DSMs that had varying degrees of decomposition. The resulting system level gradients were shown to be independent of the degree of decomposition as long as the partial derivatives were properly calculated. However, the propagated uncertainty was shown to depend on the degree of decomposition. This emphasized that the path of uncertainty should be identified when laying out the DSM and led to a set of three design rules for DSM development.

Design Rule 1: Contributing analyses need to be decomposed to a level where no output of a given CA is a function of any other output of that same CA.

This decomposition rule results from the fact that in SSA, partial derivates are calculated at the outer CA level and do not recognize any relationships that are internal to the CA. A similar rule is also described relating to equality constraints at the system level.

Design Rule 2: Contributing analyses need to be formulated so that equality constraints at the system level are eliminated.

Since SSA uncertainty estimates are based on CA level partially derivatives, the method also cannot propagate uncertainty through equality constraints at the system level. The third design rule is based on formulating the CAs so that they provide a logical path of uncertainty from inputs to outputs that would correspond to experiments designed to estimate the uncertainty.

Design Rule 3: Contributing analysis should be formulated using the same input and output data flow that would correspond to an experiment designed to estimate the uncertainty.

CHAPTER 5

MODEL DECOMPOSITION AND VALIDATION

One of the significant gaps in the design of near-term fuel cell UAVs is the lack of a validated multidisciplinary analysis. In order to address this gap, a baseline aircraft configuration was chosen that is representative of the current state of the art fuel cell aircraft and could be sized and validated within the time constraints and budget of a university graduate degree research project. In order to develop a validated analysis, a high level sensitivity study was performed to determine how uncertainties in key aircraft parameters would propagate into important design metrics such as endurance and climb rate. This uncertainty study was used to guide decomposition of the problem into appropriate contributing analyses. In addition to addressing uncertainty, the problem also had to be decomposed to an appropriate level so that validation could occur. In cases were appropriate validation data were available, contributing analyses were decomposed to a level where test conditions could be replicated in the analysis. When validation data was unavailable, the contributing analysis had to be decomposed to a level where hardware could be specified and experimental tests could be designed to provide the necessary validation data. Where available, validation was achieved using data available in the literature. After validating the analysis, surrogate models were developed for the aerodynamics and propeller propulsion contributing analyses. The surrogates provided an increase in computational speed and helped smooth out numerical noise in the aerodynamic contributing analyses.

5.1 Baseline Aircraft Configuration

Most small UAVs are very simple in design consisting primarily of an airframe, a simplified electric actuated control system, and an integrated propulsion system. Most UAVs differ mainly by their choice of propulsion system and their choice of airframe. Propulsion systems are typically off-the-shelf units with designs mainly varying by the choice of aerodynamic configuration and the materials and structural design of the airframe. To begin decomposing the problem into tractable subsystem analyses, a baseline configuration was selected.

To select a baseline configuration, a matrix of alternatives (see Table 5.1) was created based on the most common configuration options. Each row in Table 5.1 has various alternatives that can be selected to meet a necessary vehicle attribute. As with most UAVs, the options available are largely related to airframe. Adding the fuel cell system enables a few more options for propulsion including hybridization and different methods of hydrogen storage.

Even with the relatively simple matrix of alternatives in Table 5.1, there are over 20,000 different options that result from selecting various options. Downselecting from these various options was achieved through a qualitative assessment based on maximizing endurance of the vehicle, past UAV design experience, and selecting a configuration appropriate for development and testing within a 1-2 year timeframe and a ~$10,000 materials budget. The baseline vehicle is described by the alternatives highlighted in Table 5.1.

Table 5.1: Matrix of Alternatives for baseline aircraft configuration.

Attributes		Alt 1	Alt 2	Alt 3	Alt 4
Config	Vehicle	Single Wing	Biplane	Flying Wing	
	Planform	Straight	Tapered	Elliptical	
	Tail	Canard	Conventional	V-Tail	
	Fuselage	Cylindrical	Oval		
Propulsion	Hydrogen Storage	Chemical Hydrides	Gaseous H2	Liquid H2	
	Fuel Cell Type	PEMFC	SOFC		
	Type	Fuel Cell Only	Battery Hybrid		
Structures	Prop Position	Tractor	Pusher		
	Materials	Fiberglass	Composites	Wood	Combination
	Process	Monocoque	Space Frame		
	Landing Gear	Fixed	Retractable	Removable Dolly	

The propulsion system decisions were informed by both the literature review and experience with the GT FCUAV. Choosing a PEMFC was an obvious choice as they have higher specific power and are much easier for a university to procure. Gaseous hydrogen storage was selected since a wide range of commercial units are available that provide good performance for both small and medium volumes. Chemical hydride storage systems were considered, but experience gained through developing a full system proved that uncertainty was high, recharge times were high, and outperforming gaseous hydrogen was unlikely [60]. Liquid hydrogen was also briefly considered but considered too costly and time consuming to develop and validate for this research. A hybrid system using a battery and fuel cell system was considered. However, building and testing a hybrid system would require a fair amount a custom electronics and control design which would likely require adding an electrical engineering graduate student to the design team. This was considered to be outside of the budget and scope of this research effort.

However, hybridization trade studies have been included in the dissertation work of Bradley [63, 206] although no specific hybridization hardware was developed.

The basic aerodynamic configuration of the aircraft consisted of a high aspect ratio tapered wing with a cylindrical fuselage and an inverted V-tail. Since the vehicle would need to be a low-speed highly aerodynamically-efficient design to maximize endurance, a high aspect ratio sailplane-type tapered wing was chosen. An aft tail was chosen over a canard and flying wing design as this would allow the vehicle to be aerodynamically similar to most conventional UAVs of the same class. The design team also had more experience with this type of design which would both reduce risk and allow previous work to be leveraged. During the conceptual design work of the GT FCUAV, various types of aft tails were considered and found to only slightly vary in performance [60]. As a result, an inverted V-tail was chosen to capitalize on knowledge gained during the development of the GT FCUAV.

The structures were based on the building techniques used in past UAV developments including the GT FCUAV [60, 207, 208]. These included an aluminum frame for the fuselage components surrounded by a fiberglass shell, a carbon fiber spar and tailboom structure, and solid core foam wings and tail with balsa wood sheeting. Using known building techniques would allow validated weight and strength estimations to be used for developing the airframe.

5.2 Modeling Decomposition

With a notional fuel cell aircraft concept selection, the first step in the overall design methodology outlined in Figure 3.1 is decomposition and modeling. The overall

goal of this step is to obtain a valid MDA that captures the system level performance of the vehicle. As the literature review noted, some researchers have built various MDAs of fuel cell aircraft and some provided modified aircraft performance relationships that are appropriate for fuel cell aircraft. However, little guidance is given in any of the methodologies that will aid in forming a valid MDA for a revolutionary new concept. Hypothesis 1 states that uncertainty propagation should be used to guide decomposition of the design into CAs that can each be validated. A process to accomplish this task is outlined in Figure 5.1.

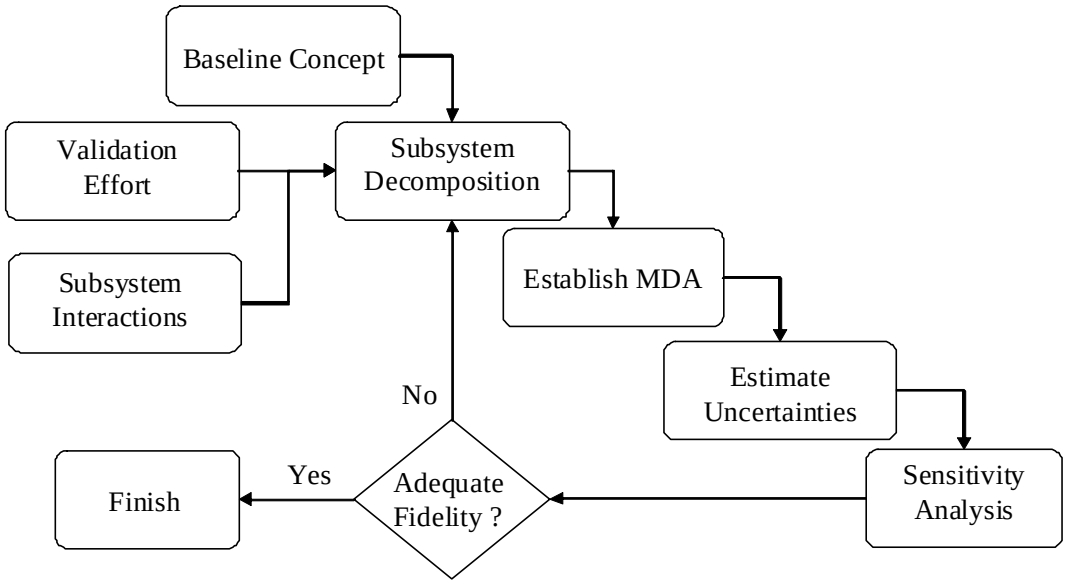

Figure 5.1: Process for design decomposition.

The process in Figure 5.1 begins with a baseline concept such as the concept selected in Table 5.1. The next step is to decompose the design into tractable CAs. In order for the CAs to be validated, some thought should be given as to how a CA would be validated as the system is decomposed. After initial decomposition, the CAs should be collected into a DSM that can be solved to create the MDA. Chapter 6 derives a

flexible framework that allows the CAs to be arranged into a DSM and solved to create the MDA. After building the MDA, estimates of the uncertainties of design variables, constants, and the output of the CAs should be made. An uncertainty propagation analysis should then be made to determine how sensitive key performance metrics are to the expected uncertainties. If the CAs can be validated, and the expected propagation of uncertainty is acceptable, then the process can be terminated. If the propagated uncertainty is too high, then the design should be further decomposed and the process can be repeated.

The process in Figure 5.1 is built upon the assumption that the MDA will become more accurate as the design is further decomposed into validated CAs. The uncertainty propagation is included as a quantitative measure to help determine how sensitive the design is to expected uncertainties so that decomposition can be focused on creating and validating the CAs that have the most impact on the uncertainties of predicted performance metrics. To better outline the process and provide a test of Hypothesis 1, the baseline UAV selected in Table 5.1 will be decomposed.

5.2.1 Initial Decomposition

The key performance metrics for an ISR UAV are typically endurance and climb rate. Endurance is the key metric while climb rate is an indication of the excess power available to the UAV needed for other flight maneuvers. A simple decomposition of the baseline UAV to enable an initial calculation of endurance and climb rate is shown in Figure 5.2. This decomposition consists of CAs to make aerodynamic, weight, propulsion, and performance calculations.

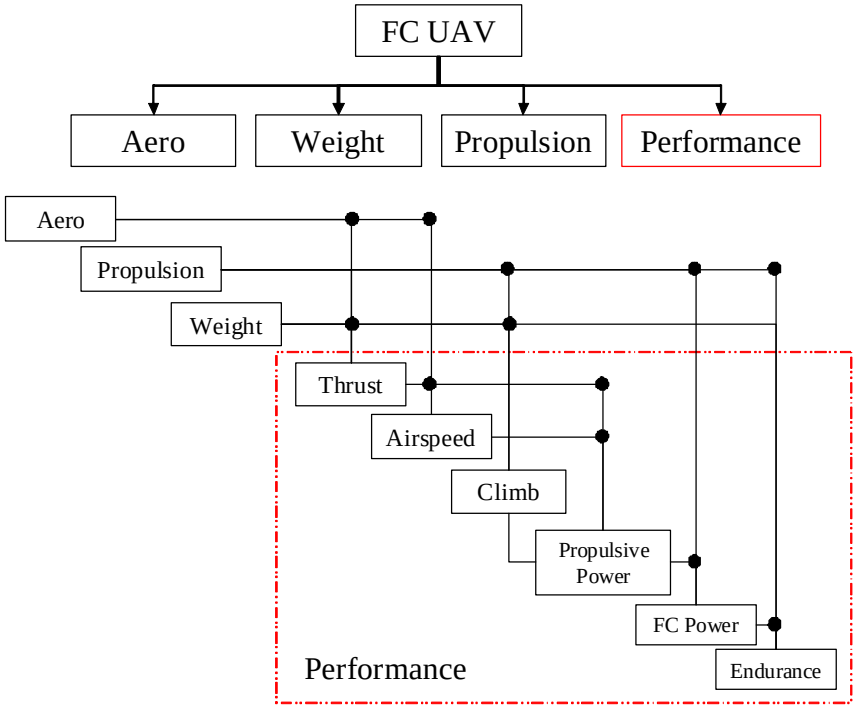

Figure 5.2: Initial decomposition.

The *Aero CA* is assumed to calculate a lift (C_L) and drag coefficient (C_D), the *Weight CA* provides the total aircraft weight (W), while the *Propulsion CA* provides the max fuel cell power (P_{FC}), motor efficiency (η_{mtr}), and propeller efficiency (η_p). These variables can then be fed into Eqs. (5.1) through (5.6) to calculate the endurance (t_E) and climb rate (C_R). Equations (5.1) through (5.6) directly correspond to the 6 individual performance CAs in Figure 5.2. Note that the performance decomposition followed *Design Rule 1* in Chapter 4 so that SSA could be applied to the MDA for uncertainty propagation.

The thrust required (T_{req}) and airspeed (V_∞) are calculated in Eqs. (5.9) and (5.10).

$$T_{req} = \frac{W}{\left(C_L / C_D\right)\cos\alpha + \sin\alpha} \qquad (5.1)$$

$$V_\infty = \sqrt{\frac{2T_{req}\cos\alpha}{\rho S_w C_D}} \qquad (5.2)$$

The climb rate (C_R) is calculated as

$$C_R = \frac{P_{FC}\eta_{mtr}\eta_p - P_{req}}{W}, \qquad (5.3)$$

where the powered required for steady level flight is defined as

$$P_{req} = T_{req}V_\infty. \qquad (5.4)$$

The fuel cell power required for cruise and the endurance can then be calculated respectively in Eqs. (5.5) and (5.6).

$$P_{fc} = \frac{P_{req}}{\eta_{mtr}\eta_p}, \qquad (5.5)$$

$$t_E = \frac{LHV_{H2}\eta_{fc}m_{H2}}{P_{fc}}, \qquad (5.6)$$

Given values provided by the *Aero*, *Propulsion*, and *Weight* CA*s*, Eqs. (5.1) through (5.6) represent a MDA of the UAV. Using estimates from the GT FCUAV as a baseline, input variables and performance metrics were calculated and are presented in Table 5.2.

The next step is to estimate input uncertainties in preparation for an uncertainty propagation analysis. For this analysis, input variables such as the drag coefficient, total weight, efficiencies, and total power are likely uncertain. Estimates for these uncertainties should be conservative estimates based on several factors. Factors that should be considered include technology readiness, experience, the fidelity of analytical tools, and the magnitude of the value in the baseline design. As an example, the baseline

aircraft weight was estimated as 165 N based on the weight of the GT-FCUAV. The original weight analysis for the GT FCUAV over predicted the weight by ~6%. However, many structural aspects of the GT FCUAV were overdesigned and it is expected that the airframe mass could be reduced for the same size aircraft. Therefore, the weight estimate of 165 N with σ = 16.5 N is likely conservative. Without prior experience, literature or other experts could be consulted. For instance, Scaled Composites is reported to historically predict their overall weight within ~7% which is considered to be excellent within the aerospace industry [209]. The remaining uncertainty estimates for the initial decomposed design are given in Table 5.2.

Table 5.2: Variables and uncertainties for initial decomposition.

Input Variable	Value	σ	Calculation	Value
Weight (N)	165	10%	Thrust Required (N)	6.1244
Angle of Attack	0.035	0%	Airspeed (m/s)	14.446
C_L	0.7	0%	Climb Rate (m/min)	83.737
C_D	0.026	20%	Propulsion Power (W)	88.474
Air density (kg/m^3)	1.2	0%	Fuel Cell Power (W)	138.78
S_w (m^2)	1.88	0%	Endurance (hr)	12.009
Prop Efficiency	0.75	10%		
Motor Efficiency	0.85	6%		
Max FC Power (W)	500	10%		
H2 Mass (kg)	0.1	5%		
LHV Hydrogen (J/kg)	1.20E+08	0%		
FC Efficiency	0.5	10%		

With the baseline design and uncertainty estimates in Table 5.2, a sensitivity analysis was performed to relate the propagated uncertainties of the performance metrics to the sources of uncertainty. Using SSA, the total propagated uncertainties due to each source of uncertainty are shown in Figure 5.3.

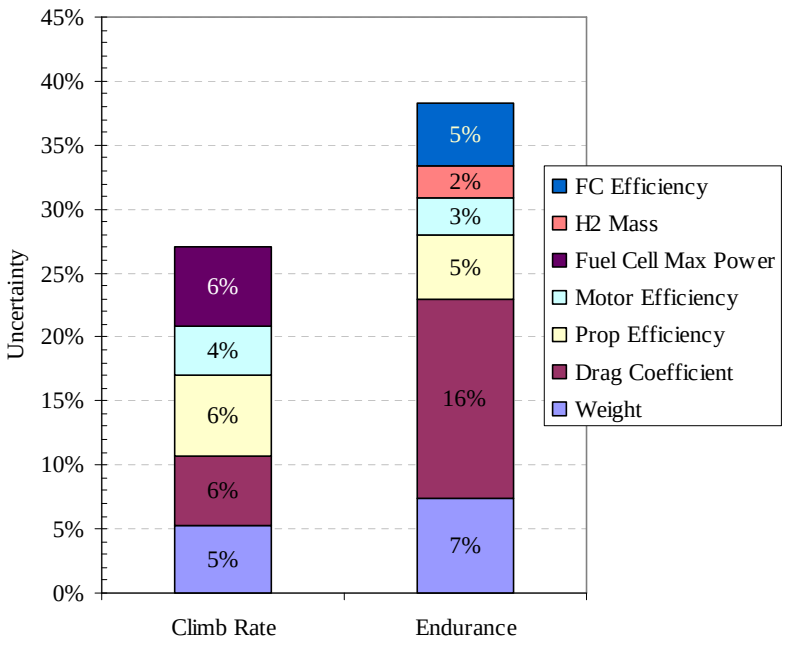

Figure 5.3: Propagated standard deviation of uncertainty for initial decomposition of the baseline vehicle.

The uncertainty propagation shows how the input uncertainties propagate into climb rate and endurance estimates. For the endurance calculation, the drag coefficient is clearly driving the uncertainty. The weight, fuel cell efficiency, and propeller efficiency are also significant contributors. For the climb rate, nearly all of the uncertainty sources have a comparable impact on the propagated uncertainty. Based on Figure 5.3, two initial conclusions can be drawn. The first conclusion is that the motor efficiency is not a primary driver in the uncertainty of both the climb rate and the endurance. Therefore a simple lumped parameter model that allows basic performance predictions is likely adequate. The second conclusion is that uncertainties in drag will dominate endurance and will also have a significant effect on the uncertainty in the climb rate calculation.

At this point, the process in Figure 5.1 asks for a design decision on the current fidelity of the MDA. Depending on the purpose of the MDA and the results of the

uncertainty propagation, the MDA may or may not be good enough to proceed. If the initial MDA decomposition was going to be used in a high level conceptual study, the result may be accurate enough. However, one of the primary objectives of this research is building a MDA that can be validated and the current level of uncertainty is too high to give much confidence in the results of the MDA.

5.2.2 Further Decomposition

Since endurance is typically the dominant metric for a UAV, and the uncertainty in predicting the endurance is rather high, a logical additional decomposition is in terms of the two input uncertainties that have the largest influence on the uncertainty in the endurance estimation. Equation (5.9) decomposes the weight into weight of the fuel cell system, the weight of the hydrogen storage, and the weight of the airframe. This assumes that we would focus more analysis on building a weight model of the fuel cell, hydrogen storage systems, and airframe, rather than just estimating the overall aircraft weight. Similarly, Eq. (5.10) decomposes the drag calculation into drag of the wing and tail, the drag of the fuselage, and miscellaneous drag. The decomposition assumes that a potential flow analysis could be used along with airfoil section data to estimate the drag due to the wing and tail. Similarly, books such as Hoerner [210], Diehl [211], and Roskam [212] provide methods of estimating the drag of various components of an aircraft.

$$W = W_{fc,system} + W_{H2,storage} + W_{airframe} \tag{5.7}$$

$$C_D = C_{Dfuse} + C_{Dwt} + C_{Dmisc} \tag{5.8}$$

Since the design is similar to a sailplane, a drag breakdown from an actual sailplane [213] was used to generate estimates of drag sources in Eq.(5.8). The weight breakdown in Eq. (5.7) was based on the GT FCUAV. Uncertainty estimates were also estimated. The baseline values and uncertainties for this decomposition of the MDA are provided in Table 5.3.

The propagated uncertainties in climb rate and endurance for the MDA relating to the parameters in Table 5.3 is provided in Figure 5.4. For comparison, the uncertainty propagation for the initial decomposition is also provided. The analysis shows the weight and drag decompositions along with the updated uncertainty estimates resulted in a significant overall decrease in the uncertainty associated with endurance. This result is expected since the total drag and total weight will have an overall lower associated uncertainty since uncertainties will add as the square root of a sum of squares. Therefore, if the baseline value and uncertainty estimates in Table 5.3 are reasonable, then decomposing the design into CAs to calculate each of the new variables will dramatically improve the accuracy of the MDA.

Although the uncertainty in the climb rate decreases, the decrease is less pronounced than the decrease in endurance uncertainty. This is expected since both weight and drag uncertainties were shown to have a stronger influence on the uncertainty in endurance. In the case of climb rate, the decrease in uncertainty was mainly due to decomposing the drag. The decomposition in weight actually caused the overall sum of the weight uncertainties to be a higher percentage of the overall climb rate uncertainty than in the initial decomposition. This demonstrates that uncertainty propagation can be non-intuitive and may not always result in expected benefits.

Table 5.3: Variables and uncertainties for a MDA with increased decomposition in drag and weight.

Design Variable	Value	σ	Calculation	Value
Airframe Weight	67.6	8%	Weight (N)	164.99
Fuel Cell System Weight	62.06	12%	C_D	0.026
H2 Storage Weight	35.33	10%	Thrust Required (N)	6.12
C_{Dwt}	0.0195	16%	Airspeed (m/s)	14.45
C_{Dfuse}	0.00338	20%	Climb Rate (m/min)	83.74
C_{Dmisc}	0.00312	50%	Propulsion Power (W)	88.47
Angle of Attack	0.035	0%	Fuel Cell Power (W)	138.77
C_L	0.7	0%	Endurance (hr)	12.01
Air density (kg/m3)	1.2	0%		
S_w (m2)	1.88	0%		
Prop Efficiency	0.75	10%		
Motor Efficiency	0.85	6%		
Max FC Power (W)	500	10%		
H2 Mass (kg)	0.1	5%		
LHV Hydrogen (J/kg)	33.333	0%		
FC Efficiency	0.5	10%		

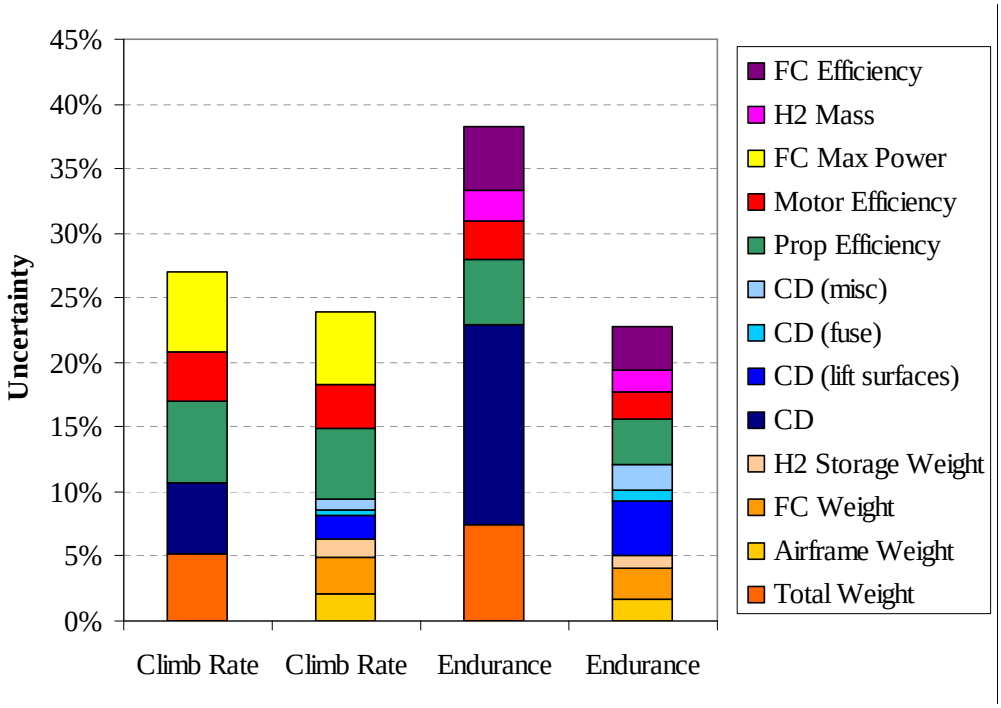

Figure 5.4: Uncertainty propagation for a MDA increased decomposition in weight and drag.

For the level of decomposition and uncertainties specified in Table 5.3, the primary drivers in endurance will be the drag of the lifting surfaces, and propeller efficiency. For the climb rate, propeller efficiency will have the biggest influence on uncertainty followed by the max power of the fuel cell. In addition, making good estimates of weight and properly estimating the fuel cell efficiency will also help decrease the uncertainty in endurance and climb rate.

At this point, it is clear that emphasis should be placed on creating CAs that can make accurate estimates of drag, propeller efficiency, fuel cell power and efficiency, and mass. Before choosing analysis methods, it is useful to understand how making these estimates will be coupled. The estimated interactions for the baseline UAV are shown in Figure 5.5. The remaining decomposition should consider CAs that can capture these interactions. As an example, since motor efficiency for a brushless motor is relatively constant, a motor CA could just assume a constant efficiency. However, the motor interacts directly with the propeller, and although the motor efficiency estimate may be accurate, the motor may provide inadequate torque causing the propeller to operate at reduced efficiency. Therefore, this interaction should be captured in the decomposition.

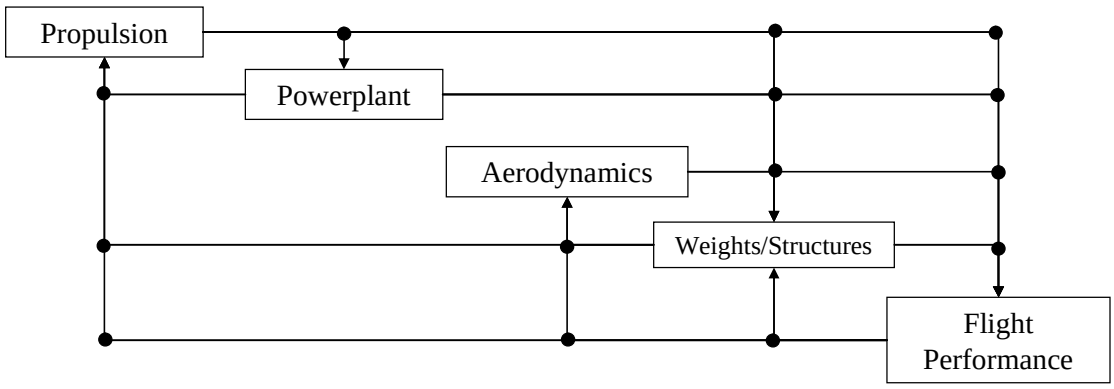

Figure 5.5: Expected interactions for the baseline fuel cell UAV.

The remaining task is to use Figure 5.4 and Figure 5.5 as guidelines in decomposing the design into CAs. In addition, in order to address Hypothesis 1, the CAs need to be able to be validated. This requirement that the CAs be validated will require the CAs be decomposed to a level where they can be compared to data. If data is not available, then experiments or high fidelity analysis may be needed.

The remainder of the chapter covers the development of various CAs for the propulsion, powerplant, weights and volume, and aerodynamics of the baseline UAV. Some background research is provided to help support the selection and development of the CAs. In addition, as required by the tasks addressing Hypothesis 1, validation is provided. Table 5.4 contains a summary of the final decomposition and validation sources.

Table 5.4: Final decomposition into contributing analyses.

Aircraft Subsystem	Contributing Analysis	Analysis Method	Verification and Validation
Propulsion	Electric Motor	Lumped Parameter	MSU Data [214]
	Speed Controller	Assumed Linear	MSU Data [214]
	Propeller	Goldstein Method	Measure Geometry, Perform Section Analysis, Compare Results
Powerplant	Fuel Cell Power	Polarization Curve	Perform Experiment [63]
	H2 Flow Rate	Electrochemistry	Perform Experiment [63]
	BOP	Scale from GT-FCUAV	Perform Experiment [63]
Weights and Volume	Fuel Cell System	Manufacturer Supplied	Perform Experiment [63]
		BCS Design	GT FCUAV
	Hydrogen Storage	Pressure Vessel Analysis	Compare with Product Lists
	Fuselage Volume	Roskam	Not Needed
	Fuselage Mass	Scale from Materials	GT FCUAV
Aerodynamics	Lifting Surfaces	Lifting Line	NACA Tests [215, 216]
	Fuselage	Roskam	Method Based on Experimental Data
	Misc	Roskam, GT-FCUAV	Method Based on Experimental Data
	Propeller Interference	Regression to Data	Method Based on Experimental Data

5.3 Propulsion System

The propulsion system consists of a brushless DC motor, an electronic speed controller (ESC), the fuel cell powerplant, the balance of plant (BOP), and hydrogen storage.

5.3.1 Electric Motor

A brushless DC motor will provide rotational shaft power. These motors represent the current state of the art for small UAVs and outperform conventional permanent DC motors in terms of speed, torque, efficiency, reliability, and lifetime [217, 218]. The electric motor is modeled using a conventional lumped parameter equivalent circuit model of the motor, as shown in Figure 5.6. This model uses a no-load current (I_0), voltage at the no load current measurement (V_0), motor internal resistance per commutating sequence (R_m), and the motor voltage constant (K_v) as constant parameters that define the motor.

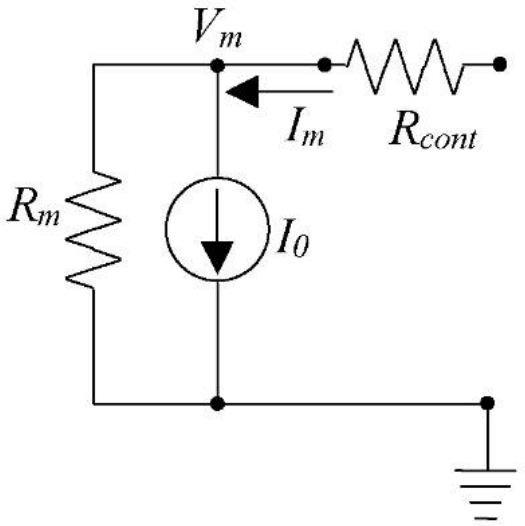

Figure 5.6: Electric motor circuit model.

The motor voltage constant is defined as

$$K_v = \frac{\omega_m}{V_m}, \qquad (5.9)$$

where ω_m is the angular speed of the motor and V_m is the motor voltage. Since $1/K_v$ is effectively a measure of torque per unit current, motor torque can be defined as

$$Q_m = \frac{1}{K_v}\left(I_m - I_0\right), \qquad (5.10)$$

where I_m is the effective motor current. Gearing can be used to change the motor shaft speed and effectively change K_v. Using a gear ratio greater than 1, ($G_R > 1$), reduces the output motor shaft speed such that Eq. (5.10) can be rewritten as

$$Q_m = \frac{G_R}{K_v}\left(I_m - I_0\right). \qquad (5.11)$$

The motor voltage constant is also used to describe the motor shaft speed as a function of the motor voltage, current, and resistance.

$$\omega_m = \frac{K_v}{G_R}\left(E_m - I_m R_m\right) \qquad (5.12)$$

If the voltage corresponding to the no-load current measurement is available, then motor friction and winding losses can be lumped into the drag coefficient (β_0) defined in Eq. (5.13).

$$\beta_0 = \frac{\left(\frac{K_V}{G_R}\right)^2 I_0}{V_0 - I_0 R_m}. \qquad (5.13)$$

Using the drag coefficient in Eq. (5.13), Eq. (5.11) can be rewritten as

$$Q_m = \frac{G_R}{K_v} I_m - \beta_0 \omega_m . \tag{5.14}$$

It should be noted that the motor resistance is defined as per commutating sequence as this is the specification typically provided by motor manufacturers. However, motor resistance can also be specified per winding which would be equal to $R_m/2$ since there are two windings in series for each commutating sequence [214].

Although the model represented by Eq. (5.9), Eq.(5.11) and Eq. (5.12) is idealized and most appropriate for DC brushed motors, it is also a standard method used to describe brushless AC motors commonly used for small UAV applications [108, 219]. Values of the lumped parameters are obtained from several different manufacturers of brushed and brushless DC motors and are available in a large online database[220].

5.3.2 Motor Speed Controller

A brushless DC motor requires an external controller to switch three phases of windings according to the rotor position. Most controllers for small motors determine the position of the rotor based on measuring the required trapezoidal shaped back electromotive forces that are required to produce a constant torque [221]. Lindahl [214] shows that if the controller is considered to be lossless, then the voltage and current at the motor terminals is simply modulated by a duty cycle D_c and is related to the current and voltage provided by the power source as given in Eqs. (5.15) and (5.16).

$$V_m = D_c V_p \tag{5.15}$$

$$I_m = \frac{1}{D_c} I_p \tag{5.16}$$

The subscript *p* given in Eqs. (5.15) and (5.16) stands for propulsion meaning that the voltage and current represent the voltage and current the power source provides for generating a propulsive force on the aircraft. For a simple system with no auxiliary loads then the propulsive current and voltage would be exactly equal to the voltage and current of the power source (fuel cell or battery).

In practice, commercially available brushless motor controllers are only near lossless when the duty cycle is near 1, i.e. full throttle. Based on experience gained from working with small scale battery powered UAVs, Phillips [222] suggests that the motor voltage relationship in Eq. (5.15) should be modified to include an efficiency and resistance term as given in Eq. (5.17).

$$V_m = \eta_{cont} D_c V_p - I_m R_{cont} \tag{5.17}$$

Although many manufacturers of commercially available speed controllers will provide resistance values for their controllers (R_{cont}), measuring the controller efficiency (η_{cont}) is often involved and difficult due to the AC power output of the controller. The setup and rigor required to measure controller efficiency is provided in reference [223]. For simplicity, it was assumed that the efficiency increases linearly with increasing duty cycle according to

$$\eta_{cont} = 1 - k_{loss}\left(1 - D_c\right), \tag{5.18}$$

where k_{loss} determines how rapidly the efficiency decreases as the duty cycle decreases.

5.3.2.1 Motor and Speed Controller Validation

To validate the motor models, experimental test data available in Lindahl [214] was used. This experimental data was collected using four different outrunner electric motors built by AXI [224] combined with a modified Jeti speed controller. To calculate motor torque as a function of motor shaft speed, three different sets of measurements could be used as inputs, I_p and ω_m, V_p and ω_m, and D_c and I_p. However, it was not initially clear which inputs were best suited for the model. All three sets of possible inputs were therefore used. The motor and speed controller model ($k_{loss} = 0$, $R_{cont} = 0$) using the different possible measurements as inputs yields Figure 5.7.

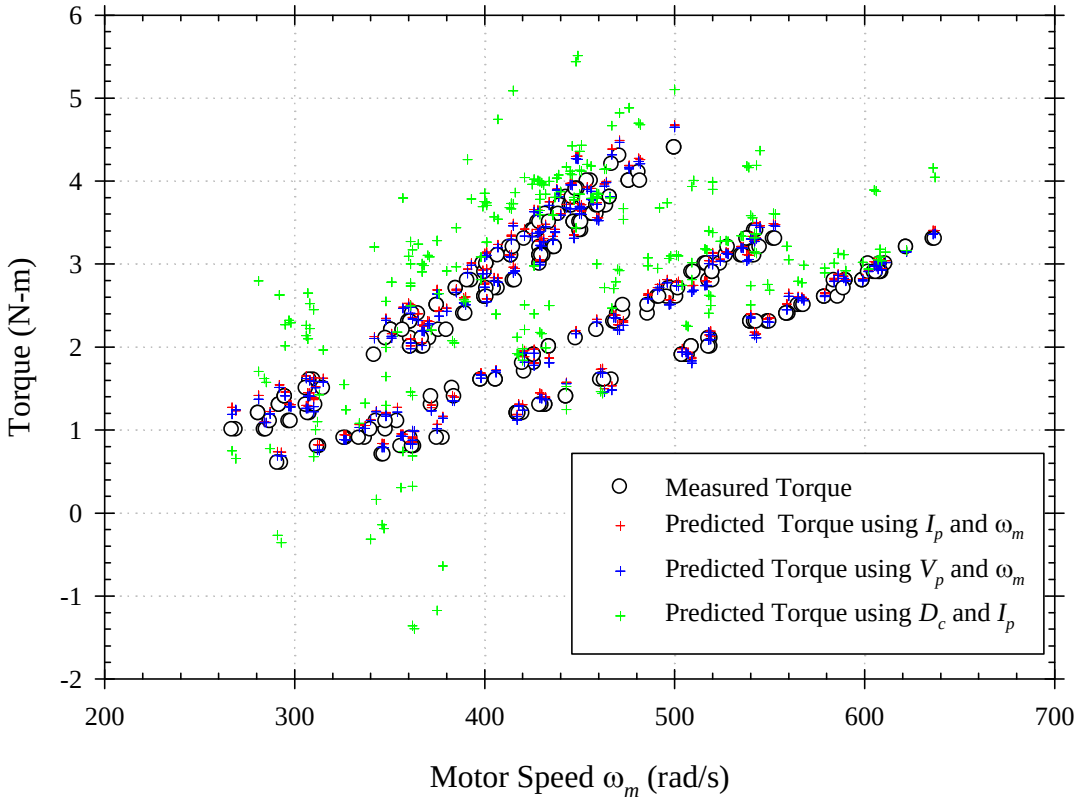

Figure 5.7: Comparison of motor torque vs. shaft speed for various experimental measurements used with the predictive motor model.

Figure 5.7 shows the predicted motor torque using various experimentally measured input values for four different motors. Using either I_p and ω_m or V_p and ω_m results in motor torque predictions that are in agreement with the experimentally measured motor torque. However, using D_c and I_p follows the general trend but yields motor torque predictions that have much greater variability and occasionally produces negative torque predictions. This is somewhat expected as experimentally measuring DC voltage and current values is more straightforward than estimating the duty cycle.

Using V_p and ω_m as inputs, the effect of speed controller losses were estimated by using a non-linear least squares regression to estimate k_{loss} and R_{cont}. The optimum value of k_{loss} was 0.0768 and R_{cont} was 0. Figure 5.8 shows the predicted and actual torque values assuming a lossless speed controller as well as optimally determined values. For the AXI motor test data, there was only a slight improvement by estimating the speed controller losses. It should also be noted that the calculated value of k_{loss} = 0.0768 is in excellent agreement with the value of 0.078 suggested by Phillips [222] based on experience gained throughout several battery powered aircraft designs [207, 208, 225].

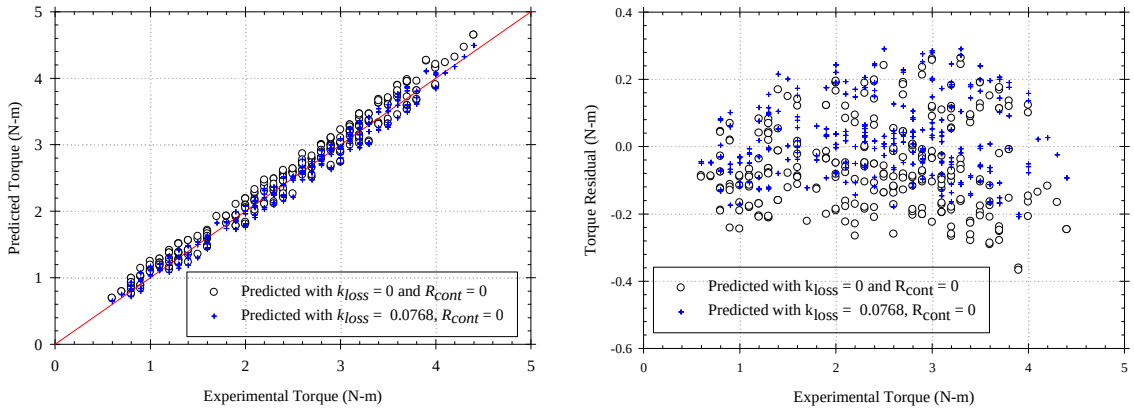

Figure 5.8: Motor model validation with varying speed controller constants.

The AXI motors in the test data set were all outrunner type electric motors with no gear reduction. To allow the motor to operate with large diameter propellers, the model would also need to estimate motor performance with inrunner type motors with gearing. Data collected during the development of the GT FCUAV using a Hacker C50-13XL motor with a 6.7:1 gear reduction and a Jeti 77-O-flight speed controller yielded a much higher estimate of speed controller losses with k_{loss} =0.36517 and R_{cont} = 0.074 Ω. Using these speed controller parameters, the motor model was compared with data collected from a NEU 1910/2Y electric motor with a 6.7:1 gear reduction using a Jeti 77-O-flight speed controller (see Figure 5.9).

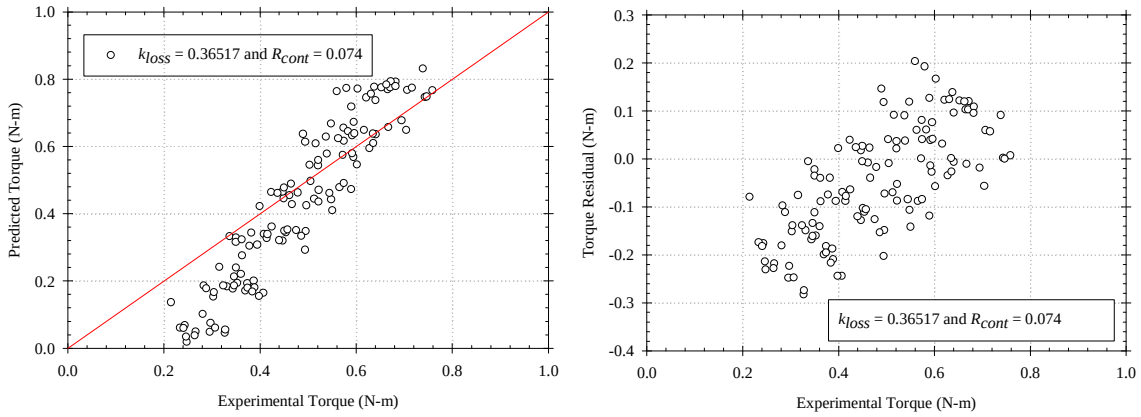

Figure 5.9: Motor model validation for NEU 1910/2Y motor with 6.7:1 gear reduction.

Experimental tests of the NEU 1910/2Y showed less agreement with the model as compared to the AXI motor tests. Model agreement was primarily lacking at low torque values. However, at the mid to high torque values expected during operation, the model provided better results. Based on the trend in Figure 5.9, there is some underlying behavior with the inrunner type motor that is not being captured by the model. This behavior is likely a complex combination of uncertainties in the speed controller

performance, the gear box, the motor constants provided by the manufacturer, and uncertainties in the experimental measurements. Regardless of this behavior, the motor is approximating the correct behavior and is well within the correct order of magnitude of the experimentally measured torque, especially in the higher torque areas where the motor is expected to operate in flight conditions.

5.3.3 Propeller

As shown in Figure 5.4, propeller performance can have a paramount influence on overall flight performance. UAV scaled propellers are typically designed specifically for the small market of hobby enthusiasts, and as a result are designed for low cost manufacturing. Low Reynolds numbers at the propulsion system and lifting surfaces (due to low speeds and small scales), large scaled surface roughness (due to the small scales and the use of materials such as composites and wood), and inconsistencies in manufacturing can lead to large variances in performance. A recent experimental study of several UAV scale propellers showed that similar propellers from different manufacturers could vary in peak efficiency by over 20% [226]. With a fuel cell providing limited specific power to a propulsion system, large variability in propeller performance would likely not be tolerable. In order to capture the effects of the propeller on the propulsions system and overall UAV, it was necessary to develop a parametric, scalable, physics-based propeller model of the propeller.

Although propeller performance has been studied for over a century, relatively few conceptual level methods are available to predict performance. Most engineering textbooks give a brief discussion on propeller momentum theory which uses simplifying assumptions to generate a 1-D flow solution that results in a theoretical limit in

performance. Phillips [227] documents the limitations of momentum theory and states that it is not recommended for design applications. The classical and most widely used technique is the vortex theory of screw propellers. Vortex theory was initially formulated by Betz [228] and Prandtl [229] although much of the solution is due to work of Goldstein [230] with a slight modification by Theodorsen [231]. Vortex theory provides a relatively direct and efficient method to derive the performance of propellers [165, 170-172] and wind turbines [232, 233], although the predictive performance of some implementations is not always acceptable, repeatable, or robust. Some modern applications of vortex theory have been demonstrated where researchers have used various methods to numerically estimate the effects of the flowfield [234, 235]. Beyond vortex theory, some efforts have been made to apply Euler and Navier-Stokes computational fluid dynamics (CFD) tools to propeller and wind turbines [236].

Since momentum theory is limited for design applications, and more recent attempts to numerically model the flowfield using both potential flow and Navier-Stokes CFD techniques are prohibitive for early design based on computational and setup costs, vortex theory was the obvious computational method of choice. Since varied derivations of the method exist in the literature, a short derivation is provided. The method and nomenclature are based on work published by Phillips [227] and Wald [237].

The vortex theory of screw propellers is based on a lifting line approximation of the blades of the propeller. This implies that the propeller is approximated by a lifting surface about which there is bound circulation. The total circulation is associated both with vorticity bound to the propeller and with the free vorticity that is continuously shed from the propeller in the form of a helical sheet [230]. The input to the vortex theory is

an aerodynamic model of the propeller section performance. The aerodynamic pitch angle (β) is defined as the angle which the propeller zero-lift line makes to direction of flight. This angle is a function of the position along the propeller (r), the zero lift angle of attack (α_{L0}), and the geometric pitch angle (β_c) which is the angle measured from the propeller chord line to plane of rotation.

$$\beta(r) = \beta_c(r) - \alpha_{L0}(r) \tag{5.19}$$

Similarly, the blade angle of attack (α_b) is defined as the angle between the velocity incident on the propeller blade (V_b) and the zero-lift line of the airfoil blade section.

$$\alpha_b(r) = \beta(r) - \varepsilon_b(r) = \beta(r) - \varepsilon_\infty(r) - \varepsilon_i(r) \tag{5.20}$$

The induced angle ε_i and advance angle ε_∞ are defined in Figure 5.10.

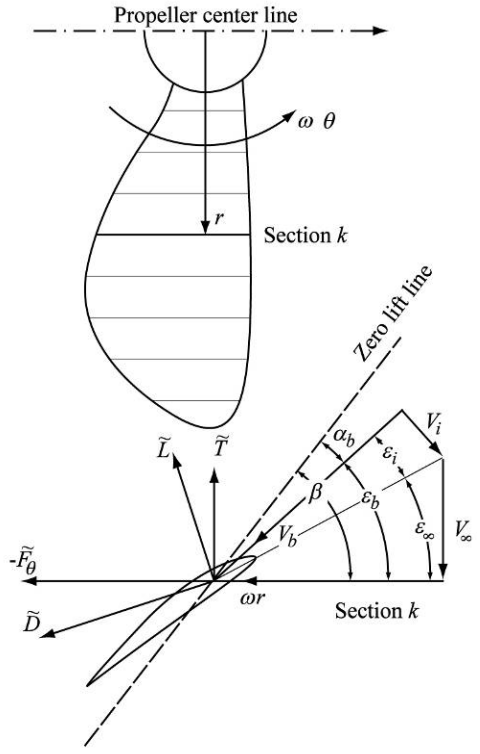

Figure 5.10: Geometry and angle definitions for propeller vortex theory.

Within the propeller circle, the velocity incident on the propeller blade (V_b) contains components of the freestream velocity (V_∞), the induced velocity (V_{xi} in the x direction and $V_{\theta i}$ in the θ direction) and the rotational velocity (ωr) such that:

$$V_b^{\,2} = \left(\omega r - V_{\theta i}\right)^2 + \left(V_\infty + V_{xi}\right)^2 = \omega^2 r^2 \left[\left(1 - \frac{V_{\theta i}}{\omega r}\right)^2 + \left(\frac{V_\infty}{\omega r} + \frac{V_{xi}}{\omega r}\right)^2\right]. \tag{5.21}$$

The propeller section lift and drag forces are defined in terms of the velocity at the propeller blade.

$$\tilde{L} = \frac{1}{2}\rho V_b^{\,2} c_b \tilde{C}_L \tag{5.22}$$

$$\tilde{D} = \frac{1}{2}\rho V_b^{\,2} c_b \tilde{C}_D \tag{5.23}$$

The propeller section differential thrust ($dT/dr = k_{blades}\tilde{T}$) and the differential torque ($dQ/dr = k_{blades} r\tilde{F}_\theta$) can be defined for a number of propeller blades (k_{blades}) in terms of the angle that the velocity incident on the propeller blade makes with the radial axis of the propeller (ε_b). Combining Eqs. (5.21) through (5.23) yields Eqs. (5.24) and (5.25).

$$\frac{dT}{dr} = \frac{k_{blades}}{2}\rho\omega^2 r^2 c_b \left[\left(1 - \frac{V_{\theta i}}{\omega r}\right)^2 + \left(\frac{V_\infty}{\omega r} + \frac{V_{xi}}{\omega r}\right)^2\right]\left(\tilde{C}_L \cos\varepsilon_b - \tilde{C}_D \sin\varepsilon_b\right), \tag{5.24}$$

$$\frac{dQ}{dr} = \frac{k_{blades}}{2}\rho\omega^2 r^3 c_b \left[\left(1 - \frac{V_{\theta i}}{\omega r}\right)^2 + \left(\frac{V_\infty}{\omega r} + \frac{V_{xi}}{\omega r}\right)^2\right]\left(\tilde{C}_D \cos\varepsilon_b + \tilde{C}_L \sin\varepsilon_b\right) \tag{5.25}$$

In order to integrate Eqs. (5.24) and (5.25) to obtain the total propeller torque (Q) and thrust (T), ε_b must be known. The Kutta-Joukowski theorem as stated in Eq. (5.26)

$$\tilde{L} = \Gamma \rho V_b \tag{5.26}$$

provides the additional relationship needed to solve for ε_b by relating the net resulting velocity vector (V_b) to the local section circulation, Γ. In order to solve for Γ, the flowfield must defined. Betz showed that a propeller with minimum energy loss would result in a trailing vortex sheet that lies along a helical surface of constant pitch with the induced velocity normal to the resultant velocity [229]. By defining V_b normal to V_i and using Figure 5.10, the relationship between the velocities (V_b V_∞ V_{xi} and $V_{\theta i}$) are defined.

$$V_b = \sqrt{\omega^2 r^2 + V_\infty{}^2}\cos\varepsilon_i = \frac{\omega r}{\cos\varepsilon_\infty}\cos\varepsilon_i \tag{5.27}$$

$$V_i = \sqrt{\omega^2 r^2 + V_\infty{}^2}\sin\varepsilon_i = \frac{\omega r}{\cos\varepsilon_\infty}\sin\varepsilon_i \tag{5.28}$$

$$V_{\theta i} = V_i \sin(\varepsilon_i + \varepsilon_\infty) \tag{5.29}$$

$$V_{xi} = V_i \cos(\varepsilon_i + \varepsilon_\infty) \tag{5.30}$$

To solve for Γ using the Betz conditions for minimum energy loss, Goldstein [230] defined the relationship between the local circumferential component of induced velocity in the plane of the propeller disk and the local section circulation via Eq. (5.31).

$$k_{blades}\Gamma = 4\pi\kappa r V_{\theta i} \tag{5.31}$$

To solve for the proportionality constant (κ), Goldstein found an exact solution to the resulting potential flow problem by expressing the circulation function as a function of multiple infinite series. Despite Goldstein's success, calculating κ still poses a difficult numerical problem. An alternative is to use a 2-D simplification proposed by Prandtl that

results in a tip loss factor f defined in Eq. (5.32) where β_t is the aerodynamic pitch angle at the propeller blade tip.

$$f = \frac{2}{\pi}\cos^{-1}\left\{\exp\left[-\frac{k_{blades}\left(1-2r/d_p\right)}{2\sin\beta_t}\right]\right\} \tag{5.32}$$

Using Eq. (5.32), Eq. (5.31) can be approximated as

$$k_{blades}\Gamma \cong 4\pi f r V_{\theta i} \tag{5.33}$$

Equations (5.21), (5.22), (5.26), (5.29), (5.30), (5.32), and (5.33) form a set of equations that can be solved to determine the induced angle of attack ε_i which uniquely defines the differential thrust (dT/dr) and differential torque (dQ/dr) of each propeller section. The thrust and torque on the propeller can be calculated by integrating the differential quantities from the hub diameter to the tip diameter using Eqs. (5.24 -5.25).

$$T = \int_{r_{hub}}^{r_{tip}} \frac{dT}{dr} dr \tag{5.34}$$

$$Q = \int_{r_{hub}}^{r_{tip}} \frac{dQ}{dr} dr \tag{5.35}$$

The formulation presented thus far is based on the Betz and Goldstein assumption of a lightly loaded propeller. However, as posed by Theodorsen [231], the lightly loaded assumption can be removed by making the circulation function only dependent on the configuration of the helicoidal sheets at a distance far behind the propeller (designated using the subscript *hv*). Using this assumption, the Goldstein circulation function can be defined as

$$G(r_{hv}) = \frac{\Gamma(r_{hv})}{hw} \tag{5.36}$$

where h is axial distance between adjacent turns of the vortex sheets and w is the axial displacement velocity of the helical vortex sheets far behind the propeller. By calculating the value of h, Eq. (5.36) can be written as

$$G(r_{hv}) = \frac{k_{blades}\omega\Gamma(r_{hv})}{2\pi w(V_\infty + w)} \tag{5.37}$$

Solving for the circulation function is not trivial. Rather than attempting Goldstein's solution, Theodorsen resorted to the use of a rheoelectrical analog. Fortunately, accurate tabulated values of the Goldstein circulation function became available through the work of Tibery and Wrench [238]. More recently, Ribner and Foster [235] provided a solution by representing the trailing sheets by sets of discrete helical vortex filaments. Similarly, Okulov et al. [234, 239] have proposed a solution by superposing the solution from a series of vortices emanating from the full span of the propeller blades and shown that their method is in agreement with the tabulated values of Tibery and Wrench.

With the circulation function known, the general solution procedure is to find the axial displacement velocity of the helical vortex sheet far behind the propeller such that the induced velocity and local section lift is consistent with the circulation corresponding to w. This is accomplished by combining Eq. (5.26) and Eq. (5.37) and rearranging to form Eq. (5.38).

$$k_{blades}c_b\tilde{C}_L = \frac{4\pi w(V_\infty + w)G(r_{hv})}{\omega V_b} \tag{5.38}$$

In order to solve Eq. (25) for *w*, the induced velocities at the plane of the propeller need to be related to the induced velocity at the corresponding point on the helicoidal vortex sheet far behind the propeller (λ_{hv}). To do this, it is useful to define the angular pitch of the helicoidal vortex sheet

$$\tan \varepsilon_{b,hv} = \frac{(V_\infty + w)}{\omega r_{hv}} = \frac{\lambda_{hv}}{\zeta_{hv}}, \tag{5.39}$$

where $\zeta_{hv} = r_{hv}/(d_{hv}/2)$. The induced velocities at the helicoidal vortex sheet far behind the propeller are given in Eq. (5.40) and (5.41).

$$V_{xi,hv} = w/\left(1 + \lambda_{hv}^{\ 2} / \zeta_{hv}^{\ 2}\right) \tag{5.40}$$

$$V_{\theta i,hv} = w\left(\lambda_{hv} / \zeta_{hv}\right)/\left(1 + \lambda_{hv}^{\ 2} / \zeta_{hv}^{\ 2}\right) \tag{5.41}$$

As shown by Wald [237], the induced velocities at the propeller plane tend to be half the induced velocity at the corresponding point on the helicoidal vortex sheet far behind the propeller resulting in the following velocity relationships.

$$V_{xi} = \frac{1}{2} w \Big/ \left(1 + \lambda_{hv}^{\ 2} / \zeta_{hv}^{\ 2}\right) \tag{5.42}$$

$$V_{\theta i} = \frac{1}{2} w(V_\infty + w)(1/\omega r) \Big/ \left(1 + \lambda_{hv}^{\ 2} / \zeta_{hv}^{\ 2}\right) \tag{5.43}$$

Finally, the radii of the propeller and the vortex sheet are related by Eqs. (5.44-5.45).

$$(r/R)^2 = (r_h/R)^2 + (r_{hv}/R_{hv})^2 \left\{1 - (r_h/R)^2\right\} \tag{5.44}$$

$$(R/R_{hv})^2 = 1/\left\{1 - (r_h/R)^2\right\} \tag{5.45}$$

In these equations, r_h is the radius of the propeller hub, R is the outer propeller radius, and R_{hv} is the outer radius of the helicoidal vortex sheet far behind the propeller.

Propeller performance can be solved using either Eq. (5.33) or Eq. (5.37). Prandtl's solution in Eq. (5.33) is much more tractable as it provides a closed form solution whereas using the Goldstein formulation requires either using tabulated data or the numerically intensive task of calculating the circulation function. The propeller performance including efficiency, thrust, torque, and power are often presented in non-dimensional form using the relations in Eqs. (5.46-5.49). Propeller advance ratio (J) is defined in Eq. (5.50).

$$\eta_p = \frac{TV_\infty}{Q\omega} \tag{5.46}$$

$$C_T = \frac{T}{\rho\left(\frac{\omega}{2\pi}\right)^2 d_p{}^4} \tag{5.47}$$

$$C_Q = \frac{Q}{\rho\left(\frac{\omega}{2\pi}\right)^2 d_p{}^5} \tag{5.48}$$

$$C_P = \frac{Q\omega}{\rho\left(\frac{\omega}{2\pi}\right)^3 d_p{}^5} \tag{5.49}$$

$$J = \frac{V_\infty}{\left(\frac{\omega}{2\pi}\right) d_p} \tag{5.50}$$

In order to predict propeller performance, the geometry of the propeller must be known. The baseline propeller geometry chosen was the APC thin electric [240]. APC thin electric propellers have high efficiency [226] and are available in various diameters and pitch lengths. The APC thin electric propellers are also easily scaled since pitch is nearly constant along the blade of the propeller (see baseline APC 16x12E in Figure 5.14).

To make the propeller scalable over different pitches, the geometric pitch length distribution of the propeller was scaled by multiplying the values that make up the linear pitch/diameter curve shown (see Figure 5.14) by a constant. By varying the linear pitch over diameter ratio (K_c), the thrust, power, and efficiency curves are shown respectively in Figure 5.11, Figure 5.12, and Figure 5.13.

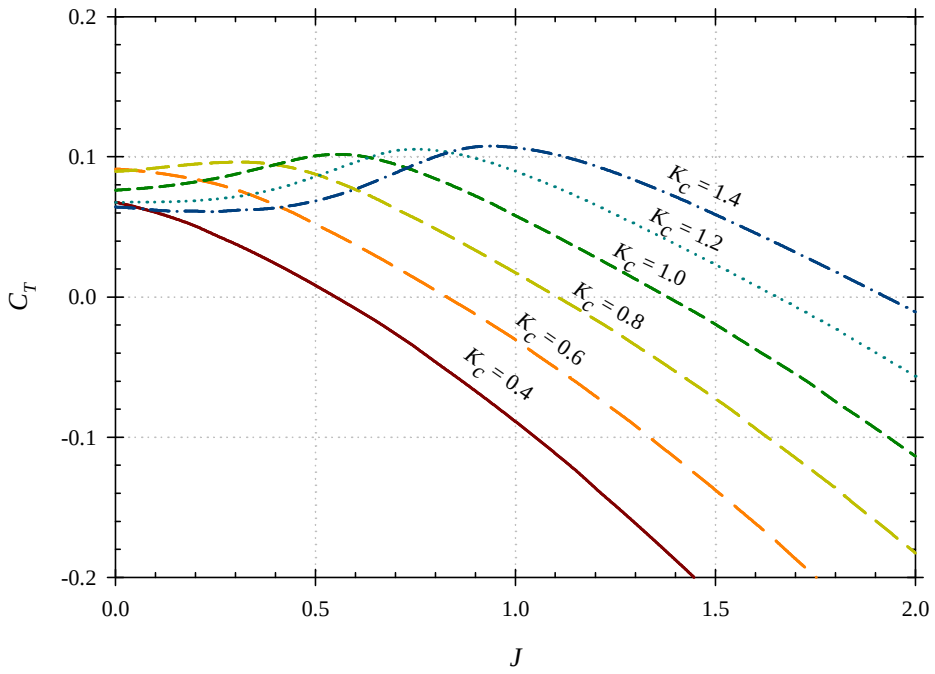

Figure 5.11: Thrust coefficients as a function of linear pitch for APC propeller model.

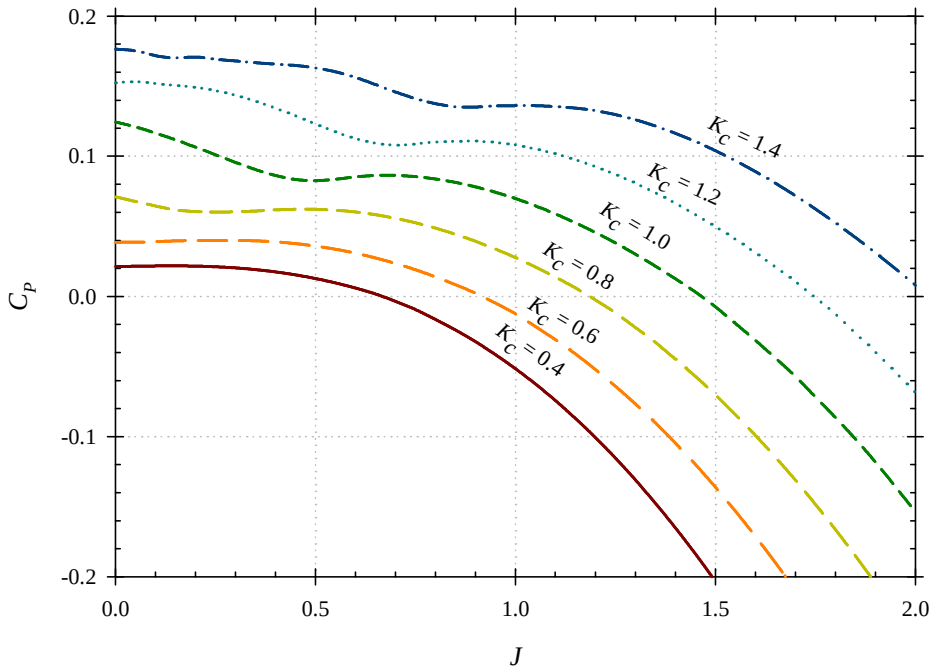

Figure 5.12: Power coefficients as a function of linear pitch for APC propeller model.

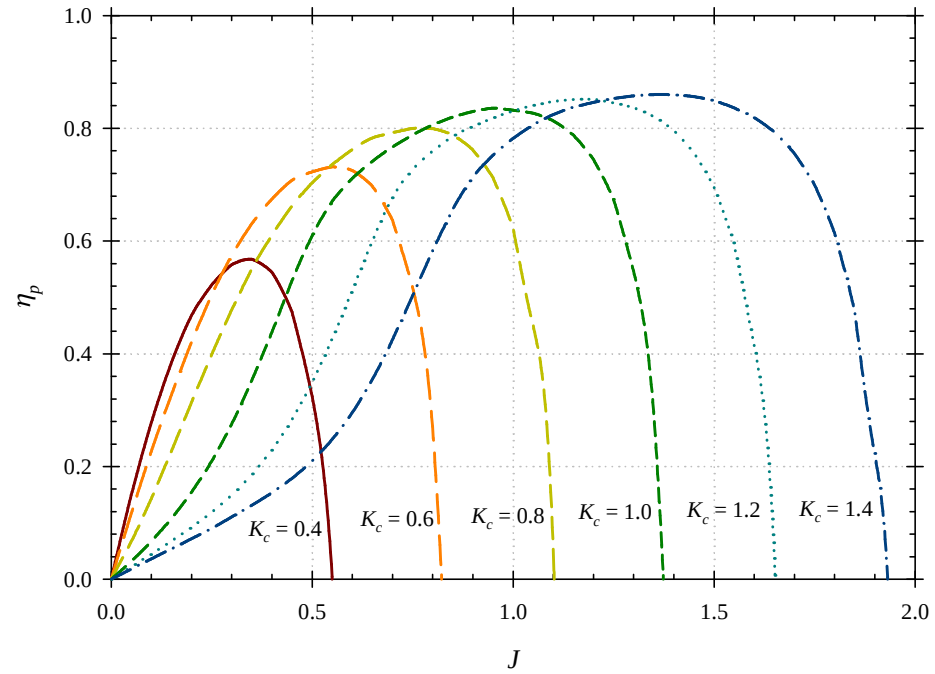

Figure 5.13: Efficiencies as a function of linear pitch for APC propeller model.

5.3.3.1 Propeller Validation

A validation study was conducted by comparing predicted performance to test data from wind tunnel testing. Wind tunnel testing was performed by Wichita State University using a facility described in Reference [226]. Table 5.5 lists the propellers that were modeled and wind tunnel tested for this study.

Table 5.5: List of UAV-scale propellers used for validation.

Manufacturer	Model	Measured Diameter (cm)	Measured Pitch Length at $\zeta = 0.75$ (cm)	Construction
Landing Products Inc.	APC 16x12E	40.6	33.2	Molded Glass Reinforced Plastic
Air Velocity Pty. Ltd.	Bolly 22x20	55.8	53.6	Molded Carbon Fiber Composite
J & Z Products Inc.	Zinger 16x6	40.6	17.1	Machined Wood

To build models of each propeller, the propeller geometry was accurately measured using techniques described by Moffitt and Bradley [241]. The pitch distributions for each propeller are provided in Figure 5.14 through Figure 5.16. Each propeller has a drastically different geometric pitch distribution. The APC 16x12E propeller has a nearly constant geometric pitch length/diameter ratio whereas both the Bolly and Zinger propellers have geometric pitch lengths that increase with increasing radial distance to a max and then decrease toward the tip of the propeller blade. Each propeller manufacturer uses its own definition with regard to reporting the propeller's geometric pitch length. For the APC propeller, the pitch length is virtually constant over span of the blade and the very close to the value specified by the manufacturer. For the Bolly propeller, the reported geometric pitch length represents a maximum that occurs near $r/R = 0.80$. For the Zinger propeller, the measured geometric pitch length is much

lower than the reported value and provides little data in estimating how Zinger defines or calculates its reported pitch length.

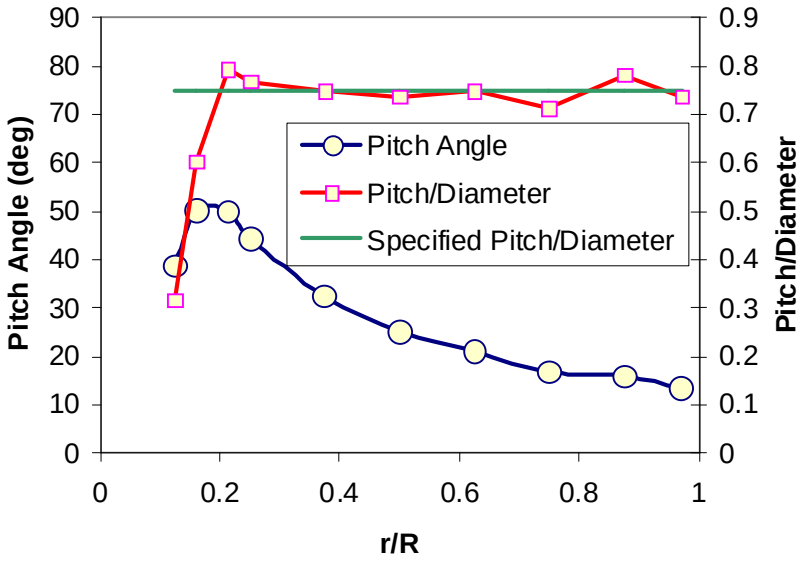

Figure 5.14: Measured pitch distribution for the APC 16x12E propeller.

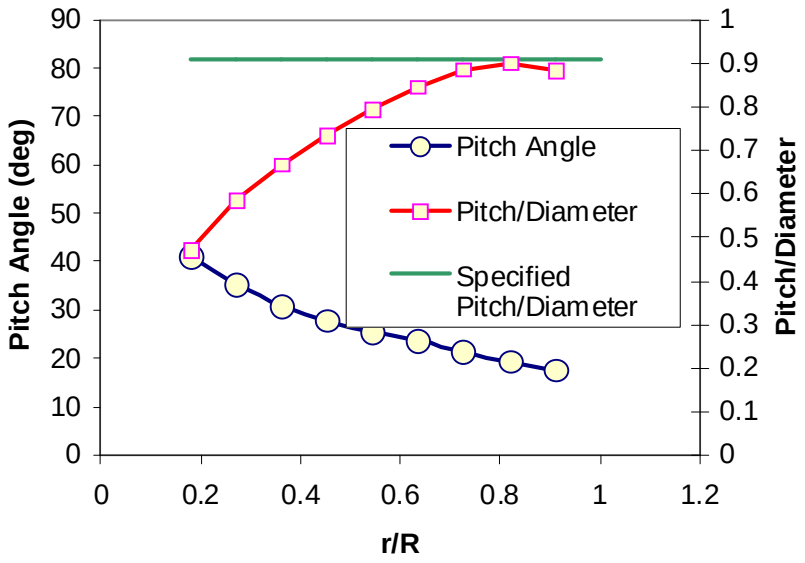

Figure 5.15: Measured pitch distribution for the Bolly 22x20 propeller.

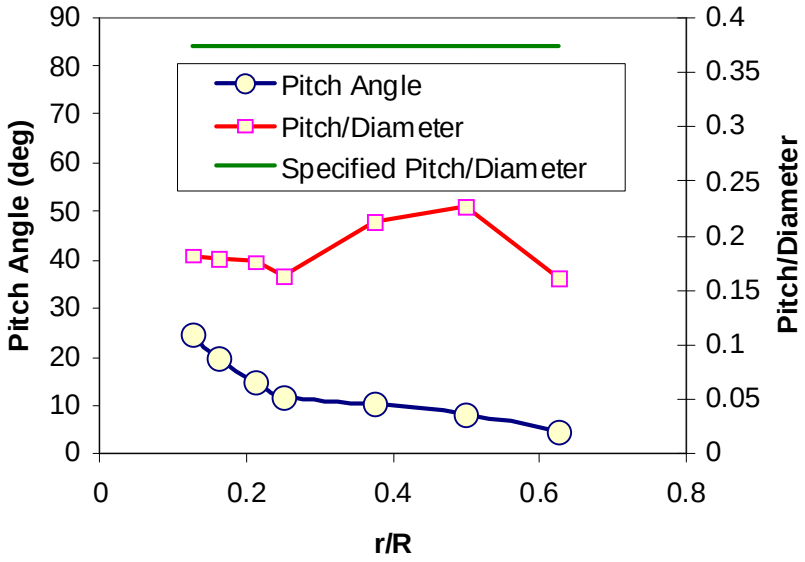

Figure 5.16: Measured pitch distribution for the Zinger 16x6 propeller.

In addition to measuring the geometric pitch of each airfoil, the airfoil geometry was also measured and used in the XFOIL [242] software to estimate the airfoil section lift and drag coefficients as a function of angle of attack. For post stall behavior at both negative and positive angles of attack, data and correlations provided by Sandia National Laboratories [243] were used. Predictions of the thrust coefficient, power coefficient, and efficiency for each propeller in Table 2.1 are provided in Figure 5.17, Figure 5.18, and Figure 5.19.

For all three propellers, the predicted and experimental results are in good agreement at high advance ratios. At low advance ratios, especially for the Bolly 22x20 propeller, (see Figure 5.18) the vortex theory over predicts both the thrust and power coefficients. This over prediction is largely due to post stall effects that occur near the hub at low advance ratios that cannot be accurately captured by the method since only 2-D section airfoil data is used and 3-D effects are entirely based on the Betz

approximation of the flowfield. These effects are more pronounced in the Bolly 22x20 propeller since it has the highest measured pitch length and will thus have a larger portion of the propeller in the stalled region at low advance ratios. Except for a relatively short time at takeoff, the propeller will not be operated at low advance ratios and thus will be significantly affected by behavior in the stalled region.

Both the Goldstein and Prandtl correlations for the section circulation are given in Figure 5.17, Figure 5.18, and Figure 5.19. In almost all instances, the results are virtually identical with the exception that the Goldstein predictions cannot be made at low advance ratios since the tabulated data from Tibery and Wrench [238] used for the analysis is limited and extrapolation of the data was not allowed in any of the calculations. The only noticeable variations occurred at lower advance ratios where the propeller would not be expected to operate for a significant amount of time.

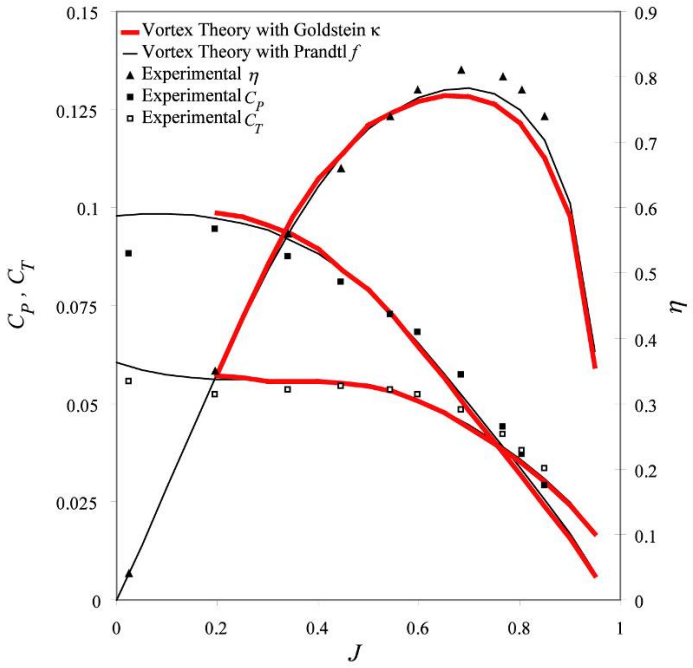

Figure 5.17: Predicted and experimental results for APC 16x12 propeller.

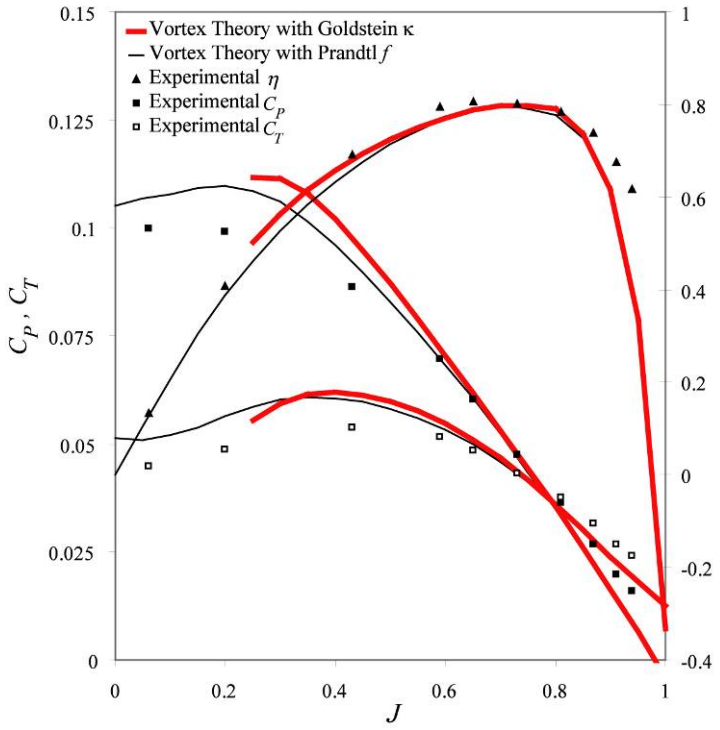

Figure 5.18: Predicted and experimental results for Bolly 22x20 propeller.

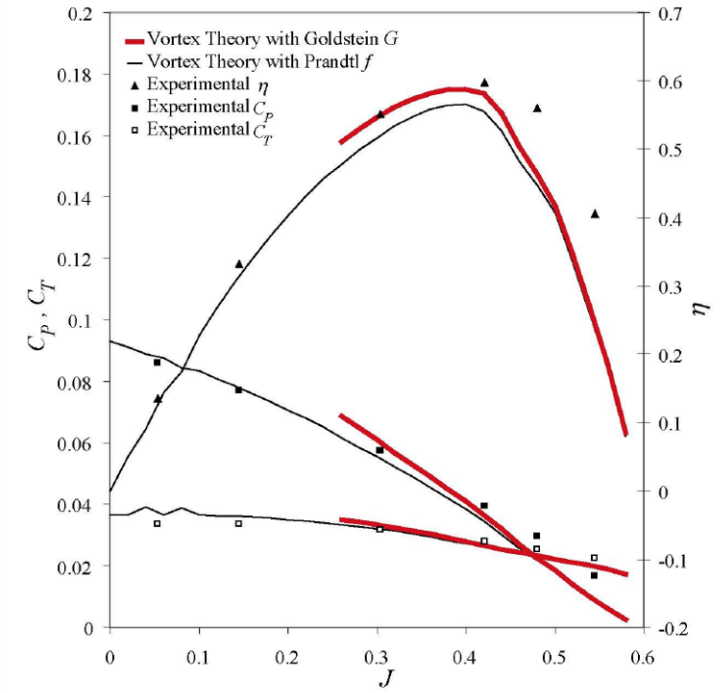

Figure 5.19: Predicted and experimental results for the Zinger 16x6 propeller.

Overall, vortex theory provided good results for all three propellers tested despite the fact that the propellers were of different sizes, geometries, and made of different materials. Since the Prandtl solution provided results at all advance ratios, was in excellent correlation with the Goldstein solution, and was much faster for the computer to execute versus the tabulated Goldstein data, the Prandtl solution was deemed most appropriate for the scope of the research.

5.3.3.2 Propeller Fuselage Interaction

To estimate how the propeller would perform when installed on either a fuselage or wing, interaction effects need to be accounted for. Although the interaction between a propeller and another aerodynamic body is very complicated, it is possible to develop simplified corrections. Wald [237] derives a relationship to account for interference between a propeller and a nacelle based on using a potential flow point source to represent the nacelle and then derives a relationship for interference in velocity caused by the point source. Wald also shows how performance can be estimated for a propeller that is operating in a wake. Experimentally, Boeing developed relationships for the B-17 Flying Fortress that calculated interference based on the propeller's geometry, engine power, and airspeed [244]. Based on the Boeing approach, Lowry [245] has used general aviation propeller data to estimate a slow down efficiency factor for both pusher and tractor propeller aircraft configurations. Although derived for general aviation aircraft, Lowry's data provides a simply correlation to adjust for efficiency effects due to interference. However, Lowry's data predicts efficiency factors above 1 when the fuselage diameter is very small compared to the propeller diameter since he was using antiquated data already included other corrections (see Figure 5.20).

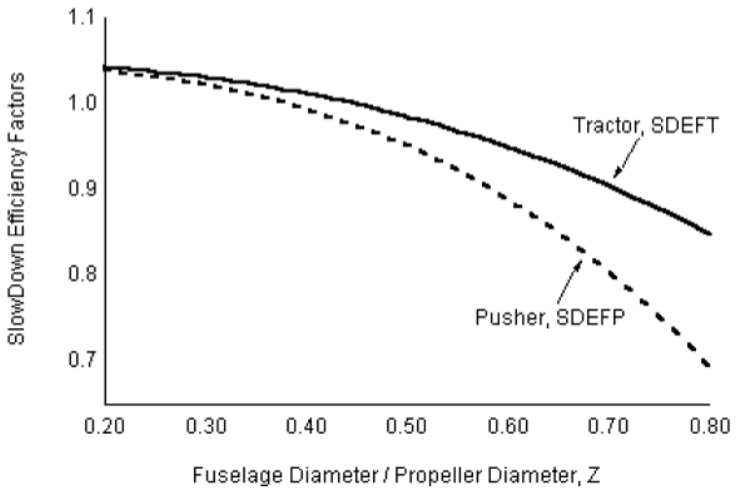

Figure 5.20: Propeller slow down efficiency factors due to interference effects.

To correct Lowry's data for use in this research, the curves in Figure 5.20 were shifted so that the slow down efficiency factor would go to unity when the fuselage diameter goes to zero. The corrected relationships for both pusher and tractor propellers are given respectively in Eqs. (5.51) and (5.52) where Z is the fuselage/propeller diameter ratio. Once the slow down efficiency factor is calculated, then the installed thrust coefficient can simply be calculated as the product of the ideal thrust coefficient and the slow down efficiency factor ($C_{T,installed} = C_T \ \eta_{SD}$).

$$\eta_{SDP} = 1 - 0.04185Z - 0.01481Z^2 - 0.62001Z^3 \tag{5.51}$$

$$\eta_{SDT} = 1 - 0.00722Z - 0.16462Z^2 - 0.18341Z^3 \tag{5.52}$$

5.3.4 Fuel Cell Analysis

The fuel cell model was based on work performed by Bradley [63]. The model is based upon polarization data at the individual cell level. The mathematical model is based on [246] which states that the voltage at the cell level (V_{cell}) is related to the cell area specific current (j) by Eq. (5.53)

$$V_{cell} = E_0 - V_\eta - R_{cell}\, j \tag{5.53}$$

The electrochemical potential term (V_η) is calculated as

$$\frac{V_\eta}{b} = \phi\left(\frac{f_\lambda\, j}{j_*}\right)\ln\left(\frac{f_\lambda\, j}{j_*}\right) - \ln k_0 - \ln\left(1 - \frac{f_\lambda\, j}{j_{D0}}\right) \tag{5.54}$$

where

$$f_\lambda = -\lambda \ln\left(1 - \frac{1}{\lambda}\right). \tag{5.55}$$

The quantities b, E_0, R_{cell}, k_0, and j_{D0} are all determined through a non-linear regression scheme to match the experimental cell data. Using the cell data, the voltage and current of the stack can be sized as a function of active area and the number of cells in a fuel cell stack.

5.3.4.1 Hydrogen Flow Rate

The hydrogen flow rate in terms of mols per unit time can be related to the fuel cell current (I_{fc}) through Faraday's law where U_{H2} is the hydrogen utilization represented as a value between 0 and 1.

$$\dot{N}_{H2} = \frac{n_{cells} I_{fc}}{2 U_{H2} F}\,. \tag{5.56}$$

5.3.4.2 Balance of Plant

The balance of plant includes all components necessary to operate the fuel cell. Typically, this includes air management, hydrogen delivery and regulation, cooling, power management, and power distribution. The balance of plant analysis is based on the

fully developed system used on the GT FCUAV. A schematic of this balance of plant is shown in Figure 5.21. A detailed description of the balance of plant is available in [57].

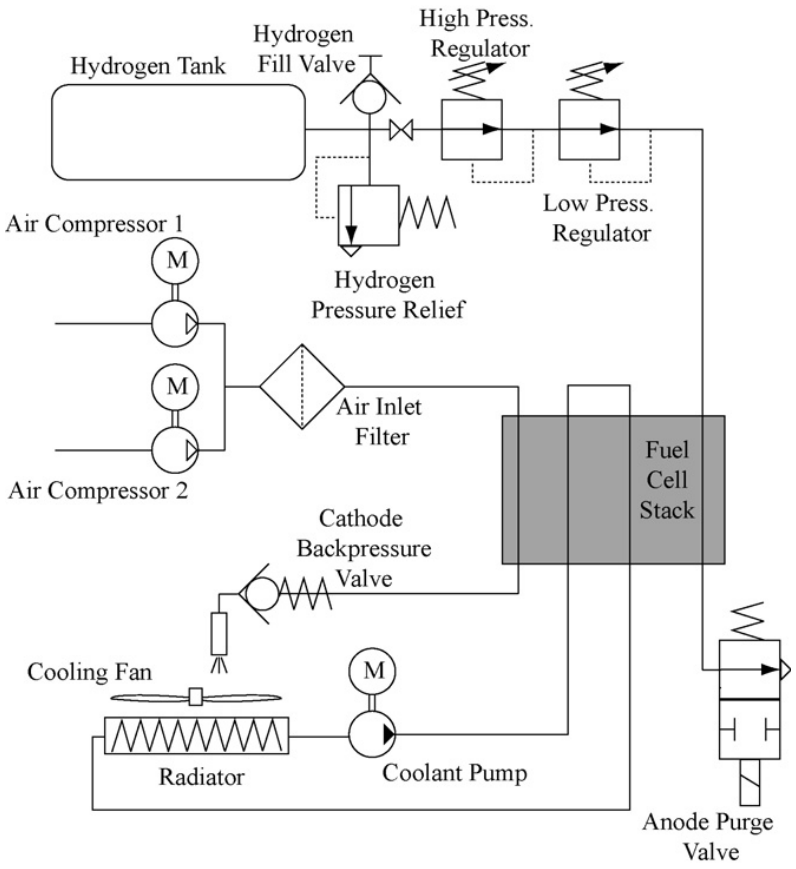

Figure 5.21: Baseline balance of plant.

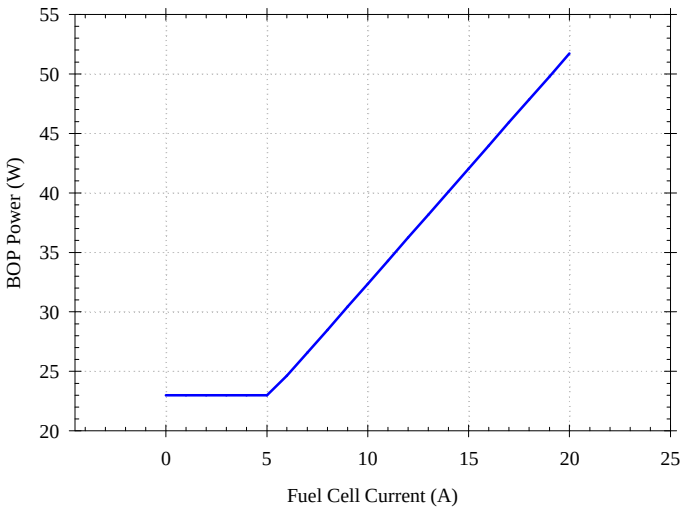

Figure 5.22: Baseline balance of plant power prediction for 32 cell BCS stack.

The predicted power as a function of the fuel cell current is shown for the 32 cell BCS fuel cell is given in Figure 5.22. Note that under idle and low current applications, a minimum amount of power is required to run the compressors and water pump.

5.3.5 Validation of Fuel Cell Model

Results of the model for the Gore 58 series membrane electrode assembly [247] are shown in Figure 5.23. Validation of the model at a stack level was generated by comparison to the BCS fuel cell used in the GT FCUAV. A comparison of predicted versus measured results is provided in Figure 5.24. Note that Figure 5.24 shows significant variations from the experiment although the mean behavior is properly captured. This behavior of the fuel cell was common during testing emphasizing the caution which must be considered when using this model for design purposes.

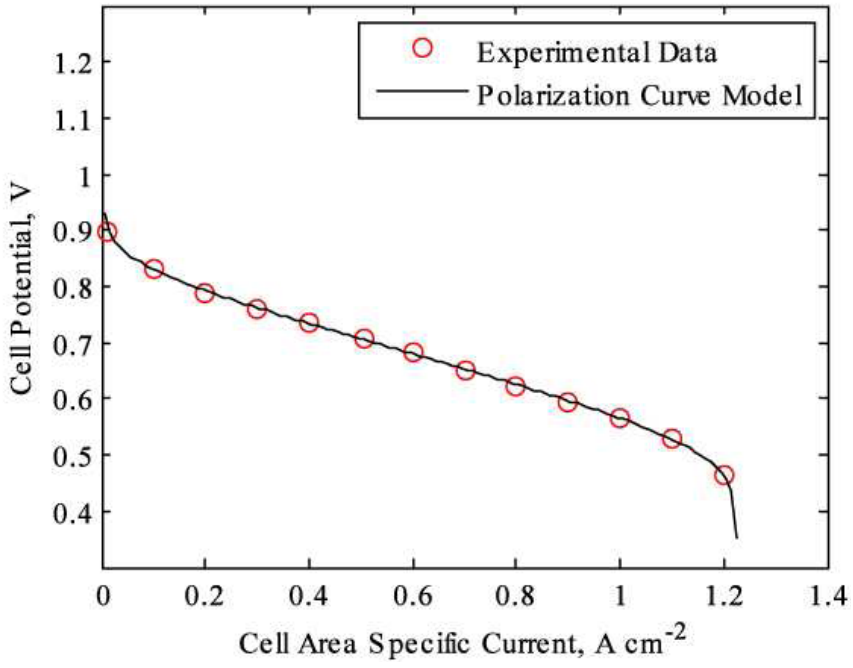

Figure 5.23: Polarization curve for Gore 58 series membrane electrode assembly [63].

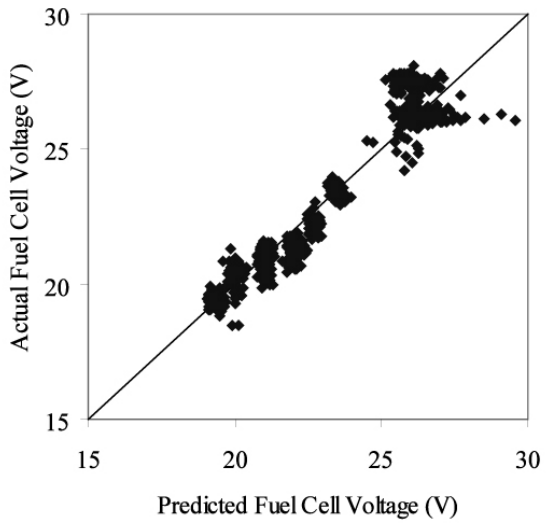

Figure 5.24: Actual performance of the fuel cell model versus measured results of the BCS fuel cell [63].

A plot of predicted versus measured hydrogen flow rates is shown in Figure 5.25. As expected, the predicted values closely match the measured hydrogen flow rates. The small difference in predicted versus actual values are due to uncertainty in the hydrogen utilization.

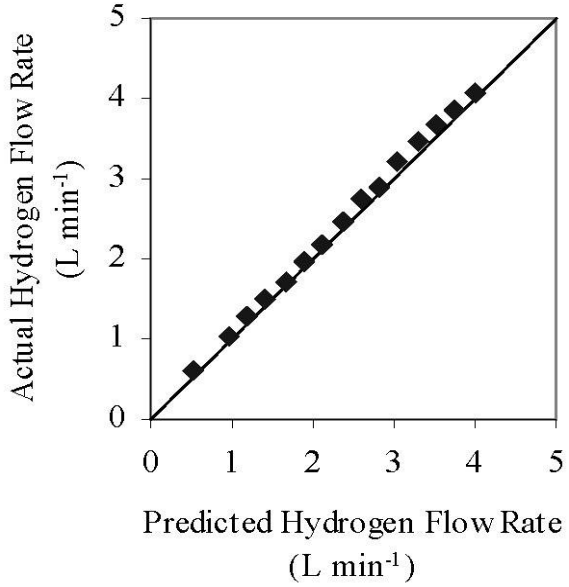

Figure 5.25: Predicted versus measured hydrogen flow rate for Horizon H-300 fuel cell stack [63].

5.4 Weights and Volume

Weight estimation is critical of any aircraft design. With the high volumes of both the gaseous hydrogen storage tank and the fuel cell stack, estimating the volume required by the fuselage would also be necessary. The primary components of the weight breakdown include the fuel cell system, the hydrogen storage system, the fuselage, the wings, and the tail.

5.4.1 Fuel Cell System

A fuel cell system weight model was developed specifically for this project as part of the research of Bradley [63]. The system includes the mass of the fuel cell and all of the balance of plant. The model sizes the fuel cell based on the BCS fuel cell used in the GT FCUAV and allows fuel cell active area and the number of fuel cells to be varied. The fuel cell bipolar plates are assumed to be constructed out of graphite and the endplates and bolts are assumed to be aluminum. For a complete description of the model, refer to reference [63].

In addition, an empirical model based on the weight and volumes of the Horizon Fuel Cell H series fuel cell systems was also developed based on specification sheets available from Horizon Fuel Cell Technologies [43]. Prediction of fuel cell length and mass for both the BCS and Horizon Fuel Cell Technologies based fuel cell models are shown in Figure 5.26. This figure was generated assuming an active area of 20 cm^2 for both models and a maximum current draw of 20A for the BCS balance of plant. As shown in Figure 5.26, different fuel cell architectures can produce vastly different mass and size for a similar number of individual fuel cells.

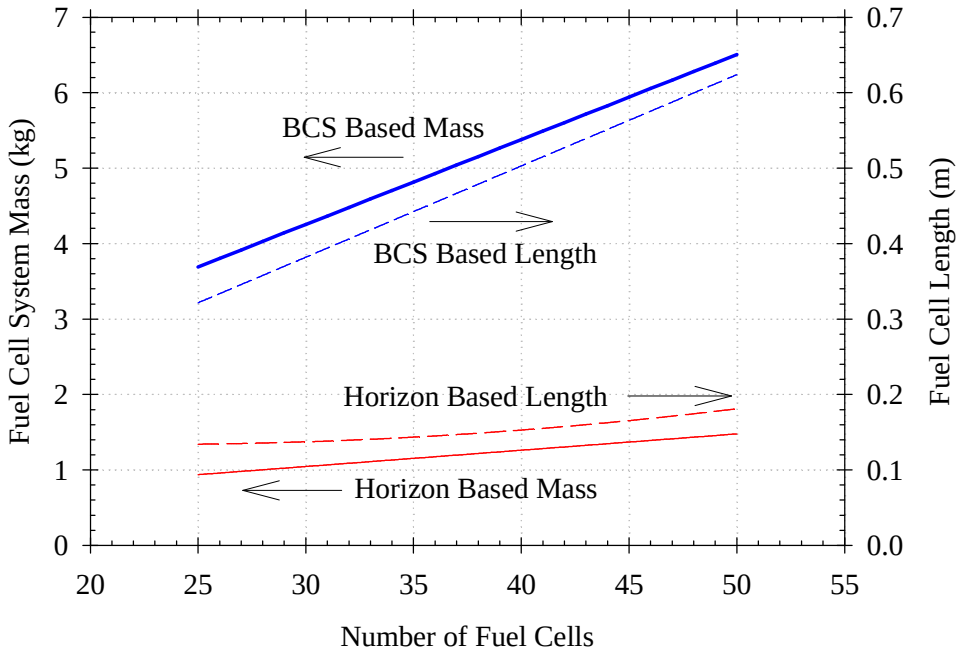

Figure 5.26: BCS and Horizon based mass and length predictions for an active area of 20 cm^2.

Note that different fuel cell designs can result in drastically different volume and mass. An increased thickness in the BCS based design results in increased length and mass, however, Figure 5.26 provides a misleading comparison since the BCS based model using Gore 58 series membranes produces more power than a Horizon stack of equal active area and cell count.

5.4.2 Hydrogen Storage

The development and validation of the gaseous hydrogen storage system model was performed as part of the research tasks of Bradley [63]. The tank design and analysis is based on state of the art composite overwrapped pressure vessels analyzed using both empirical data and mechanics of materials. The tanks are assumed to have an aluminum tank liner of constant thickness and a metallic or polymeric liner to reduce the hydrogen

leak rate [248]. Using values defined in Table 5.6, the thickness of the composite overwrap (t_{H2}) can be calculated as a function of maximum hydrogen pressure (P_{H2}), atmospheric pressure outside of the tank (P_{atm}), and the tank radius (r_{H2}).

$$t_{H2} = FOS\left[\frac{r_{H2}\left(P_{H2} - P_{atm}\right)}{\tau_{\max}} + \frac{r_{H2}\left(P_{H2} - P_{atm}\right)}{2\tau_{\max}}\right] \tag{5.57}$$

At high pressures, hydrogen will not act as a perfect gas. To estimate the real gas properties of hydrogen, the Redlich-Kwong [249] equation of state was used (see Eq. (5.58)).

$$\begin{gathered} P_{H2} = \frac{R_{gas}T_{H2}}{V_{H2} - b_{RK}} - \frac{a_{RK}}{T_{H2}^{1/2}V_{H2}(V_{H2} + b_{RK})} \\ a_{RK} = 0.1425\,\mathrm{K}^{1/2}\,\mathrm{m}^6\,\mathrm{Pa}\,\mathrm{mol}^{-2} \\ b_{RK} = 1.817\cdot 10^{-5}\,\mathrm{m}^3\,\mathrm{mol}^{-1} \end{gathered} \tag{5.58}$$

Using values in Table 5.6, the total mass of the hydrogen tank including the mass of hydrogen (m_{H2}) is calculated using Eq. (5.59).

$$m_{\text{tank}} = (1 + f_{mount})\cdot(m_{\text{liner}} + m_{\text{composite}}) + m_{\text{reg}} + m_{H_2} \tag{5.59}$$

Table 5.6: Values used for gaseous hydrogen storage model.

Design Variable	Value	Notes
Composite Overwrap Maximum Stress ($\tau_{\max}$)	1.9GPa	Kevlar-49/epoxy at 55% translation [83, 250]
Liner Density (ρ_{liner})	2700kg/m^3	Aluminum 6061
Regulator Mass (m_{reg})	0.35kg	[58]
Composite Overwrap Density (ρ_{comp})	1530kg/m^3	[251]
Liner Thickness (t_{liner})	0.762mm	Aluminum 6061 [251]
Liner Load Sharing	0%	
Factor of Safety to Yield (FOS)	2.5	
Tank Mounting/Bosses/Tubing Mass Fraction (f_{mount})	10%	Based on [251]

5.4.2.1 Hydrogen Storage Validation

The hydrogen storage model was validated by comparison to an assortment of commercially available composite overwrapped cylinders [81]. Using the tank length to diameter ratio (l/d_{H2}) and the maximum hydrogen pressure as inputs, the predicted tank mass, length, diameter, and volume were compared to reported values (see Figure 5.27 and Figure 5.28).

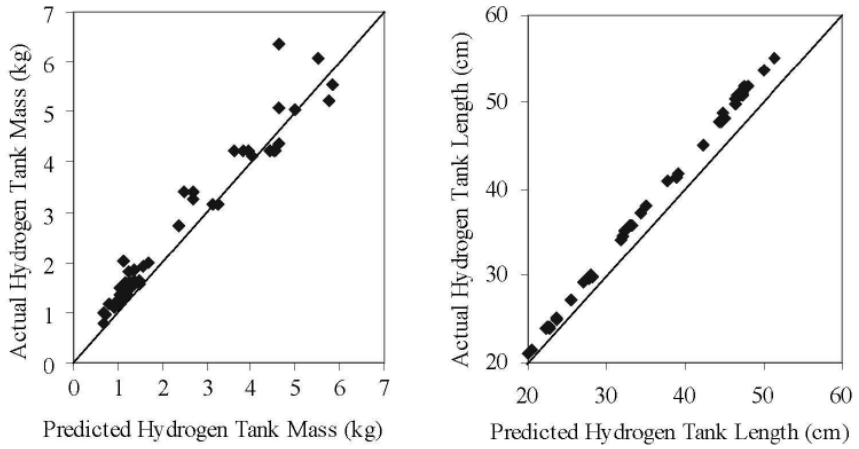

Figure 5.27: Predicted versus actual mass and length for hydrogen storage model[63].

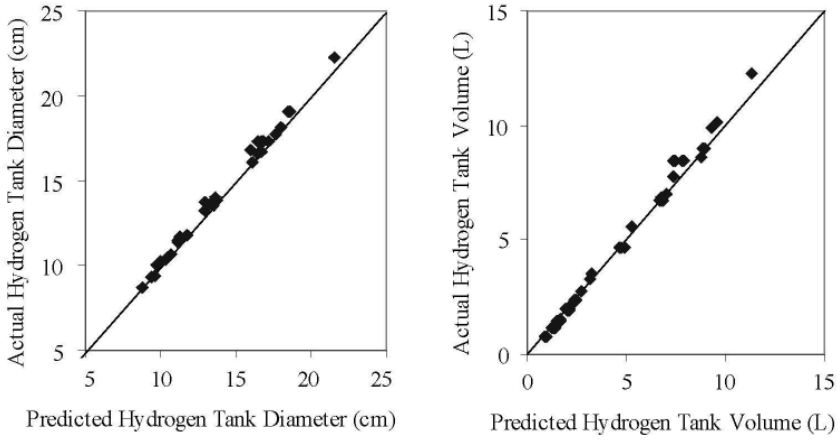

Figure 5.28: Predicted versus actual diameter and volume for hydrogen storage model [63].

5.4.3 Fuselage

The hydrogen storage system and the fuel cell system represent a significant payload volume and mass that is both enclosed and supported by the fuselage.

The fuselage was assumed to be of a circular cross section. A circular cross section was appropriate as the hydrogen storage tank would also have a circular cross section and would likely occupy the largest volume of any component within the fuselage. To specify aerodynamic tapering of the forward and aft sections of the fuselage, semi-elliptical equations recommended by Roskam were used [212]. The *x* and *y* coordinates of the forward and aft tapered equations are given respectively in Eq. (5.60) and Eq. (5.61). The parameter *a* represents the outside radius of the fuselage and was sized to give 10% excess cross sectional area relative to the payload component with the largest equivalent circular cross sectional area. The parameter *b* specifies the length that will be used to perform the aerodynamic tapering and is specified for both the forward and aft sections in Figure 5.29.

$$\left(\frac{x}{a}\right)^{9/4} + \left(\frac{y}{b}\right)^{7/5} = 1 \tag{5.60}$$

$$\left(\frac{x}{a}\right)^{3/2} + \left(\frac{y}{b}\right)^{5/4} = 1 \tag{5.61}$$

The fuel cell system, hydrogen storage system, electric motor, and payload were all assumed to be placed in series axially along the fuselage. A payload length (L_{pay}) was calculated that would allow all components to be completely enclosed. A cross sectional view of the fuselage shape for two fuselages of different diameters but equal payload lengths is available in Figure 5.29.

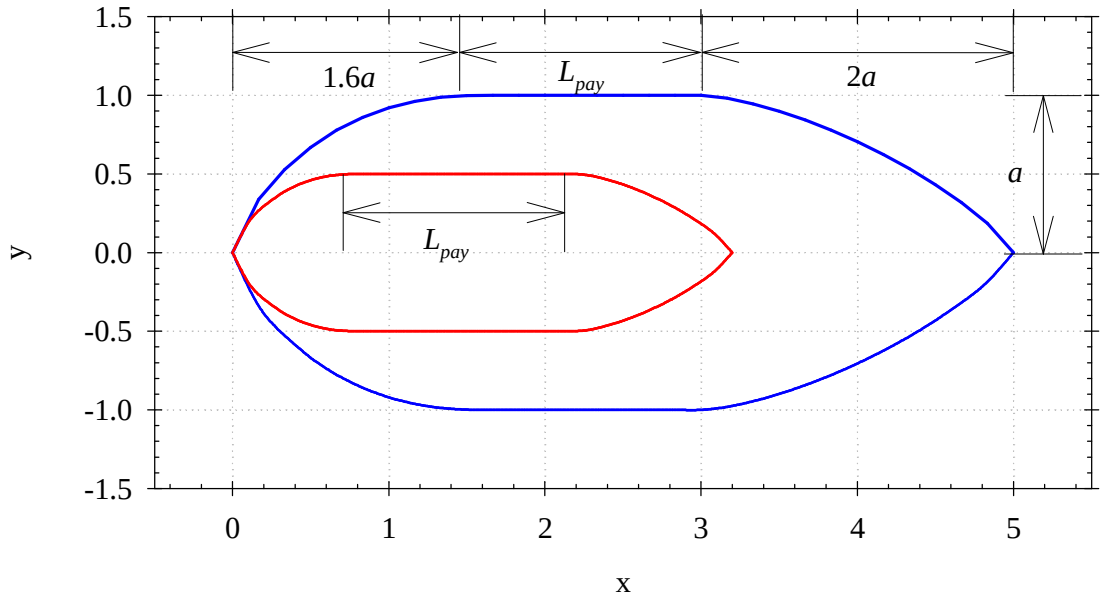

Figure 5.29: Geometric scaling of the fuselage for equal payload lengths.

Structurally, the fuselage was sized consistently with the GT FCUAV. This design used a lightweight aluminum frame to interface with a composite spar and tailboom. The aluminum frame carried the full load of the payload and transferred this load to the main spar. The mass of the aluminum frame was linearly scaled as a function of the sum of the masses of the fuel cell system, hydrogen storage system, and payload. A thin fiberglass shell was used to enclose the fuselage. The mass of this shell was scaled based on surface area relationships that were estimated using several prototype fuselage shells that were constructed at Georgia Tech.

The total mass of the fuselage designed to carry 4.5 kg (10lb) of components with varying payload length and diameter is shown in Figure 5.30. The fuselage mass scales nearly linearly with both payload length and fuselage diameter. The mass is most sensitive to changes in payload diameter since small changes in diameter result in large increases in wetted area of the fuselage.

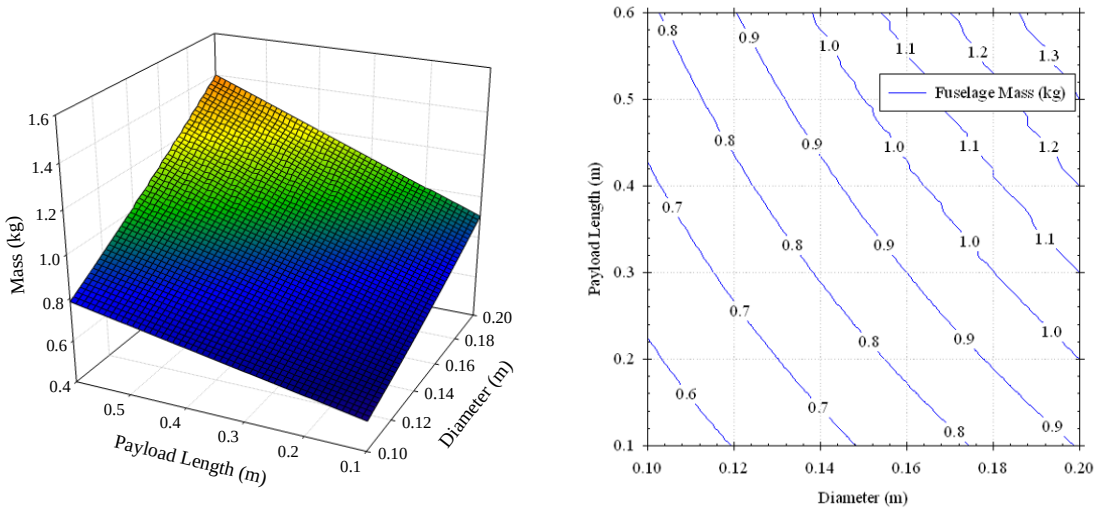

Figure 5.30: Fuselage mass as a function of payload length and payload diameter.

5.4.4 Wings and Tail Weight Estimate

The wings and tail were based on construction techniques used on the GT FCUAV. The main loads would be transferred to a carbon fiber spar and tailboom. Both the wings and tail were assumed to be constructed primarily of foam with balsa sheeting. The balsa sheeting would then be covered by a single layer of Monokote.

The main spar was assumed to have a circular cross section, a thickness of 1.5 mm, and extended the full length of the wing. The maximum stress was estimated by modeling half of the length of the spar as a simple cantilever beam with a uniform load equivalent to a force of 2.5 times the weight of the aircraft normally supported by a single wing. Using this loading as well as properties supplied by CSC Composites [252], the diameter and mass of the spar were estimated. In addition, the remaining weight of the wing and tail were then estimated using volume and surface area weight factors derived from several wing sections that were constructed during development of the GT FCUAV.

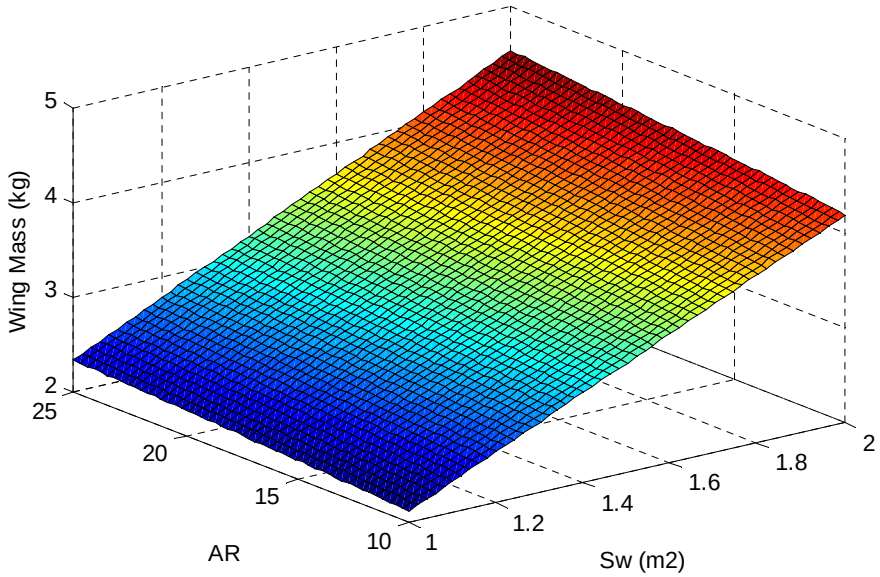

Figure 5.31: Wing mass as a function of aspect ratio and wing area for a 15 kg aircraft.

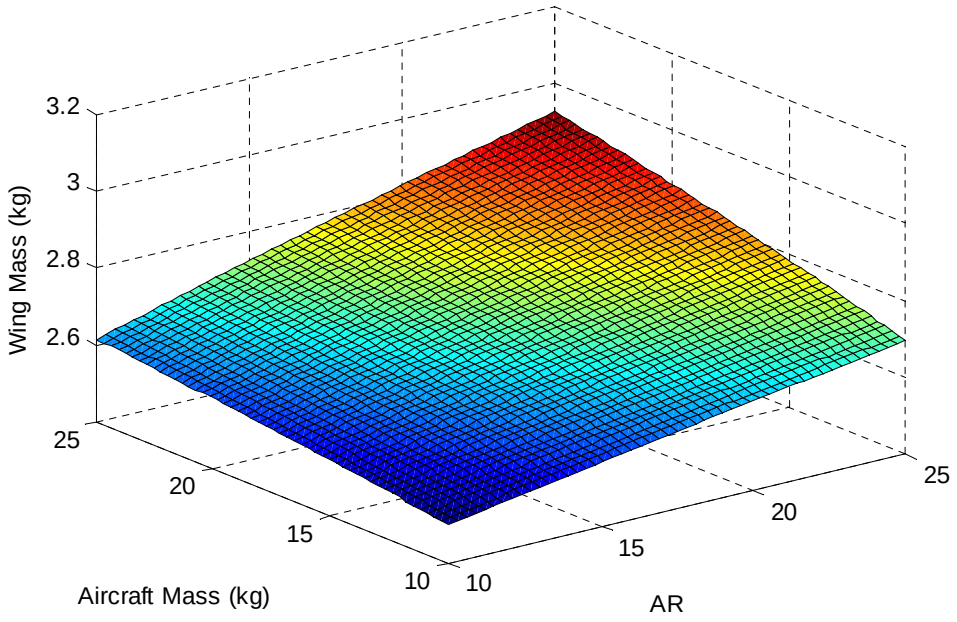

Figure 5.32: Wing mass as a function of aircraft mass and aspect ratio for a wing area of 1.2 m^2.

Figure 5.31 shows how the wing mass of a 15 kg aircraft will vary as the aspect ratio and area of the wing are varied. Most of the mass of the wing is in the foam and balsa wood structure causing the wing mass to be most sensitive to planform area. Figure 5.32 shows how the mass of the wing is related to the spar. Increases in total aircraft mass will cause an increase in mass as the spar will need to support a larger bending moment. Increases in aspect ratio will increase the span and also result in an increased bending moment and thus increase the mass of the spar.

5.4.5 Motor and Propeller Weight

The majority of the weight in a fuel cell aircraft is due to the hydrogen storage system, the fuel cell system, and the mass of the airframe. In addition to these weights, the weight of the motor, and the weight of the propeller were also estimated. Motor weights were based on the masses reported for the NEU 19 series of electric motors [253]. The propeller mass reported in grams (see Eq. (5.62)) was estimated based on a linear fit of the reported masses of several Bolly propellers [254].

$$m_{prop} = 31.201 d_p - 495.663 \tag{5.62}$$

5.5 Aerodynamics

The initial uncertainty propagation study suggested that accurately modeling the lift and drag of the aircraft would be critical to accurately estimating the endurance and climb rate. To estimate lift and drag, the aerodynamic analysis was decomposed into a lifting surface analysis and a fuselage analysis. This decomposition is typical in conceptual design practices and is appropriate for sailplane derivative designs [213]. The lifting surface analysis was used to estimate the lift, drag, and interference effects of both the

wing and tail. The lifting surface analysis would also be used to estimate the size of the tail necessary to maintain constant yaw and pitch static stability margins. The fuselage analysis would estimate the drag and interference effects due to the fuselage.

5.5.1 Lifting Surface Analysis

With specific power limitations, fuel cell aircraft are largely confined to highly efficient low speed aircraft governed by both low Mach and Reynolds numbers. With the exception of extremely low Reynolds numbers, several methods exist that appropriately model the governing physics including lifting line, vortex lattice, panel, and computational fluid dynamics methods. Choosing a method is primarily a tradeoff between accuracy and efficiency.

5.5.1.1 Description of Candidate Methods

Prandtl's classical lifting line theory was the first practical theory for predicting the aerodynamic properties of a finite wing [255]. Prandtl's lifting line theory gives an analytical solution that provides good results for estimating the lift and induced drag of straight wings of moderate to high aspect ratio. Although classical lifting line theory has been applied to biplanes by both Prandtl and Munk [256], the analytical solution is limited to single wings that have no sweep or dihedral. Although the classical lifting line theory assumes a constant lift slope, numerical solutions such as posed in Anderson [255] allow for nonlinearities that would be expected near stall. Numerical lifting line (NLL) theory is a more recent development by Phillips and Snyder [257] that extends the theory by replacing the 2-dimensional Kutta-Joukowski law applied in the classical theory with a fully 3-dimensional vortex lifting law. The resulting numerical lifting line theory is

applicable to multiple lifting surfaces that may include both dihedral and sweep. The method has also been extended to include the predictions of the onset of stall [258].

All lifting line theories are most appropriate for dealing with lifting surfaces of moderate to high aspect ratio. If the lift and induced drag are dominated by the lifting surfaces (wings and tail/canard) then the methods are useful. However, low aspect ratio wings, and more non-traditional lifting surfaces such as lifting bodies and delta wings typically cannot be accurately modeled by lifting line methods.

Vortex lattice methods are fundamentally similar to lifting line methods. However, rather than modeling a lifting surface by placing horseshoe vortices only at one chordwise location, a lattice structure of vortices and control points are used along the span and camber line of the lifting surface. Typical, a ¼ - ¾ rule is used for each panel formed by the lattice structure, meaning that a horseshoe vortex is located ¼ of the chordwise length from the front of the panel, while the control point is located at a ¾ chordwise length. The ¼-¾ rule is derived from Pistolesi who showed that single panel vortex-lattice solutions using this rule for a two-dimensional wing results in the same section lift and moment as thin wing theory [259]. Typical vortex lattice methods cannot account for thickness although multiple surfaces and arbitrary shapes including low aspect ratio wings can be modeled. Because of the lattice structure with control points and singularities required along the camber line, vortex lattice methods result in a larger system of linear algebraic equations as compared to lifting line methods.

Similar to vortex lattice, panel methods divide a wing into various panels and use control points and singularities to develop a system of algebraic equations. However, rather than applying boundary conditions on a mean surface defined by the camber line

(as is done in vortex lattice), panel method boundary conditions are applied on the actual surface. This use of boundary conditions allows thickness to be modeled. Different singularities such as sources, sinks, doublets, or vortices can be used depending on whether the flow contains lifting surfaces or not. Whereas lifting line and vortex lattice theories are typically best applied to lifting surfaces, non lifting surfaces such as non-lifting fuselages are appropriately modeled using panel methods.

Phillips and Snyder [260] compare numerical lifting line theory against the commercial panel code PMARC [261], the inviscid Euler CFD code WIND [262], and limited experimental data [263] for straight wings as well as wings with dihedral and sweep. In addition, the results have also been compared to results from a commercial vortex lattice code [264]. The calculated induced drag coefficients, lift coefficients, and rolling moment coefficients show that each method gives consistent results with experimental data with the exception of a wing with a high angle of sweep (45 degrees).

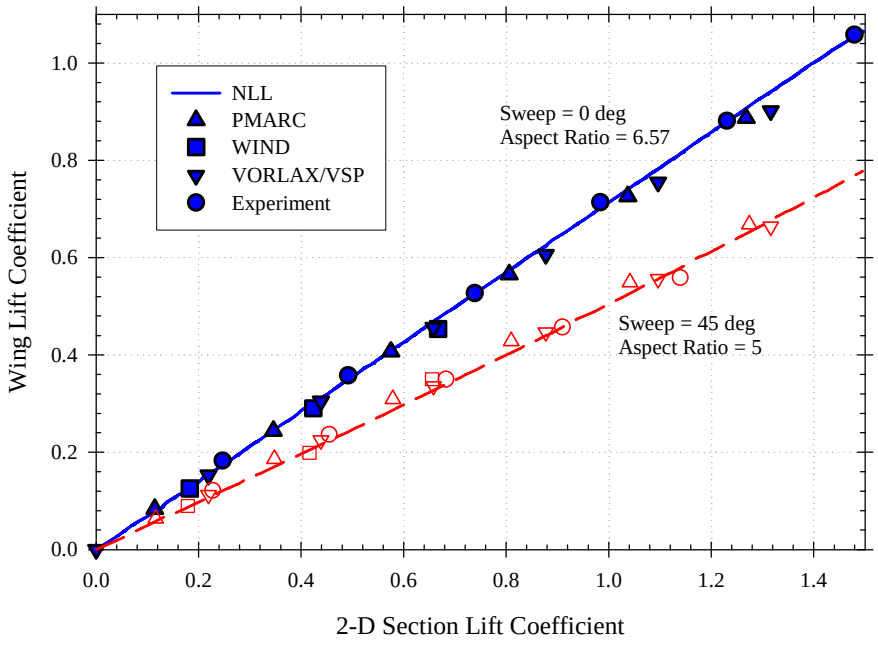

Figure 5.33: Wing lift coefficient estimation for various computational methods.

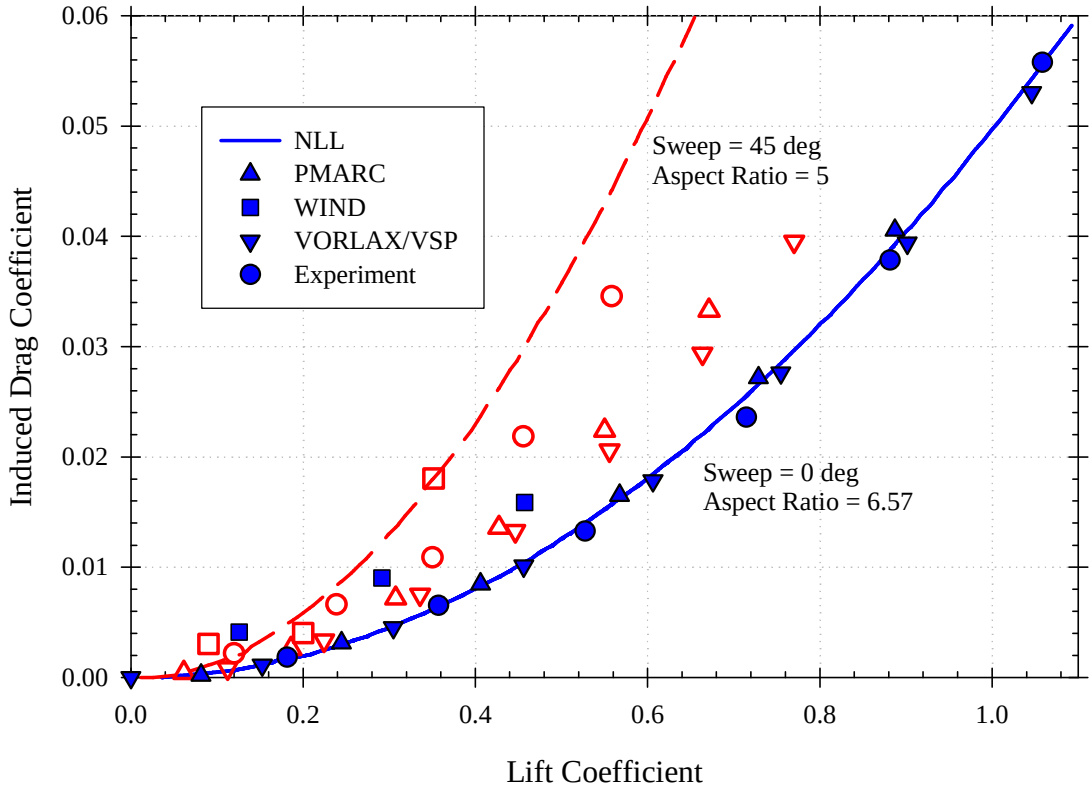

Figure 5.34: Wing induced drag coefficient for various computational methods.

Table 5.7: Normalized computational time for an inviscid analysis of a single wing.

CODE	Description	Disretization	Normalized Computational Time
WINGS	Numerical Lifting Line	40 nodes/semispan	1
VORLAX/VSP	Vortex Lattice	780 panels/semispan	$2*10^2$
PMARC	Panel Code	4500 panels/semispan	$2*10^4$
WIND	Inviscid Euler CFD	$1.25*10^6$ grid points/semispan	$2*10^6$

Although none of the methods were in agreement with the induced drag of a wing with 45 degree sweep, numerical lifting line gave results that were conservative and as good if not better than the other methods. With results comparable to panel codes and inviscid CFD, the primary advantage of numerical lifting line is that computational times are orders of magnitude faster than competing methods. For the single wing test cases described in [260, 264], the normalized computational times are given in Table 5.7.

Given the motivation that a fuel cell aircraft is primarily advantageous in a low speed long-endurance application, high aspect-ratio low Mach number lifting surfaces are expected. For this type of analysis, NLL provides good predictions of lift and induced drag and is orders of magnitude faster than other competing methods.

5.5.1.2 Lifting Surface Validation

One the primary advantages of NLL over the classical theory is the ability of NLL to analyze multiple lifting surfaces. This is especially important for analyzing the effects of canards and/or v-tails which are common on highly efficient long endurance aircraft. Although results that show that NLL provides intuitively correct results for an example involving a wing and tail combination [257], the method remains largely unvalidated against experimental results for multiple surfaces. The primary reason is that published experimental data suitable for validation, i.e. experimental data that involved only the effects between lifting surfaces, is rare. Although experimental data does exist for lifting surface interactions for wing-tail-canard [265] and biplane configurations [266], these data often include significant effects from fuselage or other surface interactions that make capturing only the lifting surface interaction impossible. However, during the earlier days of aeronautical research, many biplane studies were conducted that consisted solely

of lifting surfaces [215, 216, 267]. To help provide validation of NLL's ability to capture multiple surface interactions, NLL predictions were compared against experimental data for several biplane configurations given in reference [216]. It was assumed that if the method could correctly predict the interaction between biplanes wings, then it could also be extended to wing/tail or wing/canard configurations. This assumption assumes that the interaction effects between biplane wings are similar and as significant as the interaction effects between a wing and tail/canard.

The biplane experimental data used for validation was based upon non-tapered, non-twisted biplane wings of aspect ratio of 6 that had circular wingtips. Each biplane wing consisted of Clark Y airfoil sections. All NACA data was taken at a Reynolds number of approximately 150,000. The experimental data was provided in terms of lift and drag coefficients vs. angle-of-attack. By convention, the wing aspect ratio was calculated using only one of the two identical biplane wings. In contrast however, the reference area using in calculating all non-dimensional coefficients included the summed planform area of both wings.

To obtain the airfoil data needed by WINGS, actual Clark Y lift, drag, and moment data collected by the University of Illinois at Urbana-Champaign (UIUC) at a Reynolds number of 200,000 was used [268]. The airfoil chord line definition in the UIUC experimental data varies from the standard lower surface chord line definition used in early NACA documents [215]. Therefore, all airfoil sections in WINGS had to be rotated about the trailing edge with a nose up angle of 2.15 degrees to maintain consistency with the earlier NACA reference. Figure 5.35 shows the difference in

ordinates given by NACA and UIUC and also shows that rotating about the trailing edge brings both sets of ordinates into excellent agreement.

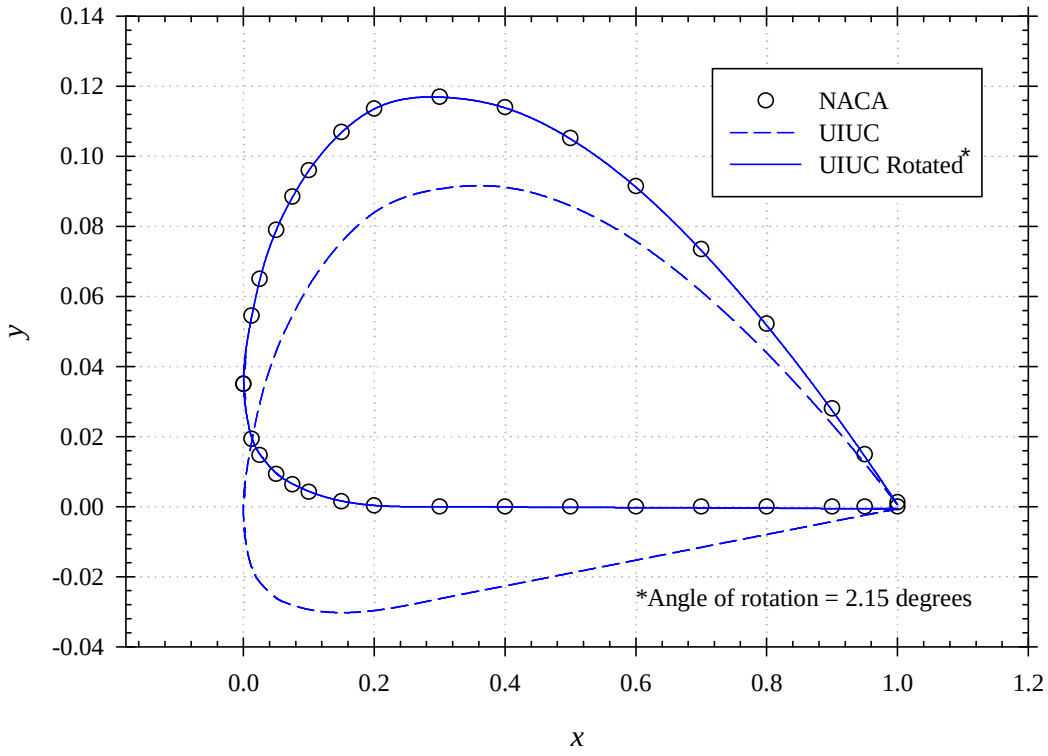

Figure 5.35: NACA and UIUC airfoil ordinates for Clark Y airfoil.

As a baseline case of the ability of NLL to predict lift and induced drag, single wings of aspect ratio (AR) = 6, root chord length (c) of 0.127 m (5 inches), with both circular and rectangular wing tips were calculated and compared to experimental data. The comparison as shown in Figure 5.36 demonstrates that NLL does a good job at predicting both the C_L and C_D variations with angle of attack. In agreement with the data, NLL predict little difference due to wing tip selection. As shown in Figure 5.36, NLL captures the onset of stall with better results for the rectangular tipped wing.

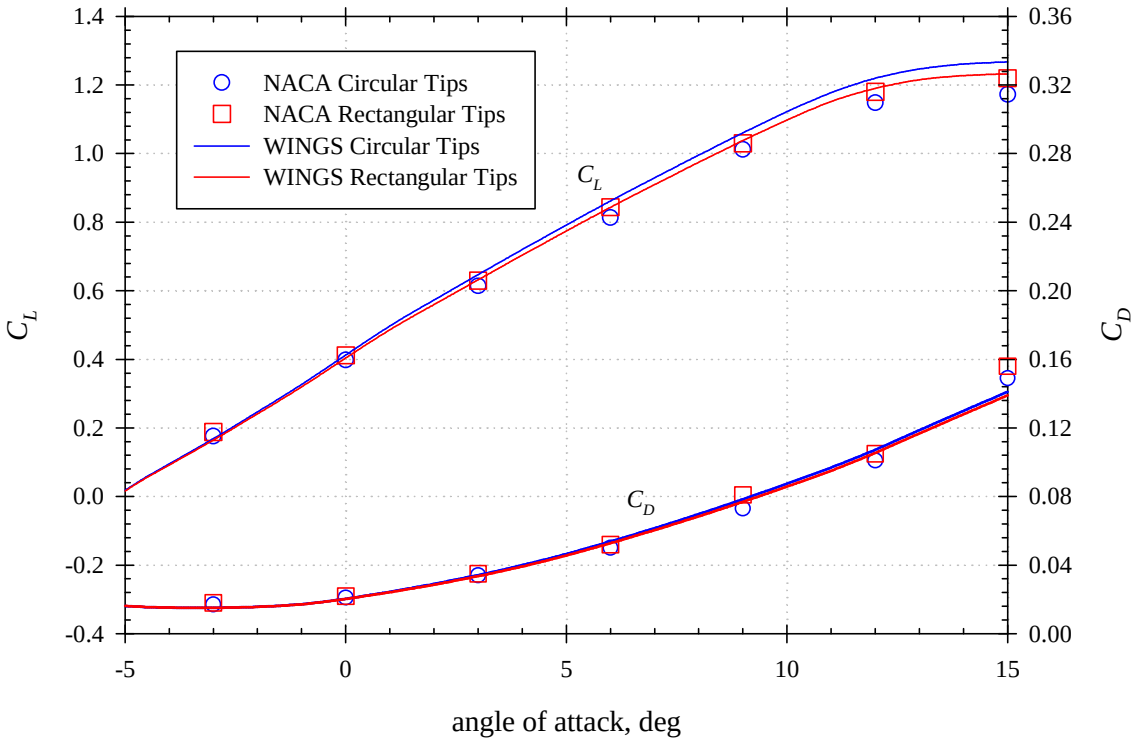

Figure 5.36: Experimental and NLL predicted results for single wings with R_a = 6 and c_r = 0.127 m.

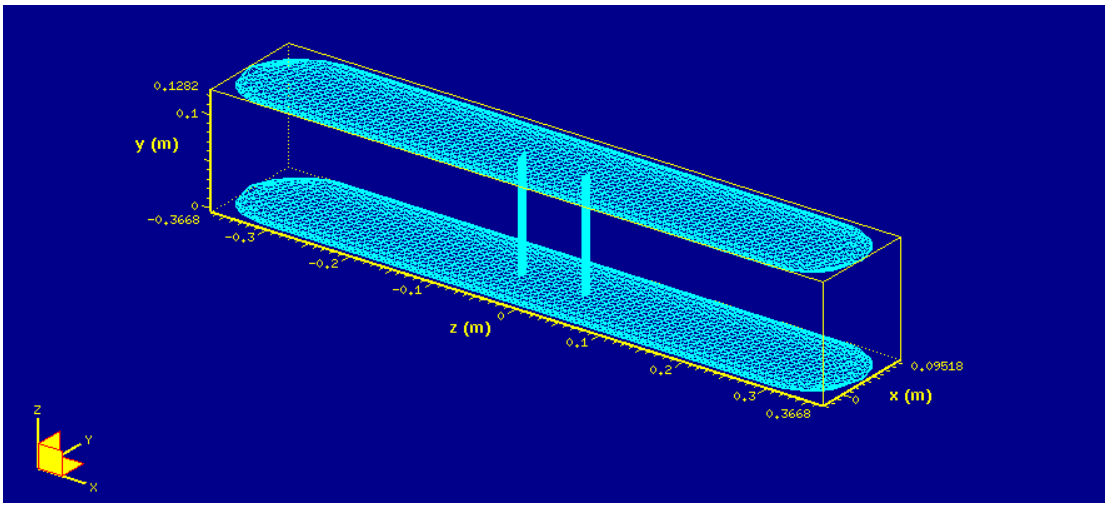

Figure 5.37: Biplane test setup with gap of 1 chord length, no stagger, and no decalage.

The NACA biplane experimental results in reference [216] consist of identical biplane wings with circular wing tips that were tested with varying vertical gap (G), stagger, and decalage. To support the biplane wings, two small struts with NACA 0012 airfoil sections were used. The basic experimental setup can been viewed in the WINGS model in Figure 5.37.

A validation study was performed by comparing the NLL predictions to the NACA data for the three different gap settings that experimentally tested. The gap distance was measured in terms of the wing chord for gap-to-chord ratios of 0.5, 1, and 1.5. The drag polars predicted by NLL compared against the NACA data are presented in Figure 5.38.

Although NLL captures the proper trends of the NACA data, the results seem to be biased by a slight drag offset (ΔC_D) as shown in Figure 5.38. This effect was assumed to be due to viscous effects in the experiment that could not be captured by NLL. Based on the way in which the coefficients were calculated, the monoplane and biplane wings should have identical drag coefficients when the lift coefficient is equal to zero. By assuming a drag offset term (ΔC_D) based on how the drag coefficient changed at zero lift, the NLL drag estimation at each lift coefficient was shifted by ΔC_D resulting in much better agreement (see Figure 5.39).

Although NLL required a slight drag offset to provide good agreement with the NACA biplane study data, the method captured the overall trends. It was assumed that since the method could capture the biplane data trends, then it could also capture the wing and tail interaction that would exist with the baseline aircraft configuration and provide results appropriate for design space exploration.

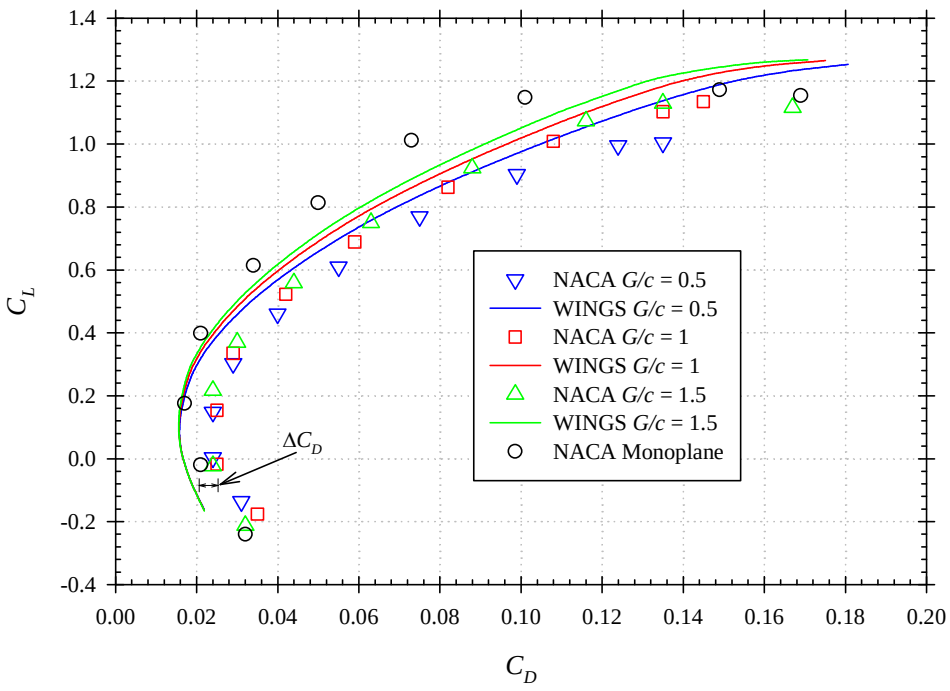

Figure 5.38: Drag polar validation for different biplane wing spacing.

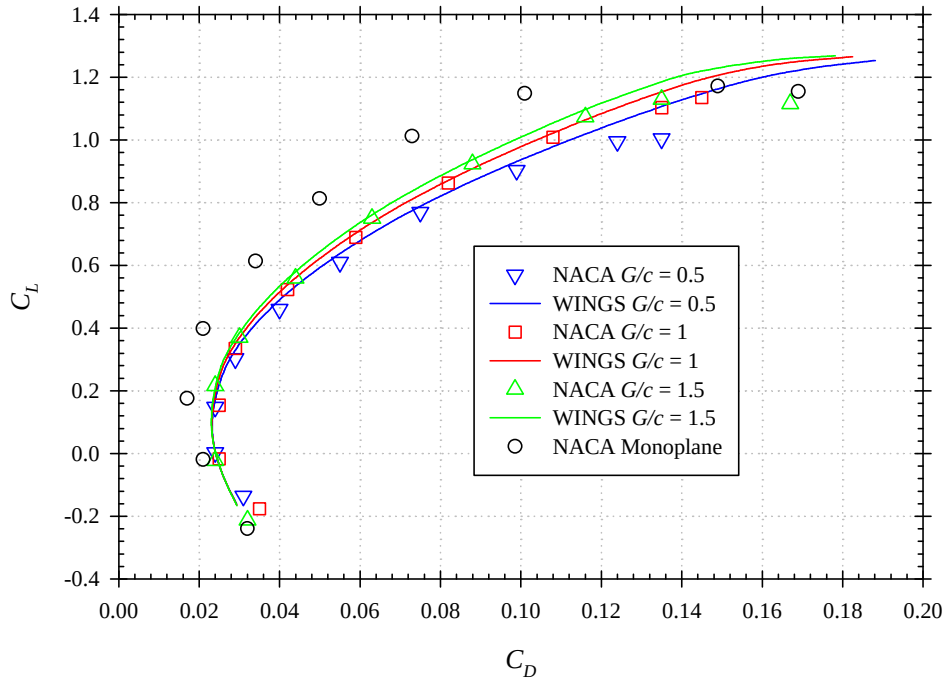

Figure 5.39: Drag polar validation for different biplane wing spacing including the drag offset.

5.5.1.3 Wing Approximation

The wing and tail airfoil geometry was fixed. Varying the airfoil geometry during preliminary design optimization has been shown to be numerically challenging while providing little benefit [207]. The SD7032 airfoil used for the wing of the GT FCUAV was selected as the baseline wing airfoil. Low Reynolds number wind tunnel data [268] for this airfoil was available and used in the input file for the NLL WINGS code. A NACA 0009 airfoil was chosen for the tail surfaces also based on experience with the GT FCUAV. Wind tunnel data for the NACA 0009 airfoil was based on reference [269].

An extensive optimization effort during detailed design of the GT FCUAV aircraft resulted in a wing that used taper and dihedral starting at 0.625 of the semi-span. The taper ratio was equal 0.67. Adding extra planform design variables such as taper ratio, dihedral, and the span location of the onset of taper (b_T) were not necessary for the design space exploration as the detailed design of the GT FCUAV had shown that a performance based optimization would drive the design to approximate an elliptical lift distribution. Figure 5.40 shows the lift distribution estimated by the NLL code WINGS for both the GT FCUAV final wing design and an elliptical wing with equivalent wing area and aspect ratio.

The GT FCUAV lift distribution is approximately elliptical as shown in Figure 5.40. A calculation of the drag polars for the GT FCUAV wing and its elliptical approximation is shown in Figure 5.41. Except at very low lift coefficients, the drag polar of the elliptical approximation has excellent agreement with the GT FCUAV tapered wing. The disagreement at low lift coefficients is unimportant as a long endurance aircraft will require a high lift coefficient to maximize aerodynamic efficiency.

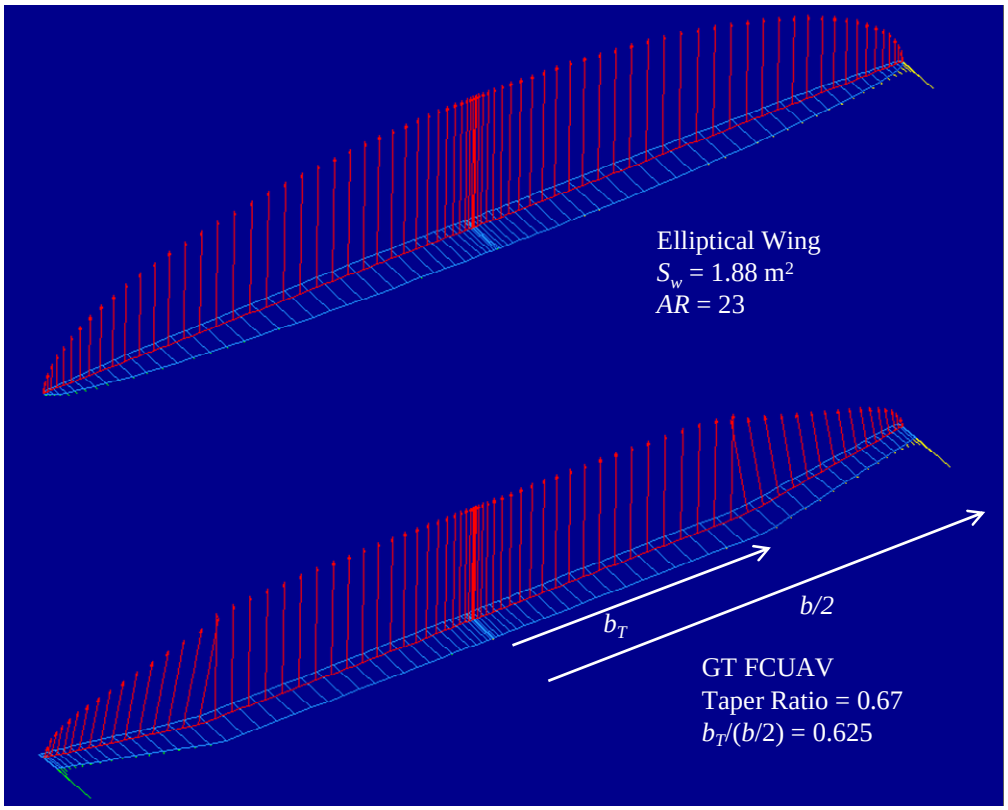

Figure 5.40: Lift distributions for GT FCUAV wing and an elliptical wing of equal area and aspect ratio.

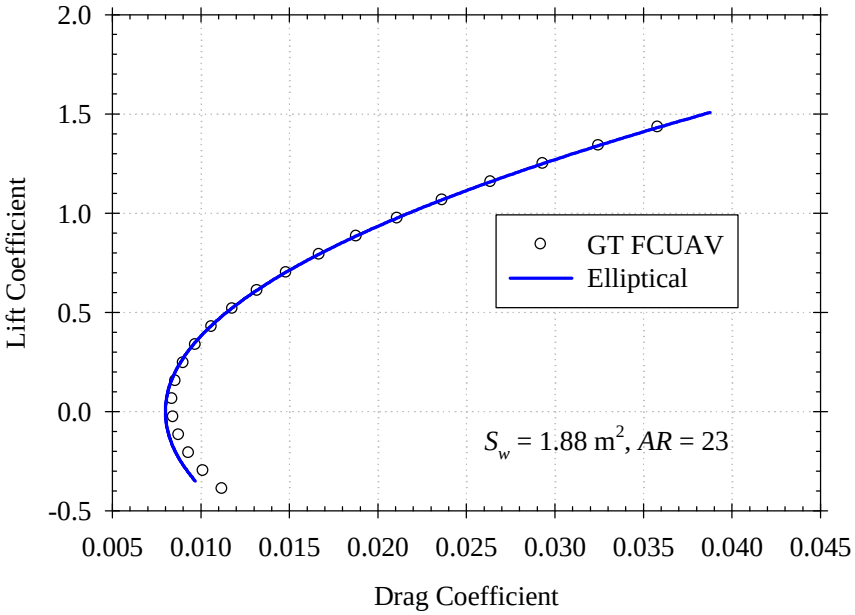

Figure 5.41: Comparison of GT FCUAV drag polar with an elliptical wing of equal area and aspect ratio.

5.5.1.4 Tail Sizing

Tail sizing is based on the inverted V-tail design used in the GT FCUAV. In developing this aircraft, multiple tail sizes were evaluated in flight to help specify conservative margins for static stability. The initial prototype had an estimated static margin (S_M) of 0.25 and a yawing derivative ($C_{n,\beta}$) of 0.04 per radian [60]. Although several successful flights were conducted with this V-tail design, as a matter of pilot preference, the yawing derivative was increased to 0.1 per radian by increasing the span of the V-tail and decreasing the angle between the two tail surfaces. However, since the spanwise distance between the two tailbooms was fixed for this aircraft by a mold built for the fuselage, increasing the span of the tail also caused the static margin to increase to around 0.31. Pilot response to flight testing indicated that the increase in yaw stiffness made the aircraft easier to fly and the increase in static margin had a small detrimental effect to the aircraft's pitching characteristics. As a result, it was determined that a combination of a static margin of 0.25 and a yawing stiffness of 0.1 per radian is preferable for this type of aircraft. As a matter of reference, the static margin definition used is provided in Eq. (5.63) where l_{np} is the axial length along the fuselage reference line from the center of gravity to the neutral point, and c_w is the mean chord length of the main wing. Equation (5.64) provides the definition of the yawing stiffness where C_n is the yawing moment coefficient and β is the sideslip angle measured in radians.

$$S_M = \frac{l_{np}}{c_w} \tag{5.63}$$

$$C_{nb} = \frac{\partial C_n}{\partial \beta} \tag{5.64}$$

Both the static margin and yawing stiffness were estimated using the NLL code WINGS using an elliptical wing as well as an inverted V-tail design based on the Georgia Tech FCUAV. At an angle of attack of zero, the aft distance of the center of gravity as well as the sideslip angle were slightly varied to estimate values for yawing stiffness and static margin. For reference, the inverted V-tail is described as a single rectangular wing defined by a span and anhedral angle. To be consistent with the Georgia Tech FCUAV, the aspect ratio of the tail was constrained to equal 7. The bottom of the V-tail was constrained to the vertical height of the wing such that the tail could be attached via dual tailbooms as was done with the Georgia Tech FCUAV.

By assuming a fixed aspect ratio rectangular surface for the tail, an inverted V-tail design for virtually any elliptical wing maintaining the desired static margin and yawing stiffness can be calculated as a function of the span, anhedral, and aft distance from the main wing. The procedure to design the tail fixes the aft distance between the wing and tail quarter chords (l_t), and then iterates on the anhedral (Γ_t) and tail span (b_t) until the desired static margin and yaw stiffness are obtained. Mathematically, tail sizing is represented as the solution to the system of coupled equations defined in Eq. (5.65).

$$\begin{gathered} \text{Given } l_t, \\ \text{Solve: } C_{nb}\left(b_t, \Gamma_t\right) = 0.1 \text{ and } S_M\left(b_t, \Gamma_t\right) = 0.25 \end{gathered} \tag{5.65}$$

To solve Eq. (5.65), a multidimensional secant method [270] was coded in Matlab that interfaced directly with the WINGS code. Figure 5.42 shows the results of solving Eq. (5.65) for an elliptical wing with the same wing area, aspect ratio, and length to tail as the GT FCUAV. Figure 5.43 shows a tail with an equivalent yaw stiffness and static margin for a lower aspect ratio wing with the tail located closer to the wing.

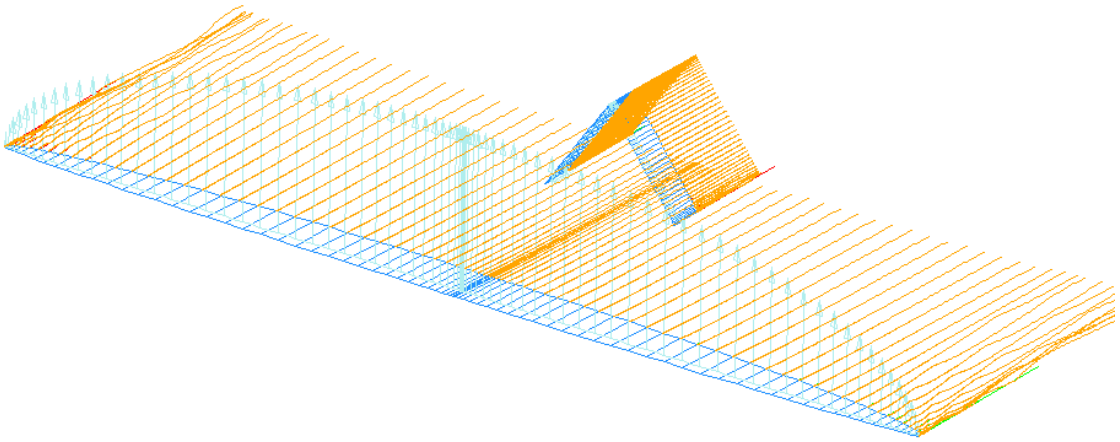

Figure 5.42: Tail sizing results for an aircraft with S_w = 1.88, AR = 23, S_t = 0.363 m^2, Γ_t = 54.12 deg, and l_t = 1.4 m.

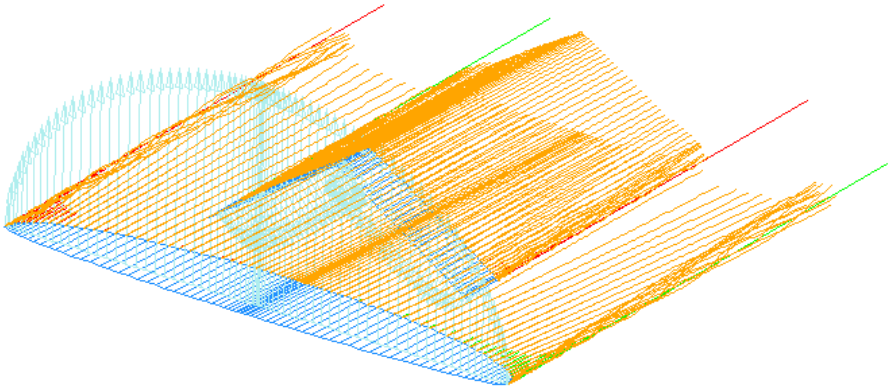

Figure 5.43: Tail sizing results for an aircraft with S_w = 1 m^2, AR = 8, S_t = 0.4247 m^2, Γ_t = 32.8 deg, and l_t = 0.57 m.

The general trends of how the inverted V-tail sizes as a function of wing area, aspect ratio, and the aft distance from the wing (given as a percentage of semi-span, $l_t/b/2$) are provided in Figure 5.44. The area of the tail is nearly a linear function of the wing area but has a strong quadratic relationship with aspect ratio. The aft tail distance has a smaller effect than both wing area and aspect ratio on the wing area. The angle of

the tail is almost entirely determined by the aspect ratio of the wing. The tail volume coefficient as defined in Eq. (5.66) is also calculated in Figure 5.44.

$$V_{tail} = \frac{l_t S_t}{S_w c_w} \tag{5.66}$$

Note that the tail volume coefficient has a strong dependence on wing aspect ratio and is therefore not a good indicator of static stability unless the reference tail volume was calculated at a similar aspect ratio.

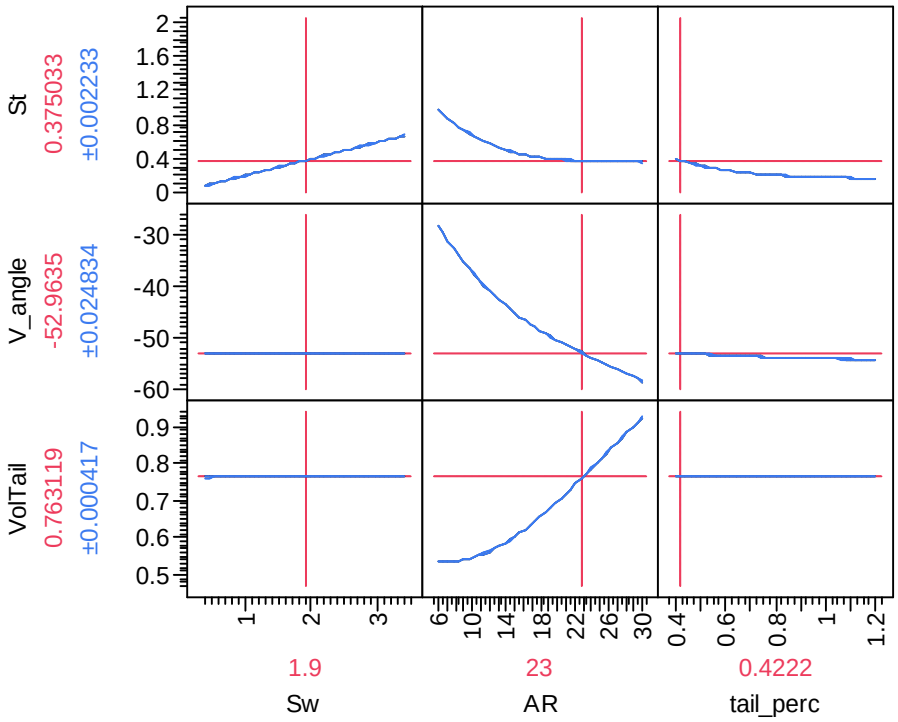

Figure 5.44: Tail sizing trends as a function of wing area, aspect ratio, and aft distance from the wing.

5.5.2 Fuselage Drag

The drag due to the fuselage (C_{Dfuse}) was estimated a summation of the drag at zero fuselage lift (C_{D0fuse}) and the drag due to lift (C_{DLfuse}).

$$C_{Dfuse} = C_{D0\,fuse} + C_{DLfuse} \tag{5.67}$$

The drag at zero fuselage lift was estimated using an empirical estimation suggested by Roskam [212]. This relationship includes a wing-fuselage interference factor (R_{wf}), a skin friction coefficient (C_{fuse}), a drag due to the aft base of the fuselage (C_{Dbfuse}), the wetted area of the fuselage ($S_{wetfuse}$) and a scaling factor based on the length to diameter ratio (l_f/d_f) of the fuselage.

$$C_{D0\,fuse} = R_{wf} C_{fuse} \left(1 + \frac{60}{\left(l_f / d_f\right)^3} + 0.0025\left(l_f / d_f\right) \right) \frac{S_{wetfuse}}{S_w} + C_{Dbfuse} \tag{5.68}$$

The values for the various parameters in Eq. (5.68) are provided by Roskam [212] in the form of tables, charts, and regression equations that are function of various cross sectional and wetted areas of the fuselage.

The drag due to lift is provided in Eq. (5.69) as a function of the angle of attack (α), the aft base area of the fuselage (S_{bfuse}), the drag ratio of a finite versus infinite cylinder (n_{cyl}), the cross-flow drag coefficient (C_{Dcross}), and the cross-sectional area of the fuselage in the 2-D wing plane (S_{plfuse}).

$$C_{DLfuse} = 2\alpha^2 \left(\frac{S_{bfuse}}{S_w} \right) + n_{cyl} C_{Dcross} \left|\alpha\right|^3 \left(\frac{S_{plfuse}}{S_w} \right) \tag{5.69}$$

The relationships for n_{cyl} and C_{Dcross} are provided by Roskam [212].

5.5.3 Miscellaneous Drag

In addition to drag due to the lifting surfaces and the drag due to the fuselage, a miscellaneous drag factor was also included. This drag factor was intended to account for on-off switches, antennae, control lines, rough surfaces, etc. that differentiate a real

airframe from an ideal approximation. A vast amount of experimental data exists in Roskam [212], Coe [271], and Hoerner [210] that can be used to provide a preliminary estimate for miscellaneous drag. Based on the previously mentioned references as well as flight tests of the GT FCUAV, a miscellaneous drag factor of 0.017652 was estimated for the baseline aircraft.

5.6 Flight Performance

The flight profile for a long-endurance aircraft performing an intelligence, surveillance, and reconnaissance mission consists mainly of loiter. A sample mission used for the analysis is shown in Figure 5.45. The mission consists of an assisted takeoff, a climb to a prescribed altitude, loiter in a long endurance orbit, and then descent and landing. The two main flight performance elements that were analyzed for this mission were climb and cruise.

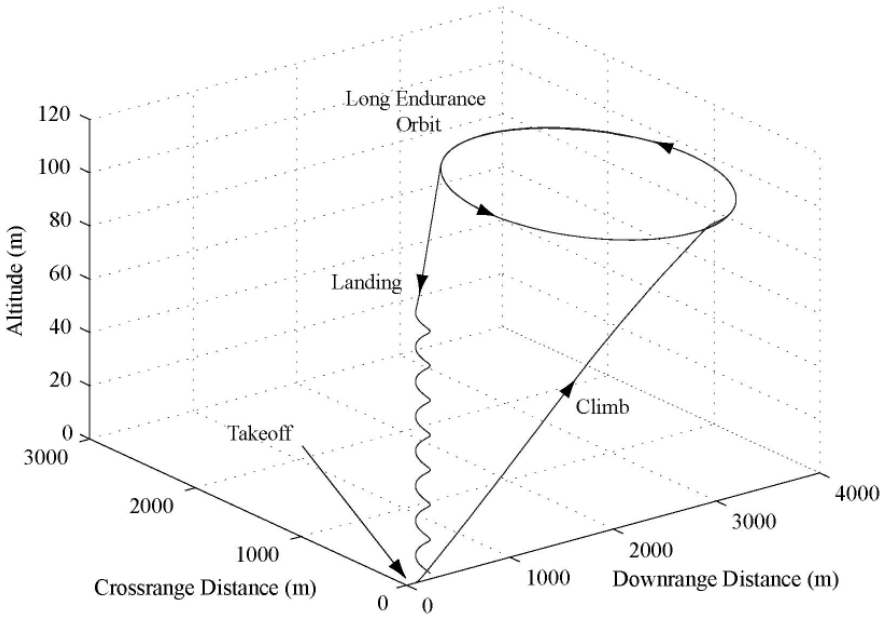

Figure 5.45: Baseline FCUAV mission [63].

5.6.1 Climb

To maximize endurance, climb would be performed at a low climb rate to a prescribed altitude. Even if performed at a higher climb rate, it was assumed that climb would account for a negligible amount of time with respect to overall mission duration. However, the rate of climb is a metric that is consistently used to measure performance. Aircraft with a high rate of climb are desirable as the excess power needed for climb is useful for operating in non-ideal weather conditions. Therefore, the climb analysis focused on predicting the maximum climb rate that is obtainable by the fuel cell aircraft.

The climb rate (V_c) can be calculated as the difference in available power (P_a) and required power (P_{req}) over the aircraft weight (W).

$$V_c = \frac{P_a - P_{req}}{W} \tag{5.70}$$

To maximize the climb rate, both P_a and P_{req} were calculated at the cruise lift coefficient. The climb rate is constrained primarily by P_a which is in turn constrained either by the motor/propeller combination, or by the fuel cell system.

5.6.1.1 Current Constrained Climb

If too much current is required of a fuel cell stack, the voltage will begin to drastically decrease (see Figure 5.23). This is potentially dangerous to both the fuel cell and aircraft and should be avoided. As part of the fuel cell analysis, a maximum current is specified based on the fuel cell MEA. This maximum current corresponds to the maximum power that the fuel cell is allowed to produce. Physically, the aircraft would be required to limit the current of the fuel cell below this maximum current value by

reducing the throttle to a value less than 1. Mathematically, this condition is represented in Eq. (5.71).

$$I_{fc} = I_{\max} \text{ and } D_c \leq 1 \tag{5.71}$$

5.6.1.2 Motor/Propeller Constrained Climb

For some motor/propeller combinations, full throttle at the climb speed can be obtained without reaching the maximum fuel cell current. In this instance, the maximum available power is limited by motor/propeller combination rather than by the fuel cell current. To check for motor/propeller constrained climb, the speed controller model can be set to full throttle (D_c = 1) and the fuel cell current can be compared to the maximum current as shown in Eq. (5.72).

$$I_{fc} < I_{\max} \text{ at } D_c = 1 \tag{5.72}$$

5.6.2 Cruise

Maximizing endurance requires that loiter occur at the maximum of $C_L^{3/2} / C_D$ ratio. For most sailplane configurations, this will be near the onset of stall. For most of the wing/tail combinations analyzed, the maximum endurance condition occurred at an angle of attack of approximately 6.5 degrees.

Assuming that the thrust is aligned with the fuselage reference line for angle of attack, the thrust required can be calculated as a function of *L/D*, weight, and angle of attack.

$$T_{req} = \frac{W}{(C_L / C_D)\cos\alpha + \sin\alpha} \tag{5.73}$$

The airspeed (V_∞) is then related to the required thrust through Eq. (5.74)

$$\frac{1}{2}\rho V_{\infty}^{2} S_{w} C_{D} = T_{req} \cos\alpha \tag{5.74}$$

Providing T_{req} will require a certain power level and hydrogen flow rate. Based on the hydrogen flow rate, hydrogen utilization, and amount of hydrogen stored, a still air endurance value can be estimated. Using this approach assumes that the mass of the aircraft does not change over the course of the mission. This is a reasonable assumption for compressed hydrogen storage as the hydrogen mass will be very small compared to the hydrogen tank mass and the overall aircraft mass. In addition, water from the fuel cell reaction that is not used for evaporative cooling of the fuel cell will remain as part of the overall mass of the aircraft thus diminishing the overall loss of mass.

5.7 Surrogate Models

Most of the subsystem models required minimal to no internal iterations and could be evaluated quickly. The models were also scalable over a large range of design parameters. However, both the propeller and the lifting surfaces routines were computationally intensive, and would require internal convergence parameter changes to provide results over a wide range of design parameters. To improve the speed of the computations and provide a more robust mathematical representation, surrogate models were constructed for both the propeller and the lifting surfaces routines.

5.7.1 Propeller Surrogate Model

By fixing the airfoil and blade planform geometry, the propeller routine was arranged to calculate the thrust and power coefficients as a function of advance ratio and pitch over diameter ratio. Although the propeller routine executed rapidly, previous

design studies using the code had shown that it dominated the overall calculation time for similar aircraft design environments [272, 273].

Three different surrogate models of the propeller analysis were created and compared. These included a response surface, a neural network, and an interpolation routine. To create these surrogates a vast amount of data from the propeller routine was generated. To build the surrogates, a full factorial design of experiments (DOE) was executed with the advance ratio ranging from 0 to 2 in increments of 0.05, and the pitch over diameter ratio ranging from 0.4 to 1.4 in increments of 0.05. In addition, a set of 1000 random points within the design space were also calculated and used as test points.

To capture the behavior of the propeller model, a cubic response surface was used. Initially a quadratic response surface was considered but deemed not appropriate due to the higher order behavior evident in the propeller coefficients (see Figure 5.11 and Figure 5.12). The form of the response surface equation is given in Eq. (5.75). The coefficients of the response surface (β) were solved for using the software JMP [274].

$$y_{cubic} = \beta_0 + \sum_{i=1}^{3} \beta_i x_i + \sum_{i<j}^{3} \beta_{ij} x_i x_j + \sum_{i=1}^{3} \beta_{ii} {x_i}^2 + \sum_{i \le j \le k}^{3} \beta_{ijk} x_i x_j x_k + \varepsilon \tag{5.75}$$

The neural network model is based on the implementation found in JMP [275]. The model uses one hidden layer and is based on S-shaped functions of the form

$$S_H(x) = \frac{1}{1+e^{-x}}. \tag{5.76}$$

The unobserved hidden nodes (H_j) are defined as

$$H_j = S_H\left(c_j + \sum_{i=1}^{N_x} \left(a_{ij} x_i \right) \right) \tag{5.77}$$

where N_x is the number of X variables. The output values (y_k) are calculated using

$$y_k = S_Y\left(d_k + \sum_{j=1}^{N_H} \left(b_{jk} H_j \right) \right) \tag{5.78}$$

where N_H is the number of hidden nodes and S_Y is the identity function. The coefficients *a*, *b*, *c*, and *d* were all estimated using JMP. For the propeller data, the optimum number of hidden nodes was found to be 7.

The interpolation routine is essentially a table lookup of the values generated in the DOE. For interpolation, a 2-D cubic spline approximation is used. The cubic spline interpolation routine is preprogrammed as an option in the Matlab interp2 function [276].

The residual plots for the thrust coefficient and power coefficient surrogate models are given in Figure 5.46 and Figure 5.47. These residuals use the random set of 1000 C_T and C_P cases rather than the DOE used to build the surrogates. The interpolation shows very low residuals for both C_T and C_P while both the neural network and response surface methods fail to capture some of the underlying behavior.

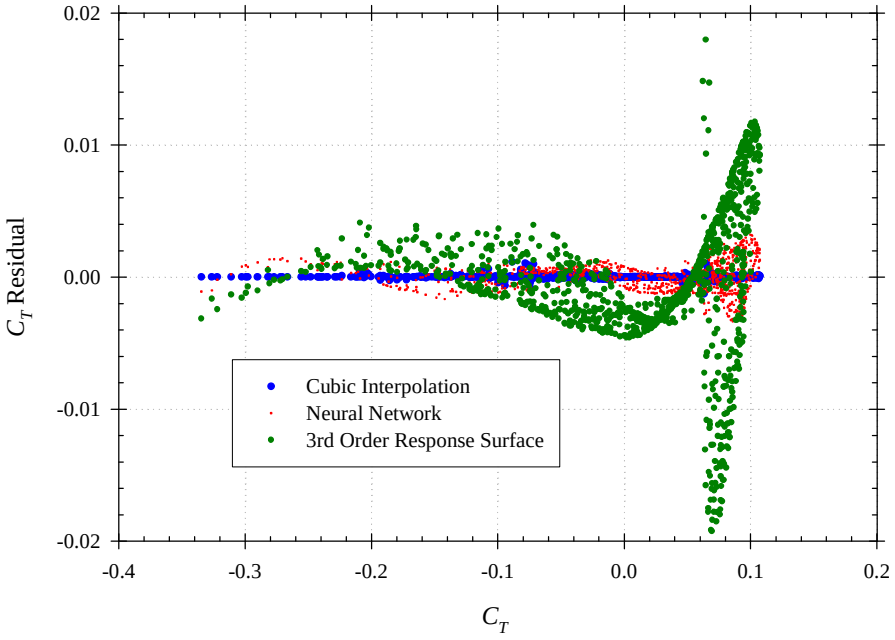

Figure 5.46: Residual plot for three different surrogate models of the propeller thrust coefficient.

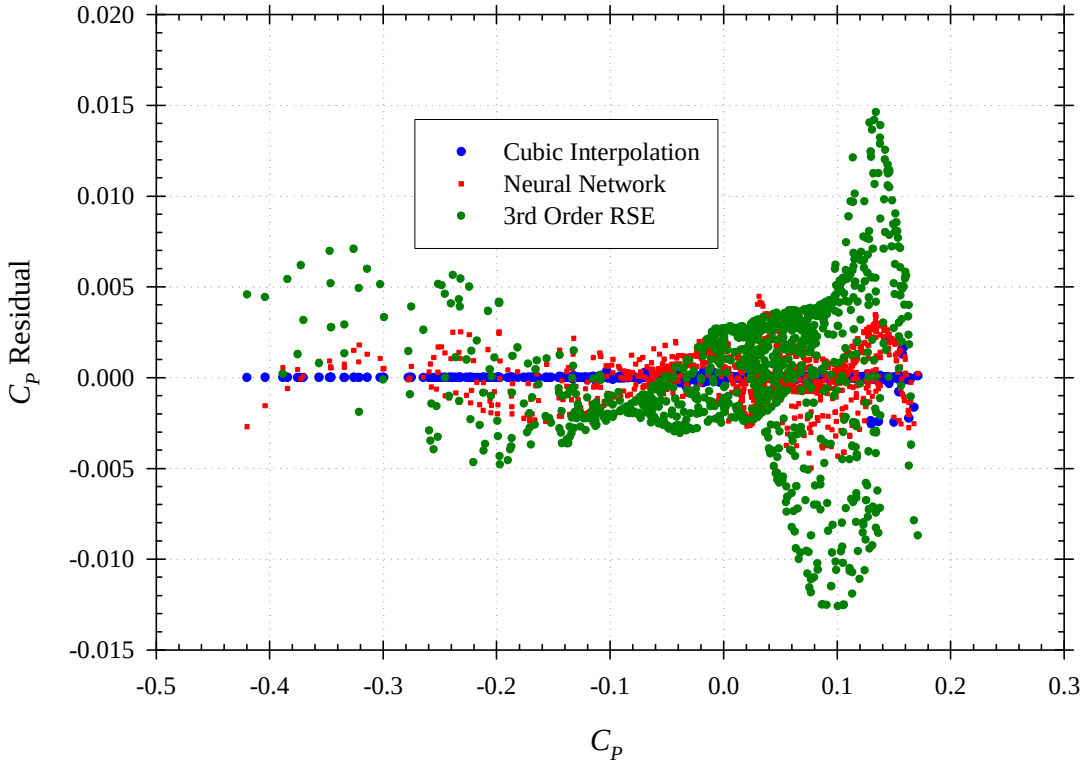

Figure 5.47: Residual plot for three different surrogate models of the propeller power coefficient.

The normalized distribution of the error is shown in Figure 5.48 and Figure 5.49. For both C_T and C_P, the interpolation routines shows very low standard deviation of the error, and the extreme cases are only in error by ~1% for C_T and ~2% for C_P. The neural network model offered better performance but had an order of magnitude higher standard deviation of normalized error.

As a final comparison, the average evaluation time for each calculation of both C_T and C_P was compared (see Table 5.8). The 3rd-order RSE was nearly 3000 times faster than the original propeller code while the interpolation routine was ~100 times faster and the neural network was only 12 times faster. Although not the fastest, the interpolation routine was chosen as the propeller model surrogate.

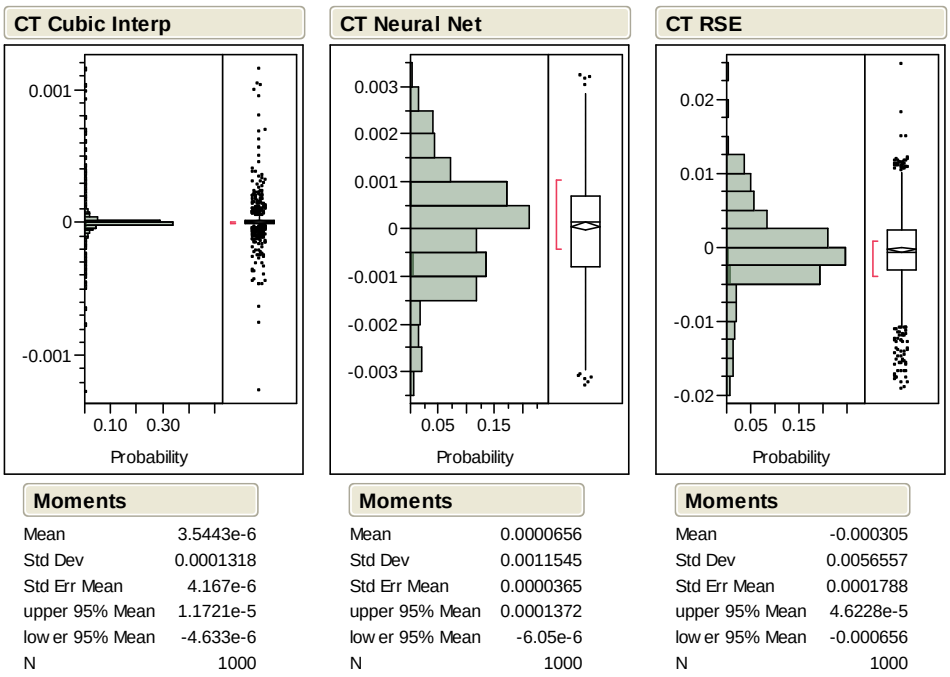

Figure 5.48: Normalized error distribution for propeller thrust coefficient surrogate models.

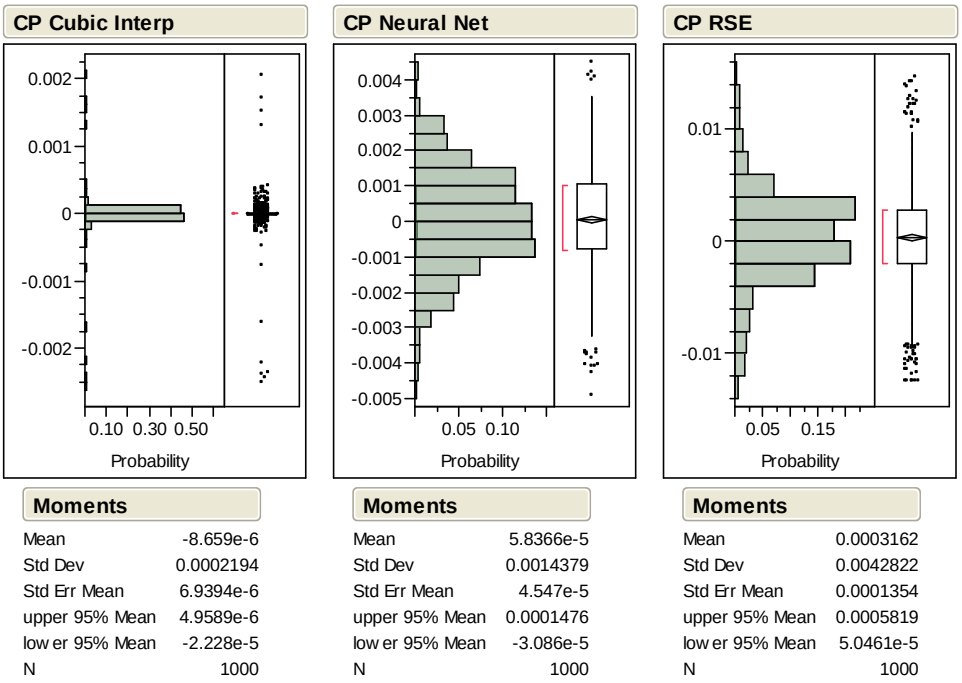

Figure 5.49: Normalized error distribution for propeller power coefficient surrogate models.

Table 5.8: Evaluation time for propeller surrogate models.

Model	Normalized Evaluation Time	Average Evaluation Time for 1000 executions
Propeller Code	1	187.5 s
3rd Order RSE	2977^{-1}	0.063 s
Interpolation	98^{-1}	1.906 s
Neural Network	12^{-1}	15.546 s

5.7.2 Lifting Surface Surrogate

One of the complications of the lifting surface NLL model was the tail sizing. The WINGS code would estimate the static margin and yawing stiffness by varying angle of attack (α) and sideslip over a small range. This procedure occasionally resulted in small errors that would complicate the convergence of the tail sizing routine. In order to make the routine robust enough to work over a large range of input variables, the convergence criteria for the static margin and the yawing moment stiffness had to be relaxed. To observe the effect of relaxing the convergence criteria, a random sample of static margin (S_M) and yawing stiffness (C_{nb}) values for $0.4\text{m}^2 \le S_w \le 3.4\text{m}^2$, $6 \le AR \le 30$, $0.4 \le l_t / (b/2) \le 1.2$, and $-4 \text{ deg} \le \alpha \le 14$ deg was generated. The statistical distribution for this sample is shown in Figure 5.50. Although the distribution is highly concentrated around the target values, the small variations in both the static margin and the yawing stiffness could potentially complicate vehicle sizing and optimization routines, especially if gradient based optimization methods are used.

To smooth out the data, a response surface surrogate model was created. To generate the data for building the response surface surrogate mode, a full-factorial design of experiments was created using the same ranges as the random sample in Figure 5.50

with 16 levels for S_w, 13 levels for AR, 5 levels for l_t / (b/2), and 10 levels for α. Initially, a 2nd order response surface was calculated. The residual plots of the lift (C_{Lwt}) and drag (C_{Dwt}) coefficients of the combined wing and tail surfaces in Figure 5.51 and Figure 5.52 show that the 2nd order response surface fails to capture critical underlying behavior. The normalized error distributions of the 2nd order response surfaces for a set of 472 random samples is shown in Figure 5.53. One standard deviation of error is 8.7% and 11.5% respectively for C_{Lwt} and C_{Dwt}.

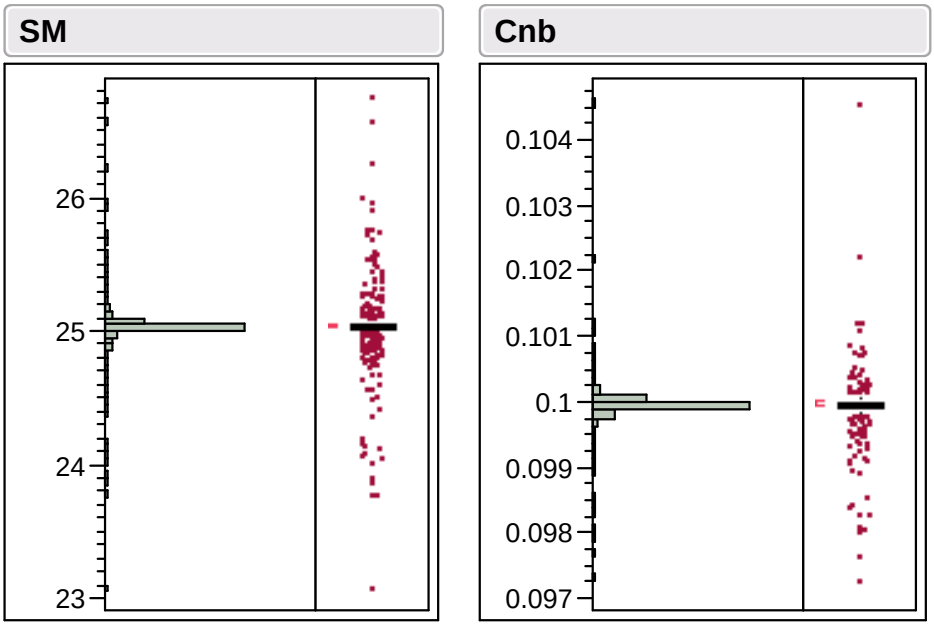

Moments	
Mean	25.031495
Std Dev	0.2809853
Std Err Mean	0.0129334
upper 95% Mean	25.05691
lower 95% Mean	25.006081
N	472

Moments	
Mean	0.099941
Std Dev	0.0004291
Std Err Mean	1.9751e-5
upper 95% Mean	0.0999798
lower 95% Mean	0.0999022
N	472

Figure 5.50: Static margin and yawing stiffness distributions.

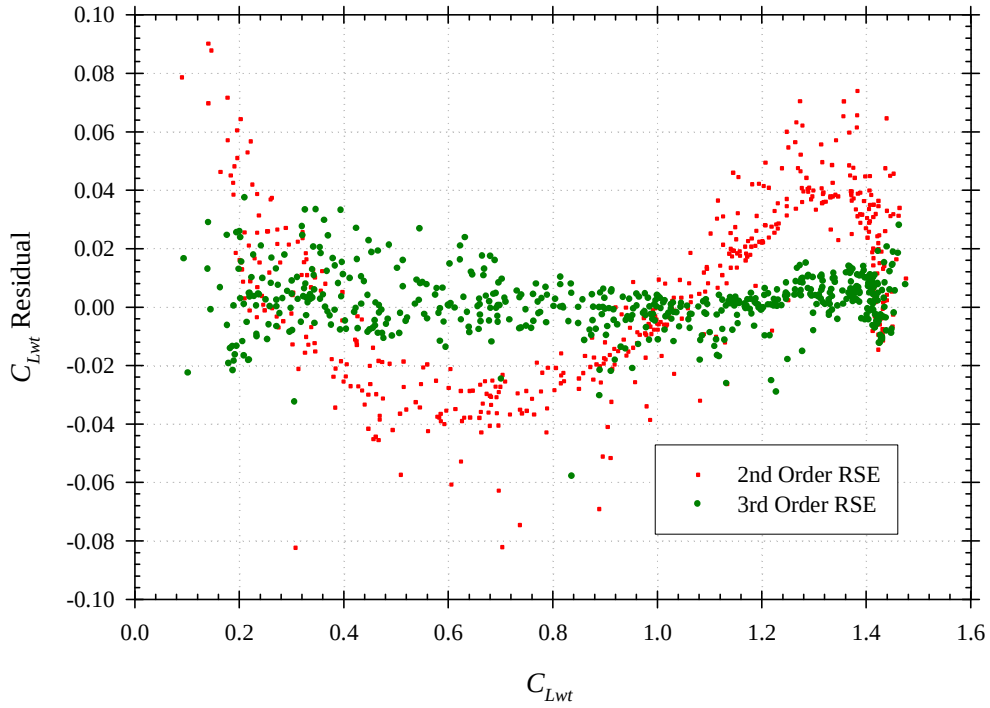

Figure 5.51: Wing and tail lift coefficient residuals for response surface surrogates.

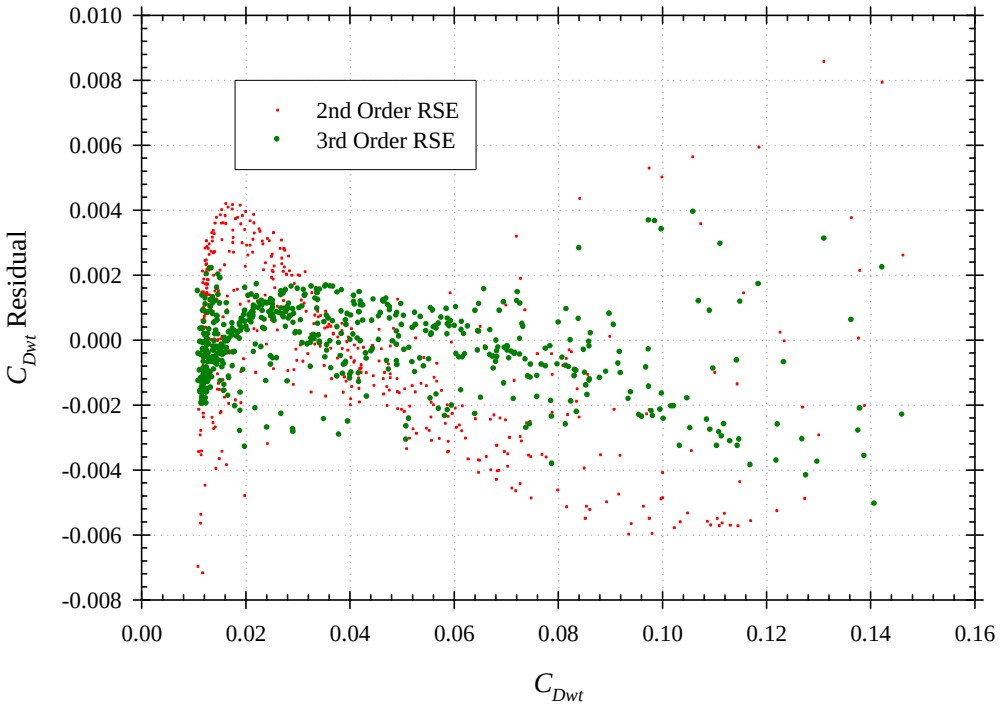

Figure 5.52: Wing and tail drag coefficient residuals for response surface surrogates.

To improve the surrogate, a 3rd order response surface of the form of Eq. (5.75) was generated using the same DOE as was used with the 2nd order response surface. The 3rd order response surface residuals are available in Figure 5.51 and Figure 5.52 and normalized error distribution is given in Figure 5.54. Adding the 3rd order terms to the response surface captures the underlying behavior of C_{Lwt} and reduces the standard deviation of the error distribution to 2.4%. The 3rd order terms also improve C_{Dwt} by reducing the error standard deviation to 5% although some underlying behavior is still not accounted for (see Figure 5.52).

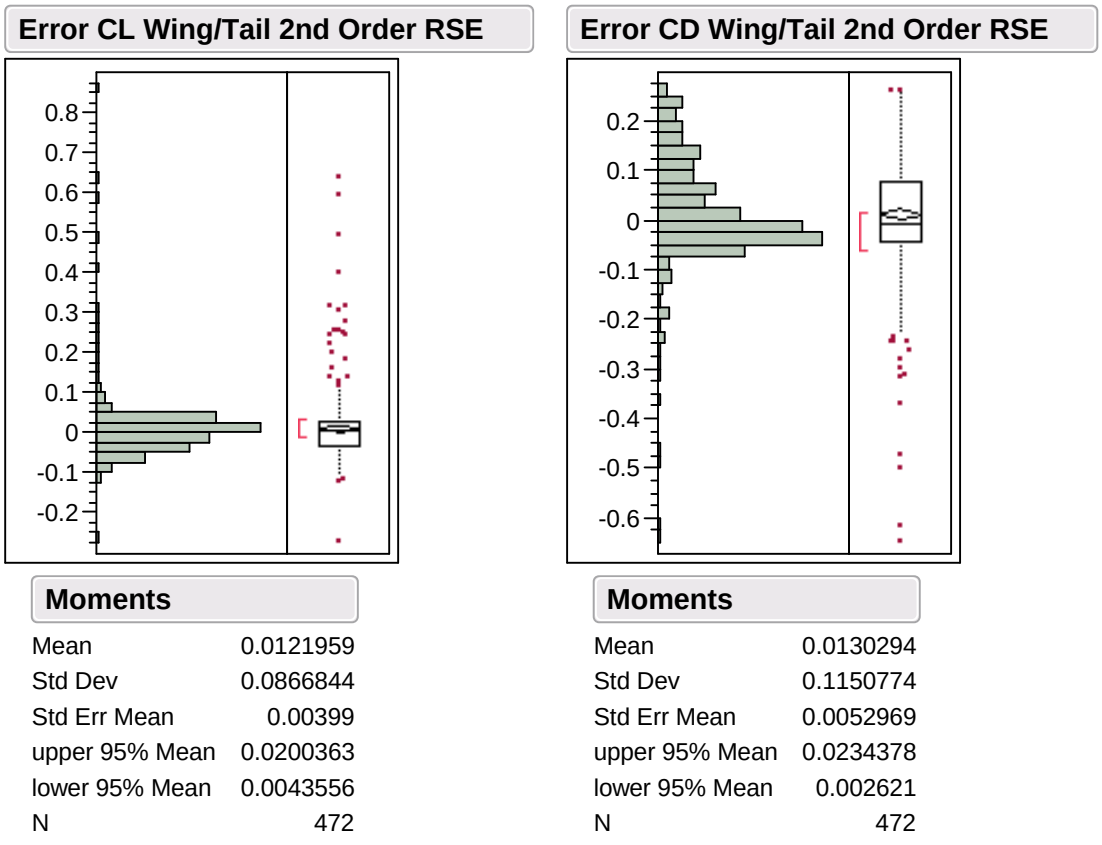

Figure 5.53: Normalized error for the wing and tail lift and drag coefficient using a 2nd order RSE.

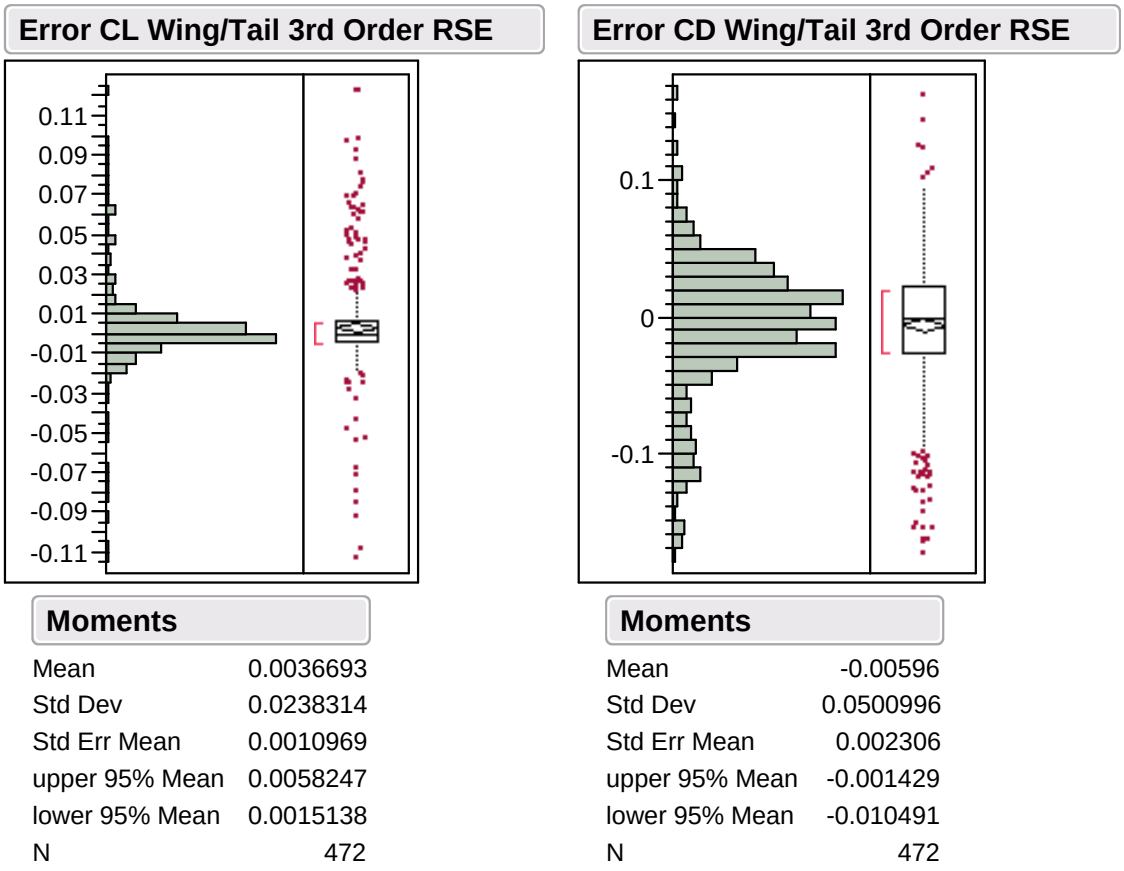

Figure 5.54: Normalized error for the wing and tail lift and drag coefficients using a 3rd order RSE.

Overall, the 3rd order response surface was considered accurate enough to use for design space exploration studies. Apart from smoothing the results of the NLL routine, the 3rd order RSE was also over 45,000 times faster than the WINGS NLL routine. Results from the 3rd order RSE that show the behavior of the RSE are given in Figure 5.55. These results show that the RSE captures the lift and drag behavior with respect to angle of attack including the onset of stall. The model also captures the reduction of the drag with aspect ratio and shows that the normalized tail distance has a small effect on drag as compared to aspect ratio and angle of attack.

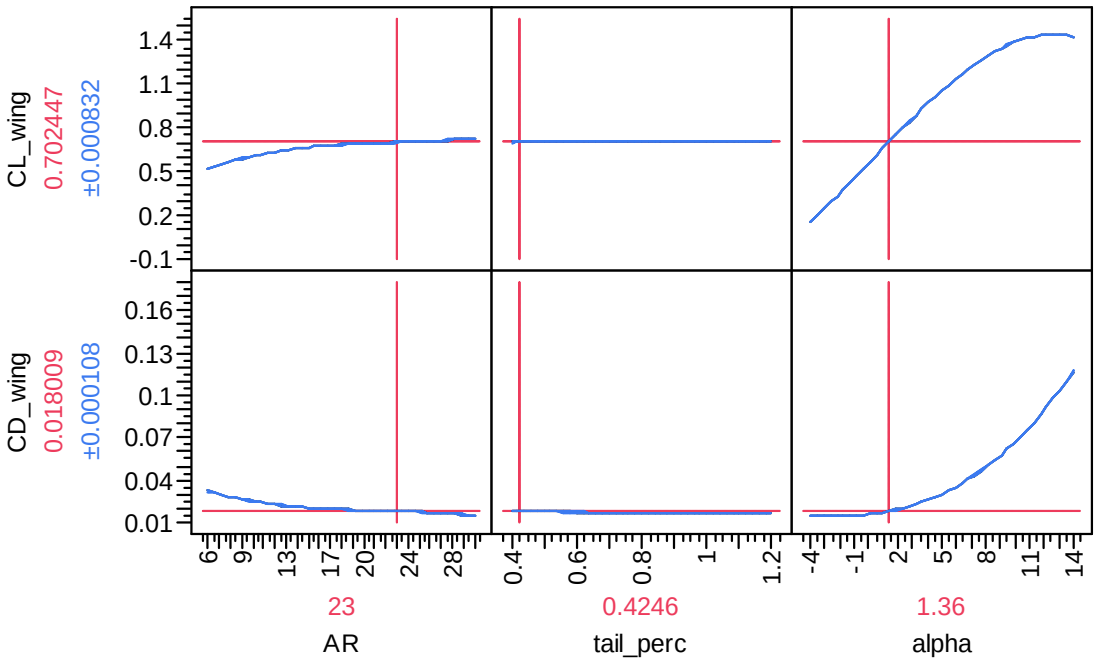

Figure 5.55: Surrogate model predictions for lift and drag coefficients of the wing/tail combination as a function of aspect ratio, tail distance, and angle of attack.

5.8 Chapter Summary

A baseline aircraft architecture was selected. This architecture was influenced by the GT FCUAV and is representative of other small UAVs with total mass less than 25 kg. The baseline aircraft is a sailplane derivative design with an inverted V-tail. The propulsion system consists of a fuel cell, single electric motor, propeller, and compressed hydrogen storage.

An uncertainty propagation analysis showed that endurance and climb rate of the baseline vehicle would be sensitive to propeller efficiency, drag, fuel cell efficiency, maximum fuel cell power, and weight. A mix of empirical and physics based models were developed to model the propulsion, mass, aerodynamics, and flight performance of the aircraft. Many of the models were based on experience gained with similarly sized UAVs including the GT FCUAV. All models were either created from empirical data or

validated using experiments or data available in the literature. Two of the models, the propeller and the lifting surface/ tail sizing analysis were used to build surrogate models. An interpolation routine was used as a surrogate for the propeller analysis to reduce computational time. A 3rd order response surface equation was used to provide a smooth surface approximation of the wing/tail sizing analysis while drastically decreasing computational time.

CHAPTER 6

FLEXIBLE DESIGN FRAMEWORK

This chapter provides a brief introduction to systems design fundamentals common to the aerospace industry. The chapter develops a flexible framework for solving a design structure matrix composed of various CAs. The method is based on simultaneous analysis whereby feedback loops are replaced by compatibility equations. A routine is discussed where feedback loops are identified by examining the hierarchy and inputs and outputs of each CA. The routine then automatically builds compatibility equations that are solved using a non-linear equation solver. Several non-linear equation solvers were tested for both robustness and efficiency.

6.1 System Level Design Introduction

Since complex systems such as a fuel cell aircraft are by nature multidisciplinary, the proper analysis of the system must include a means for exchanging information between the many disciplines. In the past, designers have successfully managed this problem by integrating the many disciplinary contributing analyses into large monolithic analysis codes. However, as technologies advance and analyses become more complex, these large complicated monolithic codes typically become difficult to modify and maintain. To address this problem, simplification and decompositions schemes have developed that provide a structured, logical, and visual method for analyzing multidisciplinary analysis (MDA) problems.

A common scheme in the aerospace industry is to decompose the overall complex system analysis into several manageable contributing analyses (CAs). Contributing analyses are often simply just traditionally defined disciplinary analyses although they can technically be any analysis that is a portion of the entire system. Figure 6.1 shows a typical aircraft MDA.

A useful method for managing the flow of information between the CAs is the use of a design structure matrix (DSM) [277]. A DSM is a hierarchical scheme where the CAs are organized in a diagonal fashion from upper left to lower right as shown in the second box from the left in Figure 6.1. Lines connecting the CAs represent the flow of data between the CAs. The DSM assumes that the CAs are executed serially starting from left to right. As a result, upper diagonally positioned lines represent data that is fed forward while the lower diagonal lines represent feedback data. With the presence of feedback between the CAs, a MDA must consist of some type of framework to execute all of the CAs in the DSM and make sure that feedback variables are in harmony with outputs of the rest of the CAs.

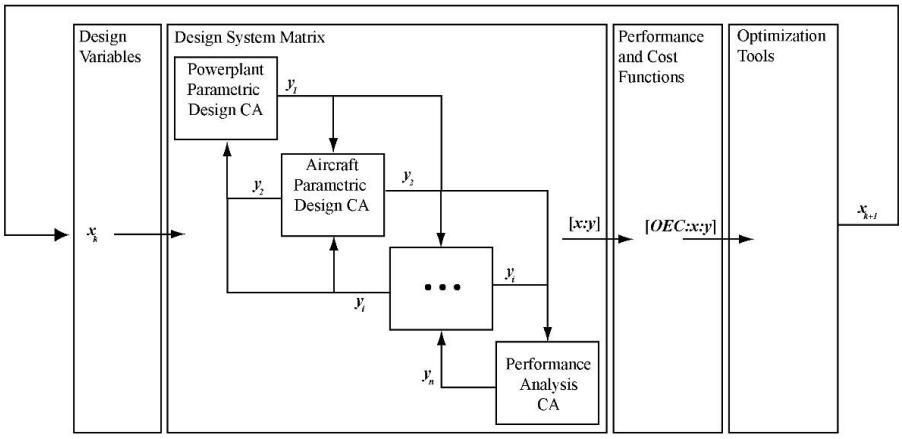

Figure 6.1: Multidisciplinary design optimization environment.

The MDA consists of the DSM and its framework for bringing the CAs into convergence. The MDA can simply be thought of as the system level analysis where design variables are used as inputs and various metrics calculated by the CAs are used as outputs. To optimize a design, an optimization tool is typically used to vary the design variables. Cost functions and constraints are then calculated based on outputs of the CAs and fed into the optimization tool. Inclusion of the optimization tool is common termed multidisciplinary design and optimization (MDO).

6.2 DSM Solution Framework

The process to organize and bring CAs into convergence has been accomplished in multiple ways. The most common practice is nested analysis (NA). In nested analysis, the problem is formulated into a set of nested analyses that are typically solved one variable at a time. Another typical process is referred to in this research as simultaneous analysis. Simultaneous analysis (SA) transforms the DSM into a set of coupled non-linear equations that can then be solved simultaneous using an iterative scheme for coupled equations.

6.2.1 Nested Analysis

The most common method is termed nested analysis (NA). Nested analysis breaks an interdisciplinary problem into a set of nested analyses that can be solved one-variable at a time. Analyses can be nested in various ways. An example of how NA is performed on the propulsion system of a fuel cell aircraft is given in Figure 6.2.

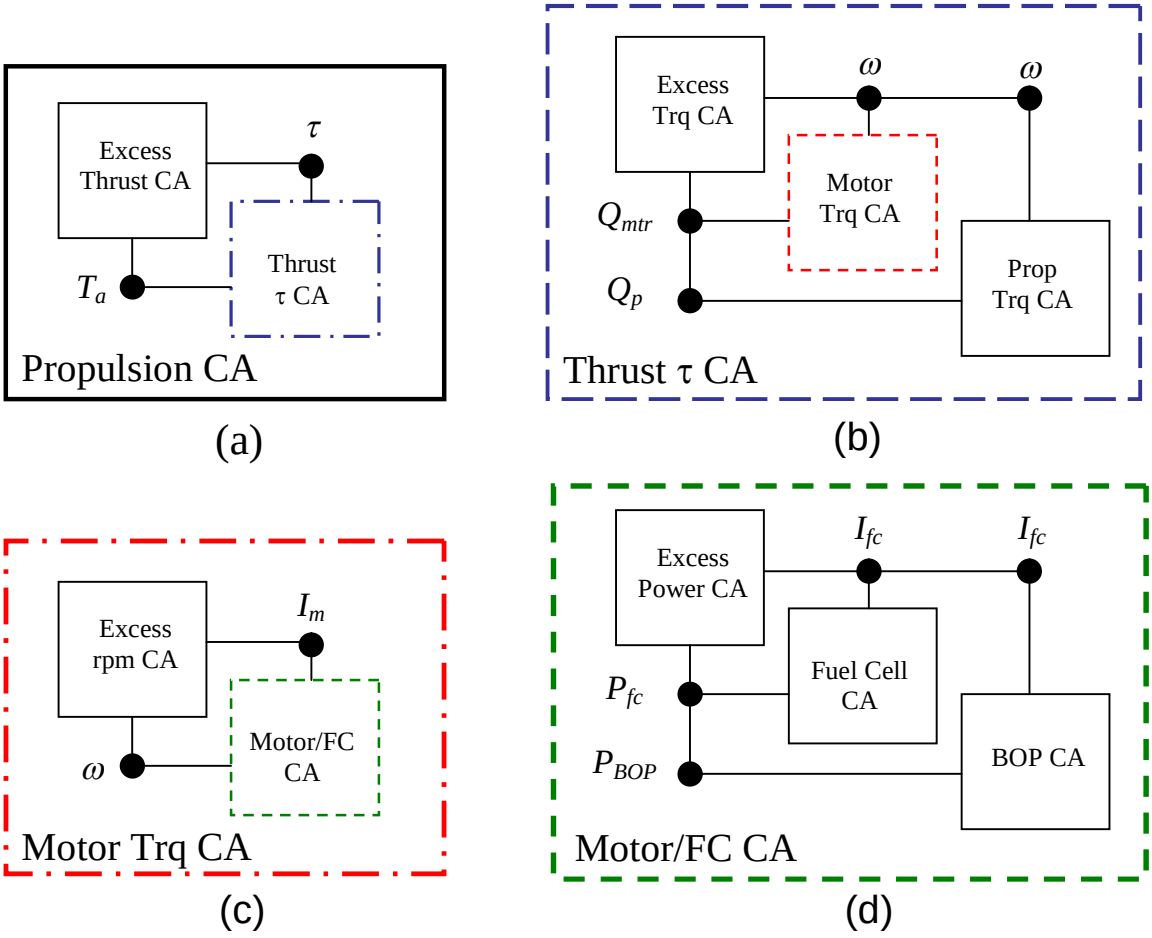

Figure 6.2: Nested analysis for propulsion simulation

Block (a) in Figure 6.2 shows how the *Propulsion CA* functions. In its simplest form, for a given propulsion system at a fixed airspeed and altitude, thrust available (T_a) can be calculated as a function of throttle setting (τ). A root solving algorithm such as the *Excess Thrust CA* routine would compare the calculated and desired thrust and vary the throttle until the calculated and desired thrust values are equal. This iterative analysis would be the outermost iteration loop. However, in order to solve for T_a, the motor and propeller torque need to be matched for a given motor shaft speed (ω). Thus, the *Thrust τ CA* consists of an *Excess Torque CA* (see Figure 6.2 (b)) that varies ω until the output torque of the prop (Q_p) and the motor (Q_{mtr}) are in agreement. This is a nested iteration loop that must be completed for each new τ provided by the *Excess Thrust CA.* The *Thrust τ CA* calls a *Motor Torque CA* (see Figure 6.2 (c)) that must solve for the motor current (I_m) to match the shaft speed creating yet another nested iteration loop. Finally, the *Motor/FC CA* will require a final iteration loop (see Figure 6.2 (d)) that will iterate on fuel cell current (I_{fc}) until the fuel cell and BOP power are in agreement with power that corresponds to the input I_m.

The advantage of nested analysis is that the problem is broken down into single unknown variable problems that can be solved with a variety of robust algorithms. Each nested analysis is relatively straightforward and represents a textbook type engineering problem. The main disadvantage is in terms of efficiency since each iteration of a nested problem will require all deeper nested problems to be brought to convergence.

6.2.2 Simultaneous Analysis

A more elegant solution to solving the *Propulsion CA* is given by the DSM in Figure 6.3. By reordering the CAs that were nested in Figure 6.2, the unknowns

calculated in the two innermost CAs in the nested analysis formulation can be directly solved for by a non-linear equation solver. The remaining problem is one of two equations and two unknowns. As shown in Figure 6.3, a solver can be used to solve these equations simultaneously.

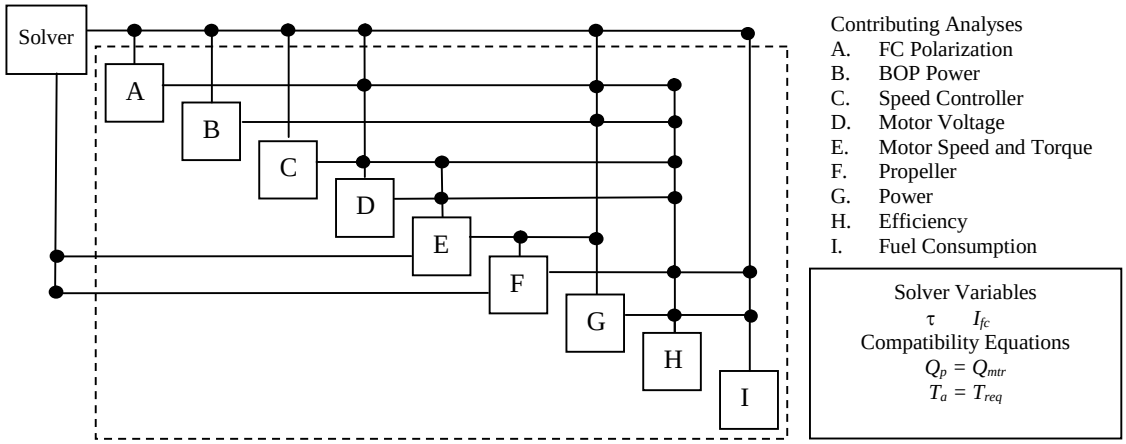

Figure 6.3: Propulsion DSM with compatibility equations for simultaneous analysis.

6.3 Formulation of Flexible DSM Framework

Traditional formulations of either nested analysis or simultaneous analysis have been somewhat ad hoc. More recently, CA scheduling codes such as DeMaid [278] have been used to try and inform the hierarchy of the CAs to reduce the number of feedback variables. However, the solution process for many problems has been specific to a given DSM. The basis of Hypothesis 2 is that the process of building and solving the compatibility equations be automated rather than requiring the designer to come up with a solution process. To automate the process, an algorithm would need to identify the feedback loops, and implement a solution technique. The solution technique would need to be robust to allow for more arbitrary arrangements of the CAs.

6.3.1 Identifying Feedback

Feedback variables can be identified by specifying the hierarchy in which CAs are to be executed, as well as the input and output variables of each CA. To understand the process in which this occurs, the example problem of the propulsion system of a fuel cell UAV is continued.

Using the design rules for creating CAs as stated in Chapter 5, the propulsion system for a fuel cell UAV can be organized into the DSM shown in Figure 6.4. Although the hierarchy of the CAs will affect the number of feedback loops, for purposes of automatically identifying the feedback loops, the ordering of the CAs can be arbitrary. A parsing routine then goes through each CA in the DSM and records the order in which it appears as well as its input and output variables. The routine can then make a comparison of each CA to all of the other CAs in the DSM to determine both the feedback and feedforward variables.

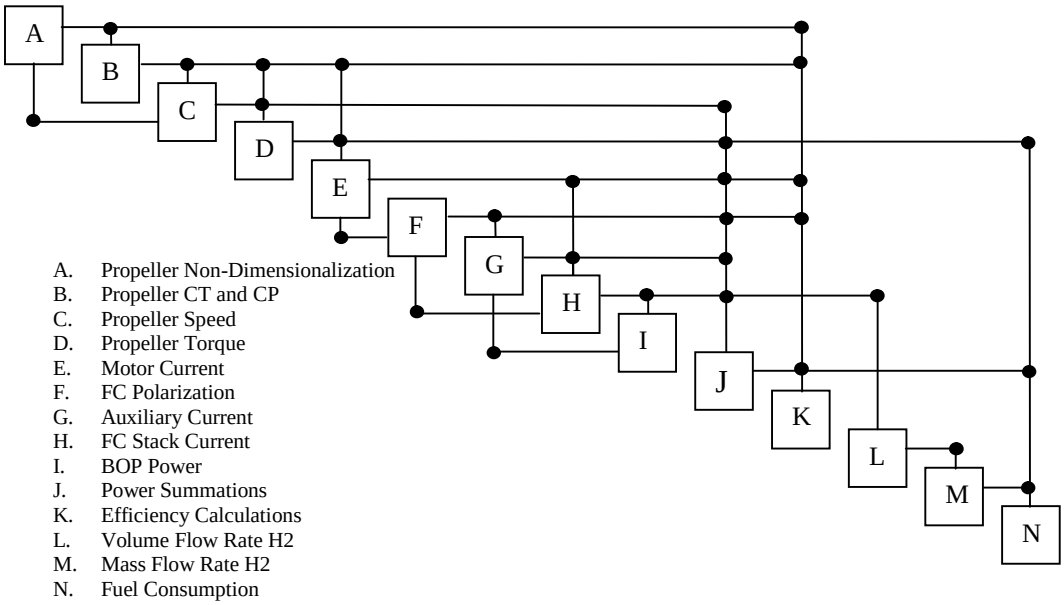

Figure 6.4: Propulsion DSM suitable for SSA.

As an example, in Figure 6.4, the CA labeled *A* calculates the previously defined non-dimensional advance ratio which is repeated here for clarity.

$$J = \frac{V_\infty}{\left(\frac{\omega}{2\pi}\right) d_p} \tag{5.50}$$

The thrust and power coefficients can be calculated in *CA B*, which is a function of advance ratio as shown in Figure 5.11 and Figure 5.12. The previous stated value of the thrust coefficient in Eq. 5.47 can then be solved in *CA C* for the propeller speed.

$$C_T = \frac{T}{\rho\left(\frac{\omega}{2\pi}\right)^2 {d_p}^4} \tag{5.47}$$

The parsing routine recognizes that *CA A* needs ω as an input. It then searches through the CAs and finds that ω is an output of *CA C* and thus creates the first feedback loop. The same process is repeated for each CA until all of the feedback loops are identified. In addition, the same logic is also used to identify all of the feedforward loops.

6.3.2 Compatibility Equations

With all of the feedback loops identified, compatibility equations can be defined. A compatibility equation (*Y*) is defined as the normalized difference between an initial guess for a feedback variable and its value when calculated as an output of a CA as shown in Eq. (6.1).

$$Y = \frac{y_{output} - y_{guess}}{y_{output}} \tag{6.1}$$

The compatibility equations are formulated so that they can be directly passed into a non-linear equation solving routine that will vary the input values (y_{guess}) to be fed into CAs in place of the feedback variables. The solver routine will then iterate on the input values for the feedback loops until all of the compatibility equations are driven to zero. Graphically, this process is shown for the propulsion system example in Figure 6.5. In Figure 6.5, all of the feedback variables have been passed to a solver routine rather than fed back to the appropriate CAs. The solver then passes the guess values to the CAs that require feedback variables. Technically, the solver could also provide the input guess values to all CAs that require the same variable. However, a Gauss-Seidel [270] type procedure can be implemented where CAs calculated after a feedback loop use the most recently calculated value of the feedback loop rather than the guess provided by the solver.

As an example of how the DSM will change if the order of the CAs are changed, Figure 6.6 was generated. To try and eliminate the feedback between *CA C* and *CA A*, the DSM could be reordered to place *CA C* before *CA A*. The resulting DSM eliminates the output of *CA C* as a feedback but instead creates a feedback from *CA B*. As a result, the DSM formulation including a solver to address the compatibility equations would take the form on Figure 6.6. Note that the reordering of the CAs in the DSM in Figure 6.6 did not actually eliminate the number of feedback loops that result in compatibility equations, but it did create a new compatibility equation based on the output of *CA B*. In some cases, reordering the CAs can result in fewer compatibility equations. In other cases, reordering may not change the number of compatibility equations but may create a system of equations that is easier for the solver to solve.

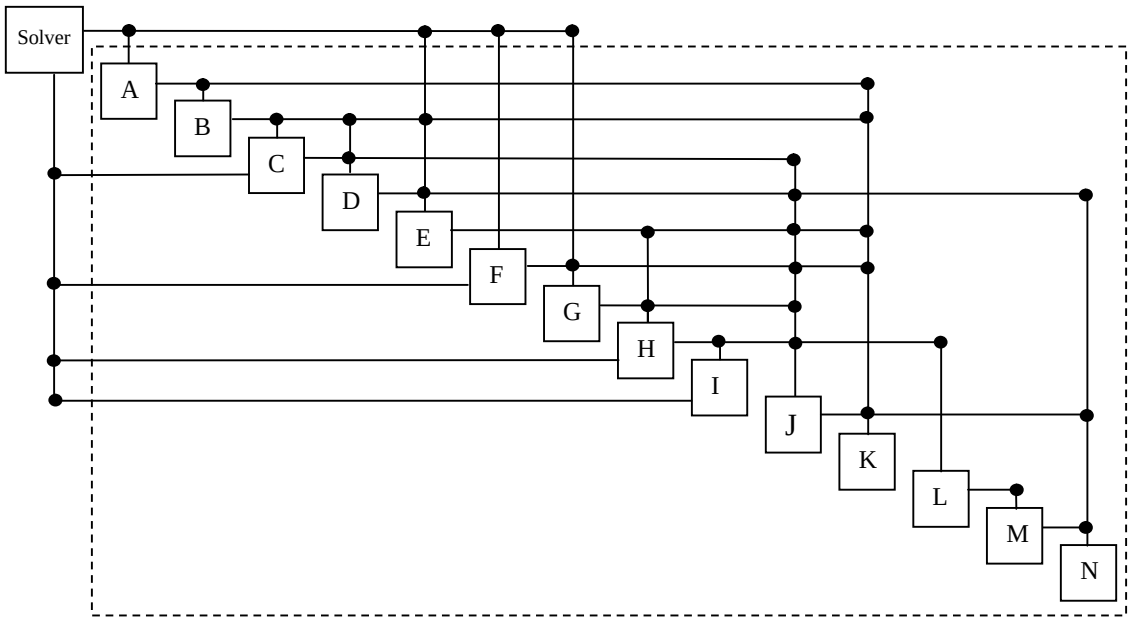

Figure 6.5: Propulsion DSM architecture I with compatibility equations.

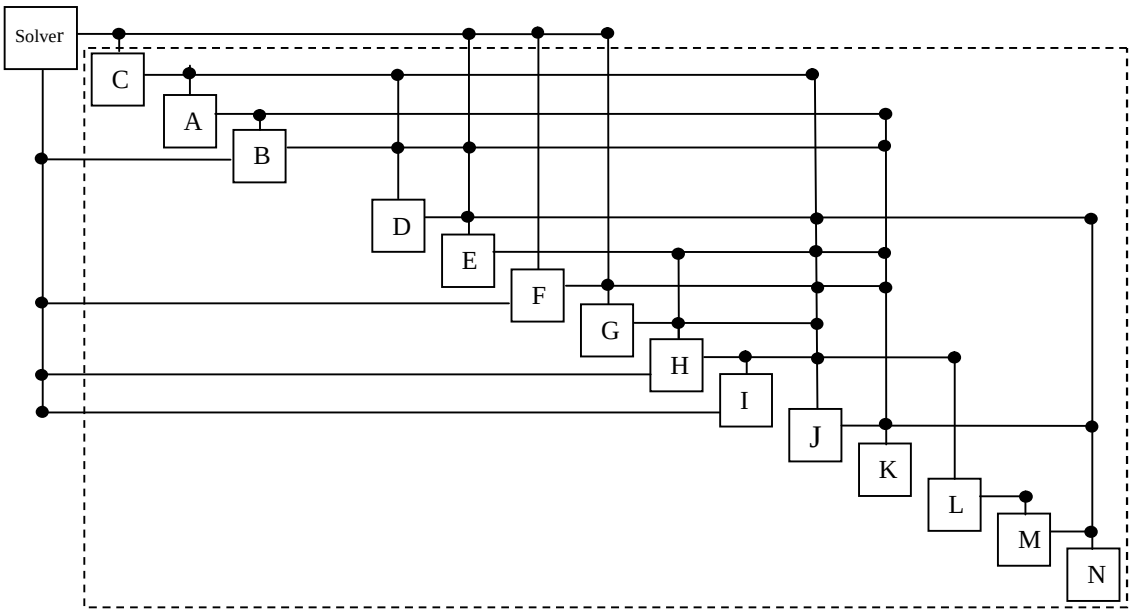

Figure 6.6: Propulsion DSM architecture II with compatibility equations.

6.3.3 Implementation Procedure

The procedure was implemented using a parsing routine. The parsing routine created a vector of all of the design variables and all of the internal variables that were outputs of each CA. A matrix was then stored for each CA that which CAs and specifically which variables for each CA it was coupled with. Looping through each of the CAs in the DSM was a simple procedure that used both the design variables and CA output variables vectors. When a CA was executed, the code looked at the positions in the design and CA output variable vectors where the necessary inputs were stored. The outputs were then written to CA output variable vector. If a CA required an input that had not yet been calculated in placed in the CA output vector, then the guess provided by the solver would be used.

In addition to making the DSM solution framework flexible, the implementation procedure also provides valuable information needed for executing the SSA. The parsing information that determines the coupling between CAs is also needed by the SSA code when calculating the partial derivatives in used in both the **LSM** and **LSV** matrices. The implementation procedure is also useful for executing Monte Carlo simulations since values in the design variable and CA output variable vectors can easily be modified according to a prescribed uncertainty distribution.

6.3.4 Nonlinear Equation Solvers

The SA method is based on the assumption that the nonlinear set of compatibility equations can be robustly solved. Fortunately, there are several techniques that have been developed to solve a system of nonlinear equations. A comparison of several methods is provided in reference [279]. To choose a nonlinear equation solver, the

DSMs shown in Figure 6.5 (Architecture I) and Figure 6.6 (Architecture II) were tested. Each architecture was tested with the Powell-dogleg [280, 281] , Levenberg-Marquardt [282, 283], Gauss-Newton [284], fixed point iteration (FPI) [285], and interior-reflective Newton [286, 287] methods. One-thousand cases were evaluated for each solution method. Initial guesses were selected randomly from the ranges in Table 6.1.

Table 6.1: Feedback inputs for nonlinear equation solver comparison.

	Feedback Variable	Converged Value	Low Guess	High Guess
Architecture I	Propeller Speed (rpm)	1945.83	1500	2500
	Fuel Cell Voltage (V)	45.1157	39.6	48.4
	Fuel Cell Current (A)	4.41989	2	6
	BOP Power (W)	6.49605	2.5	7.5
Architecture II	Propeller Thrust Coefficient	0.0407242	0.0375	0.0625
	Fuel Cell Voltage (V)	45.1157	39.6	48.4
	Fuel Cell Current (A)	4.41989	2	6
	BOP Power (W)	6.49605	2.5	7.5

The performance of each method in terms of function calls (number of times all CAs is the DSM were executed), solution time, and failure rate is summarized in Table 6.2 as well as Figure 6.7 and Figure 6.8. For DSM Architecture I, the Gauss-Newton, Powell Dogleg, and FPI methods required the fewest number of functions calls. Likewise, these same methods also required the fewest number of function calls for DSM Architecture II. Considering both architectures, the FPI method required the least number of iterations. However, for failure rate, the Powell Dogleg approach was the most robust over both architectures.

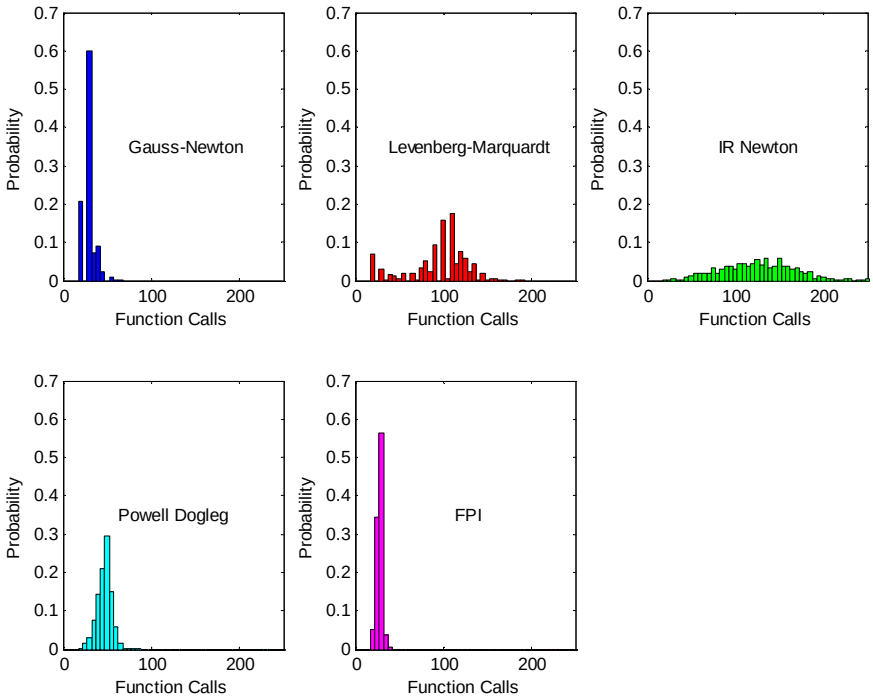

Figure 6.7: Function call distributions for various solution methods applied to DSM Architecture I.

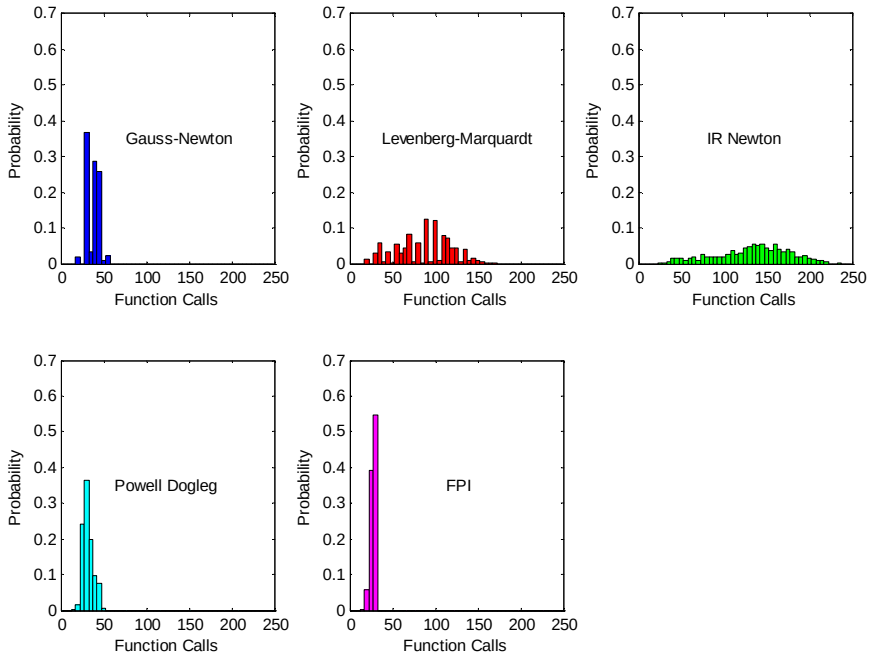

Figure 6.8: Function call distributions for various solution methods applied to DSM Architecture II.

Table 6.2: Summary of methods used to solve the different DMS architectures.

		Average Iterations		Average Function Calls		Solution Time Average (s)		Average Failure Rate	
	Design Structure Matrix	I	II	I	II	I	II	I	II
Method	Powell Dogleg	9	6	47	32	2.30	1.62	4.70%	0.00%
	Gauss-Newton	4	5	29	37	1.51	1.82	6.50%	3.50%
	IR Newton	25	27	126	134	5.85	6.35	4.70%	0.00%
	Levenberg-Marquardt	11	11	95	89	4.53	4.25	5.70%	1.40%
	Fixed Point Iteration	28	27	28	27	1.47	1.48	5.50%	0.00%

The results did vary based on the DSM architecture with Architecture II being the more robust out of the two architectures. This robustness was due to how information propagates through the propeller routine. For DSM Architecture I, the solver routine must vary the propeller rpm whereas in DSM Architecture II, the thrust coefficient must be varied. It is much easier to specify a thrust coefficient as the value does not vary as drastically for different propeller designs. Most guesses for thrust coefficient will result in feasible results for other CA variables including the propeller speed. However, it is much easier to choose a propeller rpm value that will cause a negative thrust coefficient as propeller speed can vary drastically for different designs. Regardless of the architecture, for most reasonable input guesses, the nonlinear equations are able to be solved nearly 95% of the time.

6.4 Chapter Summary

This chapter focused on the development of a flexible framework for building and solving a design structure matrix. The method was based on simultaneous analysis where the solution of the DSM was formulated into a number of coupled nonlinear compatibility equations. The compatibility equations were automatically identified by the framework through the use of a parsing routine that examined the hierarchy and input

and output variables for each CA. The framework requires a nonlinear equation solver. Five common equation solvers were tested for efficiency and robustness during the solution of a sample fuel cell propulsion system consisting of 14 CAs. The results suggested that the Powell-dogleg solution method had the best compromise between efficiency and robustness.

CHAPTER 7

OPTIMIZATION FORMULATION

Nearly all studies into fuel cell aircraft design have noted that uncertainty would play a significant role although only a few methodologies have proposed ways to include uncertainty in the analysis. According to Keane and Nair [285], design optimization in the presence of uncertainty involves three steps: (1) identification, modeling, and representation of uncertainty, (2) propagating uncertainties through computer models to quantify their impact on system performance, and (3) formulation and solution of an optimization problem with appropriate objective and constraint functions that ensure the optimum solution obtained is robust against uncertainties. Steps 1 and 2 were addressed in Chapter 4 with the introduction of SSA. In SSA, it is assumed that uncertainty in design variables and CA calculations can be modeled as statistical distributions, and then propagated through the system using the sensitivity information provided by SSA. This chapter focuses on step (3), providing a formulation and solution technique for the optimization problem.

7.1 Optimization under Uncertainty

Although not always explicitly stated, aerospace design has addressed optimization under uncertainty by various methods. A simple approach prevalent throughout past and current design methodologies is the use of safety factors. Safety factors, sometimes referred to as design margins, are applied to assure that the resulting design will remain feasible assuming that the propagated effects of uncertainty will likely

cause constraint violations. If these safety factors overly constrained the design space, designers typically proceed by performing experiments, resorting to high fidelity analyses, building prototypes, or just deciding to move forward with a risky design in hopes of learning the lessons and gathering the data needed to achieve success.

An additional method that appears in the literature is the use of an interval representation of uncertainty [192]. In its basic form, this method assumes that an uncertain parameter can be specified with both an upper and lower bound. These interval bounds are then propagated through the analysis models to arrive at the system level bounds. Optimization can then be informed by the system level bounds. Interval bounding has be demonstrated on engineering systems by researchers such as Rao and Chen [288].

An extension to the interval representation is convex modeling [289]. If uncertainty parameters are scalars, then convex modeling reduces to an interval representation of uncertainty. However, for higher dimensions, uncertainty is represented as a convex set. The use of convex sets has led to information-gap (info-gap) theory [290, 291]. For the purpose of making design decisions, info-gap theory searches for a design that is immune to failure or can tolerate the largest amount of uncertainty before failure while still meeting certain performance constraints.

The previous methods discussed are generally applied when limited information is available about uncertain parameters in the design. For uncertainty sources that are better understood, probabilistic approaches have been formulated. Probabilistic approaches are based on assuming distributions for random variables. These distributions will result in system level metrics that will also be random variables with associated probability

distributions. The general optimization problem is to minimize a given objective function subject to satisfying the probabilistic constraints. Different formulations exist, but typically either the expected value or variance of a given objective function is minimized or maximized subject to satisfying each constraint according to a specified probability.

Several approaches exist to solving probabilistic optimization problems. The simplest approach involves the use of averaging. This approach simply sets random variables at their mean value and then formulates a deterministic optimization problem. The essential problem with this method results when designs are highly constrained and thus lie at the intersection of one or more constraints. Based on the fundamental assumption of averaging, a design that lies on a constraint boundary would only have a probability of 0.5 of satisfying that constraint.

One of the most popular approaches in dealing with any design under uncertainty is reliability-based design optimization (RBDO). Using the mean values of the uncertain variables, the expected value of the objective function is optimized subject to probabilistic constraints that are satisfied at a specific reliability level. Thus RBDO quantifies the tradeoff between optimality in the objective function and probability of violating the nearest constraints [292]. Currently, several formulations exist for solving RBDO including single loop, double loop, sequential methods, and unilevel methods. A good comprehensive comparison of these methods is given by Agarlwal [195].

Reliability-based design optimization problems typically formulate constraints based on the probability of failure. This is largely due to the fact that RBDO has been largely developed and used in structural optimization problems that focus on predicting

failure modes. An equivalent formulation that states the constraints as a probability of success is often termed chance-constrained programming (CCP).

Another slightly different probabilistic method is the deterministic solution sampling (DSS) method [176]. This method solves a number of deterministic optimization problems where random variables are sampled from their corresponding probability distributions. The DSS formulation however does not guarantee that the solution will meet the given constraints with a specified probability. Instead it provides a "wait and see" approach that results in a distribution of designs that are possible based on various ways in which the constraints could vary as a result of their random parameters.

The objective of this research is to provide a methodology for a validated design space exploration of fuel cell UAVs. The existence of validation data suggests that a probabilistic approach to capitalize on this data is most appropriate. Out of the probabilistic optimization formulations, Nam has concluded that CCP is the most germane approach to formulate aircraft sizing problems involving uncertainty [176]. This research follows this recommendation by implementing the CCP formulation into the overall methodology.

7.2 Probabilistically Constrained Optimization Formulation

For a deterministic constrained optimization problem, the standard form can be written as Eq. (7.1) where **x** is a vector of design variables and g_i is the i^{th} inequality constraint.

$$\begin{aligned} &\text{Minimize: } f(\mathbf{x}) \\ &\text{Subject to: } g_i(\mathbf{x}) \le 0 \end{aligned} \qquad (7.1)$$

The CCP formulation extends the formulation in Eq. (7.1) by allowing both the constraints and objective function to become random variables. The optimization process then strives to minimize the expected value of the objective function subject to probabilistic constraints. Mathematically, the CCP formulation is given in Eq. (7.2) where $\boldsymbol{\xi}$ is a random vector that can account for uncertainty in both the design variables ($\mathbf{x}$) and in calculations that contribute to both the objective function and the constraint functions.

7.2.1 Individual Target Probabilities

The more general case is where each of the i^{th} constraints are allowed to have an unique target probability (α_{gi}) in the range of 0-1.

$$\begin{aligned} &\text{Minimize: } E\left[f\left(\mathbf{x},\boldsymbol{\xi}\right)\right] \\ &\text{Subject to: } \mathrm{P}\left(g_i\left(\mathbf{x},\boldsymbol{\xi}\right)\le 0\right)\ge \alpha_{gi} \end{aligned} \tag{7.2}$$

For uncertainty propagation, the SSA algorithm will calculate a standard deviation for each output variable assuming a normal distribution. Therefore, both the objective function and each of the constraints need to be formulated in the DSM as CAs. In standard optimization form where all inequality constraints are non-positive, the optimization problem in Eq. (7.2) can be written as Eq. (7.3).

$$\begin{aligned} &\text{Minimize: } E\left[f\left(\mathbf{x},\boldsymbol{\xi}\right)\right] \\ &\text{Subject to: } \alpha_{gi} - \Phi\left(z_i\right)\le 0 \end{aligned} \tag{7.3}$$

The standard normal cumulative distribution function in Eq. (7.3) is defined in Eq. (7.4).

$$\Phi\left(z\right)=\int_{-\infty}^{z}\frac{1}{\sqrt{2\pi}}e^{-u^2/2}\,du=\frac{1}{2}\left(1+erf\left[\frac{z}{\sqrt{2}}\right]\right) \tag{7.4}$$

Since the i^{th} constraint is assigned a standard deviation σ_{gi} by the SSA, and the right-hand-side of the constraint formulation in Eq. (7.3) is zero, the standard normal random variable for the i^{th} constraint can be written as Eq. (7.5).

$$z_i = \frac{g_i(\mathbf{x}, \boldsymbol{\xi})}{\sigma_{gi}} \tag{7.5}$$

7.2.2 Joint Probabilistic Constraints

The formulation in Eq. (7.2) allows for each constraint to be satisfied at a different target probability. In many cases, it is desirable to optimize a design such that the joint probability, or the probability of meeting all of the constraints simultaneously is at or above a given target probability. The joint probabilistic formulation is a simple modification of Eq. (7.2).

$$\begin{gathered} \text{Minimize: } E\left[f(\mathbf{x}, \boldsymbol{\xi})\right] \\ \text{Subject to: } \mathrm{P}\left(g_i(\mathbf{x}, \boldsymbol{\xi}) \le 0\right) \ge \alpha_{gi} \\ \text{where } \alpha_{gi} = \alpha_{JTP} \text{ for } i = 1 \ldots n \end{gathered} \tag{7.6}$$

In Eq. (7.6), α_{JTP} is the joint target probability value and remains constant for each constraint. When assuming normal distributions as is done in SSA, the formulation can be written as Eq. (7.7).

$$\begin{gathered} \text{Minimize: } E\left[f(\mathbf{x}, \boldsymbol{\xi})\right] \\ \text{Subject to: } \alpha_{JTP} - \Phi(z_i) \le 0 \end{gathered} \tag{7.7}$$

7.2.3 Solution Techniques

The solution process for implementing Eq. (7.3) or Eq. (7.7) is straightforward. The optimization process drives the selection of the design vector values. For each iteration of the optimization process, SSA is executed so that the standard deviations of both the objective function and each of the constraints can be calculated. This is typically referred to in the RBDO literature as a double-loop method with the outer loop representing the optimization process and the inner loop representing the uncertainty propagation (see Figure 7.1).

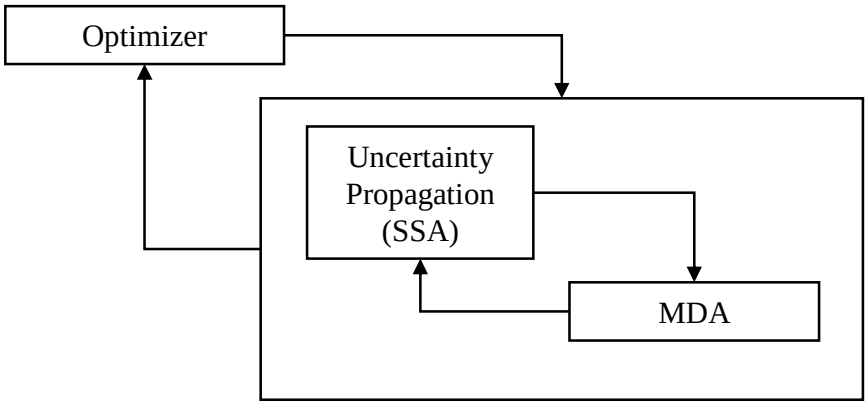

Figure 7.1: Double-loop method for implementing CCP formulation.

In general, double-loop methods are computationally expensive, especially if Monte Carlo simulations are used in the inner loop. However, for this implementation, the SSA analysis is much more efficient than Monte Carlo and has the advantage that it can be conducted in parallel. Researchers have addressed efficiency with RBDO methods and have proposed several solution methods including single loop, double loop, sequential methods, and unilevel methods. A good comprehensive comparison of these methods is given by Agarlwal [195].

7.2.4 Pareto Frontier Calculation

In most design problems, there are more than one objective functions. In many cases, the multiple objective functions will trade against each other where one will only improve at the expense of the other. In this case, it is very useful to define the limits of the design space via calculating a Pareto frontier. By definition, a Pareto optimum is a point where no improvement in one objective function can be made without causing a negative effect in another objective function. The Pareto frontier is made up of multiple Pareto optima.

Pareto frontiers are often calculated by exploring a large number of designs throughout the design space and then examining how the extremes compare to various objective function values. The Pareto frontier can also be directly calculated via multiple optimizations as described by Vanderplaats [293] and Mattson and Messac [193]. If f_{2T} is defined as a target value of a second objective function located between some low and high limits (f_{2L} and f_{2H}), the Pareto frontier can be calculated using Eq. (7.8).

$$\begin{gathered} \text{For } f_{2L} \le f_{2T} \le f_{2H} \\ \text{Minimize: } E\left[f(\mathbf{x},\boldsymbol{\xi})\right] \\ \text{Subject to: } \mathrm{P}\left(g_i(\mathbf{x},\boldsymbol{\xi}) \le 0\right) \ge \alpha_{gi} \\ E\left[f_2(\mathbf{x},\boldsymbol{\xi})\right] \le f_{2T} \end{gathered} \tag{7.8}$$

Equation (7.8) assumes that the Pareto frontier is calculated between the expected values of two competing objectives. This is useful for making a trade between two competing performance metrics such as weight and endurance. The Pareto frontier could also be calculated in the same fashion to determine the tradeoff between the expected value of the objective function and the probability of satisfying a given constraint.

$$\begin{aligned} &\text{For } \alpha_L \le \alpha_T \le \alpha_H \\ &\text{Minimize: } E\left[f(\mathbf{x},\boldsymbol{\xi})\right] \\ &\text{Subject to: } \mathrm{P}\left(g_i(\mathbf{x},\boldsymbol{\xi}) \le 0\right) \ge \alpha_{gi} \\ &\mathrm{P}\left(g_T(\mathbf{x},\boldsymbol{\xi}) \le 0\right) \ge \alpha_T \end{aligned} \qquad (7.9)$$

7.2.5 Optimization Schemes

There is a rich literature of optimization schemes that can solve the outer-loop of the CCP formulation. Some of the methods that are commonly used consist of the method of feasible direction (MoFD) [294], sequential quadratic programming (SQP) [295], and sequential linear programming (SLP) [296].

7.2.6 Penalty Function

The outer loop of the CCP formulation can also be solved with various unconstrained optimizers. To allow the use of unconstrained optimization techniques, a penalty function is defined as Eq. (7.10).

$$\varsigma(x) = \sum_{i=1}^{m} \left(\max\left[0, \alpha_{gi} - \Phi(z_i)\right]\right)^2 \qquad (7.10)$$

The resulting pseudo objective function is then defined in Eq. (7.11) where λ is a scalar multiplier that determines the magnitude of the penalty.

$$F(\mathbf{x},\boldsymbol{\xi},\lambda) = E\left[f(\mathbf{x},\boldsymbol{\xi})\right] + \lambda\zeta(x) \qquad (7.11)$$

The pseudo objective function is meant to be used as part of a sequential unconstrained minimization technique (SUMT) [297] where multiple optimizations are performed with λ increasing with each successive optimization. However, throughout this research, it was found that the non-gradient based unconstrained optimizers tested

with the pseudo objective function could reliably find an optimum in a single optimization with a sufficiently large value of λ.

7.3 Optimization Performance

In order to be useful for exploring the design space, an optimization scheme needs to be able to robustly solve a constrained optimization problem. To be robust, the optimization scheme must be able to locate the an with varied initial guesses. To determine the robustness of the various optimization methods, a performance analysis was conducted. The optimization methods consisted of SQP, as well as two non-gradient methods: the compass search, and the Nelder-Mead [298, 299] simplex method. The example problem uses the propulsion system DSM that was used as a test problem in Chapter 6. The fuel cell, motor, propeller, and BOP are based on a hardware-in-the-loop FCUAV propulsion system described in Bradley et al. [300]. The objective function seeks to minimize the hydrogen flow rate while changing multiple design variables. In the design space studied, the diameter and pitch of the propeller are they most influential design variables.

7.3.1 Sequential Quadratic Programming

The design space is shown in Figure 7.2. Contours of the throttle setting and the hydrogen flow rate are also shown. For throttle settings above 1, the design is not physically possible. Although the MDA will still converge for a few designs with a throttle setting above one as shown in the upper left corner of Figure 7.2, the MDA often fails resulting in the non-continuous contours shown in the bottom left corner of Figure 7.2. Side constraints for the propeller variables constitute the axes of Figure 7.2.

Three different feasible initial conditions are shown in Figure 7.2. Each point represents an iteration. The pink line shows the ideal behavior of SQP. In only three iterations, SQP converged to a point very close to the optimum. As SSA was used to develop all gradients for SQP, the MDA only had to be called 4 times.

Despite its efficiency, SQP lacked robustness over different initial guesses. A second initial condition resulted in the green path. This path starts out making progress over the first three iterations, but then jumps to the lower bound for pitch over diameter ratio. Unfortunately, the combination of propeller diameter and pitch at this lower bound produces an infeasible design that causes the MDA to fail which ends the optimization process. A similar trend is noted for the initial condition resulting in the red path. Here, the design immediately moves to a side constraint in the infeasible region. However, at this side constraint the MDA does not fail allowing SQP to move back into the feasible region and eventually find the solution.

The tendency of SQP to immediately move to side constraints caused many MDA failures during its testing. With a highly constrained design space, it is difficult to know *a priori* the proper side constraints that will bound the feasible space given that the SQP algorithm will allow occasional constraint violations during the solution process. An attempted remedy of this problem was a reduction in the maximum SQP step length allowed in each iteration. The results for the same initial conditions are given in Figure 7.3.

When the design step size was limited to a length of 10% of the design space, the problem of moving to the side constraints was addressed, however, SQP resulted in poor accuracy, typically finding a relatively flat region near the optimum.

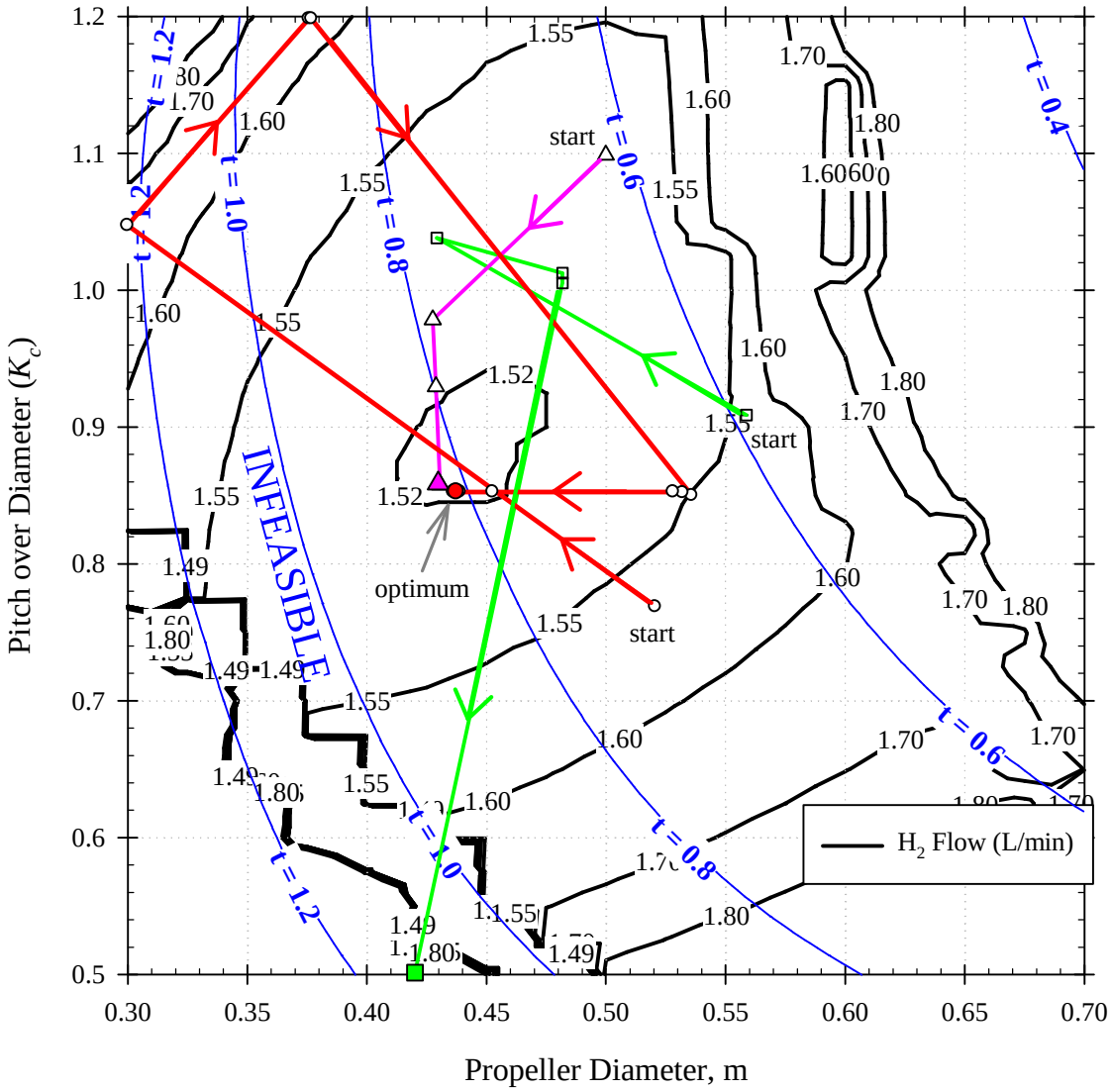

Figure 7.2: Sequential quadratic programming minimization of hydrogen flow in a FCUAV propulsion system.

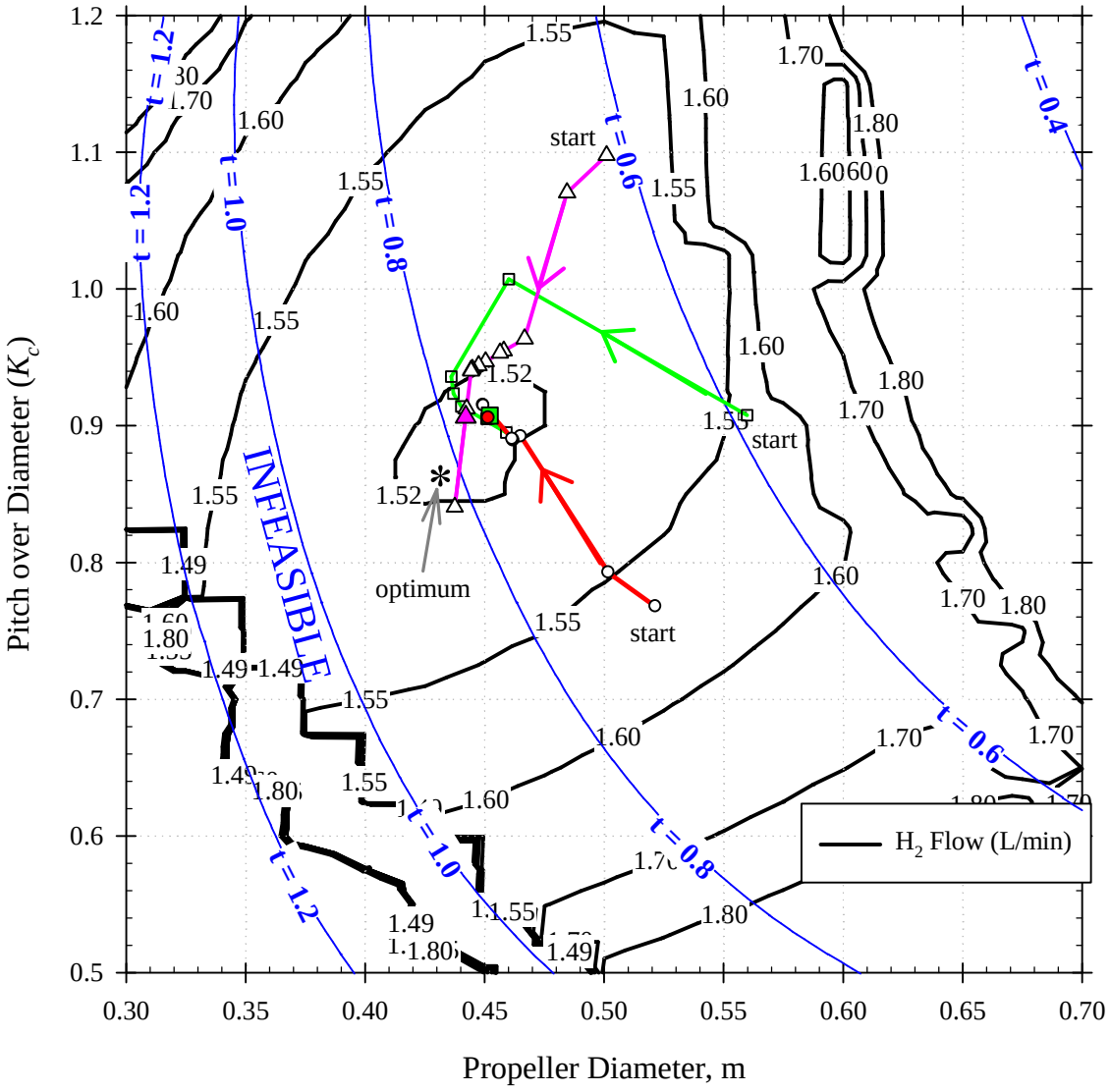

Figure 7.3: Sequential quadratic programming minimization of hydrogen flow in FCUAV propulsion system using a bounded line search.

7.3.2 Compass Search

The compass search is a simple algorithm that searches in along the axis of each design variable with a predetermined constant step size until a decrease in the objective function is found. The design then takes a step and repeats the process. Once all axes have been searched without a decrease in the objective function, the step size is halved and the method continues. Convergence occurs when the step size is below a tolerance.

Performance of the compass search using the same initial conditions as SQP are shown in Figure 7.4. For most initial conditions, the compass search easily located the optimum although several more iterations were needed than SQP. Occasionally, the compass search would converge to the same flat area near the optimum that SQP had located. This is evident with the green path shown in Figure 7.4.

7.3.3 Nelder-Mead Simplex Algorithm

The final method tested was the Nelder-Mead simplex method. This method uses the concept of a simplex which is a special polytope of $N + 1$ vertices in N dimensions. The method generates a new test point by extrapolating the behavior of the objective function measured at each test point and chooses to replace one of the test points in the simplex. The method can stretch exponentially if a new point is better than the last or can shrink otherwise. A full description of the method can be found in [298, 299].

The Nelder-Mead method performance is shown in Figure 7.5. The method proved to be very robust at finding the solution although slightly less efficient than the compass method. The Nelder Mead method is the default non-gradient based optimization method in Matlab and has been shown to be useful in other complex design problems due to its high efficiency and robustness [301].

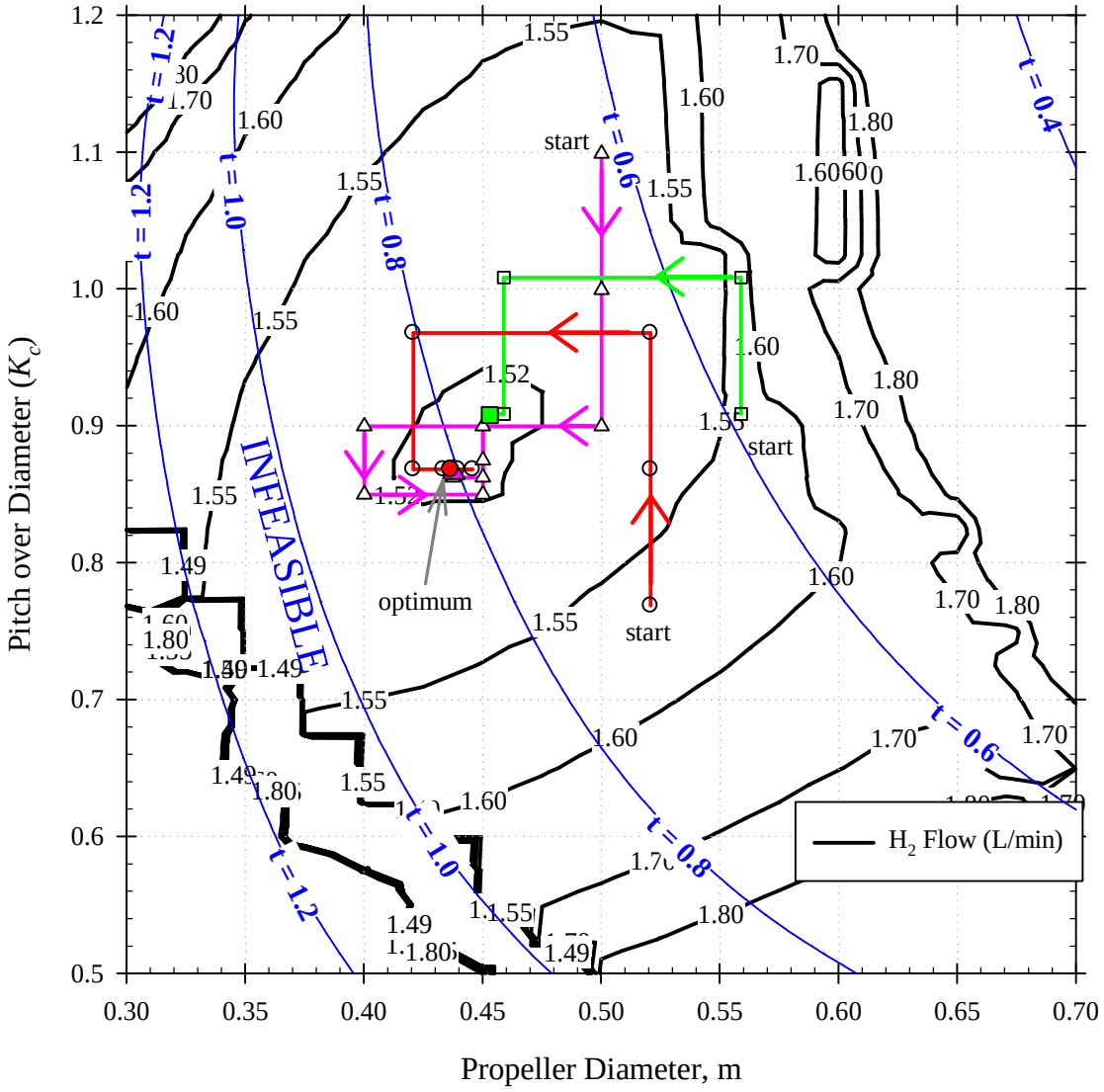

Figure 7.4: Compass search minimization of hydrogen flow.

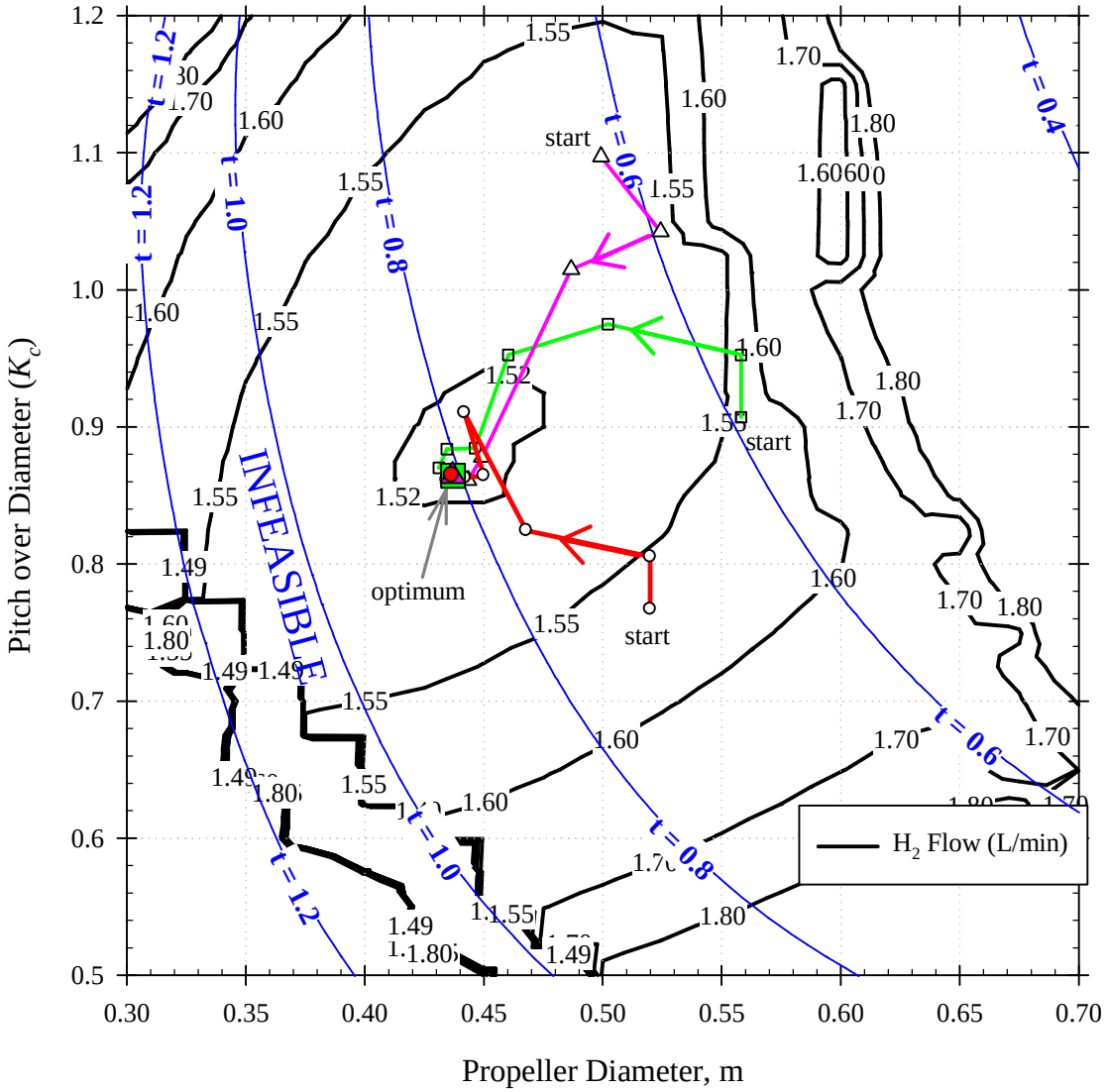

Figure 7.5: Nelder Mead optimization performance.

7.4 Summary of Results

The primary goal of testing different optimizers was to find an optimizer that was both efficient and robust in a highly constrained design space. Although SQP was extremely efficient for some initial conditions, the algorithm did allow some constraint violations that resulted in the failure of the MDA code. Although the constraint violations could be mitigated by changing the step size, the method wasn't as accurate as other methods at locating the optimum. Both a compass search method and the Nelder-Mead simplex method provided more robustness than SQP, however, the compass search would also occasionally converge to a non-optimum location. The best overall performance was achieved by Nelder-Mead which was very robust and had nearly the same efficiency as the compass method.

7.5 Chapter Summary

Optimization within the probabilistic design space is accomplished using the CCP formulation where the expected value of an objective function is minimized subject to a prescribed minimum probability of meeting each constraint. The formulation closely follows the probabilistic aircraft sizing method developed in Nam [176]. The probability of satisfying the constraints is accomplished via the uncertainty propagation in SSA. A formulation to identify the Pareto frontier using multiple optimizations is also presented. Various optimization methods including SQP, compass search, and the Nelder Mead simplex algorithm were tested on the MDA of the fuel cell UAV. Sequential quadratic programming using the SSA gradients was by far the most efficient requiring only a few iterations to reach the optimum. However, the method was prone to moving outside the

feasible design space causing the MDA to fail. Although reducing the line search step size could help mitigate this problem, it resulted is reduced efficiency and a decreased performance in locating the global minimum. Both the compass search and Nelder Mead methods were more effective although less efficient than SQP. Overall, Nelder Mead offered the best compromise between robustness and efficiency.

CHAPTER 8

IMPLEMENTATION

For implementation of the methodology, the design of a 24 hour endurance small UAV was selected. The design was part of a larger research effort meant to develop a second generation UAV to follow the GT FCUAV. The culmination of the design resulted in hardware tests that were using to validate performance results calculated during the study. To facilitate hardware development, only readily available components were considered.

To begin the implementation study, a design structure matrix (DSM) consisting of 45 different contributing analyses (CAs) was constructed based on the decomposition rules established in Chapter 4. Initial estimates for the uncertainty distributions were based on results from the GT FCUAV development. A simple process was executed where an optimum endurance was located, and then based on uncertainty attribution, hardware was developed and tested to produce updated CAs. The CAs were then integrated into the MDA allowing a test of the flexible DSM framework. The final design cruise performance was validated using a hardware-in-the-loop simulation of the propulsion system and accuracy of the final uncertainty propagation estimates were verified via a Monte Carlo simulation.

To further implement the design space exploration aspect of the methodology, a propeller design study for the aircraft was conducted. A graphical representation of both the deterministic and probabilistically feasible design was given. The tradeoff between climb rate and endurance as well the tradeoff between the probabilities of meeting

opposing constraints was studied via identifying Pareto frontiers. Key results include the identification of a highly constrained design space, the correct identification of the deterministically and probabilistically constrained designs, and discontinuities in the Pareto front due to constraint activation.

8.1 Problem Setup

8.1.1 Mission Profile

The mission was determined to be a surveillance mission consisting of a persistent fixed orbit over an area of interest. The mission consists of an assisted takeoff, an unassisted climb to an altitude of 100 m, loiter in a 1000 m turn, and then descent and landing. A visualization of the mission is shown in Figure 8.1.

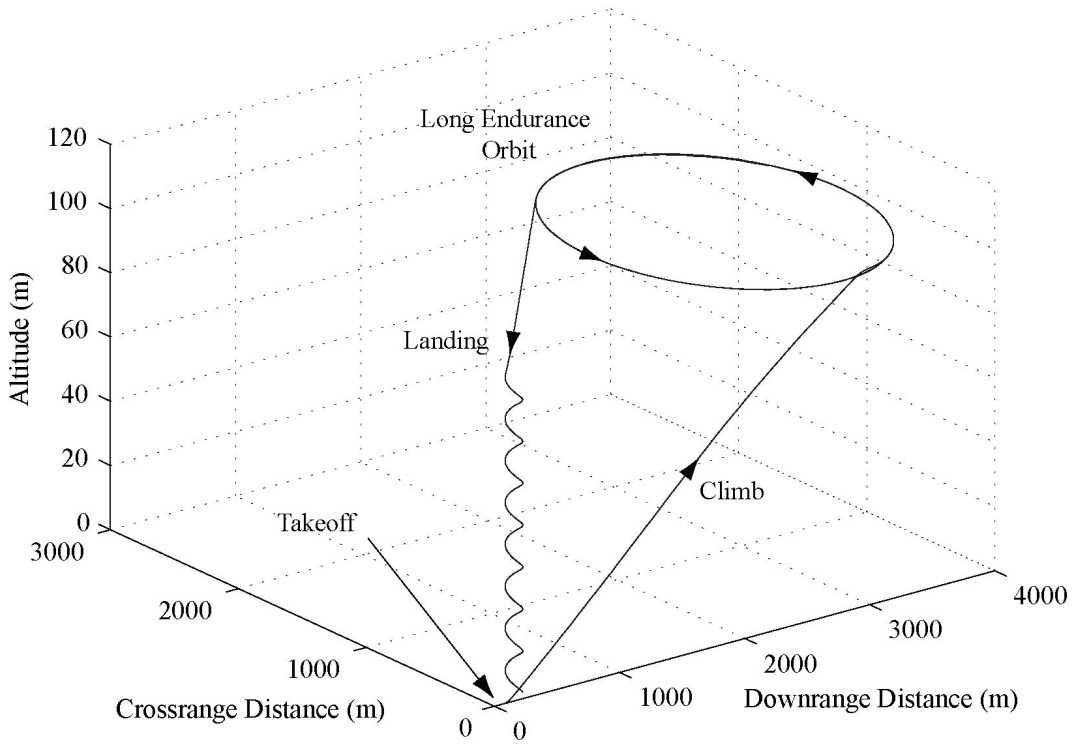

Figure 8.1: FCUAV mission profile [63].

8.1.2 Optimization Formulation

The primary objective was to optimize the endurance of the vehicle. To facilitate performance in non-ideal weather, an excess power capable of providing a climb rate of 75 m/min was assumed. In addition to the climb rate, constraints based on limits of the analysis and physical limitation of the fuel cell were imposed. This led to the optimization formulation summarized in Eq. (8.1)

$$\begin{gathered} \text{Minimize } OEC(x) = \text{ - Cruise Endurance} \\ \text{Subject to: } V_c \geq 75 \text{ m/min} \\ M_{tip} \leq 0.85 \\ \text{Re\#} \geq 200{,}000 \\ I_{fc} \leq I_{\max} \end{gathered} \tag{8.1}$$

The propeller tip Mach number (M_{tip}) is included to account for a lack of adequate compressibility effects in the propeller model. The Reynolds number (Re#) constraint is based on the region in which the wing airfoil was modeled. At Re#s below 200,000, experimental data showed that performance drastically decreased [268]. The current constraint is meant to keep the fuel cell current (I_{fc}) from exceeding the current (I_{max}) where mass transport losses cause a drastic decrease in voltage [302].

8.1.3 Design Variables

The design variables for the implementation study are contained in Table 8.1. These variables mostly consist of the propulsion system parameters. For simplicity, the airframe sizing was accomplished via selection of a wing area as the aspect ratio was fixed to 22. The same tail ratio of semi-span to tail distance as the GT FCUAV was used.

Table 8.1: Implementation study design variables.

Design Variable Description	Lower Bound	Upper Bound	Units
Hydrogen Tank Length-to-diameter Ratio	1	4	m
Hydrogen Tank Radius	0	N/A	m
Hydrogen Tank Pressure	0	N/A	MPa
Motor Series Number	2	15	-
Number of Motor Winds	1.5	3	
Motor Gear Ratio	1	10	
Propeller Diameter	0	N/A	m
Propeller Pitch	0	N/A	m
Planform Wing Area	0	N/A	m^2

The upper and lower bounds for each design variable is included in Table 8.1. Although not formally stated in Eq. (8.1), these were included in the optimization formulation as side constraints handled by the penalty function.

The fuel cells considered are the H-100, H-200, and H-300 fuel cells developed by Horizon Fuel Cell Technologies [118]. These fuel cells became available in early 2007 and were the best performing small fuel cells available when the implementation study was begun. The motors are based on the NEU 19 series [253] inrunner type motors. These motors facilitate a large design space as a large number of motors with varying power levels and motor voltage constants are available. The motor performance constants of these motors are related to the motor series number and number of motor winds design variables. The propeller model is based on APC thin electric propeller geometry described in Chapter 5.

8.1.4 Design Structure Matrix

Use of the decomposition rules stated in Chapter 4 required that 45 separate CAs be created. Nearly all of the propulsion related models had to be formed into separate CAs in order to facilitate uncertainty propagation at both cruise and climb power levels. The structuring of the DSM is shown in Figure 8.2.

8.1.5 Uncertainty Estimates

As formulated in Figure 8.4, the problem contains 28 input variables and108 variables calculated by the various CAs. The input variables consist of the design variables as well as a number of constants. For the uncertainty propagation, estimates of the standard deviations of uncertainty for both the input variables, as well for each of the values calculated by the CAs was needed. Rather than providing arbitrary guesses as had been done in all previous fuel cell aircraft implementation studies, estimates were calculated based on the validation studies performed for each analysis. The uncertainty of input variables such as hydrogen utilization, storage pressure, speed controller resistance, and air density were also estimated based on either experiments or published results.

The Horizon H series fuel cell stacks are fundamentally different in architecture as compared to the BCS fuel cell stack used in the GT FCUAV. Primarily, the BCS system uses a BOP that consists of a cooling loop and uses compressed air as a reactant. The Horizon system combines the air delivery and cooling into a small fan. Although the BCS system was used to estimate uncertainty, large estimates for the standard deviation of both CA variables and inputs were made to account for the variation in architecture.

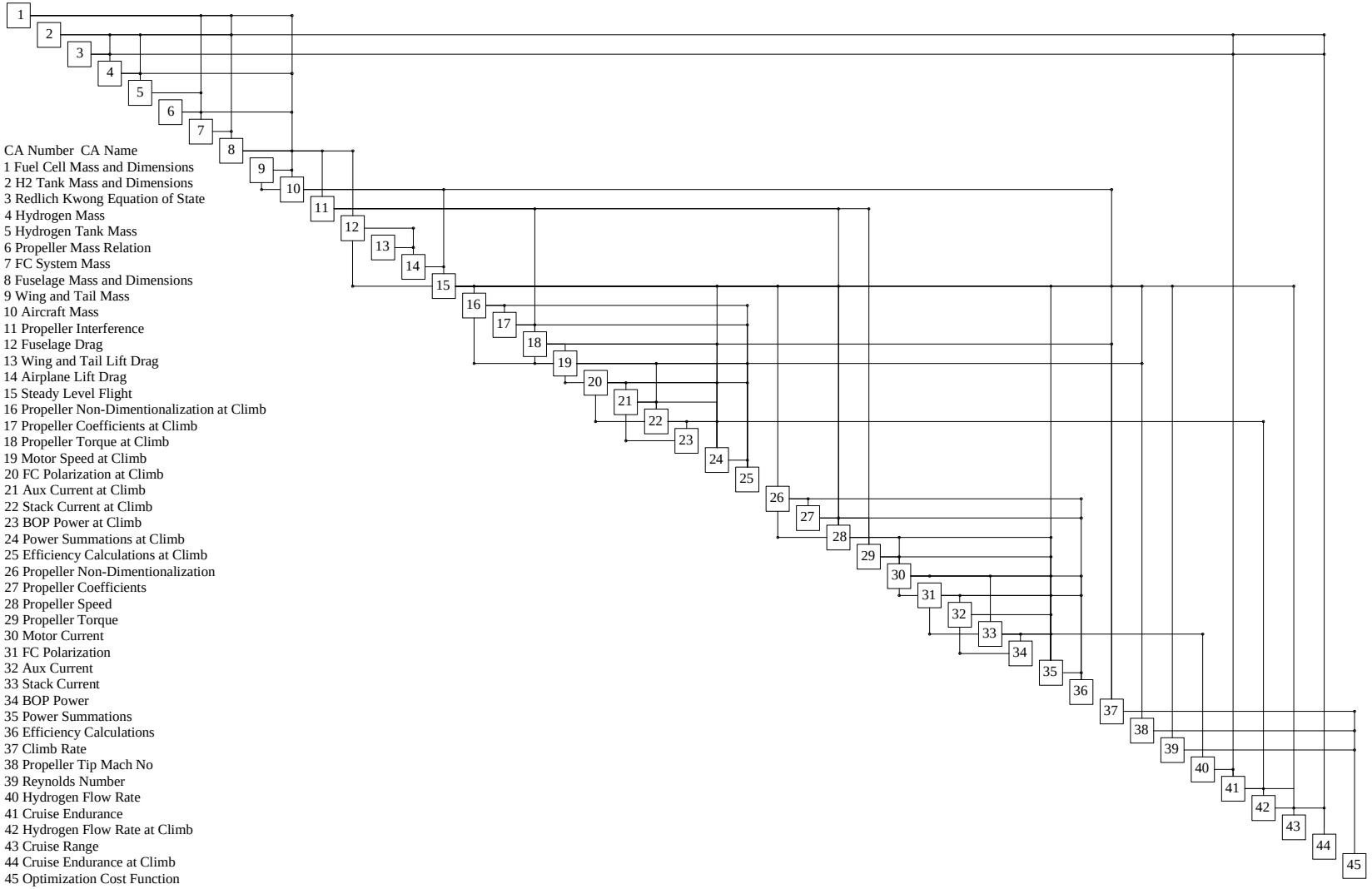

Figure 8.2: Design structure matrix for the implementation FCUAV.

8.2 Implementation Procedure

A simple implementation procedure was used to both help identify a design for the 24 hour endurance aircraft, and identify an order in which to freeze the design and select components for hardware testing. The implementation procedure is not meant to be a specific part of the methodology, rather it was a simple method to inform hardware development choices that would be needed for validation. In addition, the method mimics a typical recourse that occurs during a design process a will allow the usefulness of the flexible DSM framework to be tested.

The procedure is summarized in Figure 8.3. Using the validated subsystem models from Chapter 5 arranged into the DSM shown in Figure 8.2, a deterministic optimization is performed to estimate the initial design. The deterministic optimum is chosen simply because it is estimated that uncertainty will be extensive enough as to make optimization within the probabilistically constrained design space overly conservative. Uncertainty estimates are then made around the parameter values of the initial optimum design and uncertainty is then propagated through the design with SSA. A decision based on whether or not the total uncertainty is tolerable is then made. If the uncertainty is not tolerable, a decision based on uncertainty attribution and the cost of developing hardware was made to select a component to purchase and test. The test data is then used to develop an empirical model which replaces the original model in the DSM. The process then repeats until all the hardware is developed to build up a simulation that can be used for a system level validation. For the implementation study, the system level validation is a hardware-in-the-loop simulation.

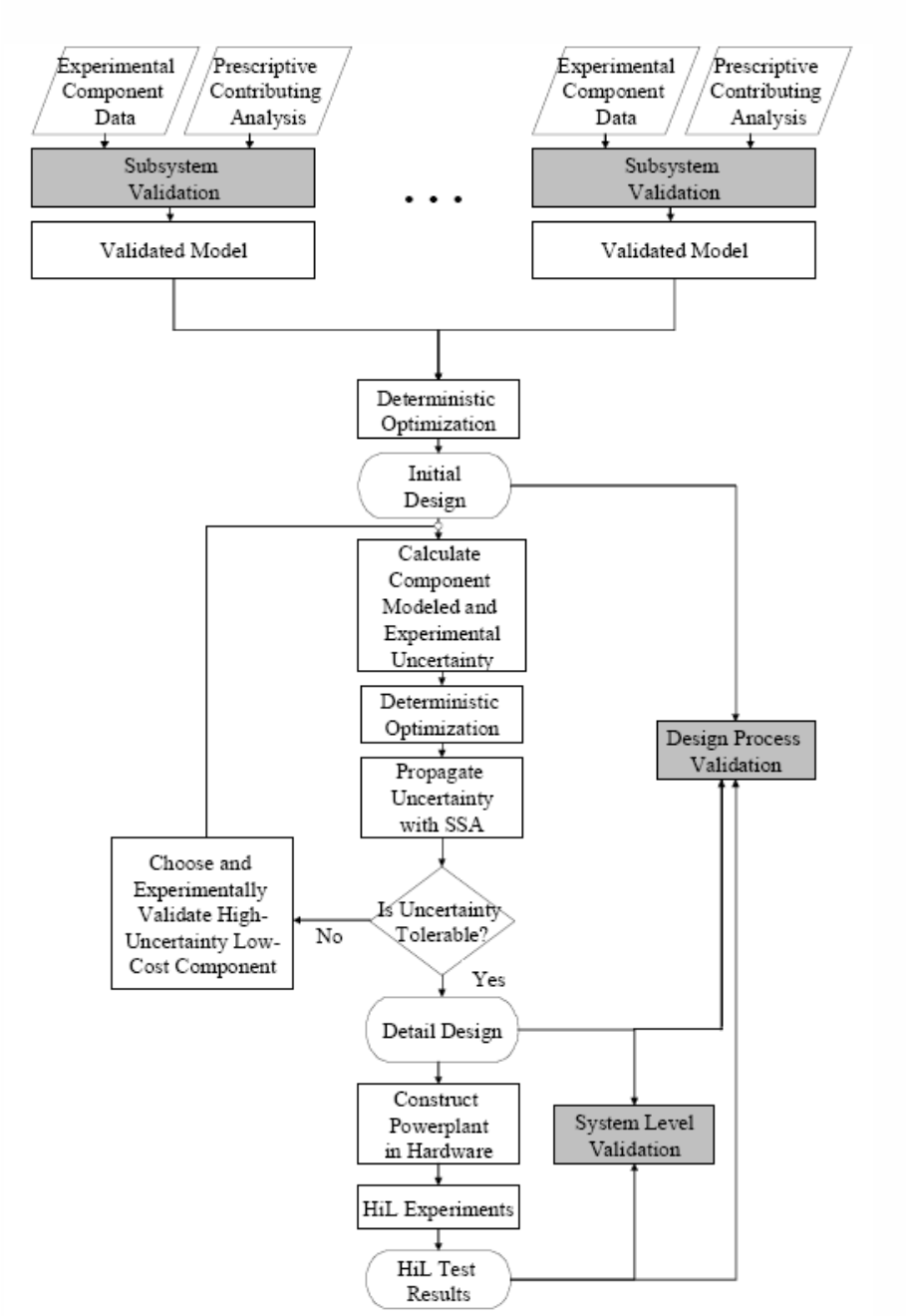

Figure 8.3: Outline of implementation procedure [63].

8.2.1 Initial Design

In the first step of conceptual design, three Horizon H series fuel cell sizes (100W, 200W and 300W) were screened for effectiveness. At the time of analysis (Spring 2007), these fuel cells offered state of the art performance for low cost portable fuel cell stacks [118]. For each stack, a separate deterministic optimization was performed. The optimum aircraft designs were compared for each fuel cell stack. The results showed that the 300W fuel cell stack was capable of greater endurance than the other fuel cell stacks, while still meeting the performance constraints. This result was expected as the 300W system showed the best overall specific power of the three fuel cells.

The 300 W fuel cell stack was chosen, its manufacturer specified performance was modeled as a CA and the design process continued to specify the initial design. The design variable values and a set of key performance metrics that were calculated are given in Table 8.2[‡]. The design results in a low wing loading and is primarily constrained by the climb rate. Note that maximum deterministic optimization is short of the 24 hour goal.

To estimate propagated uncertainty, a SSA was performed at the design point. A few of the key input uncertainties for this analysis are contained in Table 8.2. The input uncertainties are standard deviations of uncertainty as a percent of the current value. The

---

[‡] Note that the motor voltage constant resulting from a combination of the motor series number, the number of windings, and the gear reduction ratio is reported. Although the series number, the number of windings, and the gear reduction were the actual design variables and also determine motor resistance and no load current, the motor voltage constant is the dominant performance metric for the electric motor and a more useful metric for the designer.

propagated uncertainty results are shown in Figure 8.4. The contributing analyses and design variables (DVs) that contribute the first 90% of the propagated uncertainty are listed. The remaining 10% of the propagated uncertainty from all other CAs and DVs is grouped under the title *Remaining Sources*. As might be expected of a conceptual design, the total propagated uncertainty associated with both the cruise endurance and the climb rate metrics is very high. The design cruise endurance of the aircraft is 20.7 ± 8.6 hrs and the design climb rate is 74.9 ± 21.9 m/min. The two largest sources of uncertainty in both the cruise endurance and the climb rate are the motor CA (*Motor Current CA*) and the fuel cell CAs (*BOP Power CA*, *FC Polarization CA*).

Table 8.2: Data summary for initial design.

Design Variable	Value	Performance Metric	Value	CA/Design Variable	Uncertainty
Hydrogen Tank Radius	0.073m	Cruise Endurance	20.67hr	Motor Current CA at Cruise	26%
Hydrogen Tank Length to Diameter Ratio	3.02	Maximum Climb Rate	74.87m/min	Balance of Plant Power CA	81%
Hydrogen Tank Pressure	35.92MPa	Cruise Fuel Cell Power	141W	Fuel Cell Polarization CA	11%
Motor Voltage Constant	52.31rpm/V	Maximum Fuel Cell Power	342W	Hydrogen Tank Mass CA	17%
Propeller Diameter	0.66m	Wing Loading	12.4kg/m^2	Propeller Coeff. CP CA	9%
Propeller Pitch	0.64m	Thrust to Weight Ratio	0.13	Propeller Coeff. CT CA	10%
Wing Area	0.99m^2			Motor Io DV	48%

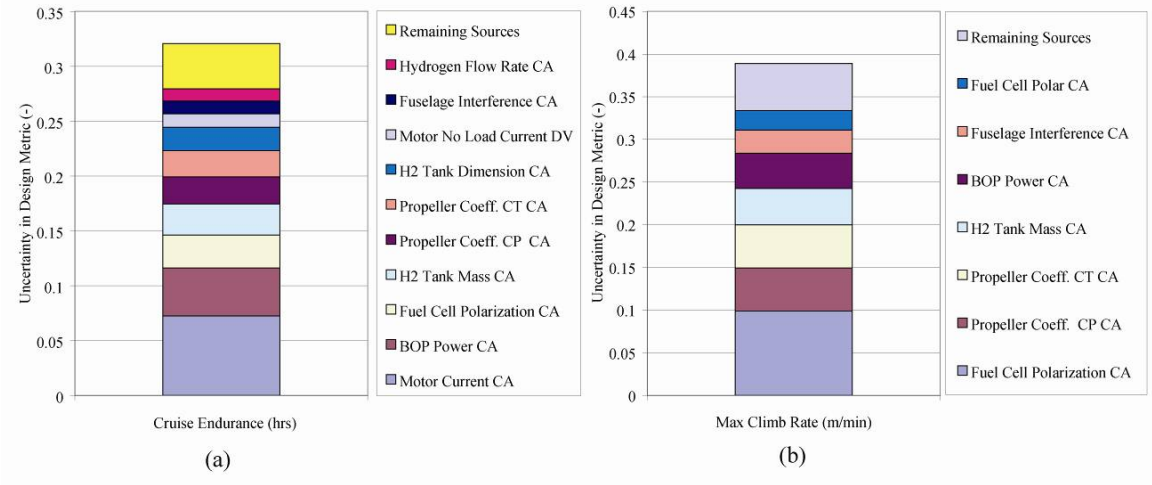

Figure 8.4: Uncertainty results for conceptual design for (a) aircraft cruise endurance design metric and (b) maximum climb rate design metric.

8.2.2 Reduction of Fuel Cell Modeling Uncertainty

Based on the results in Figure 8.4, a Horizon 300 W fuel cell stack was purchased. The fuel cell stack and its balance of plant were experimentally tested by Bradley [63]. Experimental laboratory testing of the 300 W fuel cell stack allowed for a significant reduction in the uncertainty from the fuel cell related CAs. Uncertainty in the calculation of fuel cell voltage at cruise went from a standard deviation of ±18% to ±1.8%. Uncertainty in the calculation of fuel cell balance of plant power went from a standard deviation ±81% to ±1%. A comparison of the actual versus predicted results for the initial design model and updated empirical model are shown in Figure 8.5. The Horizon H-300 stack resulted in much lower measured voltage than what was predicted using the polarization curve data provided by the manufacturer. Although the updated model shown on the right side of Figure 8.5 captures the mean voltage performance of the stack, there is still a considerable variation in voltage. As a result, at higher power levels, there is still significant uncertainty that is inherent to the fuel cell system.

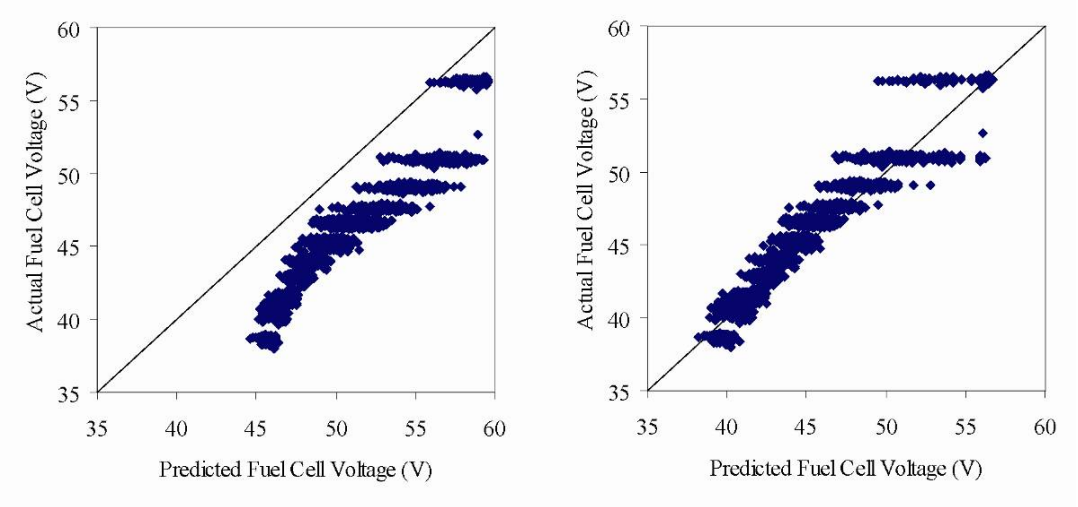

Figure 8.5: Initial fuel cell model (left) and calibrated fuel cell model (right).

With the updated fuel cell polarization model, the design of the aircraft was again deterministically optimized. The updated polarization model predicted lower voltages under the same input conditions which resulted in lower efficiency causing the cruise endurance to decrease to 15.8 ± 4.9 hrs (see Table 8.3). The wing area drastically increased from 0.99 m^2 to 1.28 m^2 and the hydrogen tank decreased in radius from 0.073 m to 0.06 m. The pitch to diameter ratio of the propeller also decreased which resulted in decreased fuel cell efficiency and lower endurance.

The propagated uncertainties for the optimum design in Table 8.3 are shown in Figure 8.6. The reduction in uncertainty that comes with the validated fuel cell model reduces the uncertainty in the design metrics at the optimal design point. The reduction in uncertainty from the updated fuel cell polarization model decreased the uncertainty in the climb rate by nearly half but had a relatively small effect on the uncertainty of the endurance. This occurs because the standard deviation is reported as a percentage of the mean value. Although the standard deviation of the uncertainty of endurance did decrease, it remained about the same percentage of the lower expected endurance value.

Table 8.3: Results for optimization with high fidelity fuel cell model.

Design Variable	Value	Performance Metric	Value	CA/Design Variable	Uncertainty
Hydrogen Tank Radius	0.060m	Cruise Endurance	15.76hr	Motor Current CA at Cruise	26%
Hydrogen Tank Length to Diameter Ratio	2.81	Maximum Climb Rate	73.09m/min	Balance of Plant Power CA	1%
Hydrogen Tank Pressure	39.76MPa	Cruise Fuel Cell Power	95W	Fuel Cell Polarization CA	2%
Motor Voltage Constant	76.53rpm/V	Maximum Fuel Cell Power	276W	Hydrogen Tank Mass CA	17%
Propeller Diameter	0.58m	Wing Loading	8.2kg/m^2	Propeller Coeff. CP CA	9%
Propeller Pitch	0.37m	Thrust to Weight Ratio	0.15	Propeller Coeff. CT CA	10%
Wing Area	1.28m^2			Motor Io DV	48%

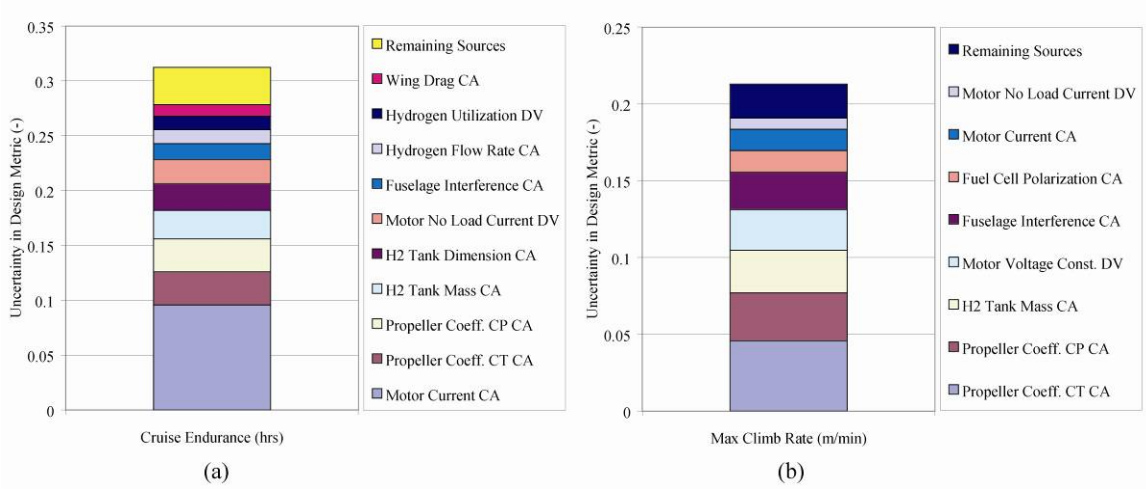

Figure 8.6: Uncertainty results for design with an experimentally validated fuel cell model for (a) aircraft cruise endurance and (b) maximum climb rate.

8.2.3 Reduced Uncertainty in Electric Motor/ESC Calculation

Based on the results in Figure 8.6, the closest electric motor and gearbox to the optimum predicted motor was purchased (NeuMotors 1910/2Y with 6.7:1 gear reduction [253]). The motor was tested over its performance range using a laboratory electric motor dynamometer. The results were fit using a 3 hidden node, multilayer neural network. The root mean squared error between the neural network model and 126 experimental test points was 2.5%. This represented a significant reduction in the error associated with the scalable electric motor model, especially at low torque (see Figure 8.7).

With the new electric motor model, the design of the fuel cell powered aircraft was deterministically optimized for endurance within the design constraints. The design cruise endurance of the aircraft at this point improved to 20.7 ± 2.7 hrs with the climb rate still constrained to 74.8 ± 23.7 m/min (see Table 8.4). This design had a similar wing area and wing loading to the initial design. Based on the neural network model, the motor actually outperformed the lumped parameter model around the optimum resulting in the increase in performance versus the previous iteration. Note that the propeller design stayed at a similar pitch-to-diameter ratio as the initial design but the diameter of the propeller changed to match the updated performance of the motor.

The uncertainty propagation results at the new optimum design point are shown in Figure 8.8. The uncertainty in endurance was reduced by the introduction of the new motor model. The primary sources of uncertainty at the new design point are the propeller model (*Propeller Coeff. CAs)* and the hydrogen tank CAs (*H2 Tank Dimension CA* and *H2 Tank Mass CA*).

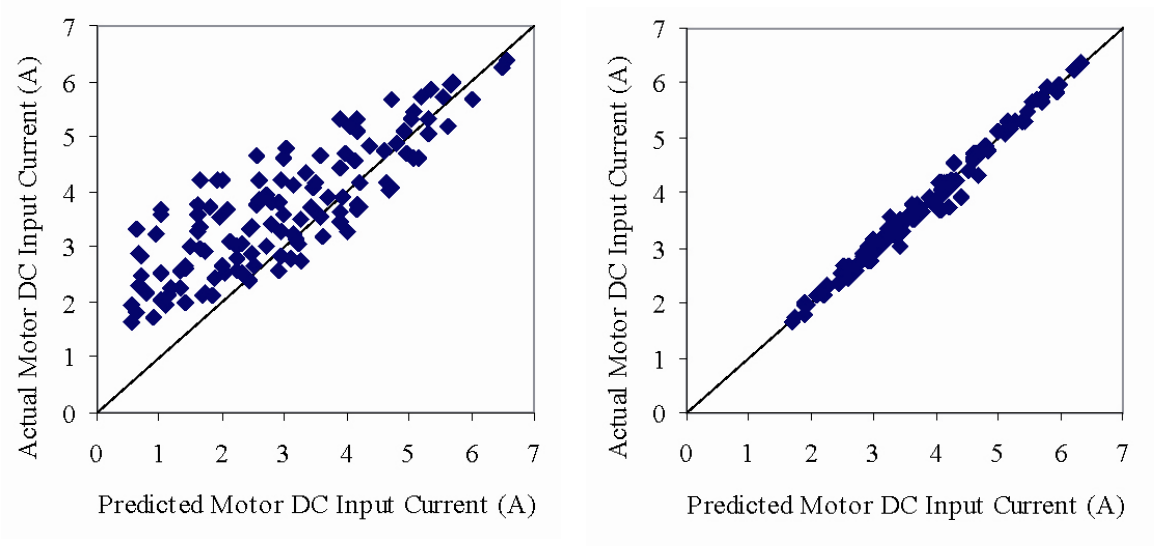

Figure 8.7: Original electric motor model (left) and neural network model (right).

Table 8.4: Results for optimization with high fidelity fuel cell and motor models.

Design Variable	Value	Performance Metric	Value	CA/Design Variable	Uncertainty
Hydrogen Tank Radius	0.078m	Cruise Endurance	20.73hr	Motor Current CA at Cruise	3%
Hydrogen Tank Length to Diameter Ratio	3.75	Maximum Climb Rate	74.83m/min	Balance of Plant Power CA	1%
Hydrogen Tank Pressure	22.7MPa	Cruise Fuel Cell Power	135W	Fuel Cell Polarization CA	2%
Motor Voltage Constant	77.61rpm/V	Maximum Fuel Cell Power	276W	Hydrogen Tank Mass CA	17%
Propeller Diameter	0.59m	Wing Loading	13.0kg/m^2	Propeller Coeff. CP CA	9%
Propeller Pitch	0.53m	Thrust to Weight Ratio	0.13	Propeller Coeff. CT CA	10%
Wing Area	0.94m^2			Motor Io DV	0%

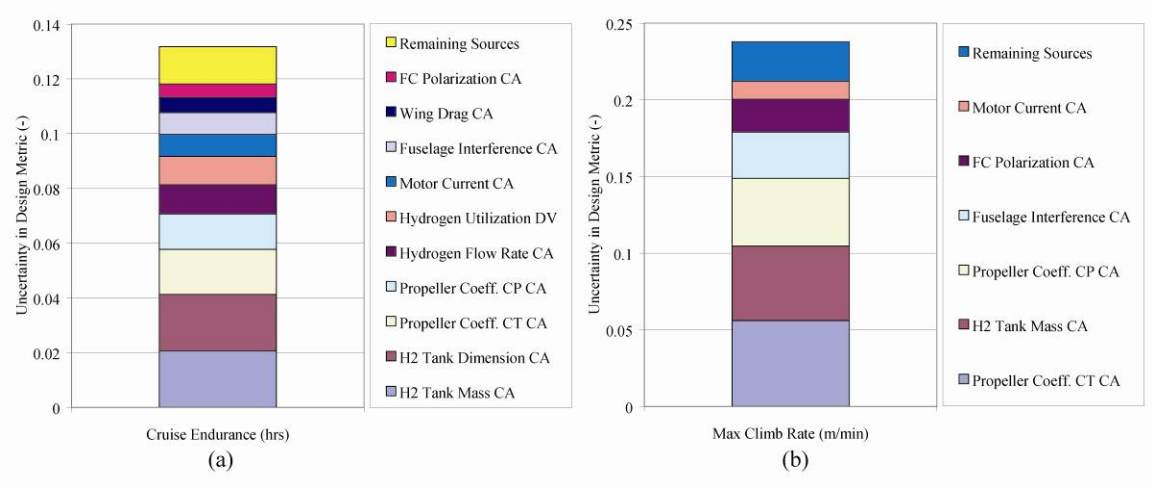

Figure 8.8: Uncertainty results for design with an experimentally validated electric motor model for (a) aircraft cruise endurance and (b) maximum climb rate.

8.2.4 Uncertainty Reduction of Hydrogen Storage Calculation

The easier of the two largest uncertainties to address in Figure 8.8 was the hydrogen storage calculation uncertainty. A hydrogen tank (Carleton Technologies PN6109) was chosen from its manufacturer's specifications so as to be as close in size, capacity and weight to the optimal tank as chosen by the optimizer. The remaining uncertainty in the hydrogen tank dimensions (0.6%) and weight (2.1%) are due to manufacturing variability. With the new hydrogen tank model, the design of the fuel cell powered aircraft was deterministically optimized for endurance within the design constraints. The design cruise endurance of the aircraft at this point improved to 22.5 ± 2.1 hrs with the climb rate still constrained at 72.6 ± 15.3 m/min (see Table 8.5). The improvement was due to a higher weight percent of hydrogen stored in the actual tank versus the sizing model used during previous iterations. The wing loading and wing area changed very little in this iteration, however, as with previous iterations, the propeller design changed to best adjust to the slight weight and wing loading changes.

Table 8.5: Summary of results with high fidelity fuel cell, electric motor, and hydrogen tank models.

Design Variable	Value	Performance Metric	Value	CA/Design Variable	Uncertainty
Hydrogen Tank Radius	0.026m	Cruise Endurance	22.48hr	Motor Current CA at Cruise	3%
Hydrogen Tank Length to Diameter Ratio	3.1	Maximum Climb Rate	72.56m/min	Balance of Plant Power CA	1%
Hydrogen Tank Pressure	31.0MPa	Cruise Fuel Cell Power	140W	Fuel Cell Polarization CA	2%
Motor Voltage Constant	77.61rpm/V	Maximum Fuel Cell Power	276W	Hydrogen Tank Mass CA	2%
Propeller Diameter	0.61m	Wing Loading	13.1kg/m^2	Propeller Coeff. CP CA	9%
Propeller Pitch	0.50m	Thrust to Weight Ratio	0.13	Propeller Coeff. CT CA	10%
Wing Area	0.95m^2			Motor Io DV	0%

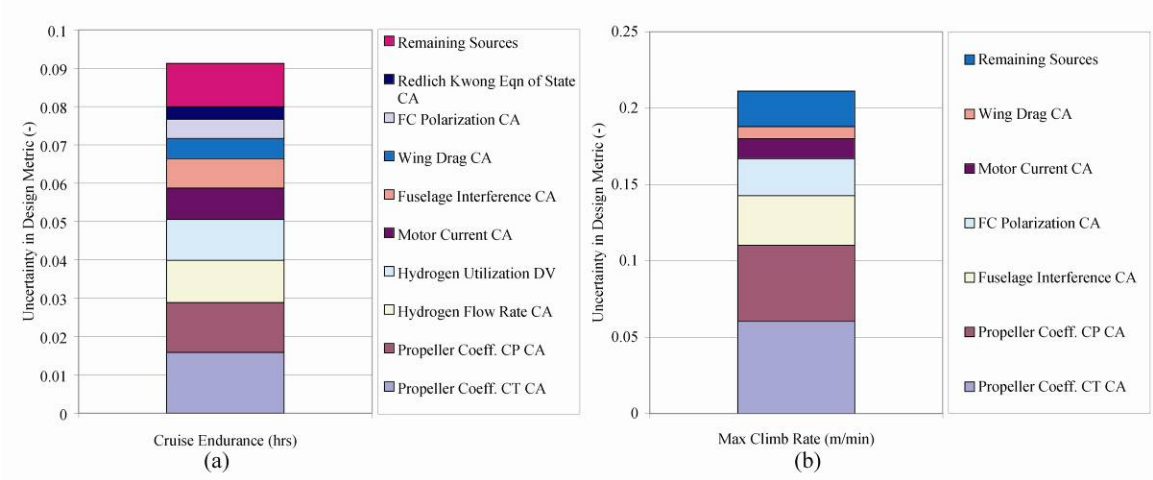

Figure 8.9: Uncertainty results for design with a hydrogen tank model for (a) aircraft cruise endurance and (b) maximum climb rate.

The uncertainty at this design point is still rather high for both the endurance and climb rate metrics. However, the uncertainty has been greatly reduced from the initial design without much change in endurance.

Figure 8.10 shows how both the endurance and the climb rate change per iteration of the implementation procedure. The expected value of the cruise endurance decreases for the first iteration and then increases for all subsequent iterations. The decrease was due to initial overestimates of fuel cell voltage and the increases resulted from under predicting the performance of the motor, and under predicted the amount of hydrogen stored in the tank. Note that for endurance, the uncertainty bounds shrink as high fidelity analyses are introduced. Figure 8.10 also shows climb rate data for each iteration. The mean value of climb rate is steady since the climb rate constraint is active. However, the uncertainty actually decreases and then increases since the addition of the high fidelity fuel cell analysis drove the optimizer to another minima in the design space. However, the final uncertainty is an improvement over the initial uncertainty. By improving the fidelity of the CAs directly effecting the climb rate calculation, the uncertainty could be further reduced.

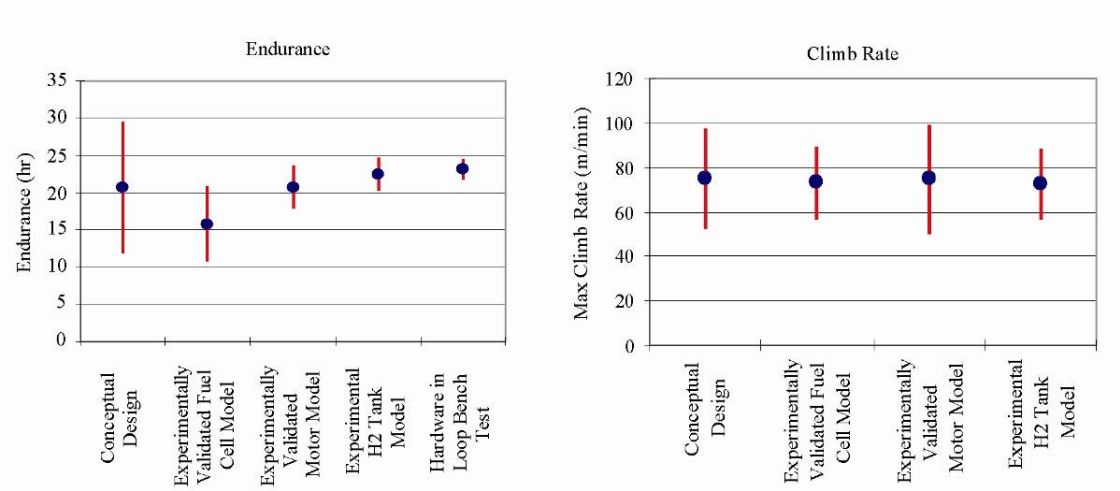

Figure 8.10: Summary of endurance and climb rate values for each iteration.

8.2.5 Validation Using Hardware-in-the-Loop

After several iterations through the implementation procedure above, enough hardware was developed to perform hardware-in-the-loop (HiL) simulations of an entire fuel cell propulsion system. The hardware would consist of the fuel cell, balance of plant, electric motor, and hydrogen storage while the aircraft and propeller would involve simulation. Development of the HiL setup and a full discussion of its results are available in reference [300].

One of the primary goals of the HiL simulation was to finalize a propulsion system for the next generation FCUAV with a target endurance of 24 hours. Although the earlier design studies had suggested that 24 hours was slightly beyond the limit of the off the shelf components selected, the HiL simulation would help determine whether detailed design changes could give the necessary increase in endurance. The final design that was extensively tested in the HiL simulations is fully described in reference [300]. A schematic of the HiL simulation is shown in Figure 8.11. This design was a slight iteration on the design in Table 8.5 with the most notable change being an off the shelf propeller.

The hardware-in-the-loop values for an average loiter condition are given in Table 8.6. The uncertainty of the HiL measurements is also provided. The predicted values from the MDA are also provided in Table 8.6. The standard deviation of each value predicted by SSA is also provided. Overall, the simulation provided similar results to the HiL. Considering the error band of the HiL measurements, all but the auxiliary power fall within one standard of deviation of the simulation. Fortunately, the auxiliary power prediction was conservative.

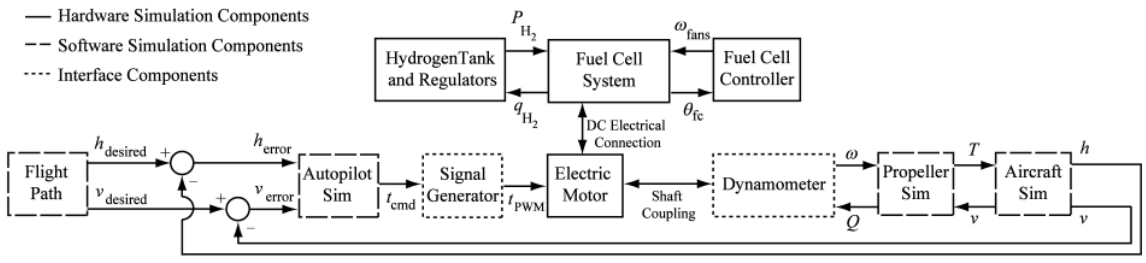

Figure 8.11: Schematic and control system causality flow chart for hardware-in-the loop simulation.

8.2.6 Uncertainty Propagation Validation

In addition to validating the values predicted by the MDA, a validation of the uncertainty propagation was also performed. This validation was intended to verify that SSA was accurately predicting the propagated uncertainty for the entire MDA.

The validation was accomplished using a Monte Carlo simulation (MCS). The MCS used normal distributions to model the uncertainty of the input parameters as well as the uncertainty of values calculated by each CA. The values of the design variables, the outputs of the CAs, and the estimated standard deviation for both design and CA calculated variables are given in Table 8.7. A total of 1000 cases were run in the MCS.

Table 8.6: Propulsion system validation with HiL.

	Simulation		Experiment	
	Value	σ	Value	Δ
Prop Speed (rpm)	2260.70	27.10	2246.95	60.35
Prop Torque (N-m)	0.40	0.02	0.43	0.01
Prop Brake Power (W)	93.88	6.20	101.00	2.00
Fuel Cell Voltage (V)	43.08	7.00	40.04	0.45
Fuel Cell Current (A)	3.10	0.51	3.56	0.21
Aircraft Power Available (W)	69.88	0.00	70.00	3.00
Fuel Cell Power (W)	133.69	12.33	150.00	9.00
Auxiliary Power (W)	9.55	0.48	8.00	0.10
H_2 Flow Rate (L/min)	1.60	0.28	1.54	0.04

Table 8.7: Inputs for propulsion uncertainty propagation simulation.

Design Variable	Value	σ
Prop Diameter (m)	0.5207	0.00%
Prop Pitch (m)	0.3556	0.00%
Cruise Airspeed (m/s)	13.26	0.00%
Prop Blades	2	0.00%
Air Density (kg/m^3)	1.2	0.00%
Prop Slow Down Efficiency	0.973	0.00%
Thrust Required (N)	5.27	0.00%
ESC Loss (kloss)	0.365	3.40%
Motor K_v (rpm/V)	520	5.00%
Motor Gear Ratio	6.7	0.00%
No Load Current (I_o)	0.6	48.00%
Motor Resistance (Ohm)	0.037	10.00%
ESC Resistance (Ohm)	0.074	10.00%
Fuel Cells	62	0.00%
Fuel Cell Stacks	1	0.00%
Payload Power (W)	3.84	0.00%
H_2 Utilization	0.9	3.30%

Calculation	Value	σ
Prop Advance Ratio	0.631	0.00%
Prop Pitch/Diameter	0.683	0.00%
Prop Thrust Coefficient	0.038	5.24%
Prop Power Coefficient	0.041	4.23%
Prop Speed (rpm)	2423.050	0.00%
Prop Torque (N-m)	0.492	0.00%
Prop Brake Power (W)	124.779	0.00%
Thrust Available (N)	5.270	0.00%
Propulsion Current (A)	3.785	0.00%
Throttle	0.823	0.00%
Motor Current (A)	4.597	0.00%
Motor Voltage (V)	31.390	0.00%
Motor Efficiency	0.936	0.00%
Fuel Cell Voltage (V)	41.190	14.20%
Max Fuel Cell Current (A)	8.100	0.00%
BOP Current (A)	0.160	81.00%
Payload Current (A)	0.093	0.00%
Auxiliary Current (A)	0.253	0.00%
Fuel Cell Current (A)	4.038	0.00%
BOP Power (W)	6.582	0.00%
Motor Brake Power (W)	124.779	0.00%
DC Power to Controller (W)	155.909	0.00%
Aircraft Power Available (W)	69.880	0.00%
Fuel Cell Power (W)	166.332	0.00%
BOP Power (W)	6.582	0.00%
Auxiliary Power (W)	10.423	0.00%
Fuel Cell Efficiency	0.612	0.00%
Motor Efficiency	0.807	0.00%
Speed Controller Efficiency	0.930	0.00%
Prop Efficiency	0.575	0.00%
H2 Flow Rate (L/min)	2.085	3.40%
H2 Mass Flow (kg/min)	1.75E-04	0.00%
H2 Weight Flow (N/s)	2.86E-05	0.00%
Fuel Cell SFC (N/W-s)	1.72E-07	0.00%
Motor Brake Power SFC (N/W-s)	2.29E-07	0.00%
Thrust SFC (1/s)	5.42E-06	0.00%

Table 8.8: Propulsion system uncertainty validation of SSA vs. Monte Carlo.

		Standard Deviation		Maximum Error	
	Value	**SSA**	**MC**	**SSA**	**MC**
Prop Advance Ratio	0.631	0.95%	0.95%	0.95%	0.98%
Prop Pitch/Diameter	0.683	0.00%	0.00%	0.00%	0.00%
Prop Thrust Coefficient	0.038	1.90%	1.90%	1.90%	1.96%
Prop Power Coefficient	0.041	4.31%	4.30%	5.08%	4.96%
Prop Speed (rpm)	2423.050	0.95%	0.95%	0.95%	0.99%
Prop Torque (N-m)	0.492	5.04%	5.08%	6.98%	6.91%
Prop Brake Power (W)	124.779	5.62%	5.68%	7.92%	7.89%
Thrust Available (N)	5.270	0.00%	0.00%	0.00%	0.00%
Propulsion Current (A)	3.785	15.70%	16.87%	29.09%	28.86%
Throttle	0.823	13.27%	14.24%	19.53%	18.32%
Motor Current (A)	4.597	8.80%	8.93%	16.68%	15.24%
Motor Voltage (V)	31.390	5.04%	5.07%	6.01%	5.99%
Motor Efficiency	0.936	4.27%	4.57%	6.38%	5.85%
Fuel Cell Voltage (V)	41.190	16.79%	16.71%	19.72%	18.54%
Max Fuel Cell Current (A)	8.100	0.00%	0.00%	0.00%	0.00%
BOP Current (A)	0.160	84.82%	84.37%	117.36%	105.67%
Payload Current (A)	0.093	16.79%	18.80%	19.72%	22.76%
Auxiliary Current (A)	0.253	22.02%	19.47%	30.23%	20.98%
Fuel Cell Current (A)	4.038	15.99%	16.90%	29.16%	28.20%
BOP Power (W)	6.582	9.12%	4.56%	16.64%	11.20%
Motor Brake Power (W)	124.779	5.62%	5.68%	7.92%	7.89%
DC Power to Controller (W)	155.909	8.62%	8.73%	17.49%	15.67%
Aircraft Power Available (W)	69.880	0.00%	0.00%	0.00%	0.00%
Fuel Cell Power (W)	166.332	8.13%	8.22%	16.46%	14.71%
BOP Power (W)	6.582	81.51%	78.02%	97.64%	81.61%
Auxiliary Power (W)	10.423	5.76%	2.88%	10.51%	7.08%
Fuel Cell Efficiency	0.612	15.82%	16.10%	19.59%	19.32%
Motor Efficiency	0.807	6.36%	6.22%	8.42%	7.23%
Speed Controller Efficiency	0.930	4.03%	4.30%	6.06%	5.44%
Prop Efficiency	0.575	5.62%	5.67%	7.92%	7.67%
H_2 Flow Rate (L/min)	2.085	16.68%	17.68%	35.86%	27.88%
H_2 Mass Flow (kg/min)	1.75E-04	16.68%	17.68%	35.86%	27.88%
H_2 Weight Flow (N/s)	2.86E-05	16.68%	17.68%	35.86%	27.88%
Fuel Cell SFC (N/W-s)	1.72E-07	17.44%	19.50%	26.42%	25.76%
Brake Power SFC (N/W-s)	2.29E-07	15.75%	16.68%	28.35%	24.18%
Thrust SFC (1/s)	5.42E-06	16.68%	17.68%	35.86%	27.88%

Table 8.8 contains the resulting standard deviations of each output metric of interest. Both the SSA and MCS predictions are shown. In addition, assuming that the standard deviation inputs in Table 8.7 represent absolute bounds on the error, the maximum error is also calculated and compared to a MCS in Table 8.8. The SSA estimates for the propagated uncertainty were all in excellent agreement with MCS. The absolute error estimates were also in good agreement given that only 1000 cases were executed in the MCS. With more cases in the MCS simulation, the bounds of the MCS predicted absolute error are expected to increase to values closer to the SSA predictions.

8.3 Summary of Implementation Procedure Results

The practical goal of the implementation procedure was to work toward the development of a 24 hours fuel cell aircraft using the validated subsystem models. The procedure was designed with planned iterations to inform the development of hardware and showcase flexibility of the DSM framework. Overall, the HiL simulation results provide a validation that enough detail is captured in the MDA to make it useful for design purposes. A MCS also validated that the SSA code was providing accurate estimates of the propagated uncertainty. Although not mentioned previously, once alternative CAs were generated in each iteration of the implementation procedure, setup time to re-execute the optimization analysis was on the order or minutes. Furthermore, the code did not fail a single time throughout each of the procedure iterations.

During each iteration, the aircraft resized itself around the propulsion system. Wing loadings changed to compensate for reductions and increases in propulsion power. In addition, slight variations in the propulsion system caused the propeller to more

drastically resize than other design variables. This emphasizes the importance of designing the right propeller for the mission.

The propagated uncertainty was very high for most of the output metrics. Although decreases were made through each iteration, the final uncertainty was still significant. This was especially true for the climb rate constraint. If the climb rate constraint was strictly enforced, the designs presented would be very risky as uncertainty is high and the deterministic optimization approach places the design on the constraint boundary. However, the high uncertainty would also cause a significant change in endurance if probabilistic constraints were considered.

8.4 Design Space Exploration

The first part of the implementation study focused on building an MDA that was validated by hardware-in-the-loop simulations. In addition, uncertainty propagation estimates for this MDA were verified with Monte Carlo simulations. The second part of the implementation study was intended to test the ability of the methodology to explore the limits of the design space using the same MDA that was validated by the HiL simulation. To allow for visualization, the design space would consist of just two design variables. These variables were the propeller pitch and the propeller diameter. These propeller variables changed significantly during the optimization iterations that were part of the earlier implementation procedure. These parameters also directly relate to propeller efficiency which was shown to have a significant impact on propagated uncertainty during the decomposition study in Chapter 5.

To allow a visualization of the design space, the validated MDA was executed for propeller diameters ranging from 0.3 m to 0.7 m. For each propeller diameter, the linear pitch over diameter ratio was varied from 0.5 to 1.2. The design space in shown in Figure 8.12. The x and y axis-limits represent side constraints corresponding to the limits that that propeller diameter and the pitch over diameter ratio were allowed to vary. The objective function is the hydrogen flow rate at cruise which is reported in standard liters of hydrogen per minute. Minimizing the hydrogen flow rate will have the same effect on the design as maximizing endurance. Only two constraints are active in any part of the design space specified by propeller side constraints. These constraints are the climb rate and the excess fuel cell current at max power. Contours of these constraints are shown in Figure 8.12. The excess current is simply the difference between the maximum fuel cell current at climb and the maximum current allowed by the fuel cell. The excess current should remain negative. A positive excess current value would result in a rapid voltage decrease in the fuel cell stack which could lead to fuel cell stack damage. The shaded areas represent infeasible locations of the design space. The blue shaded region represents an area where not enough power is available for cruise as a positive climb rate cannot be maintained in this region. Note that in the lower left hand corner of Figure 8.12, the hydrogen flow contours collapse and become discontinuous as violations of the climb rate constraint has caused the MDA to either fail in premature iterations, or provide non-physical results. The region shaded in red represents the region where the fuel cell maximum current would be exceeding when the propulsion system reaches full power. Feasible propeller designs are all located within the white space. Note that there is an unconstrained global minimum in hydrogen flow rate just below 1.52 standard L/min.

The uncertainty of the hydrogen flow rate calculation is added in Figure 8.13. Contours of the standard deviation of hydrogen flow in units of standard L/min are given. Note that the uncertainty distribution does not change drastically throughout the design space. On the border of the excess current constraint of the feasible space lies a region where the uncertainty in the flow rate is minimized. Designs in this region would be considered to be robust in terms of endurance as the standard deviation of the hydrogen flow rate would be minimized. However, these designs would be near the excess current constraint which would result in a low probability of meeting this constraint.

By assuming a climb rate and excess current constraint, probability contours can be plotted. Figure 8.14 shows the probability contours assuming that the climb rate must be greater than 20 m/min and the excess current must be below 0 A. There is a tradeoff between meeting the climb rate constraint with a high probability and meeting the excess current constraint with a high probability. The intersection of the probability contours show that there is a limit to the probability in which both constraints can be met. The maximum joint probability of satisfying both constraints occurs where equal probability contours of both constraints intersect.

The tradeoff between the two constraints is expected. Pushing the design toward the maximum current constraint will translate into higher fuel cell power as all the fuel cell power will be available to help increase the climb rate. Likewise, leaving a margin in excess current will reduce power and adversely affect the probability of meeting the climb constraint. With an assumed climb rate constraint of 20 m/min, the global optimum will have will only have a probability of 0.61 of meeting the climb rate constraint although the probability of meeting the excess current constraint is 0.998.

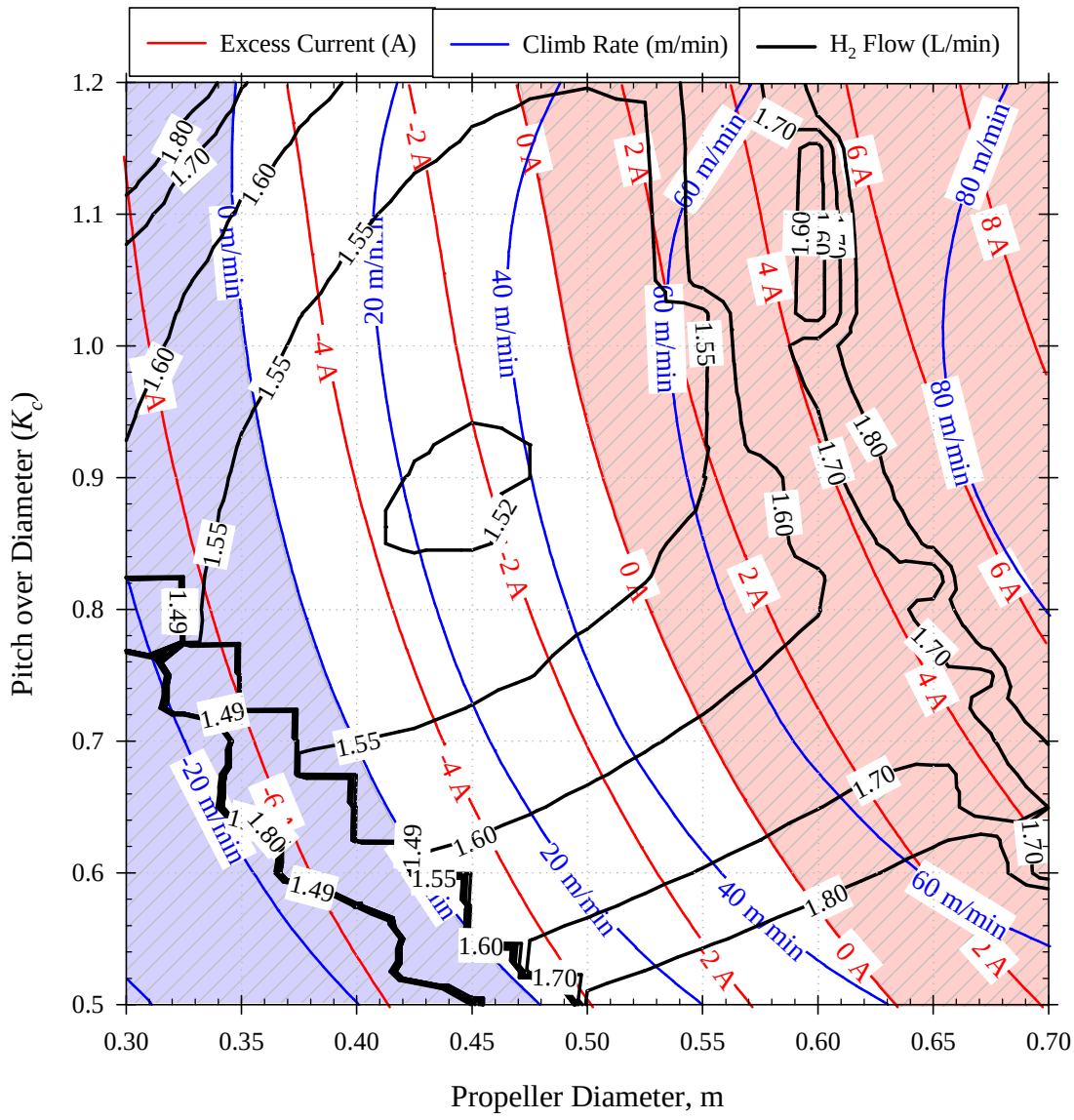

Figure 8.12: FCUAV design space showing excess current and climb rate contours.

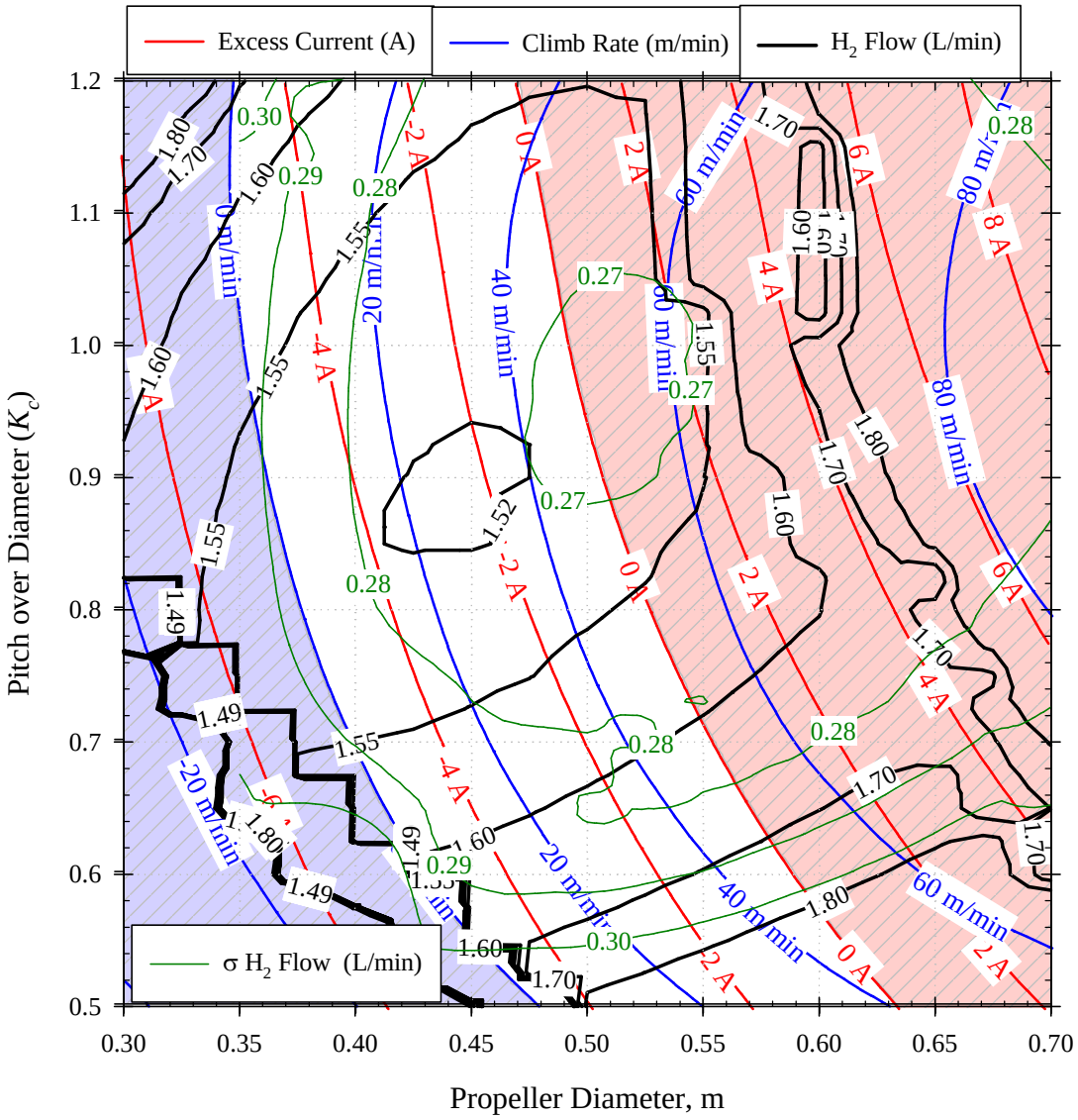

Figure 8.13: FCUAV design space showing standard deviation contours of the hydrogen flow rate.

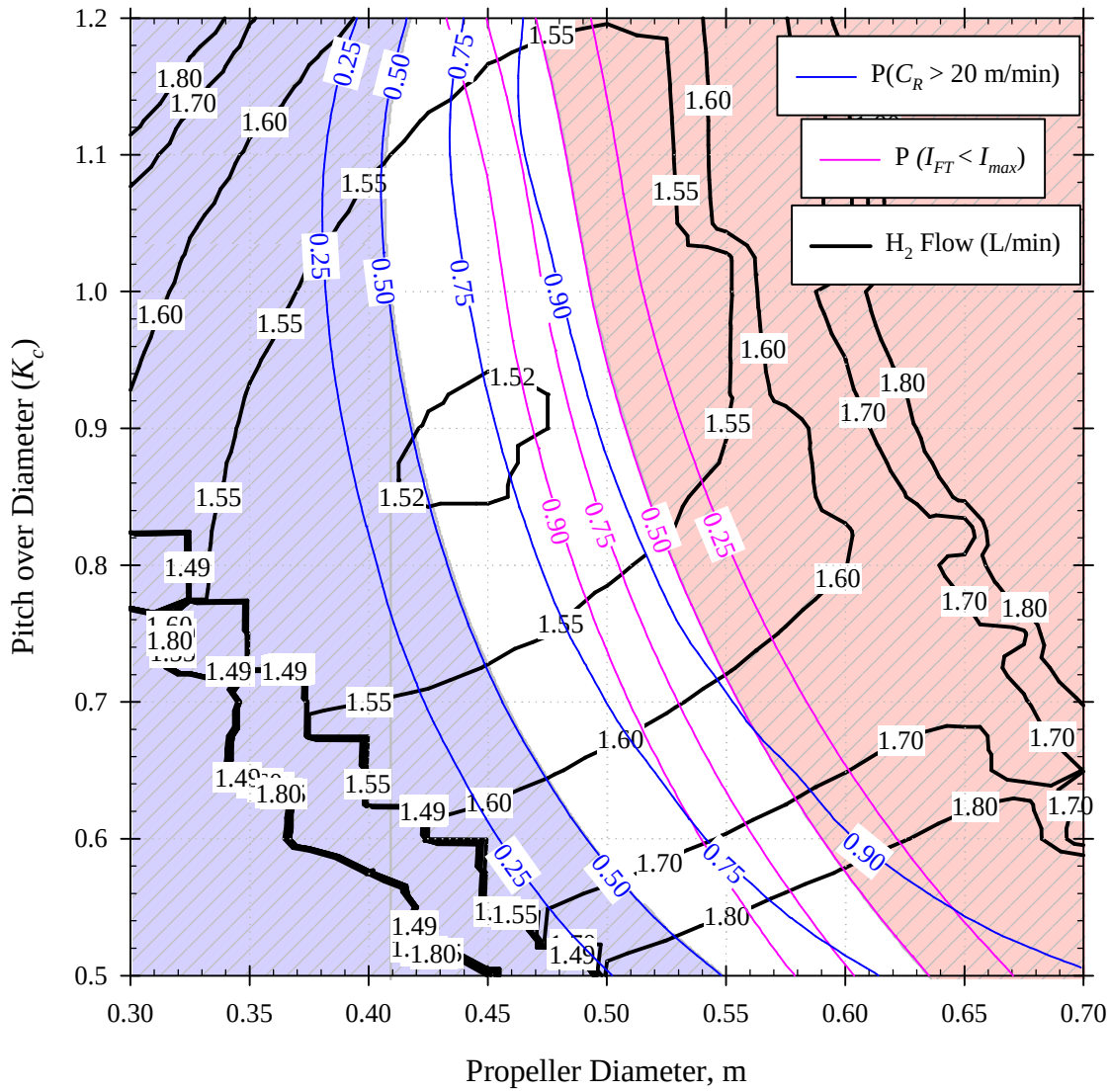

Figure 8.14: FCUAV design space with probability contours shown for both meeting the excess current and climb rate constraints.

To further understand how the hydrogen flow rate is related to the maximum climb rate, a Pareto frontier was generated. To generate the Pareto frontier, climb rate target values from 0 to 50 m/min were used in the formulation given in Eq. (8.2).

$$\begin{aligned} &\text{Minimize: } H_2 \text{ Flow} \\ &\text{Subject to: } C_R \geq \text{Climb Rate Target} \\ &I_{FT} \leq I_{max} \end{aligned} \qquad (8.2)$$

The Pareto frontier along with the constraint values for both the climb rate and max current are given in Figure 8.15. The constraint values in Figure 8.15 have been converted to standard form so that any value greater than zero represents a constraint violation.

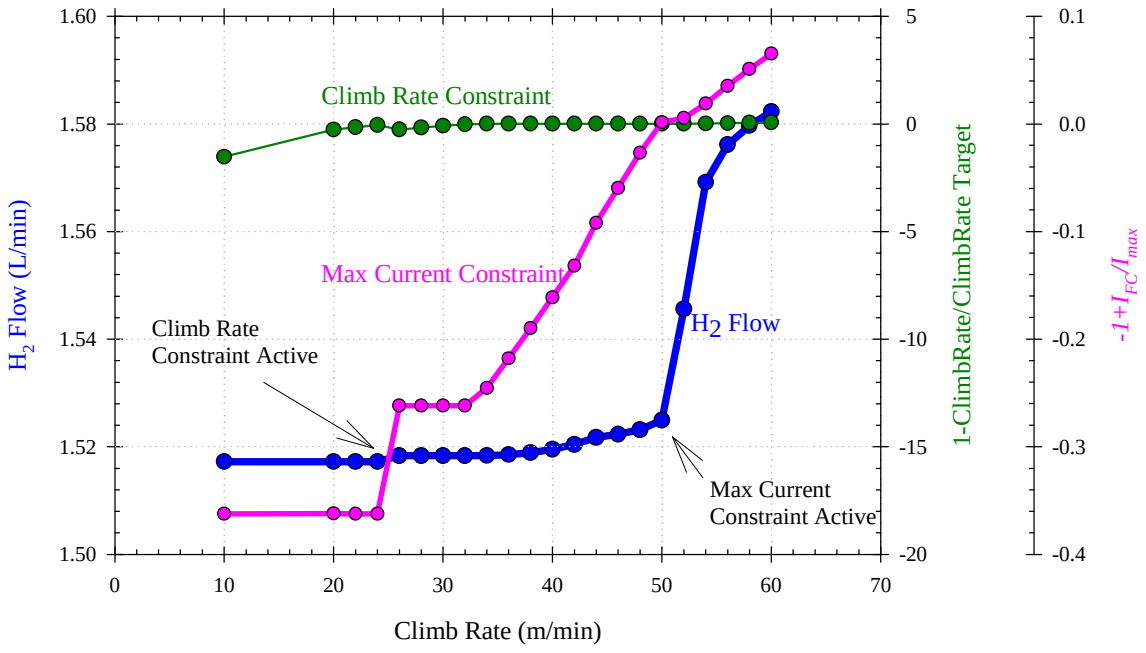

Figure 8.15: Pareto frontier of climb rate and H_2 flow shown with design constraints.

The Pareto frontier in Figure 8.15 gives insight into how the aircraft performance is constrained throughout the feasible design space. At low climb rates (C_R < ~25 m/min), the minimum hydrogen flow rate required for cruise stays constant at the global minimum. Neither the max current constraint nor the climb rate constraint is active at low climb rates so changing the climb rate target will not change the minimum hydrogen flow rate. As the target climb rate is increased, the climb rate constraint will be active (equal to zero in Figure 8.15). The climb rate constraint then stays active and the aircraft requires more hydrogen at cruise in order to continue to satisfy the climb rate constraint. As the climb rate increases further, the probability of keeping the current below the maximum allowable current decreases until the maximum fuel cell current constraint becomes active. Once this maximum current constraint becomes active, the hydrogen flow required increases rapidly. When the climb rate target exceeds 50 m/min, the aircraft system can no longer meet both the climb rate and maximum fuel cell current constraints.

The same Pareto frontier with the probabilities of meeting a climb rate constraint of 20 m/min and an excess current of 0 A are plotted in Figure 8.16. At low climb rate targets when the design is at the global minimum hydrogen flow rate, changes in climb rate target does not influence the probability of satisfying the constraints. Once the climb rate constraint becomes active, increasing the climb rate target will both increase the probability of satisfying the climb rate constraint and decrease the probability of satisfying the maximum current constraint. Note that the maximum current constraint only stays active for a climb rate targets of 50-52 m/min. Above a climb rate target of 52 m/min, probability of meeting the maximum current constraint drops below 0.5.

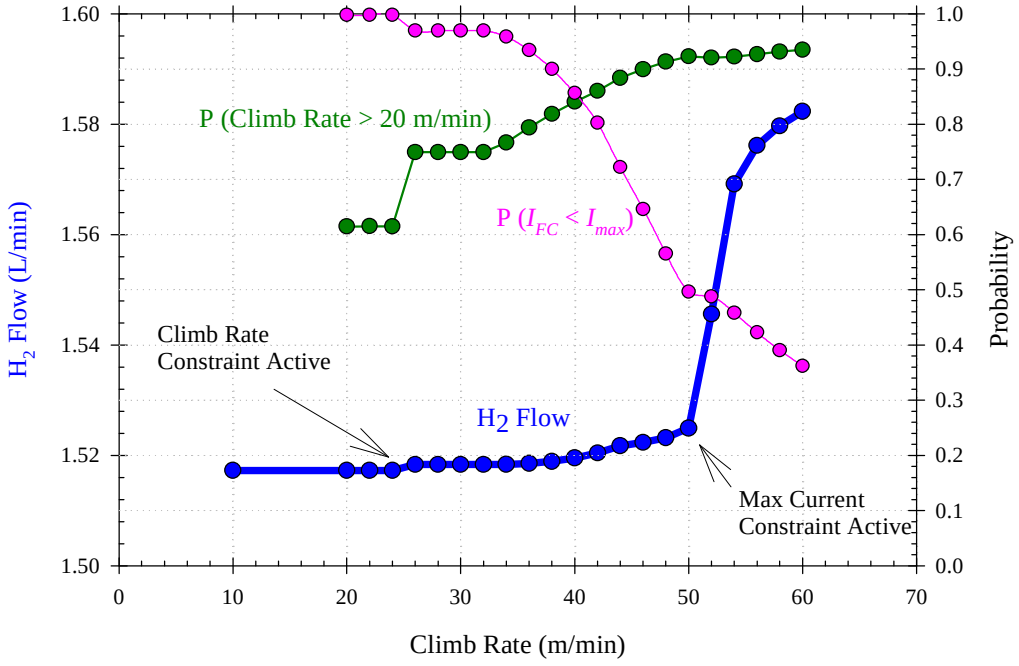

Figure 8.16: Pareto frontier of climb rate and H_2 flow with probability of meeting constraints.

The maximum joint probability of meeting both constraints can be deduced from Figure 8.16. This point is represented at the intersection between the climb rate probability curve and the fuel cell current probability curve. Thus the maximum probability at which both constraints can be satisfied simultaneously while minimizing the hydrogen flow rate is ~ 0.85.

The Pareto frontier in both Figure 8.15 and Figure 8.16 can be viewed in the two dimensional plot of the design space (see Figure 8.17). At low climb rates, the design is not constrained and the propeller diameter and pitch-over-diameter ratio remain constant. When the climb rate constraint becomes active, the propeller pitch and diameter must be increased which increases the flow rate of hydrogen and appears as a step change in Figure 8.17. As the climb rate is increased further, the propeller diameter is increased with only a slight increase in pitch as the increased diameter allows the design to move

normal to the climb rate contours. Note that another drastic change results as the design follows the steep contour of the hydrogen flow rate. Once the excess current constraint becomes active, the design begins following the constraint boundary. The propeller pitch is drastically decreased with a slight increase in diameter to move along the feasible boundary. As the climb rate is further increased, the Pareto front moves into the infeasible region where the current constraint is likely to be violated. Note that even though the constraint is being violated, the optimization method identified the region with the shortest path to meeting the increased climb rate constraint. This information is of value to a designer as it identifies the design space region that will require the least amount of relaxation in the active constraints.

In addition to identifying the tradeoff between climb rate and excess current, improving the design while maintaining high probabilities of meeting the constraints can be achieved by reformulating the optimization problem into Eq. (8.3).

$$\begin{aligned} &\text{Minimize: } H_2 \text{ Flow} \\ &\text{Subject to: } P(C_R \geq 20 \text{ m/min}) \geq \text{Target} \\ &P(I_{FC} \leq I_{max}) \geq 0.75 \end{aligned} \tag{8.3}$$

By repeating the optimization for various values of climb rate target probabilities, Figure 8.18 was generated. Figure 8.18 provides similar information to Figure 8.15. As the probability of meeting the climb rate constraint increases, the hydrogen flow rate slightly increases and the probability of meeting the excess current decreases. When the probability of meeting the excess current constraint becomes active, the hydrogen flow begins to drastically increase.

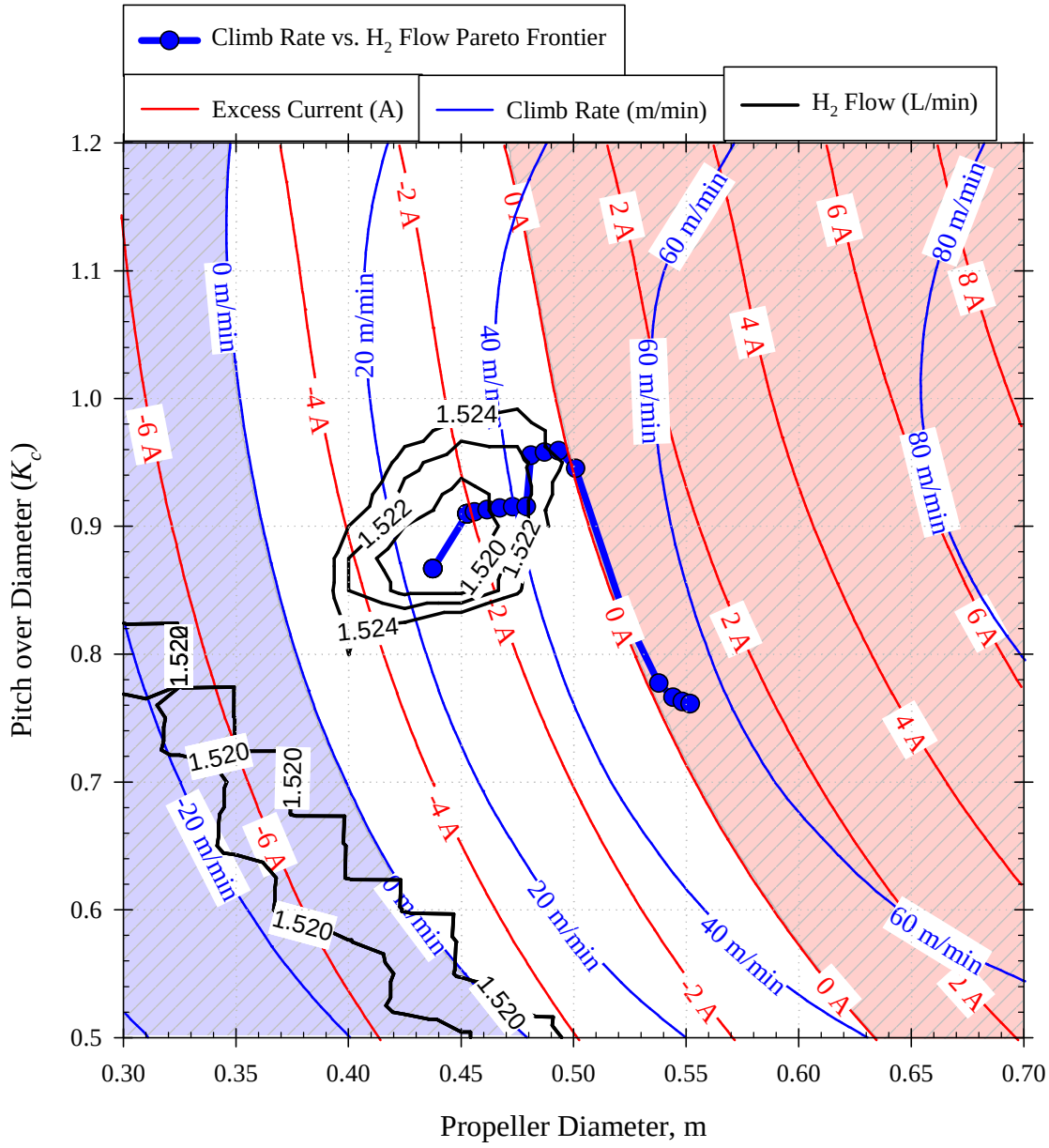

Figure 8.17: FCUAV design space with Pareto frontier of climb rate and H_2 flow.

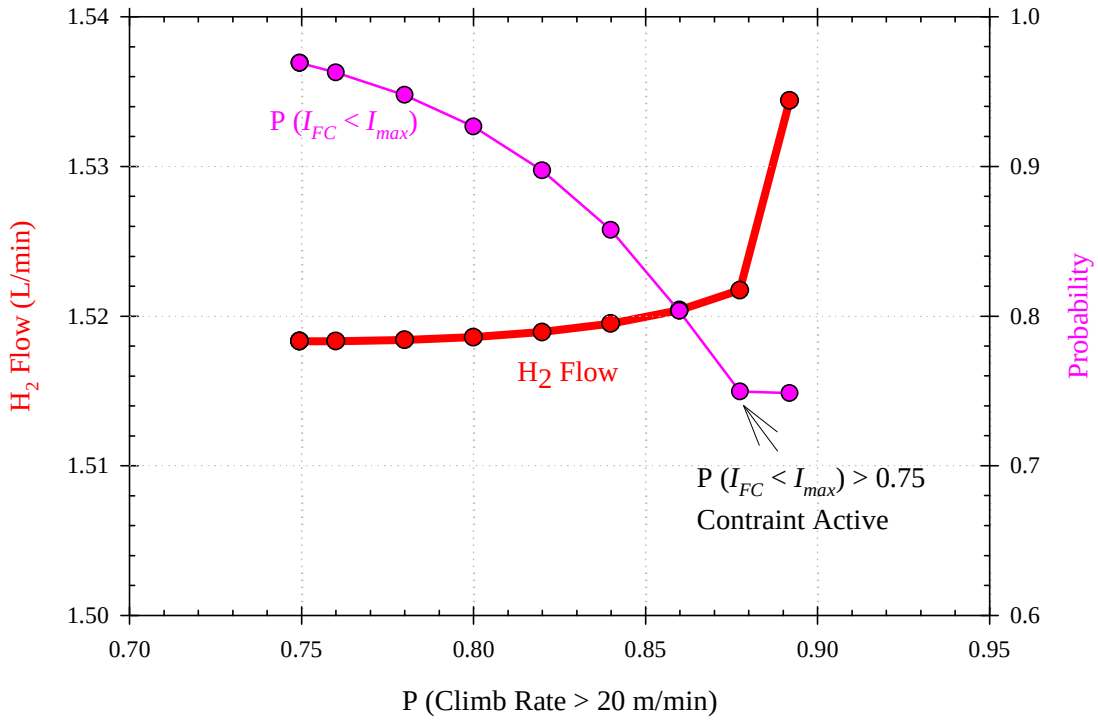

Figure 8.18: Pareto frontier of H_2 flow and the probability of exceeding the climb rate constraint.

To increase the probability of meeting the climb rate constraint while maintaining the probability of meeting the excess current constraint, the design must follow a probabilistic contour line. This behavior is verified by plotting the Pareto frontier of Figure 8.18 on the plot of the probabilistic design space (see Figure 8.19).

The Pareto frontier of hydrogen flow rate versus the probability of meeting the design constraint initially follows the same path as the Pareto between H_2 flow and climb rate. However, the additional constraint of meeting to excess current constraint with a minimal probability of 0.75 causes the Pareto fronts to diverge when this constraint became active. As the excess current probability constraint is active, the design is forced to follow the constraint boundary until no more improvement can be made in hydrogen flow rate within the probabilistic constraints.

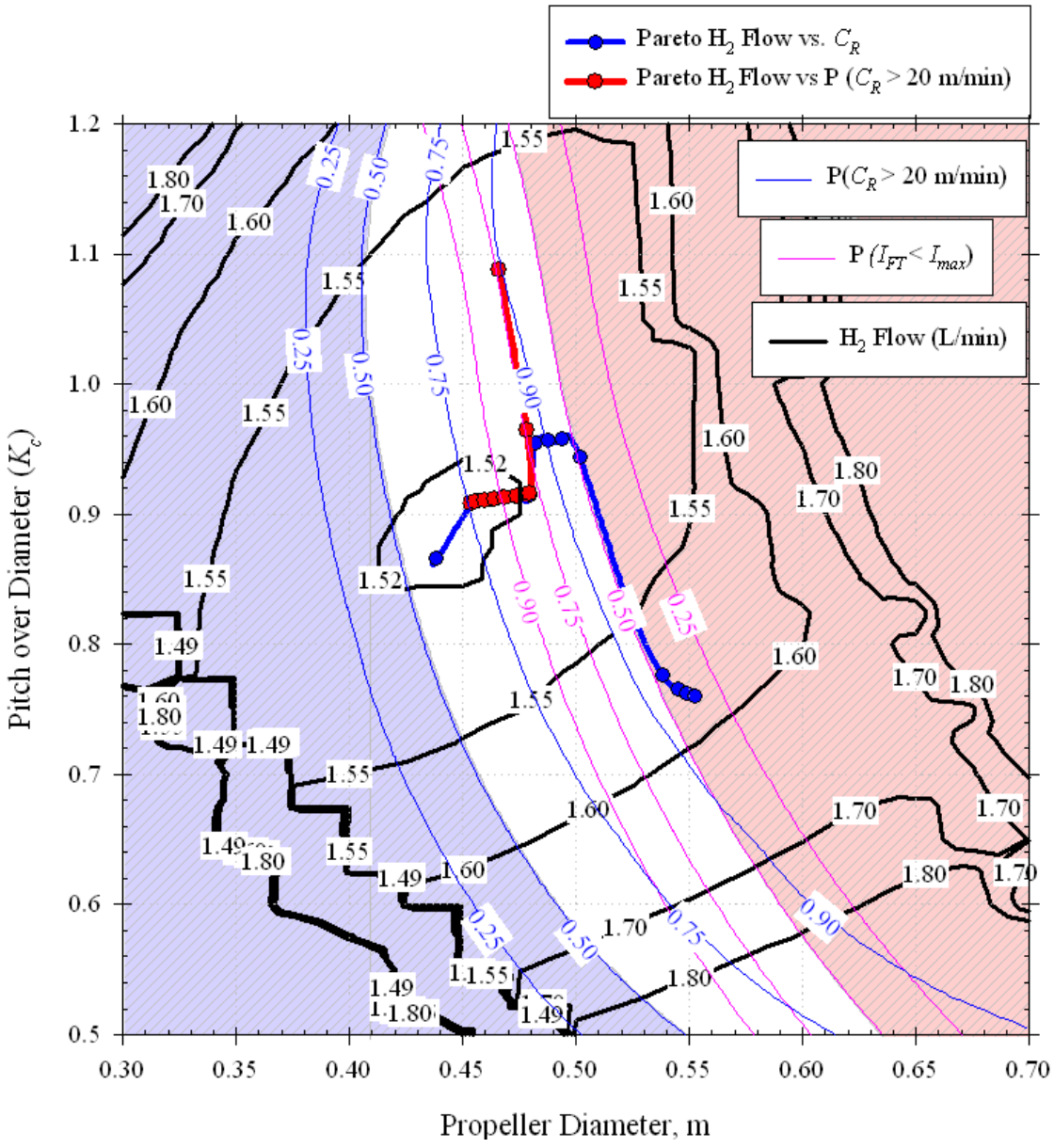

Figure 8.19: FCUAV design space with multiple Pareto frontiers shown.

8.5 Lessons Learned from the Implementation Study

Application of the methodology to the study of a near-term fuel cell UAV provided many insights into both the methodology and into fuel cell UAV design. Applying the decomposition rules that accompany the assumptions of SSA created far more CAs in the DSM than originally expected. For the implementation study, the rather simple cruise and climb simulation required the decomposition of the MDA into 45 CAs. This was easily accomplished as the author developed all of the CAs. However, if the use of legacy codes were required, the decomposition would be much more involved. For instance, if a legacy code for propeller performance could only calculate propeller speed as a function of thrust but the known uncertainty distribution of thrust was known as a function of rpm, then a shooting point type wrapper routine would be required to reformulate the CA with the desired inputs and outputs. Likewise, if legacy codes are not fully decomposed and contain outputs that are functions of other outputs, additional code may be needed to achieve an acceptable degree of decomposition.

The uncertainty in fuel cell performance is significant. The Horizon Fuel Cell Technologies H-300 fuel cell power performance was far below the polarization curve that was provided by the manufacturer. In addition, tests run under controlled conditions yielded fluctuations in performance. This uncertainty in actual performance will have an important effect on the design as uncertainties will need to be included to assure that the design can meet its constraints with an acceptable probability.

Uncertainty can vary significantly throughout the design space. Introducing test data in an attempt to reduce uncertainty did not always result in an overall reduction in

uncertainty as the design could re-optimize to other areas of the design space where the performance metrics may be more sensitive to uncertainty.

The optimization methodology proved to be very robust. Other than finding a semi-feasible initial condition, no effort was needed to adjust parameters with the optimization scheme. The Nelder Mead simplex algorithm was able to consistently locate the optimum without causing the code to fail. The DSM solution process also proved to be efficient and robust. The Powell-dogleg method was executed tens of thousands of times throughout the design space during optimization as well the development of figures in this chapter. The method only failed when trying to generate figures where the code was asked to solve using a set of design variables that would provide a non-physical solution. The use of a penalty function to handle constraints also proved valuable. The exterior penalty method allowed constrained designs to be determined without excessive violations of the constraints. The method was also useful when constraints were violated as it provided an insight into the "least painful" constraint violation paths.

The methodology was very useful in its ability to assess the limits of the design space. The method was able to accurately assess the Pareto frontiers for the propeller design study that was conducted. These calculated frontiers were verified by plotting them on contour plots of the design space.

The results provided some insight into the design of small fuel cell powered UAVs. With an emphasis on endurance, the design was very sensitive to changes in the propulsion system. Higher than expected error in predicting the expected value of the fuel cell voltage resulted in significant changes in the wing loading of the vehicle. Also,

small changes in fuel cell or motor performance required significant propeller changes. The influence of uncertainty in the propulsion system could be mitigated by using a variable pitch propeller, but the analysis also suggested that changes in propeller diameter could also be needed.

8.6 Chapter Summary

The methodology was implemented by examining the design of a small UAV with the goal of achieving 24 hours of endurance. The MDA was decomposed into 45 contributing analyses. This degree of decomposition was necessary to stay within the design rules specified by SSA in Chapter 4. An iterative procedure was performed to replicate a design cycle and provide a method by which to develop hardware for validation testing. The procedure consisted of performing a deterministic optimization, then using the propagated uncertainty at the optimum design to inform hardware development choices. As the hardware was purchased and tested, the empirical data was used to reduce the input uncertainty estimates and the design was then re-optimized. After several iterations, enough hardware was developed to perform a hardware-in-the-loop simulation that was able to validate the MDA. A Monte Carlo simulation was also performed on the design corresponding to the HiL setup to verify that the SSA method was capturing the propagation of uncertainty. Finally, a design space exploration using key propeller design variables was performed. The optimization formulation in Chapter 7 was used to generate Pareto frontiers of the both the deterministic and probabilistic design space. These frontiers were compared to contour plots of the design space and found to be accurate.

CHAPTER 9

CONCLUSION

The overall objective of this thesis was to develop a methodology to enable the near-term performance of a fuel cell UAV to be determined. A review of the literature identified key gaps in existing methodologies for fuel cell aircraft design. These key deficiencies include the lack of a validated multidisciplinary analysis, the lack of a flexible design framework, and an incomplete quantification of the effects of uncertainty. The research questions and hypotheses that resulted from these gaps have been restated and results that both support the hypotheses are provided. A number of contributions unique to this research are then presented along with future work opportunities.

9.1 Research Questions and Hypotheses

The research objective was decomposed into a series of research questions. These research questions and their corresponding hypotheses are restated. A discussion of the results that resulted from the research tasks that supported each hypothesis is then provided.

Research Question 1: How can a validated multidisciplinary design analysis be created for a fuel cell powered UAV?

Hypothesis 1: By using uncertainty propagation to guide decomposition, a fuel cell propulsion system can be decomposed into validateable contributing analyses that will facilitate a multidisciplinary design analysis that will agree with system level performance.

Five different tasks were executed to address this area of the research. The first task dealt with using uncertainty propagation to guide problem decomposition. Using the GT FCUAV as a baseline, a simplified MDA was built and uncertainty was propagated. The results suggested that efforts should be focused decomposing drag and weight as well as focusing on reducing the uncertainty in estimating propeller efficiency and fuel cell efficiency. Using this as a guideline, mathematical models were researched and built for all of the major subsystems expected in a fuel cell UAV. The models consisted of both physics based and empirically based models. For the non-empirically based models, either the literature or experiments were carried out to validate the models. The final task was to validate the analysis at the system level. This was accomplished in Chapter 8 during the implementation study of a 24 hour endurance small UAV. Using a hardware-in-the-loop simulation of an entire fuel cell propulsion system, output values of the multidisciplinary analysis were validated thus supporting Hypothesis 1. However, the system level validation did not occur in isolation. Data collected from both the fuel cell and electric motor were needed to get an accurate estimate of the performance of these components. However, when validated at the component level, the contributing analyses as posed in Chapter 5 proved to be decomposed to an adequate level to produce sufficient system level results.

Research Question 2: How can the framework for a MDA be created that is flexible enough to adapt to various powerplant architectures?

Hypothesis 2: By specifying the MDA as a function of the hierarchy, inputs, and outputs of each contributing analysis, an automated procedure can be developed to transform the system into a set of solvable compatibility equations.

Based on the limited data on fuel cell systems and their architectures, as well as the rapid development of fuel cell technology, near-term performance requires a design framework that can adapt as design knowledge increases. Hypothesis 2 addressed this by proposing that an automated process could be developed to specify and solve a set of compatibility equations. To support this hypothesis, three tasks were performed. The first task resulted in the development of a parsing code that used the hierarchy of CAs within a DSM as well as their respective inputs and outputs to determine where feedback loops would exist. The feedback loops were then eliminated by introducing compatibility equations. A simple procedure was developed that sequentially stepped through each CA in the hierarchy in which it appeared in the DSM and formulated the compatibility equations for a non-linear equation solver. Multiple non-linear equation solvers were tested for both robustness and efficiency. In the end, the Powell-dogleg method provided an adequate compromise between efficiency and robustness. The automated process was tested by using different CA hierarchies and comparing the results to a more traditional nested solution framework. Finally an implementation study was performed that performed several iterations where the DSM had to be slightly restructured as empirically based CAs were used to replace original models. The results supported the hypothesis as the flexible framework proposed automated the process of building and solving compatibility equations. As a result, updating the MDA proved to be straightforward and efficient requiring very little setup effort.

Research Question 3: What generalized method will allow the determination of an optimal solution under the effects of uncertainty?

Hypothesis 3: An optimal solution under the effects of uncertainty can be obtained by using System Sensitivity Analysis to calculate the probabilistically feasible space and inform optimization via a robust optimization scheme.

The final research question would address optimization under uncertainty. Nearly all fuel cell design studies have concluded that uncertainty is significant yet most studies do not account for uncertainty and the few studies that include uncertainty have been forced to make arbitrary uncertainty estimates due to a lack of data. Hypothesis 3 proposed a method using systems sensitivity analysis (SSA) to both estimate propagated uncertainty, and provide gradients for use an optimization routine. A SSA code was developed and verified against Monte Carlo simulations for both an example problem as well as a simulation of the entire fuel cell propulsion system. A successful routine was then developed that allowed gradients estimated in SSA to be used in SQP optimization. However, testing proved that the SQP optimization was problematic. In a highly constrained design environment, it is difficult to determine appropriate side constraints for design variables. As a result, the SQP optimization could easily move into areas of the design space where design constraints were violated to an extent that would cause the MDA to fail. Attempts were made to mitigate this by providing limits to the length of line searches allowed in SQP but the method did not prove to be robust enough to be trusted for design space exploration. In addition to SQP, compass search and Nelder Mead optimization routines using penalty functions to account for constraints were tested. Both proved to be more robust than SQP with the Nelder Mead method proving to be the best overall in terms of robustness and efficiency.

Overall, the synthesis of the of the chance constrained programming formulation, uncertainty propagation via SSA, and the validated MDA proved valuable in studying the design space of a near-term fuel cell UAV. The Pareto frontier showing the tradeoff between climb rate and hydrogen flow rate was efficiently calculated and clearly showed how that frontier changed as different design constraints became active. The Pareto frontier that was calculated was verified by plotting the Pareto frontier on a contour plot of the design space and verifying that the frontier followed the correct probability contours in the design space.

9.2 Summary of the Methodology

After performing the research tasks to address each of the hypotheses, it is useful to provide an overall summary of the methodology. The methodology consists of taking a notional concept, using uncertainty propagation as well as data for verification and validation to help inform the construction of a validated MDA, and then synthesizing the MDA with an uncertainty propagation technique as well as a chance constrained optimization formulation to explore the design space. One of the key areas addressed in this dissertation that was absent from previous work was the development of a MDA and verified uncertainty propagation technique that can be used for probabilistic design space exploration. This dissertation showed that SSA was efficient and accurate if the MDA was properly decomposed. Figure 9.2 outlines the process of preparing an MDA for use with SSA. After completing the steps in Figure 9.2, Chapter 7 contains the formulation for exploring the design space by identifying Pareto frontiers. Chapter 8 provides an example of how this was accomplished for a near-term fuel cell UAV.

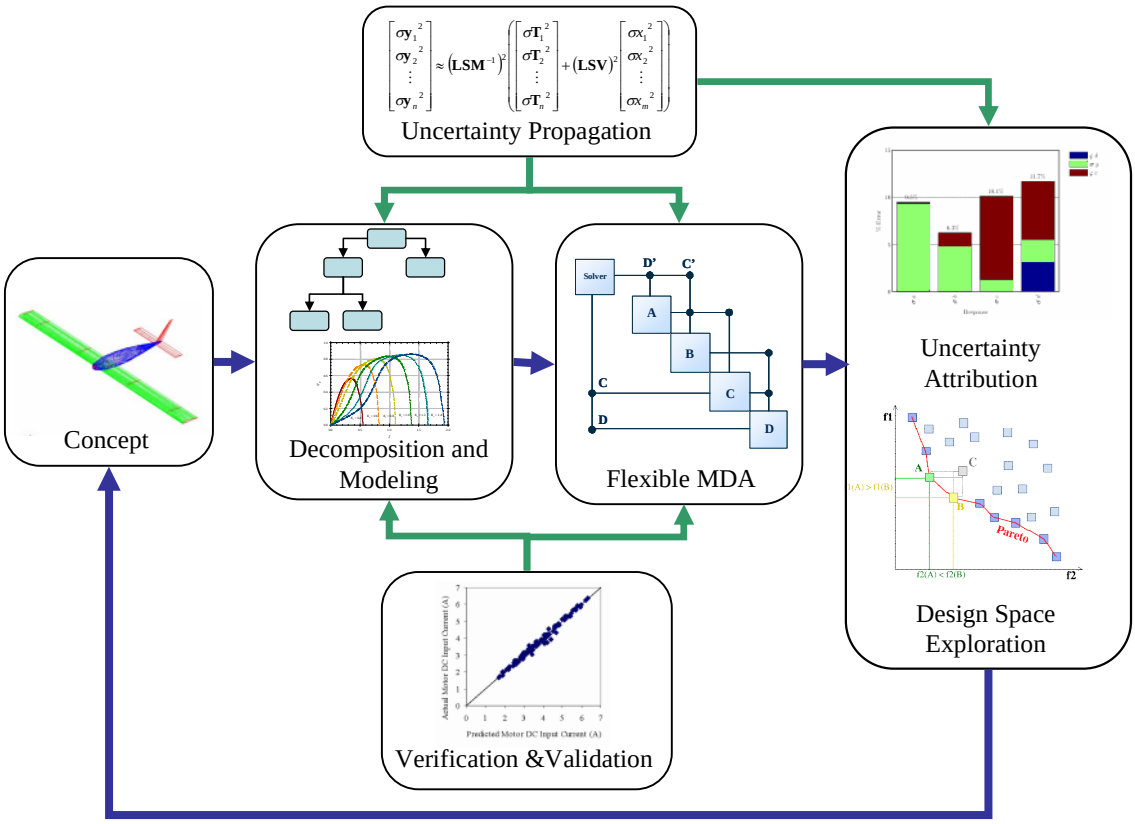

Figure 9.1: Summary of design methodology.

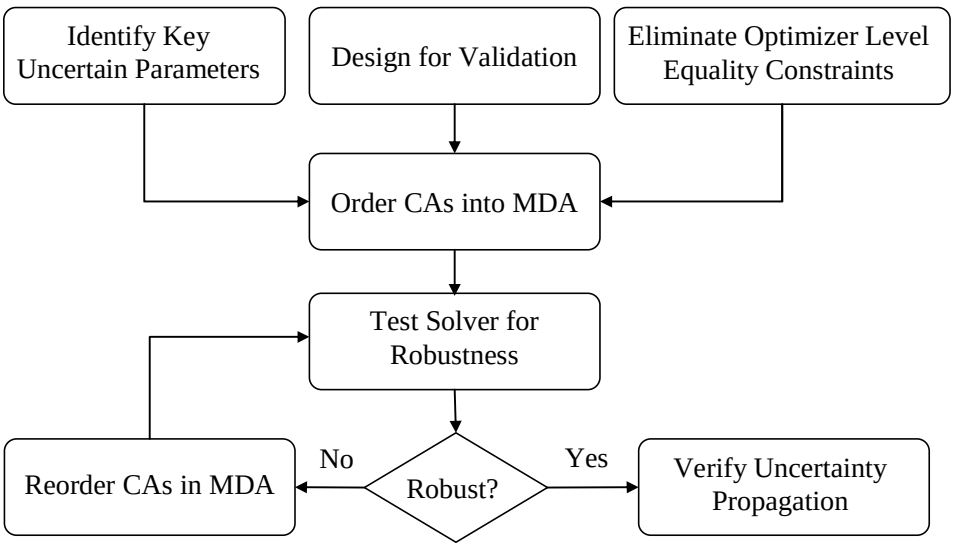

Figure 9.2: Process of building of preparing a MDA for use in CCP.

9.3 Contributions

The research summarized in this dissertation has resulted in several contributions to the methodology and development of fuel cell UAVs. These contributions are summarized as follows.

- An extensive survey of fuel cell powered aircraft. A considerable effort was made to indentify, understand, and document all available information in the public domain on fuel cell powered aircraft.
- A set of validated contributing analyses for fuel cell powered aircraft. This research resulted in the development of several custom models needed to analyze a fuel cell aircraft. In addition to the fuel cell and balance of plant, detailed models to perform weight estimates, propeller and electric motor analysis, and aerodynamic analysis were developed. These models were validated to the extent that they were used in this research and most are appropriate for use in other design studies that may or may not include fuel cell propulsion.
- Development of a validated MDA for a fuel cell propulsion system. This research provides the first publically available validation of the system level performance predicted by a fuel cell propulsion MDA.
- Successful implementation of SSA on a complex engineering problem. Most applications of SSA have been on simplified example problems. This analysis applied SSA to a very complex MDA involving 45 different CAs. The calculated uncertainty for the complex propulsion system of a fuel cell aircraft was verified using a Monte Carlo simulation. In addition, the research resulted in 3 basic design rules that inform the development of MDA for uncertainty propagation. These

address the degree of decomposition, the input and output flow needed for validation and uncertainty estimates, and the elimination of system level equality constraints.

- Automated flexible design framework for solving a DSM. To facilitate flexibility in replacing, reordering, or updating CAs, an automated framework was created to solve a DSM. This framework is straightforward to implement and allows the MDA to easily adapt to different models without requiring significant setup effort.
- Informed uncertainty propagation results for a small fuel cell powered UAV. The implementation study performed an uncertainty propagation using input uncertainty distributions that were largely measured experimentally. Most studies in the past have used arbitrary estimates for uncertainty distributions since adequate data was not available.
- Successful design space exploration of a fuel cell powered UAV. The implementation study showed that the proposed method correctly identified multiple Pareto frontiers which allow the designer to explore the limits of the design space. This exploration showed that discontinuities often occur in the Pareto frontier due to activation of design constraints. However, without design space exploration, it is difficult to anticipate when and if certain constraints become active. Of particular interest was the activation of the climb rate constraint during the propeller design portion of the implementation study. The results suggested that the FCUAV design was only constrained by the climb rate if the climb rate was sufficiently high. This contradicts an oft used assumption in fuel cell design that

directly sizes the fuel cell to the maximum power constraint regardless of the maximum power required.

9.4 Lessons Learned

Several important lessons were learned during the research. The primary lessons are summarized as follows:

- Importance of having a flexible MDA when working with rapidly developing technology. With fuel cell aircraft, the design was shown to be largely dependent on the performance of the propulsion system. Changes in fuel cell, motor, or propeller power caused significant changes in the aircraft. Therefore, a MDA that can be continually updated as information is learned about the design is extremely valuable, especially if the design is as highly constrained.
- Design in a highly constrained environment was more robust with non-gradient based solvers with limited step sizes. The primary problem in optimization was significant constraint violations that caused the MDA to fail. Using a path based optimization method with a limited step size helped solve this problem. Although SQP proved to be extremely efficient when it worked, it was simply not robust enough for design space exploration.
- Importance of accounting for uncertainty. Uncertainties in design performance can prove to be detrimental in achieving a feasible design. Designing within a probabilistic design space provided an effect means to mitigate the effects of uncertainty by choosing designs that were not on deterministic constraint

boundaries. This is expected to result in less redesign work when implemented throughout a design process.

9.5 Future Work

Over the course of the research, a number of research areas were identified that could enhance both the design methodology and the understanding of the potential performance of near-term fuel cell aircraft.

An obvious extension of this research would be to include more implementation studies. Small fuel cells have continued to rapidly develop since the bulk of the implementation work was performed for this research. State of the art fuel cells systems are now available that have more than two times the specific power of the Horizon fuel cell used in the implementation study. This will allow for new configurations and missions to be studied in addition to persistent ISR missions.

Another useful area of future work is in the area of uncertainty identification. Even with all the experience and data gained from the GT FCUAV development, estimating the uncertainties in the design variables and calculations made by the contributing analyses was difficult and required more time and effort than would typically be afforded during a conceptual design. A refined method that allows for the identification and estimation of key uncertainties would be valuable. To a certain extent, the iteration procedure in the implementation study addressed this, however, a much more refined method is desired.

Similar to introducing better methods for uncertainty identification, a multi-stage method with recourse would be valuable. The implementation study provided a simple

approach to going through multiple stages to develop the propulsion system hardware that was used in the HiL simulations. However, it is expected that a much more useful method could be developed that could capitalize on the unique ability to rapidly prototype and test UAV subsystems. For the implementation study, it was found that the initial estimates of propagated uncertainty were too high to be very useful in selecting a probabilistically constrained design. Therefore any method would have to address this problem and propose a method for determining the order in which important design decisions are made.

Finally, improvements could be made in the flexible design framework implementation. One improvement would be to include an algorithm to help determine an optimum hierarchy of the CAs. This could improve efficiency and increase robustness by simplifying the number of simultaneous non-linear equations that must be solved. Robustness could also be improved by determining a hierarchy that provides a better conditioned set of coupled equations. Results in Chapter 6 proved that a simple reordering of the propeller CAs could greatly decrease instances where the DSM could not be solved. It is likely that a sensitivity study performed on the CAs could help inform hierarchy decisions that result in compatibility equations that are optimized to be well behaved.

9.6 Concluding Remarks

Fuel cells will continue to be a developed for small UAV applications. The implementation study showed that using off the shelf technology circa 2007 could provide a useful fuel cell powered UAV with nearly 24 hours endurance. As recently as

October 2009, over 23 hours of endurance has been demonstrated by a similarly sized fuel cell powered vehicle. Moreover, advances in fuel cell technology will continue to improve performance and open up new applications.

This research has begun the development of a methodology for exploring the design space of fuel cell UAV. Analyses that were validated at both the subsystem and system level were developed and help determine an appropriate degree of fidelity that can be used in future UAV designs. The research also provided a flexible design framework that can be easily adapted for use in later stages of design as more information becomes available or higher order analyses are implemented. In addition, the flexible framework could be used to reduce the setup time required to study various architectures that are afforded by an all electric propulsion system. Finally, the methodology includes the means for exploring a probabilistically constrained design space. It is hoped that the methodology presented in this research will continue to be developed, refined, and applied to additional engineering problems ultimately enabling improved designs.

REFERENCES

[1] "Collecting the History of Fuel Cells," Smithsonian National Museum of American History, 2004, http://americanhistory.si.edu/fuelcells/index.htm, [Online; accessed September 27, 2006].

[2] OTTO, N. A., (to the Gas-Motoren Fabrik - Deutz), "Gas-Motor Engines," U.S. Patent 194,047, August 14, 1877.

[3] DIESEL, R., (to the Diesel Motor Company of America), "Internal-Combustion Engine," U.S. Patent 608,845, August 9, 1898.

[4] LEFEBVRE, A. H., *Gas Turbine Combustion*, Taylor & Francis Group, Philadelphia, PA, 1998.

[5] HACKER, B. C. and GRIMWOOD, J. M., *On the Shoulders of Titans: a History of Project Gemini*, NASA, Washington, DC, 1977.

[6] "Fuel Cell Vehicles: Race to New Automotive Future," Technology Administration Report, US Department of Commerce, January 29, 2003.

[7] CHAIKIN, A., *Air and Space*, Bulfinch Press/Little, Brown and Company, Boston, 1997.

[8] NEWCOME, L. R., *Unmanned Aviation: A Brief History of Unmanned Aerial Vehicles*, American Institute of Aeronautics and Astronautics, Reston, VA, 2004.

[9] BURROWS, W. E., *This New Ocean: The Story of the First Space Age*, Random House, Inc., New York, NY, 1998.

[10] JONES, C. A., "Unmanned Aerial Vehicles (UAVS): An Assessment of Historical Operations and Future Possibilities," USAF Air Command and Staff College, Maxwell Air Force Base, AL, 1997.

[11] DICKERSON, L., "Outlook: Calling All UAVs," *Aviation Week and Space Technology 2008 Source Book*, McGraw-Hill, vol. 168, no. 4, pp. 110-113, January 28, 2008.

[12] PINCUS, W., "Air Force Training More Pilots for Drones Than for Manned Planes," Washington Post, 2009, http://www.washingtonpost.com/wp-dyn/content/article/2009/08/10/AR2009081002712.html?hpid=sec-nation, [Online; accessed August 12, 2009].

[13] SWEETMAN, B., "Insitu- Now Boeing's Biggest Aircraft Producer," Aviation Week, 2009, http://www.insitu.com/index.cfm?navid=299&cid=3750, [Online; accessed August 12, 2009].

[14] CURRAN, M., "UAVs: A Critical Multiplier for Current and Future Forces," Rusi Defence Systems, 2005, http://www.rusi.org/downloads/assets/19Curran.pdf, [Online; accessed May 1, 2009].

[15] CAPPS, R., "The Good Enough Revolution: When Cheap and Simple is Just Fine," Wired Magazine: 17.09, 2009, http://www.wired.com/gadgets/miscellaneous/magazine/17-09/ff_goodenough?currentPage=1, [Online; accessed August 24, 2009].

[16] MATTHEWS, W., "Flying High on Hydrogen Power: Fuel Cells May Keep Smaller UAVs Aloft and Watching Longer," Defense News, 2009, http://www.defensenews.com/story.php?i=4046002&c=FEA&s=TEC, [Online; accessed April 20, 2009].

[17] DRELA, M., PROTZ, J. M., and EPSTEIN, A. H., "The Role of Size in the Future of Aeronautics," in *AIAA/ICAS International Air and Space Symposium*

and Exposition: The Next 100 Years, Dayton, OH, AIAA 2003-2902, July 14-17, 2003.

[18] BRAYBROOK, R., "Drives for Drones," *Armada International*, vol. 31, no. 1, pp. 20-24, February/March, 2007.

[19] EGOZI, A., "IAI Looks at Fuel Cells for UAVs," Flight International, 2004, http://www.flightglobal.com/articles/2004/03/09/178649/iai-looks-at-fuel-cells-for-uavs.html, [Online; accessed August 1, 2009].

[20] "Fuel Cell Powered Unmanned Aerial System Achieves Flight Endurance Milestone," Science Daily, 2009, http://www.sciencedaily.com/releases/2009/08/090806141720.htm, [Online; accessed August 7, 2009].

[21] "Puma AE Technical Specifications," AeroVironment, 2009, http://www.avinc.com/downloads/AV_PUMAAE_V10109.pdf, [Online; accessed May 1, 2009].

[22] "Aerosonde Mark 4.4 Series: Strength and Flexibility," AAI Corporation, 2009, http://www.aerosonde.com/pdfs/aerosonde02-20-09.pdf, [Online; accessed May 1, 2009].

[23] "Protonex Introduces Fuel Cell Power System at UAV Symposium," *Fuel Cells Bulletin*, vol. 2006, no. 10, p 11, 2006.

[24] "NRL/ONR Press Release 31-09r: Surveillance Vehicles Take Flight Using Alternative Energy," Naval Research Laboratory, 2009, http://www.nrl.navy.mil/pressRelease.php?Y=2009&R=31-09r, [Online; accessed April 3, 2009].

[25] "QinetiQ's Zephyr UAV Flies for Three and a Half Days to Set Unofficial World Record for Longest Duration Unmanned Flight," QinetiQ, 2008, http://www.qinetiq.com/home/newsroom/news_releases_homepage/2008/3rd_quarter/qinetiq_s_zephyr_uav.html, [Online; accessed August 25, 2008].

[26] CHAVANNE, B. H., "Work on Quiet UAVs Shows Promise," McGraw-Hill, 2009, http://www.aviationweek.com, [Online; accessed April 8, 2009].

[27] DAVIS, B., "Paris Air Show Anniversary Spotlights Unmanned Aircraft," *Unmanned Systems*, AUVSI, vol. 27, no. 8, Arlington, VA, pp. 22-27, August, 2009.

[28] MCCONNELL, V. P., "Military UAVs Claiming the Skies with Fuel Cell Power," *Fuel Cells Bulletin*, vol. 2007, no. 12, pp. 12-15, 2007.

[29] THOMAS, J. P., QIDWAI, M. A., and KELLOGG, J. C., "Energy Scavenging for Small-Scale Unmanned Systems," *Journal of Power Sources*, vol. 159, pp. 1494-1509, 2006.

[30] SPIEGEL, C. S., *Designing and Building Fuel Cells*, McGraw-Hill, New York, 2007.

[31] JACOBSON, D., "PEM Fuel Cells," National Institute of Standards and Technology, 2004, http://physics.nist.gov/MajResFac/NIF/pemFuelCells.html, [Online; accessed March 21, 2009].

[32] SCHLAPBACH, L. and ZÜTTEL, A., "Hydrogen-Storage Materials for Mobile Applications," *Nature*, vol. 414, pp. 353-358, 2001.

[33] BREWER, G. D., *Hydrogen Aircraft Technology*, CRC Press, Boca Raton, 1991.

[34] "Comparative Properties of Hydrogen and Fuels," U. S. Department of Energy Hydrogen Analysis Resource Center, 2009, http://hydrogen.pnl.gov/cocoon/morf/hydrogen/article/701, [Online; accessed April 5, 2009].

[35] GREEN, D. and PERRY, R. H., *Perry's Chemical Engineers' Handbook, 7th Edition*, McGraw-Hill, 1997.

[36] "Introducing AEROPAK Long Endurance Power System for 5-10 kg Class UAS," Horizon Fuel Cell Technologies, Singapore, 2009, http://horizonfuelcell.com/aerospace.htm, [Online; accessed August 1, 2009].

[37] MCCONNELL, V. P., "Composites and the Fuel Cell Revolution," *Reinforced Plastics*, vol. 46, no. 1, pp. 38-40, 2002.

[38] MESSAC, A. and HATTIS, P. D., "High Speed Civil Transport (HSCT) Plane Design Using Physical Programming," in *AIAA/ASME/ASCE/AHS/ASC 36th Structures, Structural Dynamics, and Materials Conference*, New Orleans, LA, AIAA 95-1401, 1995.

[39] BEALS, J., BRAUN, R., CHEN, F., CROTEAU, P., EMERSON, S., HAWKES, J., HAUGSTETTER, C., RADCLIFF, T., SUN, E., TEW, D., YAMANIS, J., and ERIKSTRUP, N., "Development of a kW-Class Power Dense Solid Oxide Fuel Cell System," United Technologies Research Center, East Hartford, CT, 2008, http://www.topsoefuelcell.com/tofc/PDF/Development%20of%20a%20kW-Class%20Power%20Dense%20SOFC%20System.pdf, [Online; accessed January 15, 2009].

[40] "3W-28i Specification Sheet," 3W-Modellmotoren GmbH, Roedermark, Germany, http://www.3w-modellmotoren.com/deutsch/3W_Modellmotoren.htm, [Online; accessed 1 August, 2009].

[41] LINDEN, D. and REDDY, T. B., *Handbook of Batteries, 3rd Edition*, McGraw-Hill, New York, 2002.

[42] DORNHEIM, M. A., "Fuel Cells Debut," *Aviation Week and Space Technology*, vol. 158, no. 22, p 52, June 2, 2003.

[43] "H-300 PEM FC System," Horizon Fuel Cell Technologies, 2007, http://www.horizonfuelcell.com/store/h300.htm, [Online; accessed June 2, 2007].

[44] MITCHELL, W. L. and TORO, A., "Advanced Fuel Cell Development for Automotive Operation," in *SAE 2006 World Congress*, Detroit, MI, SAE 2006-01-0035, April 3-6, 2006.

[45] BASU, S., *Recent Trends in Fuel Cell Science and Technology*, Springer, New York, 2007.

[46] CLARKIN, J., "Hydrogen: Opportunities and Challenges," in *AIAA/ICAS International Air and Space Symposium and Exposition: The Next 100 Years*, Dayton, OH, AIAA 2003-2881, July 14-17, 2003.

[47] DECICCO, J., FUNG, F., and AN, F., "Global Warming on the Road: The Climate Impact of America's Automobiles," Environmental Defense, 2006.

[48] PENNER, J. E., ELLIS, J. H., HARRIS, N. R. P., and LISTER, D. H., *Aviation and the Global Atmosphere*, Cambridge University Press, Cambridge, 1999.

[49] SHAHEEN, S. A., WRIGHT, J., and SPERLING, D., "California's Zero Emission Vehicle Mandate - Linking Clean Fuel Cars, Carsharing, and Station Car

Strategies," University of California, Davis, TRB Paper 02-3587, Davis, CA, 2001.

[50] "H2Mobility: Hydrogen Vehicles Worldwide," Tüv Süd Industrie Service, 2008, http://www.netinform.net/h2/H2Mobility/Default.aspx, [Online; accessed November 24, 2008].

[51] YAMAGUCHI, J., "Japan Stays on High Tech Course," *Automotive Engineering International*, SAE, p 70, September, 2003.

[52] WYCZALEK, F. A., "Hydrogen Fuel--Defining the Future," in *2nd International Energy Conversion Engineering Conference*, Providence, RI, AIAA 2004-5606, August 16-19, 2004.

[53] "FCX Clarity: Zero-Emission Hydrogen Powered Fuel Cell Sedan," Honda, 2008, http://automobiles.honda.com/fcx-clarity/, [Online; accessed August 1, 2008].

[54] DÉES, S., KARADELOGLOU, P., KAUFMANN, R. K., and SÁNCHEZ, M., "Modeling the World Oil Market: Assessment of a Quarterly Econometric Model," *Energy Policy*, vol. 35, no. 1, pp. 178-191, 2005.

[55] KAUFMANN, R., "World Oil Market: Living Off the Past, Planning for the Future," Center for Energy and Environmental Studies, Boston University, Boston, 2008.

[56] "Daily Cushing, OK WTI Spot Price FOB," Energy Information Administration, 2008, http://tonto.eia.doe.gov/dnav/pet/hist/rwtcd.htm, [Online; accessed November 24, 2008].

[57] BRADLEY, T. H., MOFFITT, B. A., MAVRIS, D., and PAREKH, D. E., "Development and Experimental Characterization of a Fuel Cell Powered Aircraft," *Journal of Power Sources*, vol. 171, pp. 793-801, 2007.

[58] BRADLEY, T. H., MOFFITT, B. A., PAREKH, D. E., and MAVRIS, D., "Test Results for a Fuel Cell-Powered Demonstration Aircraft," in *Society of Automotive Engineers Power Systems Conference*, New Orleans, LA, November 7-9, 2006.

[59] BRADLEY, T. H., MOFFITT, B. A., PAREKH, D. E., and MAVRIS, D., "Flight Test Results for a Fuel Cell Unmanned Aerial Vehicle," in *45th AIAA Aerospace Sciences Meeting and Exhibit*, Reno, NV, AIAA 2007-32, 2007.

[60] MOFFITT, B. A., BRADLEY, T. H., PAREKH, D. E., and MAVRIS, D., "Design and Performance Validation of a Fuel Cell Unmanned Aerial Vehicle," in *44th AIAA Aerospace Sciences Meeting and Exhibit*, Reno, NV, AIAA-2006-823, January 9-12, 2006.

[61] MOFFITT, B. A., BRADLEY, T. H., PAREKH, D. E., and MAVRIS, D., "Design Space Exploration of Small-Scale PEM Fuel Cell Unmanned Aerial Vehicle," in *6th AIAA Aviation Technology, Integration, and Operations Conference*, Wichita, KS, AIAA 2006-7701, September 25-27, 2006.

[62] MOFFITT, B. A., BRADLEY, T. H., MAVRIS, D., and PAREKH, D. E., "Reducing Uncertainty of a Fuel Cell UAV through Variable Fidelity Optimization," in *7th AIAA ATIO Conference, 2nd CEIAT International Conference on Innovation and Integration in Aero Sciences, 17 LTA Systems*

Technical Conference; , Belfast, Northern Ireland, AIAA 2007-7793, September 18-20, 2007.

[63] BRADLEY, T. H., *Modeling, Design and Energy Management of Fuel Cell Systems for Aircraft*, PhD thesis, Georgia Institute of Technology, Atlanta, GA, December, 2008.

[64] PERRY, M. L. and STRAYER, E., "Fuel-Cell Based Back-Up Power for Telecommunication Applications: Developing a Reliable and Cost-Effective Solution," in *INTELEC 2006 Proceedings*, 2006.

[65] MATSUNAGA, M., FUKUSHIMA, T., and OJIMA, K., "Advances in the Power Train System of Honda FCX Clarity Fuel Cell Vehicle," in *SAE 2009 World Congress*, Detroit, MI, SAE 2009-01-1012, April 20-23, 2009.

[66] HIRSCHENHOFER, J. H., STAUFFER, D. B., ENGLEMAN, R. R., and KLETT, M. G., *The Fuel Cell Handbook, 4th Edition*, Parsons Corporation, Reading, PA, 1998.

[67] "Fuel Cell Handbook, 5th Edition," US Department of Energy, Office of Fossil Energy, National Energy Technology Laboratory, Morgantown, WV, 2000.

[68] BRADLEY, T. H., MOFFITT, B. A., PAREKH, D. E., and MAVRIS, D., "Aviation: Fuel Cells. In:," J. GARCHE, C. DYER, P. MOSELEY, Z. OGUMI, D. RAND, and B. SCROSATI, ed., *Encyclopedia of Electrochemical Power Sources*, Elsevier, Amsterdam, 2009.

[69] BREIT, J. and SZYDLO-MOORE, J., "Fuel Cells for Commercial Transport Airplanes Needs and Opportunities," in *45th AIAA Aerospace Sciences Meeting and Exhibit*, Reno, NV, AIAA 2007-1390, January 8-11, 2007.

[70] "Fuel Cell Types," UTC Power, 2006, http://www.utcpower.com/fs/com/bin/fs_com_Page/0,11491,0269,00.html, [Online; accessed September 27, 2006].

[71] LIANG, A., "Emerging Fuel Cell Developments at NASA for Aircraft Applications," NASA Glenn Research Center, 2003, http://www.netl.doe.gov/publications/proceedings/03/seca/Anita%20Liang.pdf, [Online; accessed March 31, 2009].

[72] CRUMM, A., "Solid Oxide Fuel Cell Systems," in *Proceedings of the Fuel Cell Seminar*, Honolulu, HI, November, 2006.

[73] MOCK, P. and SCHMID, S. A., "Fuel Cells for Automotive Powertrains - A Techno-Economic Assessment," *Journal of Power Sources*, vol. 190, no. 1, pp. 133-140, 2009.

[74] MURAKAMI, Y. and UCHIBORI, K., "Development of Fuel Cell Vehicle with Next-Generation Fuel Cell Stack," in *SAE 2006 World Congress*, Detroit, MI, SAE 2006-01-0034, April 3-6, 2006.

[75] "General Motors Introduces World's Most Powerful Fuel Cell Stack," General Motors, 2001, http://www.auto123.com/en/news/car-news/general-motors-introduces-worlds-most-powerful-fuel-cell-stack?artid=1393&pg=1, [Online; accessed March 27, 2009].

[76] "UTRC Demonstrates First-ever Fuel Cell-Powered Vertical Flight," United Technologies Research Center, East Hartford, CT, 2008, http://www.utrc.utc.com/pages/NewsArticles/20081114_helicopter.html, [Online; accessed January 10, 2009].

[77] "Mini-Helicopters with Fuel Cells," ScienceDaily, 2008, http://www.sciencedaily.com/releases/2008/06/080606102558.htm, [Online; accessed October 15, 2008].

[78] ABUELSAMID, S., "Honey, I Shrunk the Fuel Cell! Next-gen GM Hydrogen Stack Gets Small," Autobloggreen, 2009, http://green.autoblog.com/2009/08/17/honey-i-shrunk-the-fuel-cell-next-gen-gm-hydrogen-stack-gets-s/, [Online; accessed August 18, 2009].

[79] FREESE, C., "Surviving the Advanced Tech Valley of Death," General Motors, 2009, http://fastlane.gmblogs.com/archives/2009/11/surviving_the_advanced_tech_valley_of_death.html, [Online; accessed November 11, 2009].

[80] KIZAKI, M., MIZUNO, H., NONOBE, Y., TAKAHASHI, T., MATSUMOTO, T., and KOBAYASHI, N., "Development of New Toyota FCHV-adv Fuel Cell System," in *SAE 2009 World Congress*, Detroit, MI, SAE 2009-01-1003, April 20-23, 2009.

[81] GRANDE, R., "Composite Pressure Vessel Product List," Carelton Technologies Inc., 2007.

[82] MITLITSKY, F., COLELLA, N. J., MEYERS, B., and ANDERSON, C. J., "Regenerative Fuel Cells for High Altitude Long Endurance Solar Powered Vehicles," in *Intersociety Energy Conversion Engineering Conference*, Atlanta, GA, Lawrence Livermore National Laboratory, August 8-13, 1993.

[83] COLOZZA, A. J., "Hydrogen Storage for Aircraft Applications Overview," NASA/CR-2002-211867, Cleveland, OH, September, 2002.

[84] WALL, R., "Research and Development: EADS Refines Technology Plans," *Aviation Week and Space Technology*, February 2, 2009.

[85] AMENDOLA, S. C., SHARP-GOLDMAN, S. L., JANJUA, M. S., KELLY, M. T., PETILLO, P. J., and BINDER, M., "An Ultrasafe Hydrogen Generator: Aqueous, Alkaline Borohydride Solutions and Ru Catalyst," *Journal of Power Sources*, vol. 85, pp. 186-189, 1999.

[86] KOJIMA, Y., SUZUKI, K.-I., FUKUMOTO, K., SASAKI, M., YAMAMOTO, T., KAWAI, Y., and HAYASHI, H., "Hydrogen Generation Using Sodium Borohydride Solution and Metal Catalyst Coated on Metal Oxide," *International Journal of Hydrogen Energy*, vol. 27, pp. 1029-1034, 2002.

[87] KOJIMA, Y., SUZUKI, K.-I., and KAWAI, Y., "Hydrogen Generation from Lithium Borohydride Solution over Nano-Sized Platinum Dispersed on LiCoO2," *Journal of Power Sources*, vol. 155, pp. 325-328, 2005.

[88] CHAHINE, R. and BOSE, T. K., "Low-Pressure Adsorption Storage of Hydrogen," *International Journal of Hydrogen Energy*, vol. 19, no. 2, pp. 161-164, 1994.

[89] KOJIMA, Y. and SUZUKI, N., "Hydrogen Adsorption and Desorption by Potassium-Doped Superactivated Carbon," *Applied Physics Letters*, vol. 84, no. 20, pp. 4113-4115, 2004.

[90] NOH, J. S., AGARWAL, R. K., and SCHWARZ, J. A., "Hydrogen Storage Systems Using Activated Carbon," *International Journal of Hydrogen Energy*, vol. 12, no. 10, pp. 693-700, 1987.

[91] DILLON, A. C., JONES, K. M., BEKKEDAHL, T. A., KIANG, C. H., BETHUNE, D. S., and HEBEN, M. J., "Storage of Hydrogen in Single-Walled Carbon Nanotubes," *Nature*, vol. 386, pp. 377-379, 1997.

[92] YE, Y., AHN, C. C., WITHAM, C., and FULTZ, B., "Hydrogen Adsorption and Cohesive Energy of Single-Walled Carbon Nanotubes," *Applied Physics Letters*, vol. 74, no. 16, pp. 2307-2309, 1999.

[93] CHAMBERS, A., PARK, C., TERRY, R. T. K., and RODRIGUEZ, N. M., "Hydrogen Storage in Graphite Nanofibers," *The Journal of Physical Chemistry B*, vol. 102, no. 22, pp. 4253-4256, 1998.

[94] ACEVES, S. M., BERRY, G. D., and RAMBACH, G. D., "Insulated Pressure Vessels for Hydrogen Storage on Vehicles," *International Journal of Hydrogen Energy*, vol. 23, no. 7, pp. 583-591, 1998.

[95] SILVERSTEIN, A. and HALL, E. W., "Liquid Hydrogen as a Jet Fuel for High-Altitude Aircraft," National Advisory Committee for Aeronautics, RM E55C28a, Washington DC, 1955.

[96] "STS-96 Shuttle Reference and Data: Space Shuttle External Tank," 1999, http://www.shuttlepresskit.com/STS-96/REF66.htm, [Online; accessed March 25, 2009].

[97] "Space Shuttle External Tank," Wikipedia, http://en.wikipedia.org/wiki/Space_Shuttle_external_tank, [Online; accessed March 25, 2009].

[98] SULLIVAN, R. M., PALCO, J. L., TORNABENE, R. T., BEDNARCYK, B. A., POWERS, L. M., MITAL, S. K., SMITH, L. M., WANG, X. Y. J., and

HUNTER, J. E., "Engineering Analysis Studies for Preliminary Design of Lightweight Cryogenic Hydrogen Tanks in UAV Applications," NASA/TP 2006-214094, May, 2006.

[99] OGDEN, J. M., KREUTZ, T. G., and STEINBUGLER, M. M., "Fuels for Fuel Cell Vehicles," *Fuel Cells Bulletin*, vol. 3, no. 16, pp. 5-13, 2000.

[100] NAES, L. B., LLOYD, B., and SCHICK, S., "WISE Cryogenic Support System Design Overview and Build Status," *Advances in Cryogenic Engineering, Transactions of the Cryogenic Engineering Conference (CEC)*, vol. 53, pp. 815-822, 2008.

[101] COSTANZO, B. J., MENTEUR, P. A., and SCHICK, S., "Design and Performance Analysis of the Wide-Field Infrared Explorer H2/H2 Cryostat," in *Cryogenic Optical Systems and Instruments VII*, SPIE Symposium, 1996.

[102] CIARAVINO, J. S., *Study of Hydrogen as an Aircraft Fuel*, MS thesis, Naval Postgraduate School, Monterey, CA, June, 2003.

[103] MARSH, G., "Building Momentum: Renewables are Making Headway on Land, at Sea and in the Air," *Refocus*, vol. 7, no. 6, pp. 52-55, November/December, 2006.

[104] "Lycoming O-235 Engine Specification," Lycoming Engines, 2009, http://www.lycoming.textron.com/engines/series/235-series-engines.html, [Online; accessed March 5, 2009].

[105] BROWN, G. V., KASCAK, A. F., EBIHARA, B., JOHNSON, D., CHOI, B., SIEBERT, M., and BUCCIERI, C., "NASA Glenn Research Center Program in

High Power Density Motors for Aeropropulsion," NASA/TM-2005-213800, Cleveland, OH, December, 2005.

[106] HARRIS, M. M., JONES, A. C., and ALEXANDER, E. J., "Miniature Turbojet Development at Hamilton Sundstrand, the TJ-50, TJ-120 and TJ-30 Turbojets," in *2nd AIAA "Unmanned Unlimited" Systems, Technologies, and Operations Conference and Exhibit*, San Diego, CA, AIAA 2003-6568, 15-18 September, 2003.

[107] PARSCH, A., "Directory of U.S. Military Rockets and Missiles, Appendix 2: Modern UAVs," 2006, http://www.designation-systems.net/dusrm/app2/q-11.html, [Online; accessed April 3, 2009].

[108] PALOMBO, D., "Motion Control Primer," Aveox, 2006, http://www.aveox.com, [Online; accessed January 5, 2006].

[109] "Desert Aircraft Products List," Tucson, AZ, 2008, http://www.desertaircraft.com/index.php, [Online; accessed November 8, 2008].

[110] "Products," Zanzottera Technologies srl, 2008, http://www.zanzotteraengines.com/product.html, [Online; accessed February 2, 2009].

[111] HENDRICKSON, S. P., "A Miniature Powerplant for Very Small, Very Long Range Autonomous Aircraft," DOE Phase II SBIR Final Report, The Insitu Group, Bingen, WA, 1999.

[112] "US Navy Commissions Cosworth for Heavy Fuel UAV Engine Development," Flightglobal, 2008, http://www.flightglobal.com/articles/2008/03/07/222052/us-

navy-commissions-cosworth-for-heavy-fuel-uav-engine-development.html, [Online; accessed March 1, 2009].

[113] "Sonex Combustion Processes," Sonex Research Inc., Annapolis, MD, 2009, http://www.sonexresearch.com/, [Online; accessed March 15, 2009].

[114] "UAV Engines, the Product Range," UAV Engines LTD, 2009, http://www.uavenginesltd.co.uk/index.php?id=393, [Online; accessed February 18, 2009].

[115] "FCVelocity-HD6 Specification Sheet," Ballard, 2009, http://www.ballard.com/files/pdf/Spec_Sheets/FCvelocity-HD6_docmetrics.pdf, [Online; accessed April 3, 2009].

[116] DUNNE, J., "Honda's New FCX V3 Hydrogen Fuel-Cell Car," *Popular Mechanics*, December, 2000.

[117] "Honda FC Stack: The Honda FCX," Honda, 2009, http://world.honda.com/FuelCell/FCX/fcstack/evolution/, [Online; accessed April 3, 2009].

[118] "Horizon Fuel Cell Technologies H-Series Specification Sheet," 2007, http://www.horizonfuelcell.com/file/H-Series.pdf, [Online; accessed September 1, 2007].

[119] BOUCHER, R., "Project Sunrise, Flight of the Worlds First Solar Powered Aircraft," http://www.projectsunrise.info/First_Solar_Powered_Aircraft.html, [Online; accessed October 5, 2009].

[120] NASA, "Past Project ERAST- Pathfinder/Pathfinder Plus," http://www.nasa.gov/centers/dryden/history/pastprojects/Erast/pathfinder.html, [Online; accessed October 7, 2009].

[121] YOUNGBLOOD, J. W. and TALAY, T. A., "Solar-Powered Airplane Design for Long-Endurance, High-Altitude Flight," in *2nd International Very Large Vehicles Conference*, Washington, D. C., AIAA-1982-811, May 17-18, 1982.

[122] COLOZZA, A. J., "Effect of Power System Technology and Mission Requirements on High Altitude Long Endurance Aircraft," NASA Contractor Report 194455, February, 1994.

[123] NOLL, T. E., BROWN, J. M., PEREZ-DAVIS, M. E., ISHMAEL, S. D., TIFFANY, G. C., and GAIER, M., "Investigation of the Helios Prototype Aircraft Mishap, Volume I: Mishap Report," NASA, Hampton, VA, January, 2004.

[124] "UAS Advanced Development: Hornet," AeroVironment, http://www.avinc.com/uas/adc/hornet/, [Online; accessed October 12, 2008].

[125] "AeroVironment Flies World's First Hydrogen Powered Plane," *Fuel Cells Bulletin*, vol. 2005, no. 9, pp. 2-3, 2005.

[126] "Betriebsanleitung fur das brennstoffzellenbetriebene Modellflugzeug," FH-Wiesbaden, 2005.

[127] KELLOGG, J. C., MONFORTON, L., WHITE, D., and VICK, M., "Fuel Cells for Micro Air Vehicles," in *Joint Service Power Expo*, Tampa, FL, May 5, 2005.

[128] LEBRECHE, T., "Solid Oxide Fuel Cell Power Systems for Small UAVs," in *Joint Service Power Expo*, April 24-26, 2007.

[129] "Fuel Cell Powered UAV Environmentally Friendly," CSLA MFDCLab, http://www.calstatela.edu/centers/mfdclab/research/fcuav.htm, [Online; accessed October 7, 2009].

[130] "World's First Zero Emission, Hydrogen Fuel Cell Jet," Horizon Fuel Cell Technologies, 2007, http://www.horizonfuelcell.com/hyfish.htm, [Online; accessed October 7, 2009].

[131] KAZ, T., "HyFish," SmartFish GmbH, 2006, http://www.smartfish.ch/index.cfm/fuseaction/show/path/1-129.htm, [Online; accessed October 7, 2009].

[132] "Small Unmanned Aerial Vehicle Again Surpasses Record Flight Time Using Protonex Fuel Cell System Technology," Protonex, 2008, http://www.protonex.com/downloads/press-releases/3-11-08_UAV-Flt-Milestone_FINAL.pdf, [Online; accessed March 11, 2008].

[133] CHIANG, C., HERWERTH, C., MIRMIRANI, M., KO, A., MATSUYAMA, S., CHOI, S. B., and NOMNAWEE, N., "Systems Integration of a Hybrid PEM Fuel Cell/Battery Powered Endurance UAV," in *46th AIAA Aerospace Sciences Meeting and Exhibit*, Reno, NV, AIAA 2008-151, January 7-10, 2008.

[134] HERWERTH, C., CHIANG, C., KO, A., MATSUYAMA, S., CHOI, S. B., MIRMIRANI, M., GAMBLE, D., ARENA, A., KOSCHANY, A., GU, G., and WANKEWYCZ, T., "Development of a Small Long Endurance Hybrid PEM Fuel Cell Powered UAV," in *AeroTech Congress & Exhibition*, Los Angeles, CA, SAE 2007-01-3930, 2007.

[135] "Korean Scientists Build Fuel Cell-Powered UAV," Chosun.com, http://english.chosun.com/w21data/html/news/200710/200710100024.html, [Online; accessed June 1, 2008].

[136] MECHAM, M., "Boeing Fuel Cell Flights Point to UAVs," AviationWeek.com, 2008, http://www.aviationweek.com/aw/generic/story_channel.jsp?channel=comm&id=news/CELL04038.xml, [Online; accessed October 7, 2008].

[137] "Fuel Cell Plane in Aviation First," Intelligent Energy, 2008, http://www.intelligent-energy.com/index_article.asp?SecID=8&secondlevel=25&artid=4001, [Online; accessed October 7, 2009].

[138] FRIEND, M. G. and DAGGETT, D. L., "Fuel Cell Demonstrator Airplane," in *AIAA/ICAS International Air and Space Symposium and Exposition: The Next 100 Years*, Dayton, Ohio, AIAA 2003-2868, July 14-17, 2003.

[139] "Adaptive Materials and AeroVironment Achieve 7-Hour UAV Test Flight," Adaptive Materials, 2008, http://www.adaptivematerials.com/internal.php?sid=5&nid=45, [Online; accessed October 7, 2009].

[140] ROONEY, N. and KLESH, A., "SolarBubbles and Adaptive Materials Set World Record with Fuel Cell Powered Aircraft," *Space Times*, American Astronautical Society, pp. 4-6, January/February, 2009.

[141] "Antares DLR-H2 Fuel Cell Aircraft Presented at Stuttgart Airport," German Aerospace Center, 2008, http://www.dlr.de/en/desktopdefault.aspx/tabid-1/86_read-13650/, [Online; accessed September 30, 2008].

[142] "DLR Motor Glider Antares Takes Off in Hamburg - Powered by a Fuel Cell," German Aerospace Center, 2009, http://www.dlr.de/en/desktopdefault.aspx/tabid-1/86_read-18278/, [Online; accessed July 10, 2009].

[143] "Above the Clouds with the Fuel Cell," BASF, 2009, http://www.basf.com/group/corporate/en/news-and-media-relations/science-around-us/fuel-cell/story, [Online; accessed October 5, 2009].

[144] "Boomerang: Long Endurance, Fuel-Cell Powered Mini UAV," Bluebird Aero Systems, 2009, <http://www.bluebird-uav.com/PDF/Boomerang.pdf>, [Online; accessed October 7, 2009].

[145] EGOZI, A., "Paris Air Show: Israeli Bluebird Fuel Cell UAV Completes Development," Flightglobal, 2009, http://www.flightglobal.com/articles/2009/06/14/327952/paris-air-show-israeli-bluebird-fuell-cell-uav-completes.html, [Online; accessed June 14, 2009].

[146] EGOZI, A., "Bluebird Aims for 10h Endurance Fuel Cell For Thunderbird," Flight International, 2008, http://www.flightglobal.com/articles/2008/11/28/319528/bluebird-aims-for-10h-endurance-fuel-cell-for-thunderbird.html, [Online; accessed October 7, 2009].

[147] "NRL's XFC UAS Achieves Flight Endurance Milestone," Naval Research Laboratory, 2009, http://www.nrl.navy.mil/pressRelease.php?Y=2009&R=85-09r, [Online; accessed October 7, 2009].

[148] "Surveillance Vehicles Take Flight Using Alternative Energy," Naval Research Laboratory, 2009, http://www.nrl.navy.mil/pressRelease.php?Y=2009&R=31-09r, [Online; accessed April 5, 2009].

[149] MCCONNELL, V. P., "Education programs: Inquiring student minds want to know how fuel cells work, and how to design them better," *Fuel Cells Bulletin*, vol. 2008, no. 3, pp. 12-15, 2008.

[150] OFOMA, U. C. and WU, C. C., "Design of a Fuel Cell Powered UAV for Environmental Research," in *3rd Unmanned Unlimited Technical Conference, Workshop and Exhibit*, Chicago, IL, AIAA 2004-6384, September 20-23, 2004.

[151] "Protonex Wins More Funding to Advance UAV Power," *Fuel Cells Bulletin*, vol. 2007, no. 9, pp. 3-4, 2007.

[152] "USAF Contract for Protonex UAV Power," *Fuel Cells Bulletin*, vol. 2009, no. 3, pp. 2-3, 2009.

[153] "NanoDynamics Wins ONR Contract to Develop SOFCs for UAVs," *Fuel Cells Bulletin*, vol. 2009, no. 3, pp. 2-3, 2009.

[154] COPPINGER, R., "PICTURE: United Technologies Claims Fuel Cell Helicopter First," Flight International, 2009, http://www.flightglobal.com/articles/2009/12/07/335861/picture-united-technologies-claims-fuel-cell-helicopter-first.html, [Online; accessed December 15, 2009].

[155] MELANSON, D., "Hydrogen Fuel Cell Powered Hyfish Jet Takes Flight," Engadget, 2007, http://www.engadget.com/2007/04/19/hydrogen-fuel-cell-powered-hyfish-jet-takes-flight/, [Online; accessed May 8, 2007].

[156] "Antares DLR-H2 in der Luft," Deutsches Zentrum für Luft-und Raumfahrt, http://www.dlr.de/DesktopDefault.aspx/tabid-5106/8599_read-18278/gallery-1/gallery_read-Image.1.10123/, [Online; accessed November 1, 2009].

[157] "PEM Fuel Cell System for UAV," KAIST Rocket Lab, 2009, http://rocket.kaist.ac.kr/03_sub_05.htm, [Online; accessed October 7, 2009].

[158] SMITH, H. R., "Soaring High," NASA, 2008, http://www.nasa.gov/audience/forstudents/postsecondary/features/soaring-high.html, [Online; accessed November 1, 2009].

[159] "BlueBird Aero Systems, Horizon Unveil World's First Commercial Fuel Cell UAS," Horizon Fuel Cell Technologies, 2009, http://www.hes.sg/files/BlueBirdHorizonAugust62009.pdf, [Online; accessed August 20, 2009].

[160] "NRL's Ion Tiger Sets 26-Hour Flight Endurance Record," Naval Research Laboratory, 2009, http://www.nrl.navy.mil/pao/pressRelease.php?R=126-09r&Y=2009, [Online; accessed November 24, 2009].

[161] SANDERS, V., "On a Wing and a Fuel Cell," WPI Transformations, 2003, http://www.wpi.edu/News/Transformations/2002Fall/onawing.html, [Online; accessed October 7, 2009].

[162] DUNN, J. P., "Fuel Cell Powered Electric Aircraft," U.S. Patent 6,568,633 B2, May 27, 2003.

[163] ROMEO, G., MORAGLIO, I., and NOVARESE, C., "ENFICA-FC: Preliminary Survey and Design of 2-Seat Aircraft Powered by Fuel Cells Electric Propulsion,"

in *7th AIAA Aviation Technology, Integration and Operations Conference (ATIO)*, Belfast, Northern Ireland, AIAA 2007-7754, September 18-20, 2007.

[164] "SkySpark: Eco-Friendly Aircraft World Record Challenge," SkySpark, 2009, http://www.skyspark.eu/web/eng/index.php, [Online; accessed October 8, 2009].

[165] "BlueBird Continues Use of Fuel Cell Technology with Upcoming Release," *Unmanned Systems*, Association for Unmanned Vehicle Systems International, vol. 27, no. 7, July, 2009.

[166] WENTZ, W. H., MYOSE, R. Y., and MOHAMED, A. S., "Hydrogen-Fueled General Aviation Airplanes," in *5th AIAA ATIO and 16th Lighter-Than-Air Sys. Tech. and Balloon Systems Conferences*, Arlington, VA, AIAA 2005-7324, 2005.

[167] KOHOUT, L. L. and SCMITZ, P. C., "Fuel Cell Propulsion Systems for an All-Electric Personal Air Vehicle," NASA/TM 2003-212354, Cleveland, OH, June, 2003.

[168] BERTON, J. J., FREEH, J. E., and WICKENHEISER, T. J., "An Analytical Performance Assessment of a Fuel Cell-Powered, Small Electric Airplane," NASA/TM - 2003-212393, Cleveland, OH, 2003.

[169] WENTZ, W. H. and MOHAMED, A. S., "Preliminary Design Considerations for Zero Greenhouse Gas Emission Airplanes," in *General Aviation Technology Conference and Exhibit*, Wichita, KS, SAE 2004-01-1803, April 20-22, 2004.

[170] "Numerical Propulsion System Simulation User Guide and Reference," NASA-Industry Cooperative Effort, Software Release NPSS 1.5.0, May 7, 2002.

[171] KOEHLER, T., "Into the Wild Green Yonder," *Boeing Frontiers*, The Boeing Company, vol. 06, no. 03, Seattle, WA, pp. 12-15, July, 2007.

[172] NICKOL, C. L., GUYNN, M. D., KOHOUT, L. L., and OZOROSKI, T. A., "High Altitude Long Endurance Air Vehicle Analysis of Alternatives and Technology Requirements Development," in *45th AIAA Aerospace Sciences Meeting and Exhibit*, Reno, NV, AIAA 2007-1050, January 8-11, 2007.

[173] GUYNN, M. D., FREEH, J. E., and OLSON, E. D., "Evaluation of a Hydrogen Fuel Cell Powered Blended-Wing-Body Aircraft Concept for Reduced Noise and Emissions," NASA TM-2004-212989, Hampton, VA, February, 2004.

[174] CHOI, T. P., SOBAN, D. S., and MAVRIS, D., "Creation of a Design Framework for All-Electric Aircraft Propulsion Architectures," in *3rd International Energy Conversion Engineering Conference*, San Francisco, CA, August 18, 2005.

[175] CHOI, T. P., NAM, T., and SOBAN, D. S., "Novel Synthesis and Analysis Methods Development towards the Design of Revolutionary Electric Propulsion and Aircraft Architectures," in *Infotech*, Arlington, VA, AIAA 2005-7188, September 26-29, 2005.

[176] NAM, T., *A Generalized Sizing Method for Revolutionary Concepts Under Probabilistic Design Constraints*, Ph. D thesis, Georgia Institute of Technology, Atlanta, GA, May, 2007.

[177] SOBAN, D. S. and UPTON, E., "Design of a UAV to Optimize Use of Fuel Cell Propulsion Technology," in *Infotech*, Arlington, VA, AIAA 2005-7135, September 26-29, 2005.

[178] MAVRIS, D., BANDTE, O., and DELAURENTIS, D. A., "Robust Design Simulation: A Probabilistic Approach to Multidisciplinary Design," *Journal of Aircraft*, vol. 36, no. 1, pp. 298-307, 1999.

[179] BANDTE, O., *A Probabilistic Multi-Criteria Decision Making Technique for Conceptual and Preliminary Aerospace System Design*, PhD thesis, Georgia Institute of Technology, Atlanta, GA, September, 2000.

[180] CHOI, T. P., *A Recourse-Based Solution Approach to the Design of Fuel Cell Aeropropulsion Systems*, PhD thesis, Georgia Institute of Technology, Atlanta, GA, April, 2008.

[181] CADOU, C., MOULTON, N., and MENON, S., "Performance Measurement and Scaling in Small Internal Combustion Engines," in *41st Aerospace Sciences Meeting and Exhibit*, Reno, NV, AIAA 2003-671, January 6-9, 2003.

[182] WICKENHEISER, T. J., SEHRA, A. K., SENG, G. T., FREEH, J. E., and BERTON, J. J., "Emissionless Aircraft - Requirements and Challenges," in *AIAA/ICAS International Air and Space Symposium and Exposition: The Next 100 Years*, Dayton, OH, AIAA 2003-2810, July 14-17, 2003.

[183] ALEXANDER, D. S., "Advanced Energetics for Aeronautical Applications," NASA / CR-2003-212169, Hampton, VA, February, 2003.

[184] GUYNN, M. D. and OLSON, E. C., "Evaluation of an Aircraft Concept with Over-Wing, Hydrogen-Fueled Engines for Reduced Noise and Emissions," NASA / TM-2202-211926, Hampton, VA, 2002.

[185] SMITH, J. R., BATISH, P. G., BRANDT, S. A., and MORTON, S. A., "A Student Developed Sizing Methodology for Electric Powered Aircraft Applied to Small UAVs," in *2000 World Aviation Conference*, San Diego, CA, AIAA 2000-5536, October 10-12, 2000.

[186] HARMATS, M. and WEIHS, D., "Rigid Sizing Procedure for Hybrid-Propulsion System," *Journal of Aircraft*, vol. 36, no. 2, pp. 321-331, 1999.

[187] ZHOU, L. and CURRIE, K., "Uncertainty Analysis in the Preliminary Stage for Robust Multidisciplinary Design," in *10th AIAA/ISSMO Multidisciplinary Analysis and Optimization Conference*, Albany, NY, AIAA 2004-4469, August 30-September 1, 2004.

[188] TORENBEEK, E., *Synthesis of Subsonic Airplane Design*, Kluwer Academic Publishers, Norwell, MA, 1982.

[189] MORIKAWA, H., KIKUCHI, H., and SAITO, N., "Development and Advances of a V-Flow FC Stack for FCX Clarity," in *SAE 2009 World Congress*, Detroit, MI, SAE 2009-01-1010, April 20-23, 2009.

[190] SOBIESZCZANSKI-SOBIESKI, J., "Sensitivity of Complex, Internally Coupled Systems," *AIAA Journal*, vol. 28, no. 1, 1990.

[191] MCDONALD, R. A., *Error Propagation and Metamodeling for a Fidelity Tradeoff Capability in Complex Systems Design*, PhD thesis, Georgia Institute of Technology, Atlanta, GA, August, 2006.

[192] GU, X., RENAUD, J. E., and BATILL, S. M., "An Investigation of Multidisciplinary Design Subject to Uncertainty," in *7th AIAA/USAF/NASA/ISSMO Symposium on Multidisciplinary Analysis and Optimization*, St. Louis, MO, AIAA 98-4747, September 2-4, 1998.

[193] MATTSON, C. A. and MESSAC, A., "Pareto Frontier Based Concept Selection under Uncertainty, with Visualization," *Optimization and Engineering*, vol. 6, pp. 85-115, 2005.

[194] OBERKAMF, W. L., DELAND, S. M., RUTHERFORD, B. M., DIEGERT, K. V., and ALVIN, K. F., "Estimation of Total Uncertainty in Modeling and Simulation," Sandia National Laboratories SAND2000-0824, Albuquerque, NM, 2000.

[195] AGARWAL, H., *Reliability Based Design Optimization: Formulations and Methodologies*, PhD thesis, Notre Dame, December, 2004.

[196] SUPLEE, C., "Weighing Our World: 300 Years after Newton, Measuring Gravity Still a Heavy-Duty Task," *The Gazette*, Montreal, Quebec, p J10, May 6, 2000.

[197] GREEN, L. L., LIN, H.-Z., and KHALESSI, M. R., "Probabilistic Methods for Uncertainty Propagation Applied to Aircraft Design," in *20th AIAA Applied Aerodynamics Conference*, St. Louis, MO, AIAA 2002-3140, June 24-26, 2002.

[198] WU, C. F. J. and HAMADA, M., *Experiments Planning, Analysis, and Parameter Design Optimization*, John Wiley & Sons, New York, 2000.

[199] PUTKO, M. M., PERRY, A. N., TAYLOR, A. C., and GREEN, L. L., "Approach for Uncertainty Propagation and Robust Design in CFD using Sensitivity Derivatives," in *15th AIAA Computational Fluid Dynamics Conference*, Anaheim, CA, AIAA 2001-2528, June 11-14, 2001.

[200] LIU, H. and CHEN, W., "Probabilistic Sensitivity Analysis Methods for Design Under Uncertainty," in *10th AIAA/ISSMO Multidisciplinary Analysis and Optimization Conference*, Albany, New York, AIAA-2004-4589, August 30-September 1, 2004.

[201] HAJELA, P., BLOEBAUM, C., and SOBIESZCZANSKI-SOBIESKI, J., "Application of Global Sensitivity Equations in Multidisciplinary Aircraft Synthesis," *Journal of Aircraft*, vol. 27, no. 12, pp. 1002-1010, 1990.

[202] SOBIESZCZANSKI-SOBIESKI, J., "Sensitivity Analysis and Multidisciplinary Optimization for Aircraft Design: Recent Advances and Results," *Journal of Aircraft*, vol. 27, no. 12, 1990.

[203] SOBIESZCZANSKI-SOBIESKI, J., "A System Approach to Aircraft Optimization," NASA TM-104074, March, 1991.

[204] OLDS, J., "System Sensitivity Analysis Applied to the Conceptual Design of a Dual-Fuel Rocket SSTO," in *5th AIAA/NASA/USAF/ISSMO Symposium on Multidisciplinary Analysis and Optimization*, Panama City Beach, FL, AIAA 94-4339, September 7-9, 1994.

[205] MCDONALD, R. A., "Error Allocation in Complex Systems Design," in *11th AIAA/ISSMO Multidisciplinary Analysis and Optimization Conference*, Portsmouth, VA, AIAA 2006-7130, September 6-8, 2006.

[206] BRADLEY, T. H., MOFFITT, B. A., PAREKH, D. E., and FULLER, T., "Energy Management for Fuel Cell Powered Hybrid-Electric Aircraft," in *7th International Energy Conversion Engineering Conference*, Denver, CO, AIAA 2009-4590, August 2-5, 2009.

[207] "1998/1999 AIAA Foundation Cessna/ONR Student Design Build Fly Competition," Utah State University, Logan, UT, 1999.

[208] "1999/2000 AIAA Foundation Cessna/ONR Student Design Build Fly Competition," Utah State University, Logan, UT, 2000.

[209] NOLAND, D., "Steve Fossett and Burt Rutan's Ultimate Solo: Behind the Scenes," Popular Mechanics, 2005, http://www.popularmechanics.com/science/air_space/1262012.html?page=1, [Online; accessed June 1, 2007].

[210] HOERNER, S. F., *Fluid-Dynamic Drag: Theoretical, Experimental and Statistical Information*, Hoerner Fluid Dynamics, Bakersfield, CA, 1965.

[211] DIEHL, W. S., *Engineering Aerodynamics, Revised Edition*, Ronald Press Company, New York, 1936.

[212] ROSKAM, J., *Airplane Design Part VI: Preliminary Calculation of Aerodynamic Thrust and Power Characteristics*, Design Analysis and Research, 2000.

[213] THOMAS, F. and MILGRAM, J., *Fundamentals of Sailplane Design*, College Park Press, College Park, MD, 1999.

[214] LINDAHL, P. A., *Simulation, Design and Validation of a UAV SOFC Propulsion System*, MS thesis, Montana State University, Bozeman, MT, 2009.

[215] KNIGHT, M. and NOYES, R. W., "Wind Tunnel Pressure Distribution Tests on a Series of Biplane Wing Models," National Advisory Committee for Aeronautics, Report No. 310, Washington D. C., 1929.

[216] KNIGHT, M. and WENZINGER, C. J., "Wind Tunnel Tests on a Series of Wing Models through a Large Angle of Attack Range Part I -- Force Tests," National Advisory Committee for Aeronautics, Report No. 317, Washington D. C., 1929.

[217] YEDAMALE, P., "Brushless DC (BLDC) Motor Fundamentals," Microchip Technology Inc., AN885, Chandler, AZ, 2003.

[218] KIM, C. G., LEE, J. H., KIM, H. W., and YOUN, M. J., "Study on Maximum Torque Generation for Sensorless Controlled Brushless DC Motor with Trapezoidal Back EMF," *Electric Power Applications, IEE Proceedings*, vol. 152, no. 2, pp. 277-291, 2005.

[219] BOUCHER, R. J., *The Electric Motor Handbook*, AstroFlight, Marina, Del Rey, CA, 1994.

[220] "MotoCalc Motor Table," MotoCalc, 2009, http://www.motocalc.com/data/motor.html, [Online; accessed January 5, 2006].

[221] OGASAWARA, S. and AKAGI, H., "An Approach to Position Sensorless Drive for Brushless DC Motors," *IEEE Transactions on Industry Applications*, vol. 27, no. 5, pp. 928-933, 1991.

[222] PHILLIPS, W. F., "Propeller and Motor Class Notes," Utah State University, Logan, UT, 1999 (unpublished).

[223] "Vergleich eines SLS-42-220 mit einem blockkommutierended Regler mittels Leistungsmessung auf der DC-Eingangsseite," SinusLeistungsSteller, 2007, http://www.sinusleitungssteller.de/P01.pdf, [Online; accessed February 25, 2009].

[224] "AXI Model Motors," Modelmotors Ltd., 2009, http://www.modelmotors.cz/, [Online; accessed March 9, 2009].

[225] "2004/2005 AIAA Foundation Cessna/ONR Design Build Fly Competition (Extended Report)," Utah State University, Logan, UT, 2005.

[226] MERCHANT, M. and MILLER, L. S., "Propeller Performance Measurement for Low Reynolds Number UAV applications," in *44th AIAA Aerospace Sciences Meeting and Exhibit*, Reno, NV, AIAA 2006-1127, 2006.

[227] PHILLIPS, W. F., *Mechanics of Flight*, John Wiley and Sons, Inc, Hoboken, NJ, 2004.

[228] BETZ, A., "The Theory of the Screw Propeller," Reprint from "Die Naturwissenschaften," 1921, No 18, National Advisory Committee for Aeronautics, Technical Note No. 83, 1922.

[229] BETZ, A., with an appendix by PRANDTL, L., "Schraubenpropeller mit Geringstem Energieverlust," in *Nachrichten der Gesellschaft der Wissenschaften zu Göttingen, Math. physik K1*, Göttingen, pp. 193-213, 1919.

[230] GOLDSTEIN, S., "On the Vortex Theory of Screw Propellers," *Proceedings of the Royal Society of London. Series A, Containing Papers of a Mathematical and Physical Character*, vol. 123, no. 792, pp. 440-465, 1929.

[231] THEODORSEN, T., *Theory of Propellers*, McGraw-Hill, New York, 1948.

[232] TANGLER, J. L., "The Nebulous Art of Using Wind Tunnel Aerofoil Data for Predicting Rotor Performance," *Wind Energy*, vol. 5, no. 2-3, pp. 245-257, 2002.

[233] HALLISSY, J. M. and CHATTOT, J.-J., "Validation of a Helicoidal Vortex Model with the NREL Unsteady Aerodynamic Experiment," in *43rd AIAA Aerospace Sciences Meeting and Exhibit*, Reno, NV, AIAA 2005-1454, January 10-13, 2005.

[234] OKULOV, V. L. and SORENSEN, J. N., "Optimum Operating Regimes for the Ideal Wind Turbine," *Journal of Physics: Conference Series*, vol. 75, no. 012009, 2007.

[235] RIBNER, H. S. and FOSTER, S. P., "Ideal Efficiency of Propellers: Theodorsen revisited," *Journal of Aircraft*, vol. 27, no. 9, pp. 810-819, 1991.

[236] WESTMORELAND, W. S., TRAMEL, R. W., and BARBER, J., "Modeling Propeller Flow-Fields Using CFD," in *46th AIAA Aerospace Sciences Meeting and Exhibit*, Reno, NV, AIAA 2008-402, January 7-10, 2008.

[237] WALD, Q. R., "The Aerodynamics of Propellers," *Progress in Aerospace Sciences*, vol. 42, pp. 85-128, 2006.

[238] TIBERY, C. L. and WRENCH, J. W., "Tables of the Goldstein Factor," Applied Mathematics Laboratory, Washington, D.C., 1964.

[239] OKULOV, V. L., "On the Stability of Multiple Helical Vortices," *Journal of Fluid Mechanics*, vol. 521, pp. 319-342, 2004.

[240] "Advanced Precision Composites Propellers," Landing Products, Woodland, CA, 2007, http://www.apcprop.com, [Online; accessed April 1, 2007].

[241] MOFFITT, B. A., BRADLEY, T. H., PAREKH, D. E., and MAVRIS, D., "Validation of Vortex Propeller Theory for UAV Design with Uncertainty Analysis," in *46th AIAA Aerospace Sciences Meeting and Exhibit*, Reno, NV, AIAA 2008-406, January 7-10, 2008.

[242] DRELA, M., "XFOIL: An Analysis and Design System for Low Reynolds Number Airfoils," in *Conference Proceeding on Low Reynolds Number Aerodynamics*, Notre Dame, IN, June 5-7, 1989.

[243] SHELDAHL, R. E. and KLIMAS, P. C., "Aerodynamic Characteristics of Seven Symmetrical Airfoil Sections through 180 Degree Angle of Attack for use in Aerodynamic Analysis of Vertical Axis Wind Turbines," Sandia National Laboratories, SAND80-2114, Albuquerque, NM, 1981.

[244] LOWRY, J. T., "The Bootstrap Approach to Aircraft Performance (Part Two - Constant-Speed Propeller Airplanes)," AVweb, 1999, http://www.avweb.com/news/airman/182418-1.html, [Online; accessed March 1, 2006].

[245] LOWRY, J. T., *Performance of Light Aircraft*, AIAA Education Series, Reston, VA, 1999.

[246] KULIKOVSKY, A. A., "The Effect of Stoichiometric Ratio on the Performance of a Polymer Electrolyte Fuel Cell," *Electrochimica Acta*, vol. 49, no. 4, pp. 617-625, 2004.

[247] "Gore Primea 58 Series Membrane Electrode Assemblies," W. L. Gore and Associates, 2003, http://www.gore.com/MungoBlobs/primea_58_mea_datasheet.pdf, [Online; accessed August 1, 2006].

[248] TAM, W. H., GRIFFIN, P. S., and JACKSON, A. C., "Design and Manufacture of a Composite Overwrapped Pressurant Tank Assembly," in *38th AIAA/ASME/SAE/ASEE Joint Propulsion Conference and Exhibit*, Indianapolis, IN, AIAA 2002-4349, July 7-10, 2002.

[249] MCQUARRIE, D. A. and SIMON, J. D., *Physical Chemistry: A Molecular Approach*, University Science Books, Sausalito, CA, 1997.

[250] LARK, R. F., "Recent Advances in Lightweight, Filament-Wound Composite Pressure Vessel Technology," NASA TM 73699, Cleveland, OH, 1977.

[251] HARRIS, J., GRANDE, R., and HIGGINS, M., "Ultralight Propellant Tank for NASA Space Technology 5," in *39th AIAA/ASME/SAE/ASEE Joint Propulsion Conference and Exhibit*, Huntsville, AL, AIAA 2003-4608, July 20-23, 2003.

[252] "Carbon Fiber Tubes," CST Composites, 2006, http://www.cstcomposites.com/, [Online; accessed February 1, 2006].

[253] "New Motors 1910 Specification Sheet," 2007, http://www.neumotors.com, [Online; accessed September 1, 2007].

[254] "CF Propellers," Bolly Aviation, 2006, http://www.bolly.com.au, [Online; accessed August 1, 2006].

[255] ANDERSON, J. D., *Fundamentals of Aerodynamics*, McGraw-Hill, New York, 1991.

[256] PRANDTL, L. and TIETJENS, O. G., *Applied Hydro and Aeromechanics*, Dover, New York, 1934.

[257] PHILLIPS, W. F. and SNYDER, D. O., "Modern Adaptation of Prandtl's Classic Lifting-Line Theory," *Journal of Aircraft*, vol. 37, no. 4, pp. 662-670, 2000.

[258] PHILLIPS, W. F. and ALLEY, N. A., "Predicting Maximum Lift Coefficient for Twisted Wings Using Lifting-Line Theory," *Journal of Aircraft*, vol. 44, no. 3, pp. 889-910, 2007.

[259] PISTOLESI, E., "Betrachtungen über die gegenseitige Beeinflussung von Tragflügelsystemen," Mittler & Sohn, Berlin, 1937.

[260] PHILLIPS, W. F. and SNYDER, D. O., "Application of Lifting-Line Theory to Systems of Lifting Surfaces," in *38th Aerospace Sciences Meeting & Exhibit*, Reno, NV, AIAA 2000-0653, January 10-13, 2000.

[261] ASHBY, D. L., DUDLEY, M. R., and IGUCHI, S. K., "Development and Validation of an Advanced Low-Order Panel Method," NASA TN-101024, October, 1988.

[262] BUSH, R. H., POWER, G. D., and TOWNE, C. E., "WIND: The Production Flow Solver of the NPARC Alliance," in *36th Aerospace Sciences Meeting and Exhibit*, Reno, NV, AIAA 98-0935, January 12-15, 1998.

[263] MCALISTER, K. W. and TAKAHASHI, R. K., "NACA 0015 Wing Pressure and Trailing Vortex Measurements," NASA TP-3151, November, 1991.

[264] COLE, J., "Single Wing Calculations using VORLAX/VSP and Numerical Lifting-Line Theory," Georgia Institute of Technology, Atlanta, GA, 2008 (unpublished).

[265] OSTOWARI, C. and NAIK, D., "Experimental Study of Three-Lifting-Surface Configuration," *Journal of Aircraft*, vol. 25, no. 2, pp. 106-112, 1987.

[266] OLSON, E. C. and SELBERG, B. P., "Experimental Determination of Improved Aerodynamic Characteristics Utilizing Biplane Wing Configurations," *Journal of Aircraft*, vol. 13, no. 4, pp. 256-261, 1975.

[267] WENZINGER, C. J. and HARRIS, T. A., "Wind Tunnel Force Tests in Wing Systems through Large Angles of Attack," National Advisory Committee for Aeronautics, Report No. 294, Washington D.C. , August, 1928.

[268] LYON, C. A., BROEREN, A. P., GIGUERE, P., GOPALARATHNAM, A., and SELIG, M. S., *Summary of Low-Speed Airfoil Data: Volume 3*, SoarTech Publications, Virginia Beach, VA, 1997.

[269] ABBOTT, I. H. and VON DOENHOFF, A. E., *Theory of Wing Sections Including a Summary of Airfoil Data*, Dover, New York, 1959.

[270] HOFFMAN, J. D., *Numerical Methods for Engineers and Scientists*, McGraw-Hill, New York, 1992.

[271] COE, P. L., "Review of Drag Cleanup Tests in Langley Full-Scale Tunnel (From 1935 to 1945) Applicable to Current General Aviation Airplanes," NASA TN D-8206, Hampton, VA, June, 1976.

[272] BRADLEY, T. H., MOFFITT, B. A., PAREKH, D. E., and MAVRIS, D., "Validated Modeling and Synthesis of Medium-Scale PEM Fuel Cell Aircraft," in *4th International ASME Conference on Fuel Cell Science, Engineering and Technology*, Irvine, CA, ASME, June 18-21, 2006.

[273] MOFFITT, B. A., BRADLEY, T. H., PAREKH, D. E., and MAVRIS, D., "Design Space Exploration of Small-Scale PEM Fuel Cell Unmanned Aerial Vehicle," in *6th AIAA Aviation Technology, Integration and Operations Conference*, Wichita, KS, AIAA 2006-7701, September 25-27, 2006.

[274] "JMP V7.0.1," SAS Institute, Cary, NC, 2007.

[275] "JMP V7.0.1 Statistics and Graphics Guide: Neural Nets," SAS Institute, Cary, NC, 2007.

[276] "Matlab V 6.5.0 Release 13," The Mathworks, Inc., Natick, MA, 2002.

[277] KROO, I., ALTUS, S., BRAUN, R., GAGE, P., and SOBIESKI, I., "Multidisciplinary Optimization Methods for Aircraft Preliminary Design," in *5th AIAA/USAF/NASA/ISSMO Symposium on Multidisciplinary Analysis and Optimization*, Panama City Beach, FL, AIAA-94-4325-CP, September 7-9, 1994.

[278] ROGERS, J. L., "DeMaid -- A Design Manager's Aid for Intelligent Decomposition, Users Guide," NASA TM-101575, March, 1989.

[279] ARIAN, E., "Convergence Estimates for Multidisciplinary Analysis and Optimization," NASA CR-201752, Hampton, VA, 1997.

[280] POWELL, M. J. D., "A Fortran Subroutine for Solving Systems of Nonlinear Algebraic Equations," P. RABINOWITZ, ed., *Numerical Methods for Nonlinear Algebraic Equations*, Gordon and Breach Science Publishers, London, 1970.

[281] MORE, J. J., GARBOX, B. S., and HILLSTROM, K. E., "User Guide for MINIPACK 1," Argonne National Laboratory, ANL-80-74, Argonne, IL, 1980.

[282] LEVENBERG, K., "A Method for the Solution of Certain Non-linear Problems in Least Squares," *Quarterly of Applied Mathematics*, vol. 2, no. 2, pp. 164-168, 1944.

[283] MARQUARDT, D. W., "An Algorithm for the Least-Squares Estimation of Nonlinear Parameters," *SIAM Journal of Applied Mathematics*, vol. 11, no. 2, pp. 431-441, 1963.

[284] DENNIS, J. E., "Nonlinear Least-Squares," D. JACOBS, ed., *State of the Art in Numerical Analysis*, Academic Press, New York, 1977.

[285] KEANE, A. J. and NAIR, P. B., *Computational Approaches for Aerospace Design*, John Wiley and Sons Ltd, West Sussex, 2005.

[286] COLEMAN, T. F. and LI, Y., "An Interior, Trust Region Approach for Nonlinear Minimization Subject to Bounds," *SIAM Journal on Optimization*, vol. 6, pp. 418-445, 1996.

[287] COLEMAN, T. F. and LI, Y., "On the Convergence of Reflective Newton Methods for Large-Scale Nonlinear Minimization Subject to Bounds," *Mathematical Programming*, vol. 67, no. 2, pp. 189-224, 1994.

[288] RAO, S. S. and CHEN, L., "Numerical Solution of Fuzzy Linear Equations in Engineering Analysis," *International Journal for Numerical Methods in Engineering*, vol. 43, pp. 391-408, 1998.

[289] BEN-HAIM, Y. and ELISHAKOFF, I., *Convex Models of Uncertainty in Applied Mechanics*, Elsevier Science, Amsterdam, 1990.

[290] BEN-HAIM, Y., *Information Gap Decision Theory: Decisions Under Severe Uncertainty,* Academic Press, London, 2001.

[291] HEMEZ, F. M. and BEN-HAIM, Y., "Info-Gap Robustness for the Correlation of Tests and Simulations of a Non-Linear Transient," *Mechanical Systems and Signal Processing*, vol. 18, pp. 1443-1467, 2004.

[292] KOKKOLARAS, M., MOURELATOS, Z. P., LOUCA, L., FILIPI, Z., DELAGRAMMATIKAS, G., STEFANOPOULOU, A., PAPALAMBROS, P., and ASSANIS, D., "Design Under Uncertainty and Assessment of Performance Reliability of a Dual-Use Medium Truck with Hydraulic-Hybrid Powertrain and Fuel Cell Auxiliary Power Unit," in *SAE World Congress*, Detroit, MI, SAE 2005-01-1396, 2005.

[293] VANDERPLAATS, G. N., *Numerical Optimization Techniques for Engineering Design*, Vanderplaats Research and Development, Inc., Colorado Springs, CO, 2001.

[294] ZOUTENDIJK, G., *Methods of Feasible Directions: A Study in Linear and Non-linear Programming*, Elsevier, Amsterdam, 1960.

[295] LUENBERGER, D., *Linear and Nonlinear Programming, 2nd Edition*, Kluwer Academic Publishers, Norwell, MA, 1984.

[296] WALKER, R. C., *Introduction to Mathematical Programming*, Prentice Hall, Upper Saddle River, NJ, 1999.

[297] FIACCO, A. V. and MCCORMICK, G. P., *Nonlinear Programming: Sequential Unconstrained Minimization Techniques*, John Wiley and Sons, New York, 1968.

[298] NELDER, J. A. and MEAD, R., "A Simplex Method for Function Minimization," *The Computer Journal*, vol. 7, no. 4, pp. 308-313, 1965.

[299] LAGARIAS, J. C., REEDS, J. A., WRIGHT, M. H., and WRIGHT, P. E., "Convergence Properties of the Nelder-Mead Simplex Method in Low Dimensions," *SIAM Journal of Optimization*, vol. 9, no. 1, pp. 112-147, 1998.

[300] BRADLEY, T. H., MOFFITT, B. A., MAVRIS, D., FULLER, T., and PAREKH, D. E., "Hardware-in-the-Loop Testing of a Fuel Cell Aircraft Powerplant," *Journal of Propulsion and Power*, vol. 25, no. 6, pp. 1336-1344, 2009.

[301] GUR, O. and ROSEN, A., "Optimization of Propeller Based Propulsion System," *Journal of Aircraft*, vol. 46, no. 1, pp. 95-106, 2009.

[302] RAMANI, V., "Fuel Cells," *Electrochemistry Society Interface*, vol. 15, no. 1, pp. 41-44, 2006.

VITA

Blake Moffitt was born in Twin Falls Idaho in 1975. He attended Utah State University and graduated in 2000 with his Bachelor of Science in Mechanical Engineering. Blake's senior design project consisted of the design of a small aircraft that won the top prize in the 1999/2000 AIAA Design/Build/Fly student competition. In 2000, Blake began working at the Space Dynamics Laboratory (SDL) in Logan, UT and became the thermal engineer for the Combat Sentinel program. While working at SDL, Blake became an assistant to Professor Frank J. Redd and assisted in teaching graduate astrodynamics and propulsion classes. In 2003, Blake received his Master of Science in Mechanical Engineering from Utah State University and under the guidance of Professor J. Clair Batty, published his thesis entitled "Predictive Thermal Analysis of the Combat Sentinel Satellite Test Article."

In 2003, Blake joined the Aerospace Systems Design Laboratory (ASDL) at the Georgia Institute of Technology to pursue his doctorate. In 2004, Blake began collaborating with the Georgia Tech Research Institute to develop a fuel cell demonstrator vehicle. In 2006, the vehicle became one of the earliest and largest fuel cell vehicles to achieve flight. Blake's experience at ASDL helped refine his areas of interest which include multidisciplinary design optimization, unmanned aerial vehicles, probabilistic design methods, and electric propulsion.

In 2008, Blake began working at the United Technologies Research Center in East Hartford, Connecticut and is currently a member of the Integrated Total Aircraft Power Systems (ITAPS) team. Blake currently resides in South Windsor, CT with his wife Jan and his three sons, Ethan, Almy, and Nolan.